Circadian Rhythm and Cell Cycle: two Synchronized Processes

THÈSE N^{O} 6902 (2016)

PRÉSENTÉE LE 30 SEPTEMBRE 2016

À LA FACULTÉ DES SCIENCES DE LA VIE

UNITÉ DU PROF. NAEF

PROGRAMME DOCTORAL EN APPROCHES MOLÉCULAIRES DU VIVANT

ÉCOLE POLYTECHNIQUE FÉDÉRALE DE LAUSANNE

POUR L'OBTENTION DU GRADE DE DOCTEUR ÈS SCIENCES

PAR

Rosamaria CANNAVO

acceptée sur proposition du jury:

Prof. N. Harris, présidente du jury
Prof. F. Naef, directeur de thèse
Prof. F. Delaunay, rapporteur
Prof. D. Gatfield, rapporteur
Prof. P. Gönczy, rapporteur

ÉCOLE POLYTECHNIQUE
FÉDÉRALE DE LAUSANNE

Suisse
2016

"Life is about rhythm.
We vibrate, our hearts are pumping blood,
we are a rhythm machine, that's what we are."
Mickey Hart

To my family…

Abstract

Circadian rhythms are biological processes found in most living organisms, displaying a roughly 24-hour period, responding primarily to light darkness cycles in an organism's environment. At the cellular level, the circa-24h rhythmicity is generated by a molecular clock based on a transcription-translation feedback network. The circadian clock temporally orchestrates many aspects of cellular physiology and consists of a cell-autonomous and self-sustained oscillator with a period of about 24 hours. In conditions where cells proliferate, the cell division cycle can be also considered as an oscillator. Since both processes run with similar periods in several mammalian cells, it is reasonable to expect that interactions between these two cycles may cause synchronization. Many studies reported evidences of interactions between the circadian and the cell cycles in different organisms. In particular, it appeared that in several systems, specific cell cycle phases occur in distinct temporal windows rather than being randomly distributed in time. These findings led to the concept of circadian gating of the cell cycle, through which the circadian clock can favor or forbid cell cycle transitions at specific circadian phases. However, it was also reported the converse, namely an effect of cell division on the circadian oscillator. Even though interactions between the circadian clock and the cell cycle have been identified in both directions, the dynamical consequences and the directionality of the coupling at the single-cell level were not extensively investigated. In order to better characterize the potential synchronization in mammalian cells, we estimated the mutual interactions between circadian clock and cell cycle in NIH3T3 mouse fibroblasts by the use of time-lapse fluorescent microscopy in combination with statistical analysis and mathematical modeling. NIH3T3 cells, harboring a fluorescent reporter under the control of the circadian *Rev-Erbα* gene promoter, were imaged for several days allowing the simultaneous detection of circadian oscillations and time of divisions. The analysis of thousands of circadian cycles in dividing cells indicated that both oscillators are synchronized, with cell divisions occurring about 5 h before the peak of the circadian *Rev-Erbα* -reporter. In order to further analyse the observed interaction between the circadian clock and the cell cycle we tested several perturbations such as different serum concentrations, different temperatures, treatment with pharmacological compounds and shRNA- mediated knockdown of circadian regulators. Surprisingly, this showed that circadian rhythm and cell cycle remain synchronized over the wide range of conditions probed. Our data combined with stochastic modeling showed that this synchronization state reflects an unexpected predominant influence of the cell cycle on the circadian oscillator, and did not support the leading hypothesis about a

circadian gating of the cell cycle. The stochastic modeling of two interacting phase oscillators allowed us to identify the parameters of the coupling functions, revealing an acceleration of circadian phase after the division. In order to monitor cell cycle progression, we relied on the measured area of the nucleus, since the nuclear area shows a temporal pattern over the cell cycle. This analysis allowed us to reconstruct a more complete picture of the coupling between the two oscillators, identifying additional interaction points. We could then make more specific predictions on distinct cell cycle events affecting the circadian clock and to test those predictions using further markers of cell cycle events. The work presented in this thesis sheds light on the interaction between two fundamentally recurrent cellular processes in mammalian cells and provides a deeper understanding of the role of the circadian clock in proliferating cells and tissues. Since circadian dysfunction has increasingly been linked to pathogenesis of many diseases including cancer, these findings might have significant implications for chronobiology and chronotherapeutics.

Key words: cell cycle, circadian clock, synchronization, oscillators, systems biology, mathematical modeling

Résumé

L'horloge circadienne et le cycle cellulaire sont deux processus cellulaires périodiques. Au niveau cellulaire, l'horloge circadienne consiste en un oscillateur autonome avec une période d'environ 24 heures qui coordonne temporellement une multitude d'aspects physiologiques de la cellule. En condition de prolifération, la cellule progresse au travers d'une succession de phases entre deux divisions consécutives. On peut donc considérer le cycle cellulaire comme étant également un oscillateur dont la période, dans plusieurs types de cellules mammifères, est de l'ordre d'une journée. Ces deux processus ayant une période similaire, il est raisonnable de considérer l'existence d'un couplage entre eux qui pourrait provoquer leur synchronisation. Une majorité des précédentes études ayant évalué l'existence de cette interaction dans divers organismes semble supporter l'hypothèse d'un impacte du cycle circadien sur le cycle cellulaire, indiquant que l'horloge circadienne contrôle la progression du cycle cellulaire. Cependant, en marge de cette théorie dominante, plusieurs études semblent également montrer l'existence d'un effet du cycle cellulaire sur l'horloge circadienne. Même si plusieurs des interactions impliquées ont à présent été identifiées, les propriétés dynamiques et directionnelles de ce couplage n'ont pas encore été investiguées intensivement au niveau des cellules individuelles. Dans le but de mieux caractériser cette potentielle synchronisation dans les cellules mammifères, nous avons estimé les interactions mutuelles entre le cycle circadien et le cellulaire dans des fibroblastes de souris NIH3T3 en combinant les approches de microscopie à fluorescence en temps réel, d'analyses statistiques et de modélisation mathématique. Des cellules NIH3T3 comportant un reporteur fluorescent sous le contrôle du promoteur circadien *Rev-Erbα* ont été enregistrées sur plusieurs jours, permettant ainsi la détection simultanée des oscillations circadiennes et des divisions cellulaires dans des milliers de cellules. L'analyse et la caractérisation du cycle circadien dans ces cellules en prolifération a pu mettre en évidence l'existence d'une synchronisation entre les deux oscillateurs, avec une majorité des divisions cellulaires prenant place 5 heures avant l'expression maximale du reporteur circadien *Rev-Erbα* . Dans le but de mieux comprendre la nature de l'interaction entre ces deux processus, plusieurs conditions expérimentales perturbant le système furent testées, comme différentes concentrations de sérum, des variations de températures, des traitements avec des composés pharmacologiques ou encore en abaissant le niveau d'expression de régulateurs circadiens à l'aide de shRNA. Dans toutes ces conditions, le cycle circadien et le cycle cellulaire restent synchronisés. En combinant ces données avec un model stochastique, nous avons pu montrer que cet état de synchronisation est en fait causé par une influence prédominante du cycle cellulaire sur l'oscillateur circadien, ce qui contredit l'hypothèse alors dominante préconisant

un effet du circadien sur le cycle cellulaire. L'utilisation du model stochastique pour deux oscillateurs phasiques interagissant permit l'identification des paramètres de la fonction de couplage, révélant ainsi une accélération de la phase circadienne après une division cellulaire. Initialement, notre analyse se basait sur la détection des divisions afin d'estimer la phase du cycle cellulaire. De façon à mieux saisir la progression au sein du cycle cellulaire en utilisant une variable continue, la seconde partie de nos analyses repose sur une estimation de la phase du cycle cellulaire en fonction de la taille mesurée du noyau des cellules plutôt que le temps de division. En effet, la taille du noyau suit un schéma temporel précis au cours du cycle cellulaire. Cette nouvelle analyse nous permit de reconstituer une image plus précise du couplage entre les deux oscillateurs en identifiant des points d'interaction additionnels et permettant ainsi de prédire plus spécifiquement quels événements du cycle cellulaire affectent l'horloge circadienne. Le travail présenté dans cette thèse met en avant le lien entre ces deux processus fondamentaux des cellules mammifères, et offre une meilleure compréhension du rôle que joue l'horloge circadienne sur les cellules et tissus en prolifération. Etant donné le lien étroit entre le cycle circadien et la pathogénèse de plusieurs maladies dont le cancer, ces découvertes sont susceptibles d'avoir des implications significatives dans le domaine de la chronobiologie et de la chronothérapie.

Mots clefs : Cycle cellulaire, horloge circadienne, synchronisation, oscillateurs, biologie des systèmes, modélisation mathématique

Sintesi

I ritmi circadiani sono processi biologici presenti nella maggior parte degli organismi viventi, aventi un periodo di circa 24 ore, che rispondono primariamente all'alternanza di luce e buio nell'ambiente circostante. A livello cellulare, il ritmo di circa 24 ore è generato da un orologio molecolare basato su una rete di *feedback* di trascrizione e traduzione. L'orologio circadiano orchestra temporalmente molti aspetti della fisiologia cellulare ed è composto da un oscillatore cellulare autonomo e auto-sostenuto avente un periodo di circa 24 ore. In condizioni in cui le cellule proliferano, anche il ciclo di divisione cellulare può essere considerato come un oscillatore. Dal momento che entrambi i processi avvengono con periodi simili in molti tipi di cellule di mammifero, è ragionevole aspettarsi che eventuali interazioni tra questi due cicli possano causarne la sincronizzazione. Molti studi hanno riportato evidenze di interazioni tra il ritmo circadiano ed il ciclo cellulare in svariati organismi. In particolare, è stato riportato che in diversi organismi, organi o tessuti, specifiche fasi del ciclo cellulare avvengono in finestre temporali distinte piuttosto che essere distribuite casualmente nel tempo. Questi risultati hanno generato la definizione del concetto di *"gating"* (*"gate"*= cancello, barriera) circadiano del ciclo cellulare, attraverso il quale l'orologio circadiano può favorire o proibire le transizioni di fase del ciclo cellulare in specifiche fasi circadiane. Tuttavia, è stato anche riportato il contrario, ovvero un effetto della divisione cellulare sull'oscillatore circadiano. Nonostante le interazioni tra l'orologio circadiano ed il ciclo cellulare siano state identificate in entrambe le direzioni, le conseguenze dinamiche e la direzionalità dell'accoppiamento tra i due oscillatori a livello di singola cellula non sono state ampiamente studiate. Al fine di caratterizzare meglio la potenziale sincronizzazione in cellule di mammifero, abbiamo stimato le interazioni reciproche tra l'orologio circadiano ed il ciclo cellulare in fibroblasti di topo (nella linea cellulare denominata NIH3T3) mediante l'uso di microscopia a fluorescenza *time-lapse* (*"time-lapse"*= filmato generato con acquisizioni di immagini ad intervalli regolari), in combinazione con analisi statistiche e modellizzazioni matematiche. Le cellule NIH3T3, contenenti un *reporter* fluorescente la cui espressione è regolata dal promotore circadiano del gene *Rev-Erbα* , sono state filmate per diversi giorni. Le registrazioni hanno permesso la rilevazione simultanea delle oscillazioni circadiane e l'identificazione delle divisioni cellulari. L'analisi di migliaia di cicli circadiani in cellule in divisione ha indicato che i due oscillatori sono sincronizzati, con divisioni cellulari che si verificano circa 5 ore prima del picco circadiano del *reporter Rev-Erbα* . Al fine di analizzare ulteriormente l'interazione osservata tra l'orologio circadiano ed il ciclo cellulare abbiamo effettuato diverse perturbazioni tra cui l'uso

di diverse concentrazioni di siero, incubazioni delle cellule a diverse temperature, trattamento con composti farmacologici e silenziamento dell'espressione genica di specifici regolatori circadiani. Sorprendentemente, queste analisi hanno mostrato che il ritmo circadiano ed il ciclo cellulare rimangono sincronizzati in tutte le condizioni testate. I nostri dati, combinati con la modellizzazione stocastica, hanno dimostrato che, inaspettatamente, lo stato di sincronizzazione osservato riflette un'influenza predominante del ciclo cellulare sull'oscillatore circadiano, e non supportano l'ipotesi che prevede un *gating* circadiano del ciclo cellulare. Il modello stocastico di due oscillatori interagenti ha permesso di individuare i parametri delle funzioni di accoppiamento, rivelando una accelerazione della fase circadiana in seguito alla divisione cellulare. Per monitorare la progressione del ciclo cellulare, abbiamo utilizzato le misurazioni della superficie nucleare, in quanto la grandezza del nucleo presenta un avanzamento temporale caratteristico durante il ciclo cellulare. Questa analisi ha permesso di ricostruire un quadro più completo dell'accoppiamento tra i due oscillatori, individuando ulteriori punti di interazione tra i due processi. Successivamente, abbiamo potuto effettuare previsioni più specifiche su distinti eventi del ciclo cellulare che influenzano l'orologio circadiano, ed abbiamo testato tali ipotesi con ulteriori *marker* di eventi del ciclo cellulare. Il lavoro presentato in questa tesi mette in luce l'interazione tra due processi cellulari fondamentali ricorrenti in cellule di mammifero e fornisce una comprensione più approfondita del ruolo dell'orologio circadiano in cellule e tessuti proliferanti. Dal momento che disfunzioni del ritmo circadiano sono state collegate alla patogenesi di molte malattie tra cui il cancro, i nostri risultati potrebbero avere significative implicazioni sullo sviluppo della cronobiologia e della cronoterapia.

Parole chiave : Ciclo cellulare, orologio circadiano, sincronizzazione, oscillatori, biologia dei sistemi, modellizzazione matematica

Contents

1 Introduction

"The key to every biological problem
must finally be sought in the cell;
for every living organism is,
or at some time has been, a cell."
E. B. Wilson

In this chapter I will introduce the two main players of this thesis, the circadian rhythm and the cell cycle. I will first give an overview of their cellular and molecular mechanisms and subsequently I will give a perspective on their interactions by introducing concepts from the theory of synchronization of coupled oscillators.

1.1 Two cyclic cellular processes

Given all the various biological processes carried out in a cell, it is highly plausible that some of them interact at different levels. In order to resolve the complexity of biological systems, it is then crucial to understand how and under which conditions these interactions can occur and which consequences these interconnections can bring. With regards to that, the interplay between the circadian rhythm and the cell cycle represents an exemplary experimental system analyzable at the single cell level. In this section I will give an overview of each of this two major periodic processes.

1.1.1 The circadian clock

Living organisms have adapted to the daily rhythmic variations generated from the rotation of the Earth. This rotation generates alternation of day and night, light and darkness, warmer and colder temperatures. In order to adapt to these everyday rhythms and to anticipate the daily changes living organisms developed the so-called circadian oscillator [Pittendrigh, 1960], i.e. our internal clock.

The word **circadian**, introduced for the first time in 1950s by Franz Halberg, derives from the Latin words *circa diem* meaning "about a day" [Halberg et al., 1959]. This biological clock ticks with a *circa* 24h period and controls daily rhythms of most of the living organisms, spanning from cyanobacteria to fungi, plants and animals [Roenneberg and Merrow, 2005].

As human beings, we experience circadian oscillations in our sleep/wake patterns, in the feeding habits and cognitive and physical performances [Wright et al., 2002, Wright et al., 2012]. Together with these behavioral fluctuations, humans and most mammals show 24h rhythms in many physiological parameters such as body temperature, blood pressure, hormone production and metabolism [Green et al., 2008, Aschoff, 1983].

1.1.1.1 *Main Properties of the circadian clock*

The first empirical generalizations of circadian rhythms were illustrated in 1960 by one of the fathers of biological rhythms, Colin Pittendrigh [Pittendrigh, 1960]. In his landmark work Pittendrigh made a list of sixteen generalizations that can be summarized in three main essential features [Edery, 2000]:

1. Circadian rhythms are endogenously generated and self-sustained with a period of approximately 24 hours that can continue to run without any environmental time cue;
2. Circadian rhythms are adaptive and dynamical, meaning that they can be entrained by environmental conditions;
3. Circadian rhythms show temperature compensation: the period remains nearly con-

stant over a range of physiological temperatures.

The first remarkable property of the circadian clock is that it persists even in absence of light/dark cycles or other external time signals, but the rhythm is indeed able to "free-run" under constant conditions like constant light or constant darkness. For example, when the organism is deprived of rhythmic external time cues, a free-running period slightly different than 24 hours is observed. For instance, the observations recorded on a human subject who spent four months alone in a deep cave without timepieces or sunlight exposure, indicated that his free-running period was of 25.1 hours [Mills et al., 1974]. This persistence of rhythmicity exposed by this landmark study clearly indicates an internally driven and self-sustained timekeeping mechanism. Interestingly, the very first indication of the self-sustained nature of the circadian rhythm was already provided in the 1700s, when the French scientist De Mairan observed not only daily leaf movements of the plant *Mimosa pudica*, but also that, when the plant was in constant darkness, the periodic raising and lowering of the leaves persisted [De Mairan, 1729]. Astonishingly, even if the free-running period can be longer or shorter than 24 hours, it is rather precise (i.e. the fluctuations around the mean period are small). An example of this precision was given by recordings of the free-running activity/rest cycles of a blind monkey for over three years during which the variability of the period was in the order of few minutes [Richter, 1968].

The second important characteristic of the circadian clock is that, unlike a physical clock that has constant velocity and runs independently of other influences, the circadian clock is dynamic and adapts to different external stimuli. For example, the circadian clock can be synchronized, or entrained, by exogenous cues such as the light/dark cycle, food or temperature. The environmental cues that are able to synchronize the circadian clock to the 24h day are called *Zietgeber*, German word for "time giver". When such cues are present the circadian rhythm aligns to them. Equally, if a variation in the external periodic stimulus takes place, as it happens, for example, when traveling across different time zones, the rhythm is then able to re-align to the new cues. The alignment of circadian rhythms to the Zietgeber is known as entrainment. The phase response properties of the circadian clock, which describe how a clock's phase is adjusted by perturbations such as light pulses [Taylor et al., 2010], depend on the current phase. As Pittendrigh suggested [Pittendrigh, 1960], this ability to change the clock phase via external signals actually provides a way to continuously adjust to the light-dark environment.

A third essential feature of the circadian rhythm is the capability to be buffered against certain types of external perturbations. The most prominent evidence of this ability is the temperature compensation that can be observed both at the molecular and behavioral level [Pittendrigh, 1954]. In fact, the period of the clock oscillator is roughly constant at any stable temperature that is physiologically permissive, even if changes in temperature might impinge on the phase of a circadian cycle [Saini et al., 2012]. The capability of the endogenous clock to compensate for changes in temperature is crucial for predicting and adapting to the environmental changes, notably in cold blooded animals. Similar to the situation for

chemical reactions, temperature compensation is measured using the coefficient Q_{10}, which corresponds to the ratio of the reaction-rate at temperatures being 10 °C apart. A Q_{10} of 1.0 indicates thermal independence of a given reaction. Of note, most metabolic processes such as enzymatic reactions, have a Q_{10} coefficient between 2 and 3, which means that for each 10 °C increase in temperature, the reaction rate doubles or triples. In contrast, circadian rhythms have a Q_{10} between 0.8 and 1.2, indicating that they have evolved in order to ensure that their periods remain nearly constant over a broad range of temperatures [Reyes et al., 2008]. As a matter of fact, a clock that would run slower at low temperatures and faster at high temperatures, would not reliably predict the time of the day. Thus, temperature compensation of the clock period is a prominent feature that underlines the robustness of the clock circuitry. On the other hand, temperature acts as a universal Zeitgeber for circadian rhythms, from single-cell organisms to tissues [Zimmerman et al., 1968, Francis and Sargent, 1979, Merrow et al., 1999, Brown et al., 2002, Buhr et al., 2010]. In mammals, however, external temperature cycles act as very weak synchronizing inputs. Indeed, homoeothermic animals are able to modulate their body temperature and buffer against environmental temperature fluctuations[Refinetti, 2010]. The role of temperature in resetting mammalian circadian oscillators will be described in the following paragraph.

1.1.1.2 *Anatomical organization of the circadian internal clock in mammals*

The circadian clock in mammals has a hierarchical structure even from an anatomical point of view. In higher organisms exists a so called "master" clock that functions as a central pacemaker, which synchronizes "peripheral" clocks, and thereby acting as an orchestra leader for circadian physiology. In mammals, the master clock is situated in the brain, more specifically in the suprachiasmatic nuclei (SCN), a region placed in the anterior part of the hypothalamus [Gillette and Tischkau, 1999]. The SCN, which is made of nearly 20'000 neurons in mice and 100'000 in humans, receives light inputs from specialized cells in the retina, and is thus capable of sensing the environmental timing cues being directly coordinated to the light/dark cycle [Bernard et al., 2007]. The central pacemaker neurons clearly have a cell-autonomous and self-sustained rhythm. The observed synchrony of neurons within the SCN is crucial for generating coherent output signals, such as the endocrine signals, that ultimately synchronize peripheral clocks present in different tissues and organs [Ralph et al., 1990, Dibner et al., 2010]. The circadian rhythm is cell-autonomous and self-sustained not only in the central pacemaker, but also in peripheral tissues and in cultured cells in which circadian oscillations can persist without the regulation of the master clock [Yamazaki et al., 2000, Balsalobre et al., 1998]. The SCN has been shown to be responsible for coordinating all the peripheral oscillators, so that a consistent rhythm is orchestrated at the organism level [Welsh et al., 2004, Yoo et al., 2004]. Interestingly, the SCN oscillator is robust to perturbations that might arise from environmental cues, such as light pulses or temperature cycles. Indeed, phase-shifting responses to light pulses in the circadian activity rhythms of mice indicate a so-called "Type 1" phase resetting, meaning a weak or low amplitude phase shift, highlighting the robustness of the SCN pace-

maker [Vitaterna et al., 2006]. Similarly, the SCN is resistant to temperature cycles whereas peripheral oscillators are very sensitive to temperature oscillations. Mammalian cells from peripheral tissues such as lung, pituitary, liver or kidney, show a strong entrainment when exposed to low-amplitude temperature cycles mimicking the circadian body-temperature rhythms [Brown et al., 2002, Buhr et al., 2010]. Moreover, when mice peripheral tissues maintained at 36 °C are perturbed with 38.5 °C temperature pulses, they show a "Type 0" phase resetting, i.e. a strong and high-amplitude phase shift that resets the oscillator to a new phase in response to a pulse [Buhr et al., 2010]. Conversely, the SCN phase is unperturbed by the same temperature changes. Whereas temperature changes do not have any effect on an intact SCN, however, when coupling within SCN neurons is prevented, temperature pulses induce a strong resetting of the phase. These observations indicate that the master clock can drive body-temperature oscillations able to entrain peripheral clocks, without having interferences from the temperature signals on itself, and that the resistance of the SCN to temperature changes is determined by the strong coupling between its neurons [Mohawk and Takahashi, 2011].

1.1.1.3 *Molecular organization of the circadian clock*

At the molecular level, in both central and peripheral oscillators, the circadian clock is thought to consist of interlocked transcriptional-translational feedback loops driving rhythmic expression of clock core components (Figure 1.1) [Lowrey and Takahashi, 2004]. "Core" clock components are those genes, and their related proteins, fundamental for the generation and maintenance of the rhythm in individual cells [Lehmann et al., 2015, Takahashi, 2004]. The core clock components consist of positive and negative regulators. In mammals, the positive elements include CLOCK and BMAL1 transcription factors. These two proteins heterodimerize and initiate transcription of several target genes containing E-box/E'-box cis-regulatory enhancer sequences, such as *Period* genes (*Per1*, *Per2* and *Per3*) and *Cryptochrome* genes (*Cry1* and *Cry2*) [Gekakis et al., 1998]. In this primary regulatory loop, the resulting PERs and CRYs proteins act as negative elements: they form complexes that translocate back to the nucleus and inhibit their own expression by interacting with CLOCK:BMAL1 dimers and interfering with their transcriptional activity [Kume et al., 1999, Vitaterna et al., 1999, Zheng et al., 2001].

CLOCK:BMAL1 heterodimers induce an auxiliary regulatory loop, which acts in conjunction with the aforementioned primary loop, by activating transcription of the retinoic acid-related orphan nuclear receptors *Rev-Erbα/β* and *Rorα/β/γ* [Preitner et al., 2002, Sato et al., 2004] [Akashi and Takumi, 2005]. Subsequently, REV-ERBs and RORs compete for binding the *r*etinoic acid-related *o*rphan receptor *r*esponse *e*lements (ROREs) present on *Bmal1* promoter. ROR proteins activate *Bmal1* transcription, whereas REV-ERBs repress it, thus *Bmal1* rhythmicity is positively controlled by RORs and negatively regulated by REV-ERBs [Guillaumond et al., 2005].

In addition to transcriptional feedback loops, the mammalian molecular clock is significantly regulated by post-transcriptional modifications such as phosphorylation and ubiquitination.

This regulation affects the stability and nuclear translocation of PERs and CRYs and is crucial to maintain precision and set the period of the clock. More specifically, two Casein Kinases, CK1ϵ and CK1δ, phosphorylate PER proteins [Akashi et al., 2002]. This phosphorylation targets PERs for polyubiquitination by βTrCP [Eide et al., 2005]. Similarly, CRY1 and CRY2 are phosphorylated by AMPK1 and GSK3β respectively [Kurabayashi et al., 2010, Lamia et al., 2009], and are both polyubiquitinated by FBXL3 [Eide et al., 2005]. Polyubiquitination of PERs and CRYs will eventually lead to their degradation by the proteasome. This degradation is needed to cease the repression state and start a new cycle of transcription.

In addition to the "core" clock genes, there are thousands of genes that show circadian expression with significant amplitude in various tissues [Hughes et al., 2012, Zhang et al., 2014]. These "output" or "clock-controlled" genes are tissue-specific and play roles in different gene pathways such that they can be regulated to best fulfill each tissue's specific function [Buhr and Takahashi, 2013]. A schematic illustration of the molecular clock in mammals is shown in Figure 1.1.

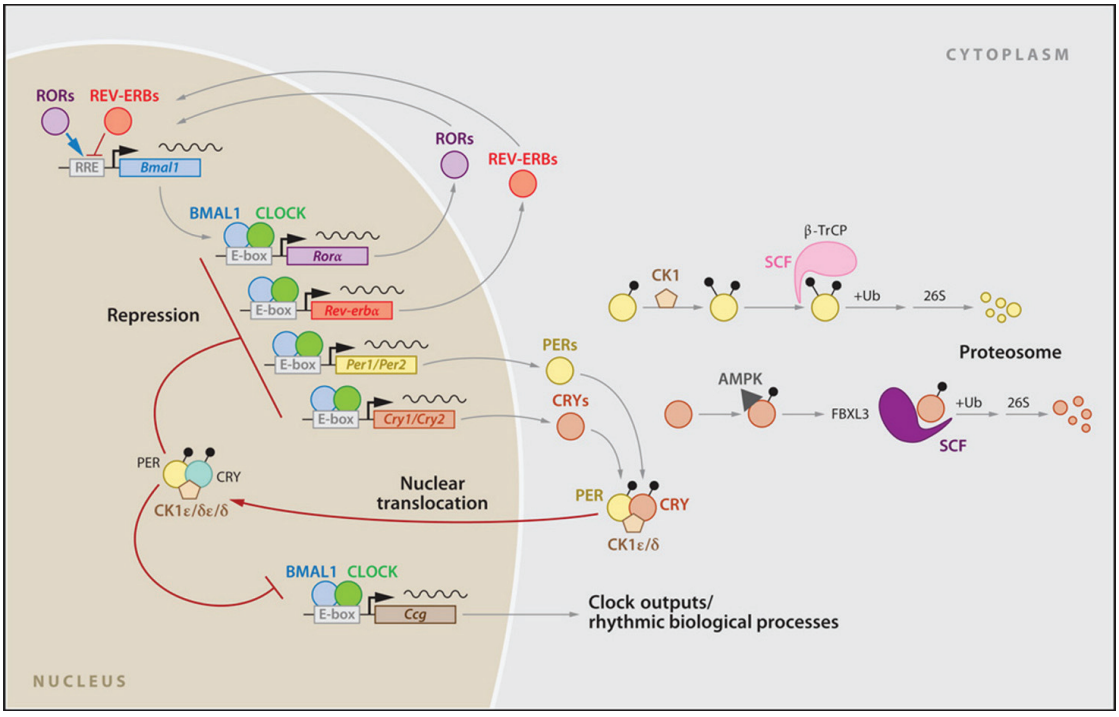

Figure 1.1 – Molecular organization of the mammalian circadian clock. Figure reproduced from [Mohawk et al., 2012]; permission for the use of the figure granted from *Annual Reviews*.

Thanks to several recent genome-wide transcriptome studies, it has been estimated that between 2 and 10% of the genome is transcribed in a circadian fashion in many different mouse tissues such as SCN, liver, lung, brown adipose tissue, white adipose tissue, adrenal gland, skeletal muscle, heart or retina [Kornmann et al., 2001, Panda et al., 2002, Akhtar et al., 2002,

Storch et al., 2002, Storch et al., 2007, Kornmann et al., 2007]. More recently, a high-resolution multiorgan expression study in mouse described that the RNA abundance of 43% of protein-coding genes is rhythmic in at least one organ and suggested that more than half of the mouse protein-coding genome cycles somewhere in the body [Zhang et al., 2014]. However, it has to be said that the variation in the number of estimated cyclic genes for a given tissue and within organs can vary significantly between different studies due to both experimental differences and differences in statistical analysis of the data.

1.1.1.4 *The Human Circadian Clock*

Humans exhibit 24-hours ryhthm in many aspects of physiology and behavior. The most prominent evidence of circadian rhythmicity in human behaviour is the sleep/activity cycle. The timing of these states is indeed strongly driven by the circadian clock.
Moreover, human beings display 24-hours oscillations in many important physiological parameters including blood pressure, temperature, circulating hormons and cognitive functions [Aschoff, 1983, Millar-Craig et al., 1978, Roenneberg and Merrow, 2005, Green et al., 2008] [Eckel-Mahan et al., 2008, Wright et al., 2012].

Distruption of the clock induced by mutations in key circadian genes or misagnlinment between the internal clock and the environmental rhytms impact on human well-being and can eventually lead to health disorders [Reid and Zee, 2009]. An example of how genetic mutations affecting the molecular circadian machinary can lead to human disorders is provided by the Familial Advanced Sleep Phase Syndrome (FASPS). Subjects with FASPS have abnormal sleep patterns charactherized by early evening bedtimes (around 7:30 pm) and early morning awakenings (around 4:30 am), associated with a phase advance of melatonin and temperature rhythms [Jones et al., 1999]. Interestingly, this disorder can result from both, a mutation in the phosporilation site of the *PER2* gene or a mutation in the *CK1δ* gene, leading to a decreased phosporilation of PER2 [Toh et al., 2001, Xu et al., 2005].

In addition to sleep-related disorders, there is a direct connection between altered circadian rhythms and health metabolic disorders [Green et al., 2008]. Indeed, circadian desynchrony and altered feeding schedules can compromise metabolic homeostasis leading to insulin resistance and obesity and increased risk of developing type-2 diabetes and heart diseases [Shi et al., 2013, Paschos, 2015]. Epidemiological studies revealed that shift workers, who have disconnetted working schedules from the environmental light/dark rhythm, associate with increased risk of metabolic disfunctions, obesity, cardiovascular disesases and cancer [Karlsson et al., 2001, Karlsson et al., 2003, Ellingsen et al., 2007] .

Interestingly, the features of the human internal clock can vary among individuals. In fact, differences in circadian rhythms were detected according to the individual person and are associated to age, gender and to the so-called *chronotype* [Kerkhof and Van Dongen, 1996, Roenneberg et al., 2007b]. A *chronotype* refers to the propensity of the individual to set the

diurnal activity and the sleeping time in a particular window of the 24-hour period. More specifically, "early" chronotypes, also defined as morning types or “larks” are associated with "morningness", i.e. the propensity of being most active during the morning. In contrast, "late" chronotypes are defined as evening types or “owls”, exhibiting "eveningness", i.e. the propensity of being most active during the evening [Vink et al., 2001, Kerkhof and Van Dongen, 1996, Duffy et al., 1999]. These interindividual differences seem to be generated by different factors, including genetic disposition [Roenneberg et al., 2003]. Roenneberg and collaborators developed the *Munich Chronotype Questionnaire* (MCTQ) thanks to which they could determine the chronotype of about 55’000 people [Roenneberg et al., 2003, Roenneberg et al., 2007a, Roenneberg et al., 2013]. The questionnaire is mainly based on investigations of individual sleep times in working days and free days. This epidemiologic study, that has been continuosly updated over the years, allowed to determine the correlation between chronotypes and factors such as age, gender and geographical locations [Adan and Natale, 2002, Roenneberg et al., 2004, Paine et al., 2006]. Importantly, it was observed that late chronotypes routinely accumulate significant sleep debt for which they need to compensate on free days. Since the human chronotype is mainly dependent on light exposure, modern conditions of living inside and using artificial light, overall shifted the timing of sleep in industrialized society in all chronotypes, leading to chronic sleep loss during working days. This observation led to the concept of "social jetlag", i.e. the misallignment between the circadian clock and the social clock, resulting in routine sleep deprivation that in turn affects cognitive performances such as learning and memory, and it has also been linked to metabolic disfunctions and increased body mass index (BMI) [Roenneberg et al., 2012]. Altogether, these observations point out the consequences of disruption of the circadian system on health and highlight the importance of synchronization between the internal biological clock with the external light/dark cycle.

1.1.1.5 *Chronotherapy*

Chronotherapy refers to the administration of drugs at specific times of the day in order to provide the highest efficacy with the the lowest side effects [Ortiz-Tudela et al., 2013]. It has been proven that efficacy and toxicity of the drug can vary according to the time of day implying significant consequences on the therapeutic approach. Indeed, several studies from the past decades highlighted daily changes in many aspects of drug kinetics such as absorption, metabolism and excretion [Ede, 1973, Ohdo, 2003]. Thus, the importance of circadian clocks for time schedules of therapeutic treatments should not be neglected. However, the field of chronotherapy is mainly still restricted to the experimental level and just a small number of drugs - such as hydrocortisone for the treatment of patients with adrenal insufficiency or hyperplasia [Chan and Debono, 2010] - are administrated by taking into account the circadian component.

Chronotherapy appeared to be very important also in cancer treatments. Several studied demonstrated that circadian rhythmicity of cell cycle phases in tumors shows asynchrony compared to the phases of the host cells. For example, in ovarian cancer, the prolifer-

ation of tumor cells showed antiphasic peak of S-phases comparing to non-tumor cells [Klevecz et al., 1987], suggesting that the timing of chemotherapy should coincide with the time of highest tumor cell vulnerability in order to maximize the efficacy of the drug and minimize its toxicity in the normal tissue. Moreover, clinical studied demonstrated that several anticancer drugs administered in specific circadian windows had increased efficacy and decreased toxicity [Levi et al., 2007]. Examples are represented by drugs such as 5-fluorouracil, cyclophosphamide, platinum complex analogs, doxorubicin and cisplatin. Impressively, the latter ones used in combination for the treatment of ovarian cancer, showed an increase of the survival rate of patients when administered with a specific chronoterapeutics strategy [Kobayashi et al., 2002]. Additional studies are still needed to better understand the molecular mechanisms underlying the advantageous effects observed with circadian administration of anticancer treatments.

1.1.2 The cell cycle

The cell cycle is a complex and highly regulated process occurring with an elaborate series of events through which one cell duplicates its components and then eventually divides giving rise to two daughter cells [Schafer, 1998]. In most eukaryotic cells, a typical cell cycle is composed of an orderly sequence of phases: G1, S, G2 and M (Section 1.1.2.1). Altogether, the cell cycle could be subdivided in two main phases, the interphase, composed of the G1, S, and G2 phases, and the mitosis (M) [Norbury and Nurse, 1992], (Figure 1.2) . In mammals, the total duration of the cell cycle varies from one cell type to another, but typically lasts between 11-16 hours in embryonic stem cells to 24 hours in most of other cell types [Orford and Scadden, 2008]. The M-phase consists of five mitotic stages - *prophase*, *prometaphase*, *metaphase*, *anaphase* and *telophase* - followed by *cytokinesis*, the final step of the cell cycle, in which the cell is split into two halves. In a typical proliferating human cell in culture, the cell cycle lasts about 24-hours, of which 23 hours are spent in interphase and 1 hour in M phase [Murray and Hunt, 1993]. In order to maintain the appropriate sequence of events and the successful completion of each phase, the cell cycle has a very accurate and reliable control system based on several checkpoints, that depend on cyclically activated Cyclin-dependent kinases and involves a large set of regulatory proteins [Pavletich, 1999]. In most of the eukaryotic cells there are three major regulatory checkpoints: the G1/S transition, the G2/M transition and the metaphase-to-anaphase transition. This control system is able to block progression through each transition phase if problems are detected in the intracellular or extracellular environment [Malumbres and Barbacid, 2009, Morgan, 2007]. The main events characterizing each cell cycle phase and additional biochemical details of the cell-cycle control system will be described in the following paragraphs (Section 1.1.2.1, Section 1.1.2.2).

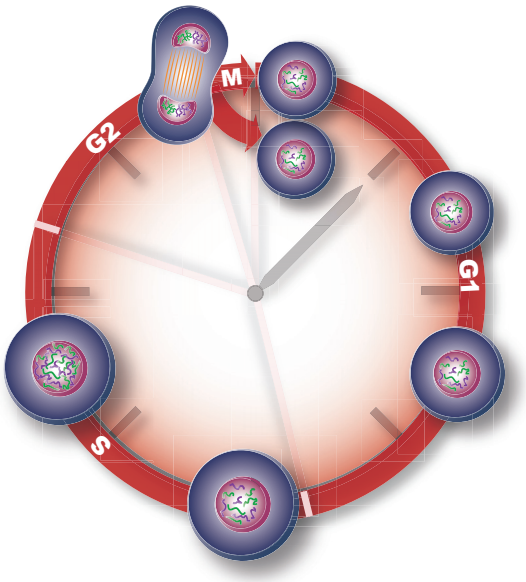

Figure 1.2 – Schematic illustration of the cell cycle.

1.1.2.1 *An orderly sequence of phases: G1, S, G2, M*

The **G1 phase** (G= gap) represents a gap between the end of Mitosis (M), being the process that culminates with nuclear and cellular division, and the beginning of the DNA synthesis (S) phase. This first part of the cell cycle is dedicated to mRNA and protein synthesis and production of organelles and allows the cell to increase its volume and grow to about double its original size. Once the required protein synthesis and cell growth are complete, the cell can commit to DNA replication and begin the S-phase [Foster et al., 2010]. This G1 phase is not just a simple time delay allowing cell growth, but represents a way for the cell to monitor the internal and external environment ensuring that the conditions are suitable for a proper cell growth and that the cell can thus commit to division [Shichiri et al., 1993]. The G1 phase can be affected by limiting growth factors such as nutrients. Indeed, its length can vary greatly depending on extracellular conditions or signals. More precisely, if the external conditions are unfavorable or no signals promoting cell division are detected, the cell can delay its own progress in G1 or even leave the G1 phase, by pausing its progress and entering in a quiescent phase known as G0. It is worth mentioning that several types of cells in the human body are considered to be - either transiently or permanently - in G0. In some case, cells withdraw from the cell cycle in an irreversible manner and enter in a terminally differentiated G0 state. This state belongs to most of neurons or skeletal muscle cells, in which the cell-cycle control system is completely and permanently dismantled [Herrup and Yang, 2007, Halevy et al., 1995]. Other types of cells exit from the cell cycle only transiently and are thus able to reassemble the cell-cycle control system and re-enter the cycle. Cells present in the kidney or liver, can also be stimulated to re-enter the cell cycle under specific circumstances like, for example, tissue damage, whereas other cells such as fibroblasts, move from G1 to G0 and vice versa repeatedly. Other types of cells, such as epithelial cells, rarely enter G0, continuing dividing throughout the organism's life. Because of that, almost all the variation in the cell-cycle length between cells of an adult body depends on the G1/G0 duration [Alberts et al., 2015, Orford and Scadden, 2008].

In the following **S phase** (S = synthesis), the cell duplicates all of its genetic material. In order to prevent abnormalities and minimize mutations, precise and accurate replication is necessary. Indeed, it has been estimated that the eukaryotic replication machinery has a base substitution error rate in the range of 10^{-6} to 10^{-8} [Kunkel, 2004]. Due to the importance of this phase, the regulatory machinery governing this process is highly conserved in eukaryotes. The first event of the S phase is the activation of a group of proteins, the DNA helicases, which unwind the DNA and initiate its replication at the replication origins, placed in various locations in every chromosome [Brosh Jr., 2013]. DNA polymerases are then loaded onto the two single DNA strands, starting the elongation, and the replication machinery moves from the origin going outward using two replication forks [Tanaka and Araki, 2013]. It is crucial for this step to be highly reliable, to inhibit the pre-replication complexes required for initiating DNA replication so that each origin can be fired just once in each S-phase [Kelly and Brown, 2000]. Importantly, not only must each chromosome be duplicated accurately but the proteins involved in DNA packaging must also be reproduced in order to ensure that the daughter cells inherit a proper chromosome structure. Indeed, during S-phase there is an increase in the synthesis of the

four-histone subunits H2A, H2B, H3 and H4, assembled into nucleosomes by assembly factors that associate with replication forks and distribute nucleosomes on the newly synthesized DNA [Ewen, 2000]. At the end of S phase, all chromosomes have been replicated; therefore, the amount of DNA in the cell has effectively doubled. Each replicated chromosome consists of a pair of identical sister chromatids kept together mainly by a large protein complex called *cohesin*, which is positioned at many locations along the length of each sister chromatid during DNA replication [Peters et al., 2008]. This cohesion is essential for appropriate chromosome segregation during mitosis.

Following DNA replication, the cell enters in the pre-mitotic **G2 phase** (G=gap). In this last part of interphase, the cell undergoes further growth and protein synthesis such as microtubules production required for the next phase mitosis. The G2 phase is not always necessary for the eukaryotic cell cycle. Indeed, in embryos from organisms like *Xenopus* or *Drosophila*, or in Chinese Hamster cell lines [Liskay, 1977], the cell cycle can pass directly from S-phase to M-phase [Morgan, 2007]. At the end of the G2 phase there is the G2/M transition checkpoint that prevents the cell from entering mitosis if DNA damage is detected, therefore allowing the DNA-repair system to restore the integrity of the genome and stopping proliferation of damaged cells [Li and Zou, 2005]. More specifically, the DNA-repair mechanism taking place during this cell-cycle phase is mainly mediated by homologous recombination and it is responsible for repairing gaps or double strand brakes that might arise during replication [Branzei and Foiani, 2008]. Because of its role in maintaining genome stability, the G2/M checkpoint is of particular interest in understanding the mechanisms underlying tumorigenesis [Stark and Taylor, 2004].

After the cell has passed the G2 transition, it enters in the shortest phase of the cell cycle, i.e., the **M-phase** (M=mitosis), composed of mitosis and cytokinesis [Morgan, 2007]. As already mentioned above, mitosis can be divided in 5 consecutive stages. During *prophase*, chromosomes undergo condensation. Meanwhile, outside the nucleus, there is the assembly of the mitotic spindle between the two centrosomes, organelles acting as the main microtubules organizing center [Walczak et al., 2010]. In *prometaphase*, the nuclear envelope of metazoan cells has an abrupt breakdown; chromosomes, made of the two sister chromatids, can attach to the microtubules via their kinetochores, the protein structures located at the centrosomes, where the two sister chromatids are linked [Alushin and Nogales, 2011, Magidson et al., 2011]. At *metaphase*, the chromosomes are aligned to the equatorial plane of the cell, half way between the two spindle poles. The microtubules attached to the kinetochore connect each sister chromatid to opposite poles of the spindle [Goshima et al., 1999]. The sister chromatids split, or segregate, at *anaphase*, when they are pulled toward the two opposite spindle poles. While the spindle poles move apart, microtubules get shorter [Meadows and Millar, 2015]. Chromosomes reach the poles of the spindle at *telophase*. They afterwards decondense while the nuclear envelop reassembles around each set of chromosomes, completing mitosis [Walczak et al., 2010]. In the cytoplasm, there is the formation of a contractile ring made of actin and myosin, that later, during *cytokinesis*, creates the cleavage of the cell that eventually divides in two daughter cells with one nucleus each [Green et al., 2012]. Of note, several

features of mitosis can vary among different organisms but basic events such as chromosome condensation, mitotic spindle assembly and attachment of chromosomes to the spindle microtubules are conserved in all eukaryotes. For example, the described nuclear envelope breakdown leading to an "open mitosis", occurs only in metazoan cells. In contrast, many unicellular eukaryotes including yeast undergo a so-called “closed mitosis” during which the nuclear envelope remains unbroken: the spindle pole bodies are associated with the nuclear membrane, and the nucleus splits only after the two daughter chromosomes have migrated towards opposite poles of the spindle[Guttinger et al., 2009].

1.1.2.2 *The cell-cycle control systems: Cyclins and Cyclin-Dependent protein kinases complexes*

As already mentioned, the cell cycle is driven by a rigorous control system that responds to specific signals and allows the appropriate amount of time for each cell-cycle event completion. This system is based on a series of biochemical switches mainly ruled by Cyclin-dependent kinases (CDKs). These protein kinases are constantly expressed but cyclically activated by proteins known as Cyclins[Malumbres and Barbacid, 2009]. Because Cyclins undergo cycles of synthesis and degradation that lead to cyclical changes in their levels, their binding and consequent activation of the CDKs can occur at specific stages of the cell-cycle. Cyclins not only activate the CDKs but also direct their phosphorylation to specific target proteins. In this way, each Cyclin-CDK complex can trigger phosphorylation of different substrates [Suryadinata et al., 2010]. In vertebrate cells there are four CDKs (CDK1, CDK2, CDK4 and CDK6) interacting with different Cyclins (Cyclin A, Cyclin B, Cyclin D1, D2, D3 and Cyclin E), according to the cell-cycle phase. In more detail, Cyclin E activates CDK2 in late G1 leading to the progression through the G1/S restriction point. As a result, the cell commits to cell-cycle entry and start the S-phase [Bresnahan et al., 1996]. The levels of Cyclin E fall during S-phase. Cyclin A activates CDK2 and CDK1 at the beginning of S-phase, promoting chromosome duplication. Cyclin A levels remain stable until the early mitosis. Cyclin B activates CDK1 at the G2/M transition stimulating the entry into mitosis. Cyclin B levels drop during mitosis. In most cells, there is a fourth class of Cyclins, Cyclin D1, D2 and D3, which activate CDK4 and CDK6 and direct the regulation of the G1/S Cyclins [Hochegger et al., 2008].

Oscillations in Cyclin levels and consequent Cyclin-CDK complexes activity at specific cell cycle phases, require different additional mechanisms involving activating or inhibitory kinases, ubiquitin ligases and other enzyme complexes. In order to fully activate a Cyclin-CDK complex, a CDK-activating kinase (CAK) is required. This kinase causes a conformational change by phosphorylation of an amino acid close to the active site of CDK1, CDK2, CDK4 and CDK6, increasing their activity [Kaldis, 1999, Lolli and Johnson, 2005].

Cyclin-CDK complexes can be inhibited by the binding of CDK inhibitor proteins (CKIs) that causes a change in structure, inactivating the CDK active site. This mechanism is mainly used during late G1 and early S-phase. In mammals, among these CKIs, the p27 enzyme sup-

presses Cyclin-CDK complexes at the G1/S transition promoting the exit from the cell-cycle [Toyoshima and Hunter, 1994]; the protein p21 suppresses the same Cyclin-CDKs complexes in case of DNA-damage [Jung et al., 2010]; p16, considered as a tumor-suppressor since inactivating mutations or deletions are frequent in cancer, suppresses CDK4 or CDK6 activity during G1 [Liggett and Sidransky, 1998]. The active Cyclin-CDK complex can be also switched off by the kinase WEE1 that phosphorylates other amino acids in the CDK active site. In contrast, dephosphorylation of these sites by the CDC25 phosphatase increases CDK activity. More specifically, the WEE1 kinase suppresses CDK1 activity before mitosis, whereas the CDC25 phosphatase induces CDK1 activity at the onset of mitosis [Potapova et al., 2009]. Later during mitosis, protein degradation is the main regulatory mechanism triggering transition from metaphase to anaphase [Bassermann et al., 2014]. The key regulator is the so-called anaphase-promoting complex, also called cyclosome, (APC/C), that ubiquitylates the *Securin* protein and Cyclin A and B [Rahal and Amon, 2008, Thornton and Toczyski, 2003]. The Securin protein (or PTTG1 in vertebrates) promotes cohesions of the two sister chromatids. In fact, *Securin* inhibits the activity of the protease *Separase* that degrades the cohesin ring binding the sister chromatids. Degradation of *Securin* allows then chromosome segregation and the start of anaphase [Waizenegger et al., 2002, Hagting et al., 2002]. On the other hand, APC/C induces the completion of M-phase by promoting degradation of Cyclins important for the activity of most CDKs. The consequent inactivation of CDKs leads to dephosphorylation of CDKs target proteins previously phosphorylated from S-phase to early mitosis. In order to allow a period of CDK inactivity, the APC/C remains active in G1. The APC/C activity changes during the cell cycle because of its association with different activating subunits such as CDC20 during metaphase-to-anaphase transition or CDH1 from anaphase to early G1 [van Leuken et al., 2008]. CDH1 continues to be active in G1 by tagging S and M Cyclins for degradation, but does not target G1/S Cyclins that can thus accumulate and, by late G1, inactivate the APC/C until a new mitotic phase [Kramer et al., 2000]. During G1, CDH1 targets various proteins for degradation. One of these targets is Geminin, a protein that binds the DNA replication factor CDT1, preventing its binding to the origin recognition complex. Since Geminin levels are low during G1, CDT1 can exert its function by licensing DNA during the pre-replication complex assembly [McGarry and Kirschner, 1998]. Later on, G1/S Cyclins phosphorylate and inactivate CDH1 leading to a new increase in Geminin levels [Qiao et al., 2010].

The cell-cycle control system has another essential ubiquitin ligase complex, the SCF (Skp, Cullin, F-box containing complex). The SCF activity depends on substrate-binding subunits called F-box proteins that recognize specific phosphorylated proteins
[Nakayama and Nakayama, 2005]. Upon association of the SCF complex with the SKP1 subunit, mainly active in late G1, this will result in ubiquitination and degradation of CKIs like p27 and p21, as well as the G1/S Cyclin E [Shaik et al., 2001]. Therefore, SCF-SKP1 promotes cell-cycle progression. In early mitosis, the SCF is associated with βTrCP, and promotes degradation of an APC/C^{Cdh1} inhibitor (EMI1) and WEE1. SCF and APC/C control each other and therefore regulate progression through the cell cycle [Vodermaier, 2004].

By exploiting these ubiquitin-ligase complexes, Sakaue-Sawano et al. developed a very elegant method for tracking cell-cycle progression in real time with high spatiotemporal resolution [Sakaue-Sawano et al., 2008]. This technique, named FUCCI system (*f*luorescent *u*biquitination-based *c*ell-*c*ycle *i*ndicator), is indeed based on cell-cycle dependent proteolysis of CDT1 and Geminin. More precisely, a fragment carefully selected by the authors of the CDT1 protein is fused to the red-fluorescent protein mKO2 whereas a portion of the Geminin protein is fused to the green-fluorescent protein mAG. Since APC/C^{Cdh1} is active during G1 phase, this leads to Geminin degradation; thus the nuclei of the cells harboring the FUCCI system will appear red in G1 (and G0) phase. In contrast, since SCF/Skp2 promotes degradation of CDT1 from S to M phase, nuclei will appear green in S/G2/M phases. During the transition from G1 to S phase cell nuclei turn yellow since CDT1 starts to be degraded and Geminin levels start increasing, clearly marking the initiation of DNA replication. Indeed, this system represents an ideal tool to visualize and analyze the dynamics of cell-cycle progression at the single-cell level [Newman and Zhang, 2008, Zielke and Edgar, 2015].

1.2 Theoretical aspects of synchronization of coupled oscillators

In this section I will introduce most of the theoretical concepts related to synchronization of coupled oscillators, which is a central theme in this thesis work. Basic notions such as oscillating dynamical systems, phase models, coupling, limit cycle, will be described in a non-technical manner.

1.2.1 The Synchronization phenomenon

The word "synchronization", deriving from the Greek words *syn*, meaning "the same" and *chronos*, meaning "time", can be defined as *"the collective adjustment of rhythms of self-sustained periodic oscillators due to their interaction"* [Pikovsky and Rosenblum, 2007]. An early description of the synchronization phenomenon comes from the observation of the Dutch scientist Christiaan Huygens in the 17th century, who discovered that two pendulum clocks suspended from a wooden beam as a common support, had perfectly coinciding oscillations with the pendula moving in opposite directions. He further noticed that if interferences were applied, this synchrony was reestablished in a short time. He finally found that this conformity of rhythms was caused by an imperceptible motion of the beam [Pikovsky et al., 2003, Kapitaniak et al., 2012]. Later in the 19th century, Lord Rayleigh reported the synchronization phenomenon in acoustical systems observing that two organ pipes of the same pitch standing side by side were influencing each other. When played at the same time, in some case they sound in absolute unison and in other conditions the two pipes could nearly reduce one another to silence [Rayleigh and Lindsay, 1945]. Another important investigation of synchronization concerns the discovery of W.H. Eccles and J.H. Vincent in 1920 on the synchronization property of a triode generator, an electrical device that produces alternating electrical current. They demonstrated that the coupling between

two triode generators having slightly different frequencies forced the systems to vibrate at a unique common frequency [Eccles and Vincent, 1920]. These experiments were later extended and confirmed by E. Appleton and B. van der Pol who showed that the frequency of a generator can be synchronized, or entrained, by an external signal having a slightly different frequency [Appleton, 1923, van der Pol, 1927]. These observations turned out to be of great practical importance since triode generators were later used as the basic elements of radio communication systems.

Nowadays we know that synchronization phenomena are not only found in constructed devices such as pendulum clocks, musical instruments or electronic generators, but also in biological systems, where synchronization occurs at different levels. Examples of natural phenomena encountering synchronization can be given by the synchronous firing of neurons, or the heart contractions, and from the biological clocks governing circadian cycles in virtually all living organisms, from lower to highly organized ones. There exist different forms of synchronization: two interacting oscillators can show *mutual synchronization*, so that they equally affect each other and mutually adjust their rhythms, or it might happen that one oscillator is subject to an *external force*. An example of synchronization generated by an external force is given by the adjustment of the internal circadian clock in living organisms. As described in Section 1.1.1, for most organisms including humans the internal period of the clock is slightly different than 24 hours, but is entrained by periodic environmental signals depending on the period of the Earth's rotation. In this case the synchronization action is obviously unidirectional, since, as described with hilarity by Pikovsky and colleagues, *"the revolution of a planet cannot be influenced by mankind (yet)"* [Pikovsky et al., 2003].

1.2.2 Self-sustained oscillators

In physics, self-sustained oscillators can be defined as active systems having an internal source of energy that is transformed into oscillatory movement. When isolated, a self-sustained oscillator continues to generate the same rhythm until the source of energy ends [Giné, 2013]. The oscillations are stable to small perturbations: when slightly disturbed, the system will transiently relax to the unperturbed oscillations. Such oscillators are called *autonomous dynamical systems*, they are *deterministic*, meaning that knowing the state of a system at a given time allows to determine its state in the future [Shafer, 1995]. Such dynamical systems are idealized mathematical models. For example, they do not incorporate natural fluctuations of the parameters and other sources of noise [Katok and Hasselblatt, 1997]. A remarkable feature of self-sustained oscillators is their ability to be synchronized. Self-sustained oscillators can have rhythms of various shapes or waveforms, from simple sine waveforms to a sequence of short pulses and oscillate with a period T, that constitutes the base time unit of the oscillations. A deterministic oscillating system can be seen as a collection of *variables* c, representing physical quantities, subject to some general dynamics F that describes the temporal variation

of c (in this notation, c is a vector):

$$\frac{dc(t)}{dt} = F(c(t)) \tag{1.1}$$

The system is oscillating if it admits as a solution a periodic function T, such that

$$c(t) = c(t+T) \tag{1.2}$$

If we want to describe the state of the oscillator at some time, we would need one or many variables. The number of required variables depends on the particular system and is called its *dimension*. For example, in order to determine unambiguously the oscillation state of a pendulum clock, we could use two variables, x and y, where x can be the angle of the pendulum with respect to the vertical and and y its angular velocity. The behavior of this system can be characterized by the time evolution of the variables pair (x, y). These variables are called coordinates in the *phase plane* and the *y(t)* vs. *x(t)* plot is called the *phase portrait* of the system, where a point with coordinates (x, y) is called a *phase point*. As the oscillation repeats itself after the period T, *c(t)=(x(t), y(t))* corresponds to a *closed curve* in the phase plane, called a *limit cycle*. If we slightly perturb the stable periodic motion of an oscillator and, thus, a phase point is pushed off its trajectory on the limit cycle, the original rhythm will be restored and the phase point will return to the limit cycle (only if the limit cycle is stable). Therefore, all the trajectories will tend to the cycle, and after some transient time there will be steady state oscillations reflecting the motion of the phase point along the limit cycle. This closed curve attracts phase trajectories and is hence called *attractor*. Moreover, dynamical systems can have more than one attractor having its own basin of attraction. Different basins of attraction are separated by repelling curves called *repellers*. The form of the limit cycle is determined by the parameters of the system and does not depend on how the system was put in motion, i.e., on the initial condition: when the solution of the system corresponds to a sine waveform, the limit cycle will be represented as a circle (Figure 1.3).

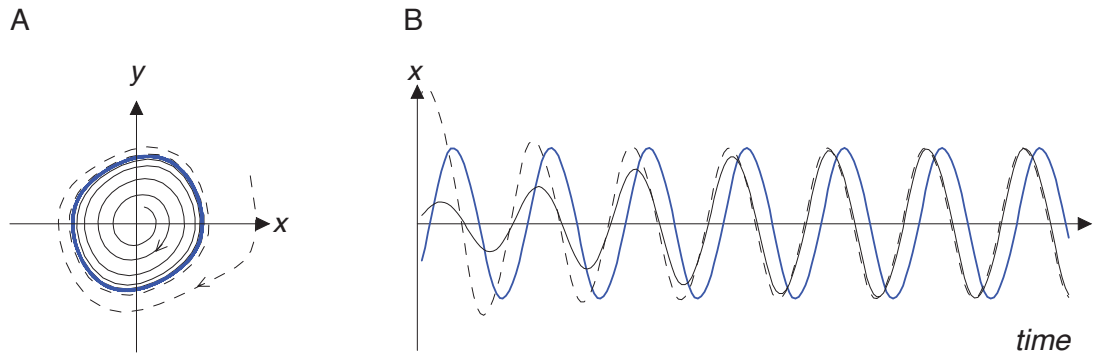

Figure 1.3 – Illustration of the limit cycle.
A. The blue closed curve (attractor) from the phase plane attracts all the trajectories and is called *limit cycle*. **B.** The same trajectories are shown as a plot time. (Modified from [Pikovsky et al., 2003])

The state of a periodic solution can be alternatively summarized by a single number, the *phase*, often indicated as θ, that indicates the position of the system along the periodic orbit. The periodic solution $c(t)$ can be related to the phase through a waveform function w that gives the values of c at a given phase, hence:

$$c(t) = w(\theta(t)) \tag{1.3}$$

The waveform of oscillators is typically 2π-periodic such that when the phase goes from 0 to 2π the system makes a whole revolution along its periodic orbit. Therefore, the oscillations can be characterized by the number of cycles per time unit, or the angular frequency ω which is related to the period of oscillation by $\omega = 2\pi/T$ (Figure 1.4 A). We can then write an ordinary differential equation for the phase θ, such that θ goes from 0 to 2π during the time T, as:

$$\frac{d\theta(t)}{dt} = 2\pi/T \tag{1.4}$$

The frequency of an autonomous isolated oscillating system is also indicated as the *natural frequency*, that can change due to external action on the oscillator or because of its interaction with another system.

Considering the neutral stability of the phase, even a small perturbation such as the coupling to another system or an external forcing can induce large deviations of the phase. The amplitude, instead, is only slightly perturbed as a result of the transversal stability of the cycle. Therefore, with a relatively small forcing, the phase and the frequency of oscillations will be adjusted without affecting the amplitude [Pikovsky and Rosenblum, 2007].

In order to take into account the effect of *external forces* that can either slow down or speed up the phase progression of the oscillator (Figure 1.4 B), we can add to the right hand side of the equation 1.4 a function of time $f(t)$, modeling the action of the external forces on the phase:

$$\frac{d\theta(t)}{dt} = 2\pi/T + f(t) \tag{1.5}$$

Similarly, random fluctuations (Figure 1.4 C) that arise in biological systems can be modeled by adding a random variable to the right hand side of the equation 1.4 as a noise term $\xi(t)$:

$$\frac{d\theta(t)}{dt} = 2\pi/T + \xi(t) \tag{1.6}$$

The addition of noise will transform the ordinary differential equation into a stochastic differential equation [D'Eysmond et al., 2013].

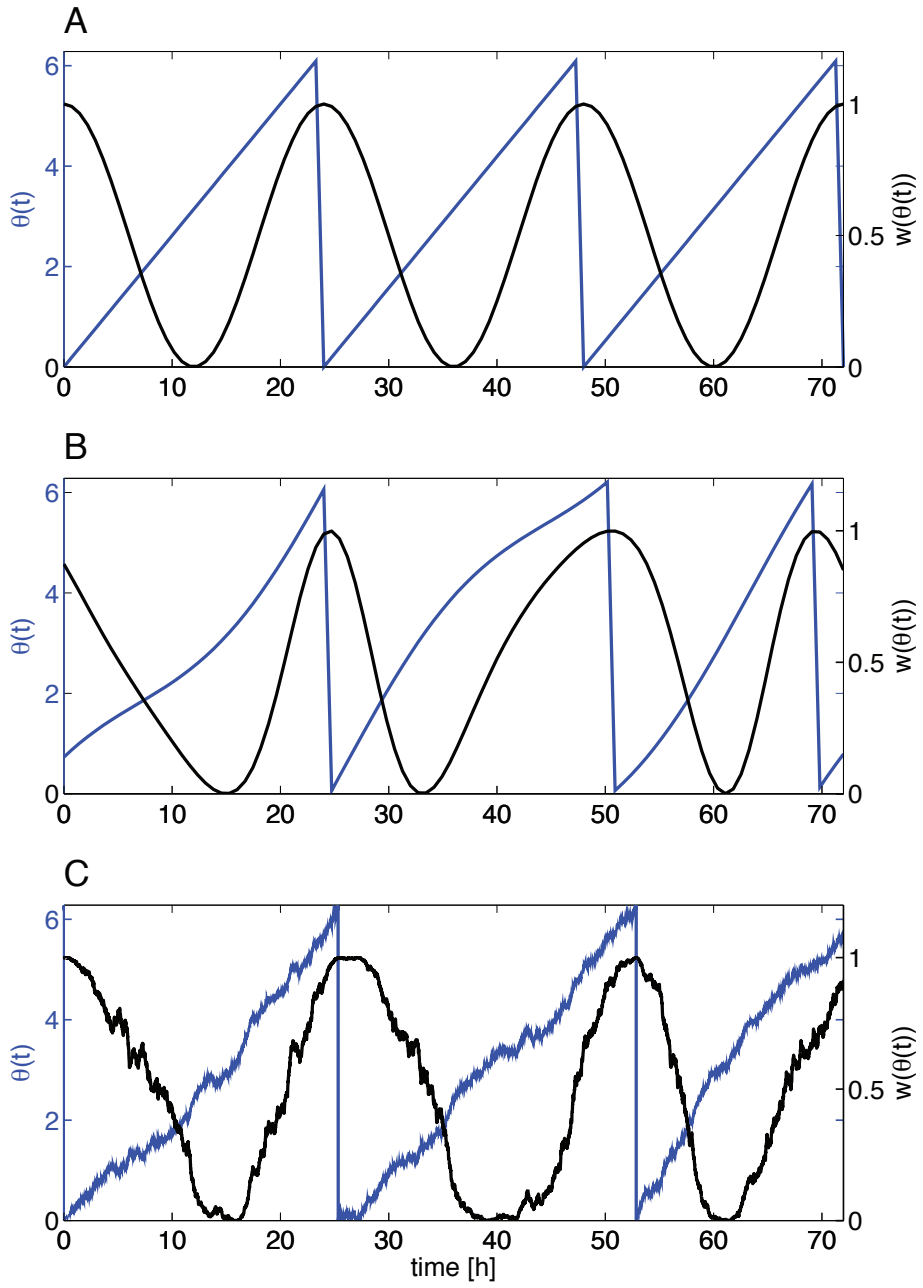

Figure 1.4 – Illustration of simple phase models.
The phase $\theta(t)$, modulo 2π, is shown in blue and the signal $w(\theta(t))$ in black. **A.** Unperturbed phase. **B.** Effect of an external force that speeds up (upward bending) or slows down (downward bending) the phase. **C.** Phase subject to random fluctuations.

1.2.3 Coupling of oscillators

There might exist various forms of interaction, or *coupling*, between two different oscillatory systems. As previously described for the pendulum clock's observation from Huygens, even a weak interaction can synchronize two oscillators (Section 1.2.1). In that case, the coupling was given by the wooden beam that allowed the two clocks to transmit their motion to each other. Indeed, two oscillators which, isolated, have different oscillation periods, if coupled can adjust their own rhythms and begin to oscillate with a common period. This phenomenon can be described as frequency *entrainment* or *locking*. In other words, when two nonidentical oscillators having their own frequencies ω_1 and ω_2 are coupled, they could start to oscillate with a common frequency. Their synchronization mainly depends on two factors: K, which is the *coupling strength* between the two oscillators, that describes how strong the interaction is, and ω_2 - ω_1, or the *frequency mismatch*, that identifies the difference between the periods of the uncoupled oscillators.

Thus, when a single phase oscillator θ is coupled to an external oscillating signal having a phase ϕ we have that:

$$\frac{d\theta(t)}{dt} = \omega_1 + K\sin(\phi - \theta) \tag{1.7}$$

where ω_1 is the intrinsic period of the oscillator (or the inverse of the period $\omega_1 = 2\pi/T_1$). The external signal oscillates with a period T_2: $\phi(t) = \omega_2 t$. The function sin of the *phase difference* ψ slows down θ when it is in advance with respect to ϕ, and speeds up when θ is late with respect to ϕ.

The phase θ is considered to be phase locked with the external signal if the phase difference $\psi = \phi - \theta$ does not change in time (there are weaker definition too, but for the sake of the argument, we will use this "strong" condition). This can be expressed by the differential equation:

$$\frac{d\psi(t)}{dt} = 0 \tag{1.8}$$

Synchronization can take place if the period mismatch between the two autonomous oscillators is not very large but this happens only if the coupling strength K is larger than the difference of the intrinsic frequencies: $K \geq |\omega_2 - \omega_1|$. When this is the case, the phase difference between the two oscillators is given by $\psi = \arcsin((\omega_2 - \omega_1)/K)$. Thus when the period of the external signal ϕ is shorter than the one of θ ($\omega_2 > \omega_1$), θ will lag behind ϕ ($\psi > 0$), while when the period ϕ is longer than the one of θ ($\omega_2 < \omega_1$), θ will precede ϕ ($\psi < 0$).

Consequently, two oscillators can synchronize even if the coupling strength is weak on the condition that the period difference between the two oscillators is small enough. The *synchronization region* can be described by the so-called *Arnold tongue* illustrated in Figure 1.5. As expected, the width of the synchronization region increases with coupling strength.

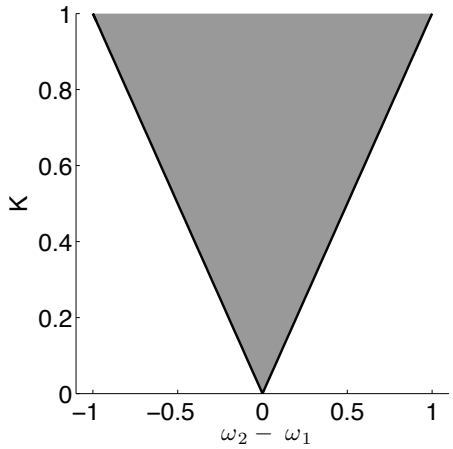

Figure 1.5 – Synchronization region.
The two oscillators synchronize inside the grey region delimited by the two black curves (corresponding to $K = |\omega_2 - \omega_1|$). This region is commonly known as Arnold tongue.

This particular type of synchronization is indicated as 1:1 *mode-locking*, because, when synchronized, the two cycles oscillate with the same frequency such that one cycle of the first oscillator is completed while the second oscillator too completes one cycle. However locking can occur for any rational number p:q such that one cycle does p full revolutions while the other one does q [Glass, 2001]. For example, in a 2:1 mode-locking state, the first oscillator will run twice as fast as the second one.

As already mentioned in Section 1.1, both the circadian rhythm and the cell cycle oscillate with a period close to 24 hours in mammalian cells. Therefore, the above-described theory makes reasonable to formulate the hypothesis that these two periodic processes might synchronize at the single-cell level.

Since synchronization can occur such that both oscillators can influence each other via different coupling functions and the synchronization can be either bidirectional or unidirectional [Palus and Stefanovska, 2003], various methods aiming to detect the directionality of the coupling from time series have been suggested [Smirnov and Bezruchko, 2003, Rosenblum and Pikovsky, 2001].

1.3 Interaction between cell cycle and circadian rhythm

In the following section, I will give an overview on past and recent research aiming to identify the interconnection between the circadian clock and the cell cycle in different organisms and cell types and from various points of view. I will describe the observed interactions from unicellular organisms to single mammalian cells, elucidating the identified crosstalk from both a cellular, molecular and mathematical standpoint.

1.3.1 Coupling between the circadian clock and the cell cycle from bacteria to metazoan cells

1.3.1.1 *Coupling between the circadian clock and the cell cycle in lower organisms*

Several studies highlighted the interactions between cell divisions and circadian oscillations from both prokaryotic and eukaryotic species.

One of the first observations of rhythmic cell divisions was made in populations of ***Gonyaulax polyedra***, a marine flagellate protist species emitting luminescence. These dinoflagellates, grown with alternation of 12 hours of light and 12 hours of darkness, were mainly dividing towards the end of the dark phase and the beginning of the light one in an interval of about 5 hours [Sweeney and Hastings, 1958]. Moreover, when these microorganisms were grown at different temperatures or light intensities, the periodicity in cell divisions was only slightly changing, while the growth rate was significantly affected. Therefore, the authors hypothesized a clock mechanisms underlying the observed rhythmicity of cell division.

Similar observations were shown in the unicellular green alga ***Chlamydomonas reinhardtii***. This eukaryote represents an excellent model organism for the circadian clock, since it displays circadian control of physiology found in processes such us phototaxis, i.e the photoaccumulation generated by the orientation of the alga toward the light [Bruce, 1970], or chemotaxis to ammonium [Byrne et al., 1992]. Importantly, temporal control of cellular division was found in these alga [Bruce and Bruce, 1981]. When isolating mutants with longer circadian periods identified by phototaxis oscillations, the rhythm in cell division was found to be affected [Bruce, 1972, Straley and Bruce, 1979]. The division behavior is shown to respect the main circadian criteria, since cell division persists with a period of about 24 hours in free running conditions, is temperature compensated and is entrainable to light/dark signals [Goto and Johnson, 1995].

Another model organism often used for investigating the circadian impact on cell cycle is the prokaryotic unicellular organism ***Synechococcus***. Investigations were conducted in populations of the strain PCC 7942 of these cyanobacteria exhibiting circadian behavior and rapid growth [Kondo et al., 1993]. Cells were monitored in rapidly growing conditions by continuously diluting the cultures in order to provide constant cell density. The results in populations dividing with a rates of about 10 hours showed that phases in which cell divisions slowed

or stopped had a circadian periodicity [Mori et al., 1996]. Thus, even cells having doubling times much faster than 24 hours expressed robust circadian rhythms of cell division indicating that *Synechococcus* sp. PCC 7942 cells are able to maintain two distinct timing states at the same time. Moreover, cultures of exponentially growing cells with doubling rates of 5-6 hours showed circadian rhythms of a bacterial luciferase reporter and mRNA abundance [Kondo et al., 1997]. This phenomenon was later analyzed at the single cell level in *Synechococcus elongatus* with the aim of determining when cell-cycle progression was slowed down as a function of circadian and cell-cycle phases [Yang et al., 2010]. By tracking cell-division events and circadian phases of individual cells and combining mathematical modeling to estimate the circadian clock effect on the cell cycle, a transition from a 1:1 to a 2:1 mode locking state was observed when the period of the cell cycle was decreased around 12 hours.

The timing of the cell cycle has been tested also in ***Zebrafish*** embryonic cells [Tamai et al., 2012], in which exposure to light represses the clock by inducing a sustained expression of *Cry1*. The authors demonstrated a clear circadian regulation of cell division time, with a peak between the late night and the early morning, and showed how repressing the clock function with light suppressed the circadian oscillations in the mitotic index. Similarly, a clock mutant cell line showed how rhythms in mitosis are lost, and clearly indicated that this effect is not light-induced but rather driven by the circadian pacemaker itself, since exposure to the light-dark cycles was not sufficient to drive a mitotic rhythm. They furthermore revealed that gene expressions of several mitotic genes such as *Cyclin B1*, *Cyclin B2* and *cdc2*) was rhythmic and their peak of expression coincided with the peak of mitotic index.

The multinucleate fungus ***Neurospora crassa***, which represents a very powerful model for elucidating the molecular circadian clock mechanism, was recently analyzed for the coupling between cell cycle and circadian clock via combination of mathematical models with validating experiments [Hong et al., 2014]. By employing a Histone1-GFP reporter, it was shown that a larger number of nuclear divisions occurred in a specific circadian window, notably in the evening. Moreover, molecular components connecting the two oscillators were identified. More specifically, the authors found that important cell cycle regulators such as the G1 cyclin CLN-1 and the G2 cyclin CLB-1, oscillate in a circadian manner, leading to synchronized mitotic divisions. These two cyclins showed a circadian light-dependent phase shift in their gene expression similar as the one observed for *frq* (*frequency*), a core clock component in *Neurospora*. Importantly, the authors found STK-29, serine/threonine protein kinase-29, which is the *Neurospora* homolog of the mammalian WEE1 kinase, as a crucial protein in mediating the coupling between circadian clock and cell cycle. Moreover, they found that oscillations of both *stk-29* and *clb-1* are lost in a circadian arrhythmic mutant.

All these studies highlighted cell cycle fluctuations with circadian time, indicating a control by the circadian clock onto the cell cycle. These observations led to a model referred to as *circadian gating of the cell cycle*, through which the circadian clock can favor or forbid certain cell cycle transitions at specific circadian phases.

1.3.1.2 *Coupling between the circadian clock and the cell cycle in mammalian cells*

In mammals, circadian variations in mitotic indices have been observed in different organisms and tissues. A comprehensive study on circadian rhythms in cell proliferation was made in 1991 by W.R. Brown, who gathered all the theretofore-published studies reanalyzing the dataset from the original studies in a systematic way [Brown, 1991]. His review was mainly focused on data from mouse, rat and human epidermis. To conform the data from the different studies, the circadian times were calculated as the percent difference from the mean at six circadian time points, 4 hours apart, and synthesized for each species for both, S-phase and M-phase. The original studies used for the generating the composite curves provided data originated from different techniques. For M-Phase, the number of mitotic cells was measured and compared to the total number of cells from skin sections by light microscopy; in some case, cells were treated with metaphase arrest drugs. For determining the S-Phase, three techniques were used: i) autoradiography of skin sections determining the percentage of labeled cells treated with tritiated thymidine; ii) scintillation counting of samples of epidermis with the same size after tritiated thymidine injection; iii) flow cytometry for identifying the amount of DNA typical of S-phase (between the diploid amount in G1 and the double diploid amount in G2). Interestingly, the observed rhythms in mice and rats were sharing the same phase and amplitudes, whereas rhythms in humans were in antiphase with the rodents' ones and had reduced amplitudes. More precisely, S-phase peaked at about 3:30 AM in mouse and rat cells and at about 3:30 PM in human cells, whereas M-phase peaked at about 8:30 AM in rodents and at about 11:30 PM in humans.

A later study [Bjarnason et al., 2001] on human biopsies obtained from the oral mucosa and skin at 4 hours intervals showed rhythmic expression of the human clock genes *Clock*, *Tim*, *Per1*, *Cry1*, and *Bmal1* in both tissues. This study, being the first one showing the epxression of rhythmic genes in peripheral human tissues, showed circadian profiles of the above mentioned genes which were consinstent with what previously found in rodents. Importantly, the authors found associations between the timing of clock genes expression and specific cell-cycle phases. Indeed, DNA synthesis showed a circadian variation with a peak in the early afternoon and *Per1* peak coincided with the G1 phase peak. Their results suggested a possible role of the circadian clock in controlling the timing of cell-cycle phases in continuosly proliferating human tissues.

A significant progress for the understanding of the circadian role in the timing of cell cycle phases was made by a study in regenerating mouse liver [Matsuo et al., 2003]. In this landmark study, partial hepatectomy was performed at different circadian times and DNA content was monitored. The authors observed that S-phase occurred always at a fixed interval after the hepatectomy, independently of the circadian time, whereas mitosis occurred at a specific circadian time. These observations suggest that, in these cells, the circadian clock gates the cell cycle by establishing a specific temporal window for M phase to occur. This effect is lost in *Cry1* deficient mice. Moreover, this study showed that circadian clock controls the expression of cell cycle related genes, indirectly modulating the expression of *CyclinB1-Cdc2* kinase, crucial

for the transition into mitosis. Interestingly, the authors identified the kinase *Wee1* as a direct target of BMAL1 and CLOCK. Indeed, *Wee1* mRNA exhibited robust circadian oscillations in liver of wild type mice, whereas *Wee1* mRNA was constitutively high or constitutively low in *Cry*-deficient or *Clock* mutant mice, respectively. Finally, in regenerating livers, the circadian oscillations in *Wee1* mRNA expression are reflected by rhythmic WEE1 protein levels and kinase activity. Altogether, these results suggested that the circadian clockwork could directly control cell cycle progression *in vivo*.

Another landmark work on the interaction between cell cycle and the circadian clock in mammalian cells at the single-cell level is the study from Nagoshi et al. on NIH3T3 mouse fibroblasts [Nagoshi et al., 2004]. These cells were engineered with a yellow fluorescent protein (Venus, VNP) under the control of the circadian gene *Rev-Erbα* allowing monitoring single cells for several days by fluorescent time-lapse imaging. This approach allows detecting both, the circadian oscillations and the time of division, characterized by a dip in the signal due the nuclear breakdown occurring during mitosis. The analysis of the time-lapse recordings, in conjunction with mathematical models, showed a circadian gating of mitosis at three specific circadian phases when the cells were synchronized with Dexamethasone, a glucocorticoid hormone analog often used for synchronization of many mammalian cell types [Balsalobre et al., 2000]. However, they also detected an effect of cell divisions on the circadian clock since the time at which the cells divided affected the length of the encompassing circadian interval.

Importantly, NIH3T3-Rev-VNP-1 (abbreviated NIH3T3-Venus) cells engineered in this study were kindly provided to us from E. Nagoshi and used in most of the experiments presented in this thesis work. Compared to the methods used in the original study [Nagoshi et al., 2004] that inspired our work, we mainly analyzed unsynchronized cells, tested different growing conditions, significantly scaled up the statistics and extended the analysis.

Surprisingly, an interaction between cell cycle and circadian clock was not found in immortalized rat-1 fibroblasts [Yeom et al., 2010]. The authors used two luminescent reporters, one under the control of *Bmal1* promoter for following the circadian oscillations, and the other under the control of *Cyclin B1* as a marker of cell cycle rhythm, peaking at the G2/M phase. By independently monitoring the luminescence from each reporter in cell populations tested under the same conditions, and comparing both, the phase and the period of the two reporters, they did not find consistent phase relationship between the cell cycle and the circadian signal. Interestingly, the authors further showed that the cell cycle rhythm, measured with the timing of mitosis and the *CCNB1*-dGluc expression, was not temperature compensated. Their results suggested that, in tin immortalized rat-1 fibroblasts, the circadian clock does not have an influence on cell division patterns. Since their findings were inconsistent with many previous observations, they proposed the hypothesis that the timing of mitosis might be synchronized via a rhythmic host environment, rather than by a direct coupling between the two systems, or that the coupling might exists but is disconnected in immortalized cells.

Another study from the same group [Pendergast et al., 2010] reached similar conclusions

in Lewis lung carcinoma (LLC) cells. These cells exhibit a functional circadian clock, as showed by stable transfection with a *Per2*-luciferase construct, and their circadian rhythm is temperature compensated. In contrast, the rhythmic timing of cell divisions monitored in LLC cells stably expressing *CCNB1*-dGluc did not show temperature compensation. Indeed, if the circadian and cell cycles would be coupled in these cells, the cell cycle rhythm should be temperature compensated as well as the circadian rhythm. Based on this assumption, the authors concluded that in LLC cells, as for rat-1 immortalized fibroblasts, circadian and cell cycles are not coupled. They furthemore proposed a novel hypothesis suggesting that the two cycles become disconnected in tumor cells rather than having a causal effect of dysregulation of the biological clock in generating uncontrolled cell division.

In support of the hypothesis of a circadian gating of the cell cycle, a recent study [Kowalska et al., 2013] showed that the nuclear protein NONO, a partner of PER proteins, acts as a cell cycle regulator by directly binding to the promoter of *p16-Ink4A*, a cell cycle checkpoint gene regulating the G1/S transition (described in Section 1.1.2). Specifically, NONO induces the circadian activation of *p16-Ink4A* in a PER protein-dependent manner in mouse fibroblasts. In this study, the authors noticed that primary fibroblasts from NONO-deficient mice, showing almost normal circadian rhythms, had both a significantly increased rate of population doubling and a decreased number of senescent cells compared to the wild type cells. In order to test role of NONO in the circadian gating of the cell cycle, they synchronized both wild type and NONO defective fibroblasts with Dexamethasone, and analyzed different time points by flow cytometry in propidium iodide treated cells. Whereas the wild type cells showed a significant circadian variation in cell divisions measured by the percentage of cells in S phase, the NONO deficient cells divided at equal levels throughout the day, indicating a lost of the circadian gating.

This PhD thesis work has recently contributed to a deeper understanding of a possible synchronization between circadian and cell cycles in mammalian cells [Bieler et al., 2014]. As it will be further described in Chapter 2 and Chapter 3, our study, combining time-lapse microscopy with mathematical models, indicated that, in NIH3T3 mouse fibroblasts, the two cycles proceed in tight synchrony over many conditions probed and that the synchronized state reflects a predominant influence of the cell cycle on the circadian cycle.

Remarkably, a simultaneous study [Feillet et al., 2014] using the same NIH3T3 cell line and a comparable large-scale time-lapse microscopy approach combined with mathematical modeling, reached very similar conclusions than the ones highlighted in our work [Bieler et al., 2014]. Feillet et al. further engineered the NIH3T3-Venus cell line [Nagoshi et al., 2004] [Bieler et al., 2014] with the cell cycle reporter system FUCCI (described in Section 1.1.2, [Sakaue-Sawano et al., 2008]) having a more precise indication of cell cycle progression that allowed them to extract the time of G1/S transitions. They analyzed cells proliferating in medium with three different concentrations of FCS, being 10%, 15% and 20% and performed time-lapse microscopy for 72 hours with a time resolution of 15 minutes. The cell cycle length was determined as the time interval between two consecutive divisions. Their results

showed that untreated cells had similar periods for both, the cell cycle and circadian rhythms, in 10% and 15% FCS conditions. For the 10% FCS condition, the mean circadian and cell cycle durations were 21.9 h and 21.3 respectively, whereas for the 15% FCS condition, both periods were decreasing to 19.4 h for the circadian clock and 18.6 h for the cell cycle. In the two conditions the system showed a 1:1 mode locking state. The speed up of the cell cycle could be directly related to an increase of nutrients in the medium, but the circadian period shortening cannot be related to the same factor, since non dividing confluent cells showed a 24h period independently on the FCS concentration. The authors tested also conditions with 2 hours Dexamethasone treatment performed right before the start of recordings. In this case, cells cultured in 10% serum showed a clock period of 24.2 h and a cell cycle period of 20.1 h, whereas in the 20% serum conditions, two different coexisting groups of cells were identified. A first group showed periods similar to the untreated conditions (21.25 h for the circadian period and 19.5 h for the cell cycle length), indicating a 1:1 mode locking state, whereas the second group showed a much longer circadian period of 29 h and a shorter cell cycle length of 16 h indicating a 3:2 (3 cell cycles for 2 circadian periods) mode locking state. They thus suggested that Dexamethasone treatment could cause a switch from the 1:1 state towards other attractors.

Even if our work [Bieler et al., 2014] indicated a unidirectional coupling reflecting a dominant effect of the cell cycle on the circadian clock, whereas Feillet et al. concluded a bidirectional coupling, both studies converged in excluding a possible circadian gating of the cell cycle, that was formerly the dominant hypothesis [Feillet et al., 2015].

1.3.2 A note on mathematical models of interacting cell cycle and circadian clock

The interaction between circadian and cell cycle oscillators have been analyzed also from a mathematical standpoint. Beside from the already mentioned studies [Nagoshi et al., 2004, Hong et al., 2014, Bieler et al., 2014, Feillet et al., 2014] in which mathematical models were combined to the experimental data, a number of theoretical studies aimed to test or predict the effects of the coupling between the two systems.

Based on the observation that a number of molecular components of the cell cycle are regulated in a circadian manner, Gerard and Goldbeter used detailed computational models for the mammalian cell cycle and circadian networks in order to explore under which conditions the cell cycle could be entrained by the circadian clock [Gérard and Goldbeter, 2012]. The authors coupled a model based on the four main cyclin/Cdk complexes driving cell cycle progression [Gérard and Goldbeter, 2009] with a model previously proposed for the circadian clock [Leloup and Goldbeter, 2003] in which CLOCK-BMAL1 complex oscillates in a circadian fashion. By assuming that the CLOCK-BMAL1 heterodimer controls the transcription of the *Wee1* gene, they incorporated in the model circadian variations of this kinase, through which the coupling might occur. They show that entrainment to a cell cycle period of either 24 or 48 hours from the circadian clock can occur only when the autonomous period of the cell cycle falls into an appropriate range of values. Moreover, they found that entrainment can occur as a consequence of circadian oscillations in the level of a growth factor regulating the entry into G1 phase.

Similarly, Zámborszky et al. [Zámborszky et al., 2007] had connected a minimal but robust version of a mammalian circadian clock model, consisting of transcription–translation feedback loops, with a previously published model for the cell cycle [Novák and Tyson, 2004], to which they added *Wee1* as being controlled by clock components. As they varied the cell cycle period, that in this study is referred to as "mass doubling time", cell divisions locked into specific phases of the circadian rhythm when Wee1 is periodically regulated by circadian components. This locking is lost in absence of coupling or when the coupling strength is significantly reduced. When they simulated cell cycle periods of 16h and 18h in the presence of a strong coupling, the circadian clock entrained the cell cycle so that multimodal distributions of cell cycle durations were generated. Their simulations also indicated that, in mammalian cells, the circadian clock has a strong influence in controlling the cell size during cell cycle progression and that periodic modulations on the cell cycle progression via *Wee1* exert cell size control when the cell cycle period is largely different from the circadian period.

Another study [Kang et al., 2008] proposed that the gating of cell cycle by the circadian clock might allow the circadian clock avoiding perturbations possibly induced by inhibition of transcription occurring during M phase. To test that, the authors introduced periodic pulses of transcriptional inhibition in an already existing model of the circadian clock
[Leloup and Goldbeter, 2003] and made simulations under constant darkness or light-dark conditions. Interestingly, they showed that, in case of constant darkness, a periodic transcrip-

tional inhibition is able to entrain the circadian clock as it happens in case of the light-dark entrainment. Moreover, they obtained different degrees of perturbation on the circadian clock according to when the transcriptional inhibitions were imposed: transcriptional inhibition imposed at middle/late night, when mitosis is more frequent, caused the minimal perturbation to the circadian clock. They also found that entrainment can occur when the cell cycle has intrinsic period of 24h, 12h or 48h, indicating a 1:1, 2:1 and 1:2 mode locking respectively. When the cell cycle period was simulated to be about 24 hours, a unimodal distribution of periods was observed; in contrast, a cell cycle period of 12 hours caused a bimodal distribution, whereas for intermediate cell cycle periods the distribution was uniform and no synchronization is detectable.

Since several models have been developed to evaluate the control of the circadian clock on the cell cycle, supporting the concept of circadian gating, Trayanard et al. [Traynard et al., 2015] performed a model-based investigation on the reverse interaction based on the latest results on NIH3T3 fibroblast [Bieler et al., 2014, Feillet et al., 2014] indicating an unexpected predominant effect of the cell cycle on the circadian clock. The authors thus hypothesize that the inhibition of transcription during mitosis in eukaryotes might lead to entrainment of the circadian clock by the cell cycle. This scenario would explain the observed acceleration of the circadian clock in actively dividing cells. They developed a differential model by combining the mammalian circadian clock model developed by Relogio et al. [Relogio et al., 2011] with a generic model of the cell cycle used to simulate both the G1/S and G2/M transitions [Qu et al., 2003]. The resulting coupled model was able to reproduce the measurements of periods and phase locking modes showed in Feillet et al. but was not able to reproduce the phase shift between the time of mitosis and the *Rev-Erbα* peak.

1.4 Objectives of this thesis

Main aim of this thesis:

- to shed light on the interaction between the cell cycle and circadian clock at the single cell level in mammalian cells.

Specific aims of this thesis:

- to investigate the presence of coupling between cell cycle and circadian oscillators;
- to investigate under which conditions the interaction between the cell cycle and the circadian clock can lead to synchronization;
- to investigate the directionality of the coupling:
- to identify which parameters modulate the interactions;
- to analyze cell type specificity of the interactions.

Even though interactions between the cell cycle and circadian clock have been reported, the dynamical consequences and the directionality of the coupling at the single-cell level were not extensively investigated.

With the aim of investigating the presence of the coupling and identifying potential synchronization between cell cycle and circadian oscillators in mammalian cells, we used the NIH3T3 mouse fibroblast cell line, a well-established model for circadian rhythm. To provide quantitative evidences of the synchronization we thus wanted to estimate the mutual interactions between the circadian rhythm and the cell cycle.

To investigate under which conditions the interaction between the cell cycle and the circadian clock can lead to synchronization and to investigate the directionality of the coupling between the two oscillators, we wanted to test several experimental conditions inducing perturbations of either the cell cycle or the circadian rhythm. More specifically, we aimed to perturb the two oscillators by:

- testing different growing conditions such as various serum concentration and different temperatures;
- treatments with pharmacological compounds affecting either the cell cycle duration or the circadian interval length;
- genetic perturbations with knockdown of circadian regulators;
- phase resetting of the circadian clock.

Moreover, we aimed at identifying the phase dynamics of the two interacting oscillators via mathematical modeling reconstructing a picture of the synchronization and identifying potential interactions between the cell cycle and the circadian clock.

Finally, we aimed at investigating the cell-type dependency of the interaction between cell cycle and circadian clock by performing the analysis in additional cell lines exhibiting circadian rhythmicity, such as the human osteosarcoma U2OS cell line.

1.5 This thesis in brief

Going through the main results (Chapter 2 and Chapter 3) I will show how we demonstrated that:

- the circadian and cell cycle systems are strongly synchronized in NIH3T3 fibroblasts;
- this synchronization is stable under a wide set of conditions tested;
- the observed synchrony is caused by a dominant influence of the cell cycle on the circadian clock.

Finally (Chapter 5), I will relate the main observations of this thesis with past and recent studies, highlighting analogies and divergences, drawing some hypothesis on possible explanations of the resulting discrepancies, and presenting possible future directions of this work.

2 Results (I)
Synchronization of coupled circadian and cell cycle oscillators in mouse fibroblasts

"Science is beautiful when it makes simple explanations of phenomena or connections between different observations."
Stephen Hawking

2.0.1 Context and statement of author contributions

The work presented in this chapter describes the analysis of a large dataset from time-lapse imaging of mouse fibroblasts, aiming to investigate, at the single-cell level, the interaction between the circadian clock and cell cycle. This analysis clearly indicated that the two periodic processes are robustly synchronized at the single-cell level. This synchronization is reflected by the shortening of the circadian intervals in dividing cells. Perturbation experiments confirmed the predominant coupling from the cell cycle to the circadian clock and were consistent with the phenomenology of coupled oscillator. The synchronization between the two oscillators is highly robust and was tested using a wide range of experimental conditions.

The majority of the results introduced in this chapter are part of a manuscript entitled *"Robust synchronization of coupled circadian and cell cycle oscillators in single mammalian cells"* ([Bieler et al., 2014] attached in Section A.1) published in 2014 in the *"Molecular Systems Biology"* journal. The manuscript is a result of a collaborative work combining experiments, statistical analyses and mathematical modeling. In this Chapter, I will present results consisting in a direct contribution from myself. Previously published figures from the main text and the supplementary data of the manuscript are here introduced in an edited format. Moreover, unpublished figures are incorporated to illustrate the experimental pipelines and to show additional analyses that were not included in the manuscript.

The majority of the experimental work was conceived, designed and performed by myself, which includes the development of the protocols necessary to obtain high-quality time-lapse acquisitions and the processing tasks illustrated in Section 2.1 and Section 2.2. The experiments introduced from Section 2.3 to Section 2.8 and in Section 2.11 were entirely designed and performed by myself, whereas the results presented in Section 2.9 and Section 2.10 were produced with the contribution of David Gatfield who generated the shRNA cell lines. Regarding the data analysis, Jonathan Bieler developed the segmentation and tracking tool and performed the final analyses in collaboration with myself, Kyle Gustafson, Cedric Gobet, and Felix Naef.

2.1 Experimental Workflow and Analysis Pipeline

To investigate the possibility that cell cycle and circadian oscillators synchronize at the single cell level, we chose the mouse fibroblast NIH3T3 cell line, which is a well-established model for circadian rhythm. In particular, we used a NIH3T3 line previously engineered in U. Shibler's lab [Nagoshi et al., 2004] with a fluorescent circadian reporter expressing an enhanced version of the Yellow Fluorescent Protein (YFP) named *"Venus"* under the control of *Rev-Erbα* promoter.In addition, the construct also contains a PEST and a Nuclear Localization Signal (NLS) to destabilize the protein and drive its expression to the nucleus enabling easy monitoring of circadian oscillations. Therefore, cells stably transfected with the construct show a nuclear localized fluorescent signal that oscillates rhythmically.

In the original study [Nagoshi et al., 2004]only a few hundred cells undergoing divisions were analyzed by fluorescent microscopy. We thus opted for a large-scale experimental approach that would allow us to significantly scale up the number of analyzed cells enabling precise quantifications of the interaction between the two oscillators. A schematic of the experimental design and the following analyses is shown in Figure 2.1.

In our typical experiment workflow, one day before the recordings, cells are seeded in multi-well dishes and treated according to the experimental plan. Cells are then recorded for 3 days with fluorescent and brightfield acquisitions every 30 minutes (Figure 2.1A).

The analysis of the resulting images, schematized in Figure 2.1B, i, is performed with segmentation and tracking tools implemented in Matlab and customized in our group. The first step in the analysis consists of a pre-processing of the acquired images that allows the correction of the background. In the second step, the corrected images are then automatically segmented. However, this automatic step is error-prone due to several factors including: drop in the reporter signal, changes in the shape of the cells around mitosis, and low intensity of the signal around the circadian trough. In order to correct for these potential errors, we perform a third step consisting in the manual validation of the automatic segmentation with a customized software shown in Figure 2.1C.

Once the manual corrections are applied, cells are tracked in time using Single Particle Tracking (SPT) [Jaqaman et al., 2008] in order to obtain the final traces. It is thus possible to proceed with the circadian peaks and cell divisions estimations for each cell traces and to perform statistical analysis on the full dataset.

This approach allowed us to record about 10'000 single traces over several days by monitoring their circadian signal and cell division events enabling us to test several conditions and to obtain sufficient statistical power to detect subtle difference in the data.

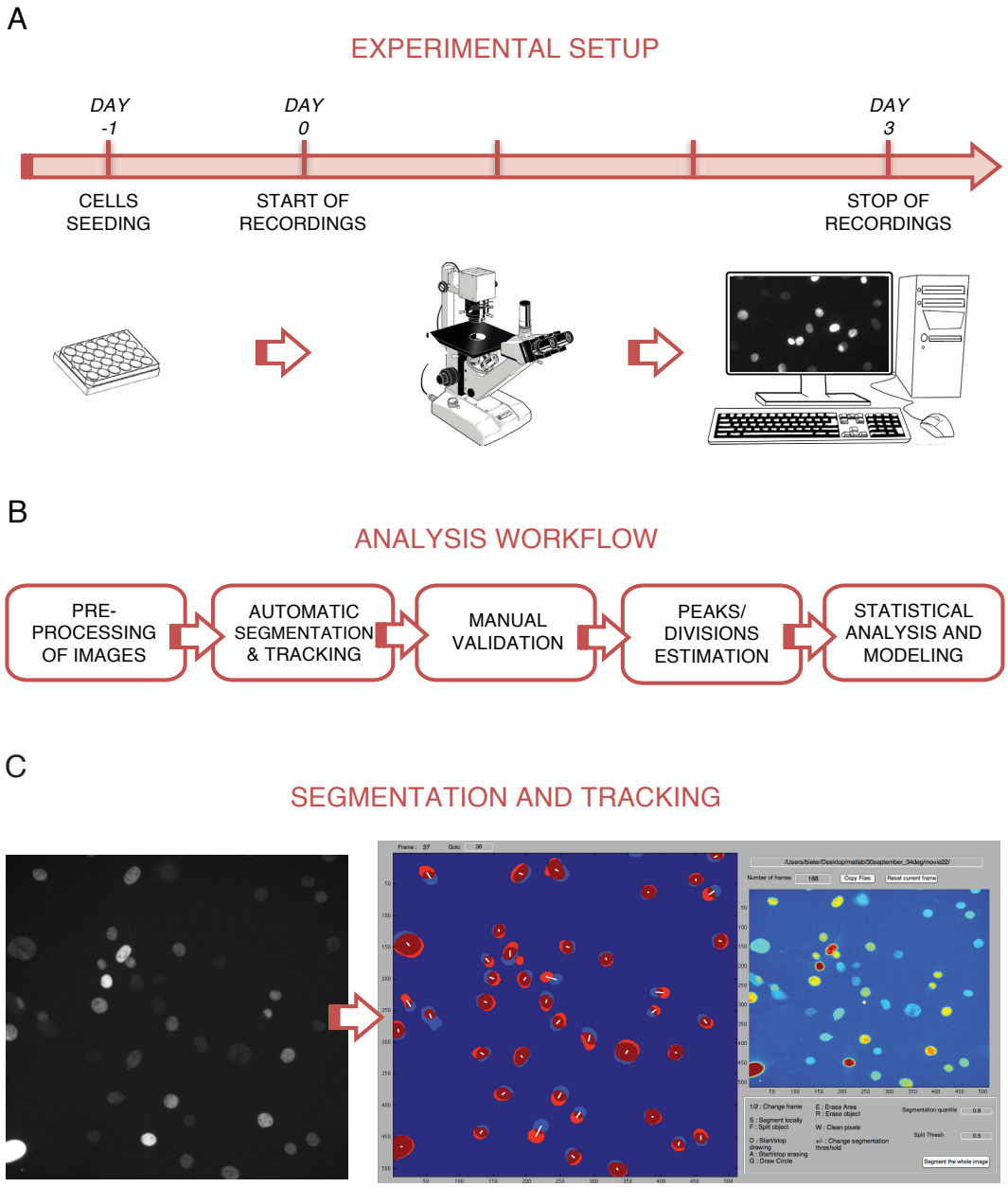

Figure 2.1 – Experimental setup and analysis workflow.
A. Illustration of the experimental time-lapse microscopy setup.
B. Analysis workflow used for the extraction of the dataset starting from the recorded time-lapse movies.
C. The left panel represents an example of acquired images showing YFP-signals in individual cell nuclei. On the right panel there is portrayal of the segmentation validation tool. The left side of the tool shows an overlay of the current segmented frame (corresponding to the acquired image shown in the left panel) with the previously segmented frame. Red areas represent the segmented nuclei recognized in the current segmented frame, whereas light blue areas correspond to the previously identified objects. The overlapping area of the objects recognized in both the current and the previous frame appears in dark red. The white line indicates the resulting tracking linking each cell between the two consecutive frames. The right side of the tool displays the image before the segmentation in a color scale corresponding to the signal intensity. It is possible to use several commands, displayed in the bottom part of the left side, for the correction of the segmentation errors.

2.2 Extraction of single-cell traces from time-lapse images

As already mentioned in the previous section, we used a standard tracking algorithm [Jaqaman et al., 2008] in order to follow cells in time. Cells are linked frame by frame based on parameters such as fluorescent intensity and distance.

The extraction of cell traces showed a significant heterogeneity in the signal intensity and amplitude. Moreover, because of the cells motion along the recordings, many cells leave or enter the field of view, generating traces of different lengths. We thus produced a dataset in which about 25% of traces span the full-length recording time (i.e. 72 hours) and in which the average cell traces length is about 55 hours.

The quantification of the fluorescent signal allows us to simultaneously extract the circadian phase from the *Rev-Erbα* reporter peaks, and information about cell division events, detectable through the characteristic dip in the fluorescent signal intensity generated by the nuclear breakdown during mitosis. Single cell traces presented in Figure 2.2 show representative examples of the identified circadian peaks and cell divisions extracted using our pipeline.

The collection of thousands of traces allowed us to extract overall about 20'000 circadian peaks and 13'000 cell divisions, gaining information about cell cycle durations and circadian intervals at the single-cell level.

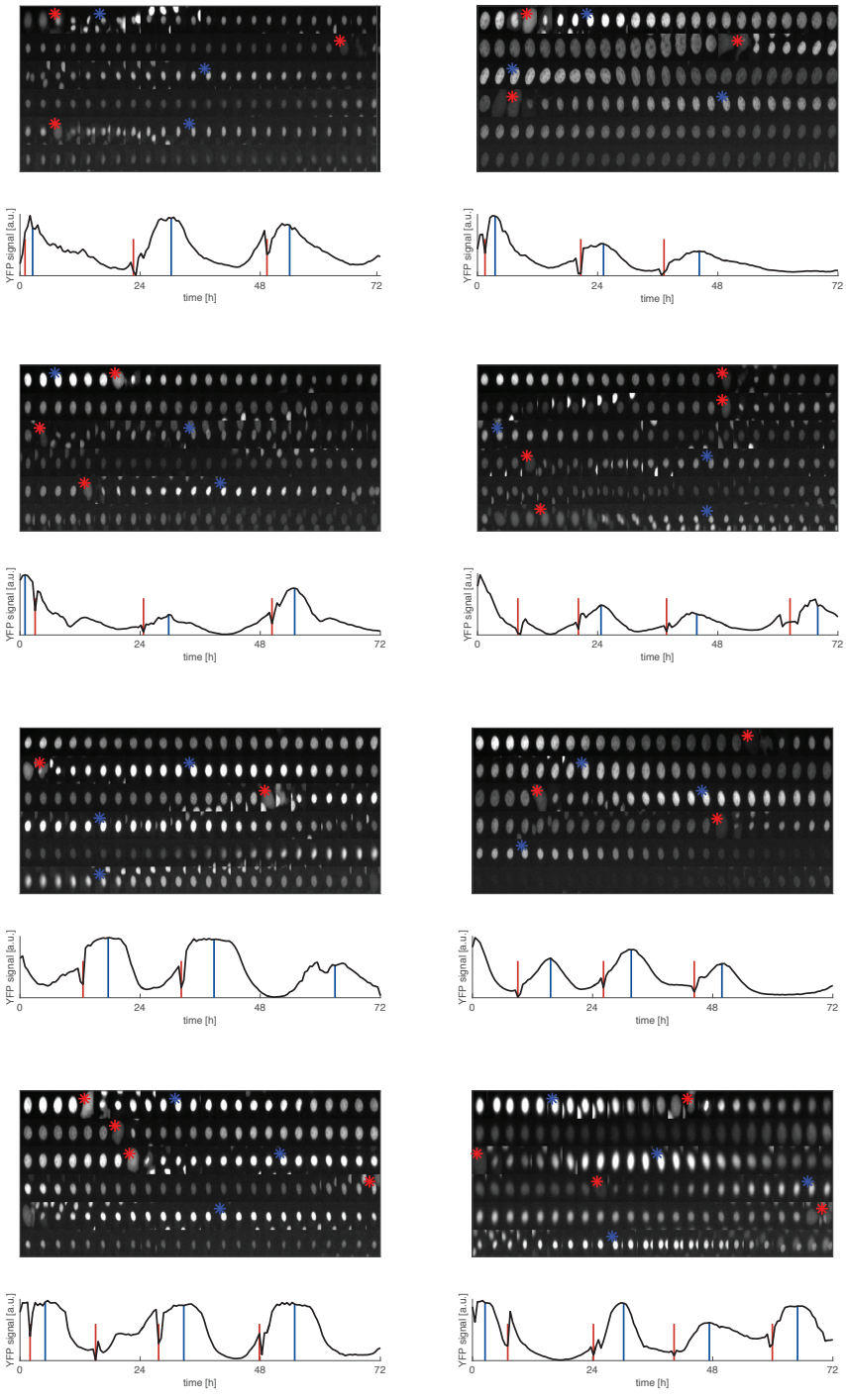

Figure 2.2 – Time series of circadian *Rev-Erbα*-YFP signals in individual cells.
Eight examples of time series of tracked nuclei are shown. For each presented cell, the upper panel shows single-frame images along the recording, where time runs from the top left to the bottom right. Since images are taken 30 minutes apart, each row corresponds to 12 hours of recording. The blue spots indicate the frame at which circadian peak is detected, as well as the red spots correspond to the detected division. In the panel below each time series, the quantified circadian signal is shown as a black trace. The identified peak of the reporter is marked with a blue vertical line, whereas the cell division detection corresponds to a red line.

2.3 Serum concentration has a small effect on cell cycle duration and no effect on the circadian period

In order to probe a range of cell cycle durations, we thought of recording cells under different growing conditions. In fact, it is well known that the concentration of serum in the media has an influence on the cell cycle [Brooks, 1976]. Consequently, we incubated cells with different serum concentrations ranging from 2% to 13% and extracted cell cycle durations and circadian intervals for each condition (Figure 2.3).

The data indicated that variations in serum concentration cause only a small effect on cell cycle, mostly lengthening the cell cycle at concentrations lower than 4% (Figure 2.3A, left panel). Interestingly, we were unable to detect any effect on the circadian intervals (Figure 2.3A, right panel).

Because of the low number of traces obtained at the lowest serum concentrations, data were clustered together in the different groups according to their serum percentage, from 2-5%, 6-9% and 10-13%.

The resulting distributions confirmed the small differences in cell cycle durations between the three clusters (Figure 2.3B) and the unaffected circadian intervals of which the distribution remains centered at about 24 hours in the three clustered serum ranges (Figure 2.3C).

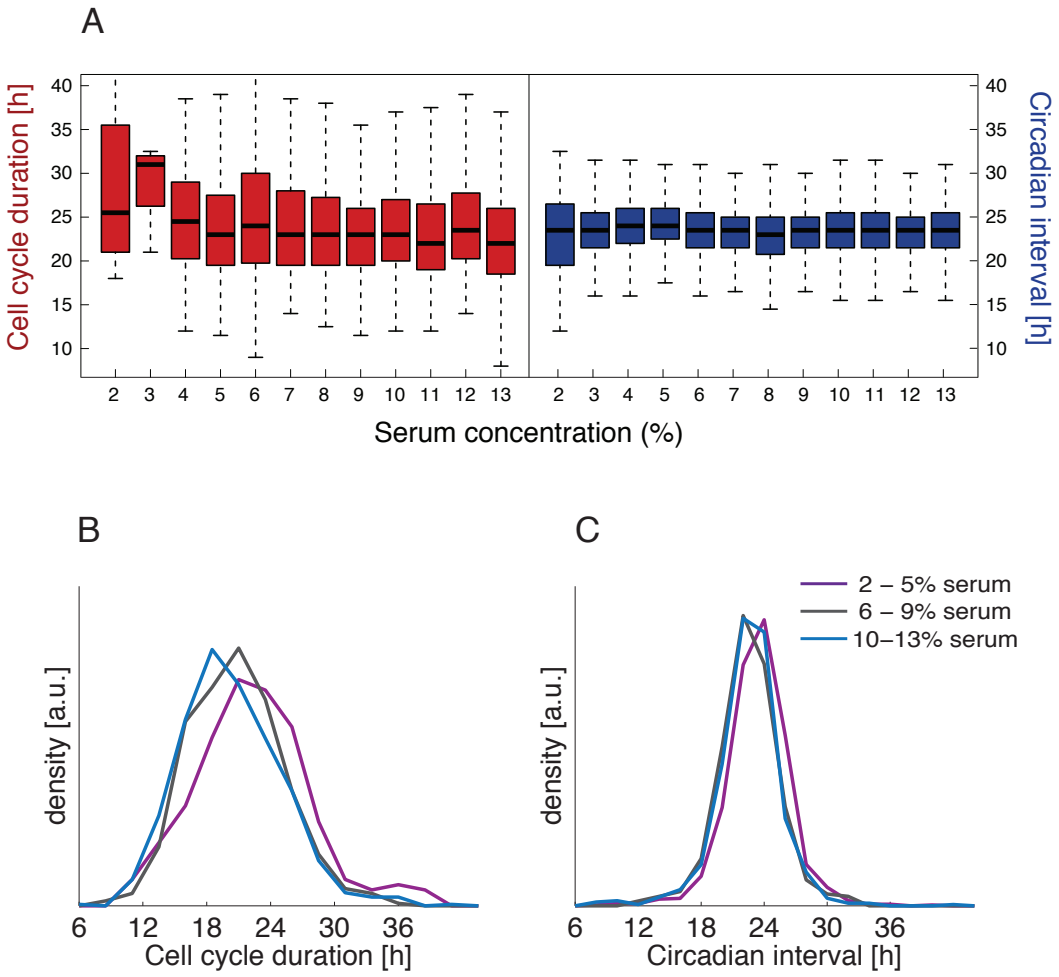

Figure 2.3 – Effects of serum concentration on cell cycle duration and circadian intervals.
A. Box plot showing the range of variation of both cell cycle duration (left) and circadian intervals (right) here depicted in red and blue respectively, for each serum concentration tested.
B. The distribution of cell cycle duration between three groups with different serum concentrations shows a slight dependency on increasing serum concentration.
C. The unimodal distribution of circadian intervals is almost undistinguishable for the three serum ranges.

2.4 Circadian and cell cycle oscillators show clear signature of synchronization in NIH3T3 cells

The analysis of our collection of single cell traces and their corresponding circadian peaks and cell division times highlighted a remarkable feature: cell divisions (d) tend to occur, on average, five hours before the circadian peak (p) of the *Rev-Erbα* reporter (Figure 2.4A, C). The unimodal distribution of division times with regard to the next circadian peak, which is centered around -5 hours, is independent on changes on serum concentration (Figure 2.4C, inset).

From our dataset is possible to observe about 30% variability in the timing of circadian peaks and cell divisions (Figure 2.4B), reflecting the inherent stochasticity of both circadian oscillations and cell cycle progression in individual cells [Nagoshi et al., 2004, Hahn et al., 2009]. Hence, the unimodal distribution of division times represents a clear signature of synchronization between circadian and cell cycle, that is maintained despite the big variation of circadian intervals and cell cycle durations.

Interestingly, even if the individual circadian and cell cycle intervals varied by more than 30%, circadian intervals and cell cycle durations measured on events “p1-d1-p2-d2” or “d1-p1-d2-p2” (where p1 and p2 stand for the first and the second detected circadian peak, respectively, as well as d1 and d2 correspond to the first and second division, respectively) are highly correlated (Figure 2.4B). To verify that this synchronization is not due to the independent running of the two oscillators that might initially be in synchrony and desynchronize over time, we compared the first (0-36 hours) and the second part (36-72 hours) of the movie. The comparison does not show significant difference in the division times distribution (Figure 2.4C). The synchrony between circadian and cell cycles, highlighted by the peaked and unimodal distribution of division times, results in a 1:1 mode-locked state, with a large majority of cells dividing late and a minority of cells dividing early in the circadian interval (Figure 2.4A, C, D).

Another observable feature is that longer circadian intervals have the tendency to include divisions that occur early in the circadian interval, i.e. closer to the previous circadian peak (Figure 2.4A, D).

Division times normalized to the enclosing circadian interval, referred to as circadian phases at division or division phases, while still showing unimodal distribution, have a bigger variability than the one observed for the division-to peak (d-p) intervals (Figure 2.4E). This variability is partially due to the fact that the included circadian intervals have variable durations, with shorter circadian intervals associated with advanced division phases and longer circadian intervals associated with delayed division phases (Figure 2.4F).

Overall, these observations indicate that circadian and cell cycle oscillators are in synchrony in NIH3T3 fibroblasts. This synchronization might be established by entrainment of one oscillator on the other or by a reciprocal entrainment of the two oscillators.

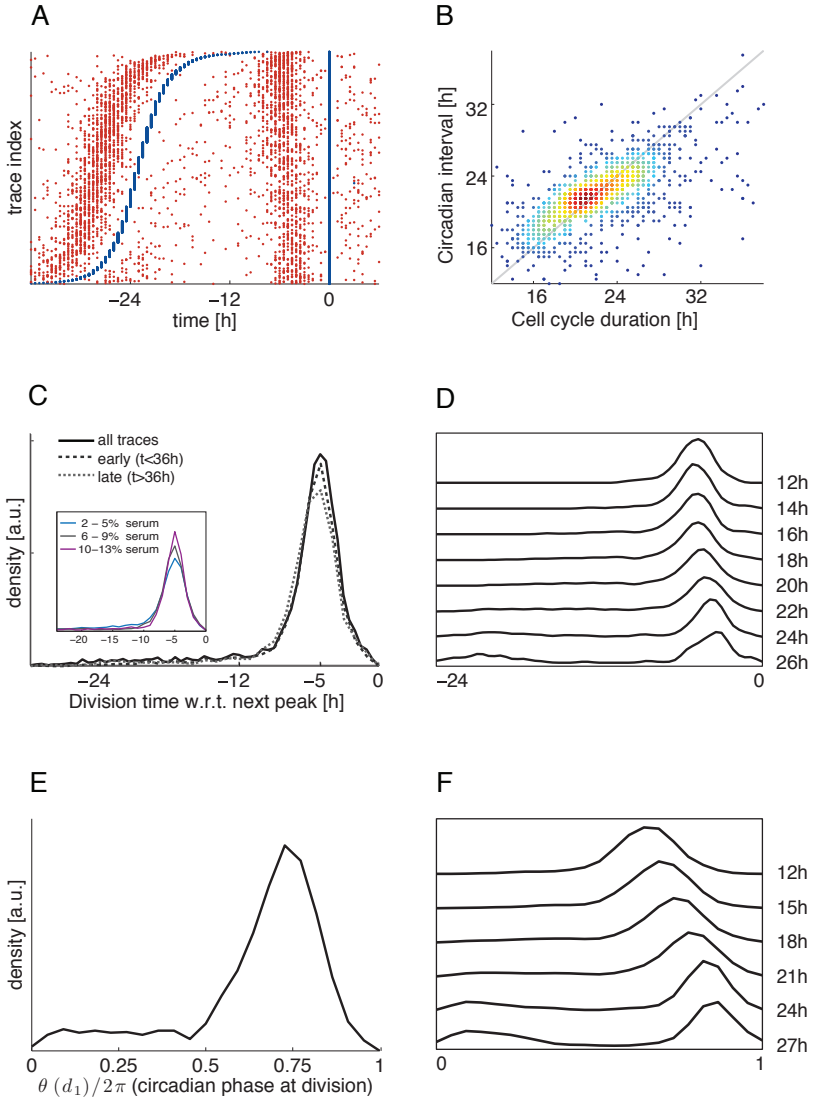

Figure 2.4 – Synchronization of circadian and cell cycle oscillators.
A. Raster plot showing cell traces (n=3160) with at least 2 circadian peaks (blue) aligned on the second circadian peak (blue straight line) and sorted according to the circadian interval (distance from the first to the second peak). Divisions events, represented as red dots, show the tendency to occur about five hours before the circadian peaks. A minority of division events occur closer to the first peak and these early divisions are mainly associated with longer circadian intervals.
B. Circadian intervals and cell cycle duration are highly correlated (R^2=0.52, n=1230, $p<10^{-16}$).
C. Division times measured with regard to the following circadian peak show a peaked unimodal distribution in our full 37 °C dataset (black solid line). The distribution of d-p intervals is centered around -5 hours and homogenous in time since events in the first half (dashed dark grey line) of the recordings are not different than during the second half (dashed dark grey line). Inset: The d-p intervals distribution does not vary with different serum concentrations.
D. Longer circadian intervals correlate with division occurring closer to the next peak and have an increased frequency of divisions occurring early in the circadian interval.
E. Normalized division times, referred to as circadian phase at division, show unimodal distribution.
F. Longer circadian intervals correlate with delayed division phases.

2.5 Cell division affects the length of circadian intervals

Since the synchronization between cell cycle and circadian clock might originate from either or both unidirectional or bidirectional influences, we aimed at investigating the directionality of their interaction by different means.

As a first approach, we compared circadian intervals with divisions (d-p-d) versus circadian intervals without divisions (p-p), exploiting the fact that cells can stochastically exit cell-cycle generating circadian intervals without divisions. Remarkably, we observed a shortening of the circadian intervals when division occurs between two consecutive peaks comparing to intervals with no division (Figure 2.5A). More specifically, while the distribution of circadian intervals without divisions is centered at 23.7 ±3.1 hours, hours, duration close to the expected length in free-running conditions, circadian intervals with one division last on average 21.9 ±3.8 hours. This difference between circadian intervals in presence or absence of divisions is highly significant ($p<10^{-16}$, t-test). This shortening of about two hours highlighted the influence of cell divisions on the circadian clock.

By comparing p-p with p-d-p intervals originating form the first and second half of the recordings, there is no significant difference in the intervals duration, excluding the hypothesis that the observed shortening originates from a temporal effect of the recordings (Figure 2.5C).

Interestingly, the duration of circadian intervals shows a variation that is dependent on the circadian phase at division (Figure 2.5B), consistently with the observation previously reported in [Nagoshi et al., 2004]), consistently with the observation previously reported in Nagoshi et al., 2004. More specifically, when divisions occur half way through two consecutive circadian peaks, we observe a lengthening of the circadian intervals that last around 18 hours. In contrast, when divisions occur earlier in the circadian phase there is a lengthening of the circadian intervals leading to longer circadian intervals that reaches around 27 hours.

Divisions occurring late in the circadian phase, composing the majority of our observations, confirm the shortening of the circadian interval from 24 to about 22 hours (Figure 2.5B, C). Consistent with this effect we observed a negative correlation between the p1-p2 and d1-p2 intervals (Figure 2.5D).

The shortening of circadian intervals in presence of division is a feature systematically observed at every tested serum concentration (Figure 2.5E). Altogether, these results highlighted the influence of the cell cycle onto the circadian clock.

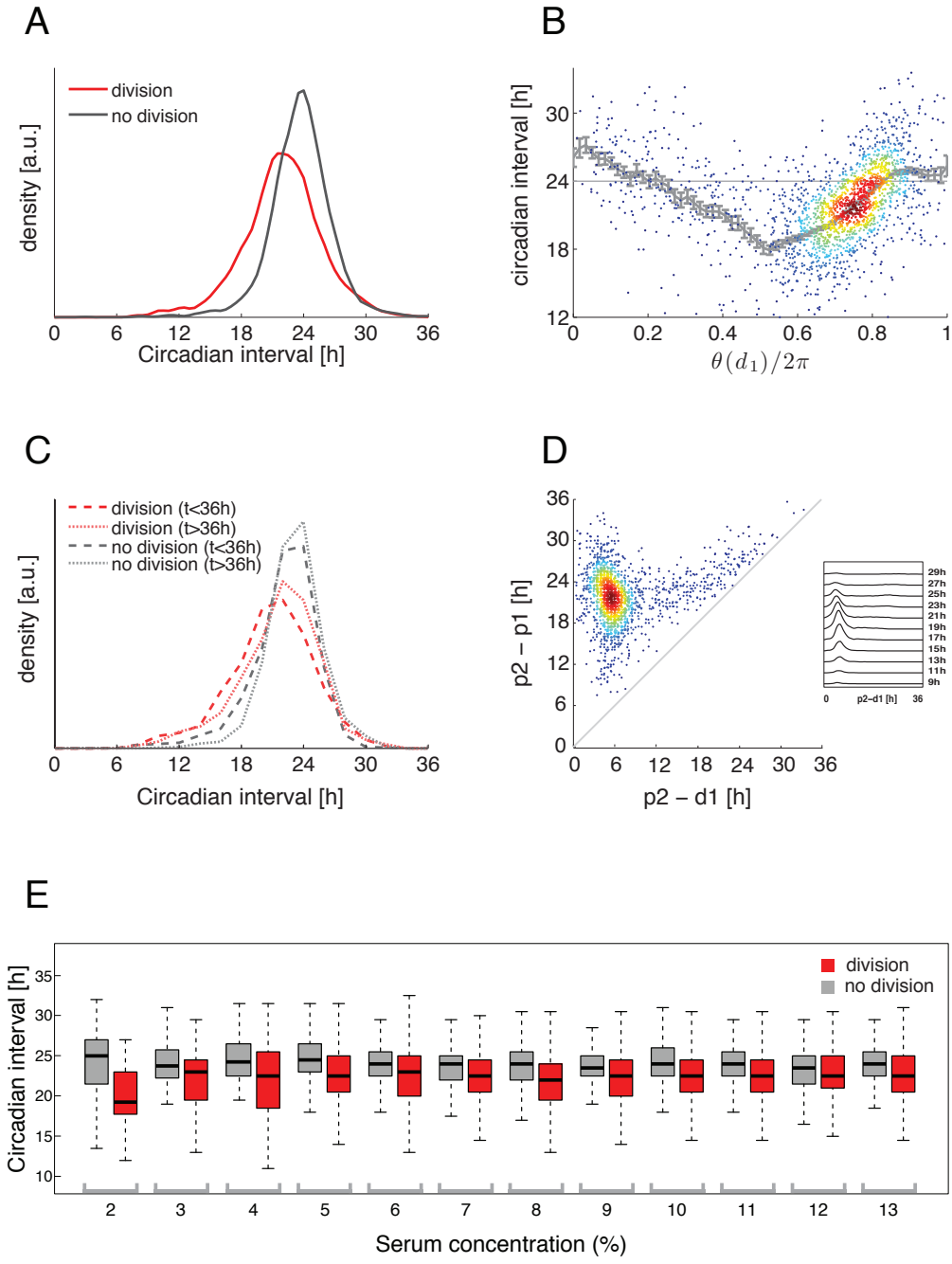

Figure 2.5 – Cell cycle influence on circadian intervals.

Figure 2.5 – Cell cycle influence on circadian intervals.
A. Circadian intervals with divisions (red) have an average duration of 21.95 ±3.8h whereas circadian intervals without division (grey) have an average length of 23.7h ±3.1h. Circadian intervals with divisions (p1-d1-p2, n=1926) have a significant shortening with $p<10^{-16}$ compared then circadian intervals without divisions (p1-p2, n=2748).
B. Scatter plot showing circadian intervals in function of circadian phase at division. A rainbow color map is used to display the data density, highlighting that the majority of events occurs around 0.75 in the circadian phase. The bold grey line indicates the running mean and the grey bars corresponds to the standard errors. It is possible to observe a positive slope for late dividing cells.
C. The shortening of circadian intervals with division (red) versus intervals without divisions (grey) is homogenous in time. The comparison of traces with and without divisions (dark red and grey dashed lines) originated from the first part of the recordings (t<36) show a significant shift with a $p<10^{-7}$ (t-test), whereas the comparison of traces with and without divisions (light red and grey dashed lines) originated from the second part of the recordings (t>36) show a significant shift with a $p<10^{-9}$ (t-test).
D. Circadian intervals p1-p2 in p1-d1-p2 events are compared to the subinterval d1-p2, showing a negative correlation between the two intervals in the center of the distribution. Earlier division events appear as outliers along the diagonal. The inset shows d1-p2 intervals on the x-axes stratified by circadian intervals on the y-axes, highlighting a shifting of d1-p2 intervals towards smaller circadian intervals.
E. Box plot displaying the comparison between circadian intervals with division (red) and circadian intervals with division (grey), show a systematic shortening when division occurs in all serum concentration probed.

2.6 Temperature changes affect cell cycle duration and shorten circadian intervals in dividing cells, but does not disrupt synchronization

Next, we wanted to further test the hypothesis that cell cycle has an impact on circadian clock by modifying the cell cycle durations and test the effects on circadian intervals. In fact, one critical feature of the circadian clock is that it is temperature compensated (Section 1.1.1.1). Because of this, we decided to probe different cell cycle duration by incubating cells at different temperatures during our time-lapse recordings. The expected impact of a change in incubation temperature is that it should not affect circadian intervals while it should increase or decrease cell cycle duration. Consequently, we recorded cells at 34 °C and 40 °C and compared their features to the ones originating from the previously analyzed 37 °C dataset.

As expected, the mean cell cycle duration shifts with the temperature changes such that lower temperatures (34 °C) corresponds to longer cell cycle intervals whereas higher temperatures (40 °C) corresponds to shorter cell cycle intervals (Figure 2.6A). The mean cell cycle length is, on average, 6 hours longer in the lowest temperature 34 °C) compared to the highest one (40 °C), spanning from 24.5 (±4.4) to 18.1 (±3.5) hours. In contrast, mean circadian intervals show a less important shift under the three different temperatures (Figure 2.6B). More importantly, when comparing circadian intervals with divisions versus circadian interval without divisions, we could clearly observe that circadian intervals without divisions do not show a significant shift across the three different temperatures, with the median being around 24 hours in all conditions, whereas circadian intervals with divisions display the typical shortening, which increased gradually with the increasing of temperature. (Figure 2.6C).

This result indicated that, while free-running and unperturbed circadian clock displays temperature compensation with a coefficient Q_{10}=0.93, division causes a perturbation of the circadian clock that prevents temperature compensation. Nevertheless, the synchronization previously observed between the two oscillators is kept, since division times w.r.t. the next peak do not change significantly with the change of temperatures (Figure 2.6D).

Circadian phases at division also have unimodal distributions at all temperatures but show significant phase advance in the 40 °C condition (Figure 2.6E). The phase advance observed at the highest temperature can be explained by the decreasing of the circadian intervals (p1-d1-p2) that, in turn, determines an increased period mismatch between the circadian oscillator and the cell cycle. This observation is consistent with the phase responses properties of entrained oscillators [Granada et al., 2013].

Thus, despite the increasing of the period mismatch between the two oscillators, the synchronization between circadian clock and cell cycle is maintained with a 1:1 mode locking state.

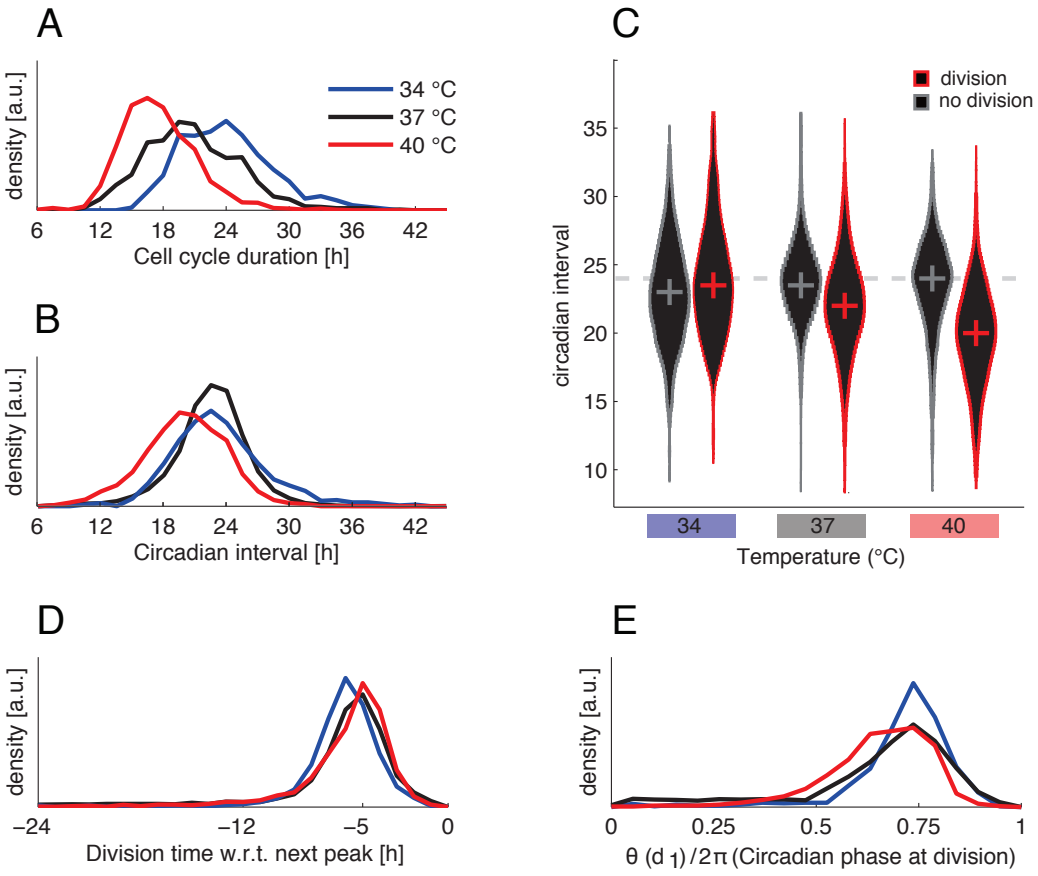

Figure 2.6 – Effects of temperature changes on circadian intervals and cell cycle durations.
A. The cell cycle duration increases with the decreasing of temperature. The mean cell cycle duration is 24.5h ±4.4 h at 34 °C , whereas is 18.1h ±3.5h at 40 °C (34 °C , n=575; 37 °C , n=1468; 40 °C , n=1180).
B. Circadian intervals show a similar distribution in the 34 °C and 37 °C condition, whereas are shorter at 40 °C .
C. Violin plots highlighting the difference in circadian intervals with and without division (black histograms with red and grey borders respectively). When no division occurs, circadian intervals (p1-p2) show temperature compensation, with a Q_{10}=0.93, indicating a slight overcompensation (34 °C , n=240; 37 °C , n=2748; 40 °C , n=246). In contrast, when division occurs, circadian intervals (p1-d1-p2) are not temperature compensated but have decreased durations that shorten with increasing temperatures (34 °C , n=544; 37 °C , n=1926; 40 °C , n=932). For each of the three different temperatures. The red and grey crosses indicate the median of circadian intervals with (p1-d1-p2) and without (p1-p2) divisions respectively.
D. Division times w.r.t. the next circadian peak do not show significant difference at the three different temperatures, occurring on average -5h before the next peak.
E. While still showing unimodal distributions, circadian phases at division are significantly phase advanced at 40 °C compared to phases at 37 °C ($p<10^{-9}$, Kolmogorov-Smirnov test), whereas division phases at 34 °C are slightly phase delayed ($p<10^{-9}$, Kolmogorov-Smirnov test).

2.7 Cell cycle lengthening via CDK inhibitors lengthens circadian intervals and delays division phase

After testing different incubation temperatures, we aimed at performing a more direct perturbation on the cell cycle. For this purpose, we treated cells with two different compounds, RO-3306 and NU 6102, affecting cell cycle progression. RO-3306 is competitive inhibitor of CDK1 that inhibits the CDK1/CyclinB1 complex and induces cell cycle arrest at the G2/M boundary [Kojima et al., 2009]. NU 6102 is a potent inhibitor of both CDK1 and CDK2 kinases. This inhibitor is most selective for CDK2 [Pratt et al., 2006] that is crucial for the G1/S transition [Thomas et al., 2011].

The effect of CDK1 and CDK2 inhibitors was first tested in an engineered NIH3T3 cell line stably transfected with a Luciferase reporter under the control of *Dbp* promoter. In presence of both CDKs inhibitors, the treatment at higher doses (10 uM) caused a decrease of the mean signal over time compared to the control population (Figure 2.7A). This observation, while reflecting an expected reduction of the proliferation rate due to the increased cell cycle durations, might also reflect an increased cell death due to the toxicity of the drugs and their induction of apoptosis after the first day of treatment.

We then performed a dose-response treatment with 1, 5, 7 and 10 uM of each of the two inhibitors in NIH3T3-Venus cells and performed time-lapse microscopy. We then estimated cell cycle durations and circadian intervals with or without division at each of the inhibitors concentrations. Unfortunately, toxicity of the drugs adds complexities in the fluorescent single-cell recordings and the corresponding analysis during a period of three days.

As expected, increased concentration of both the CDK2 and CDK1 inhibitors causes a dose dependent lengthening of the cell cycle duration (Figure 2.7C, F). Interestingly, increasing concentration of both the CDK2 and CDK1 inhibitors does not change the duration of circadian intervals without divisions (p1-p2) but progressively increases the duration of circadian intervals with divisions (p1-d1-p2) in conjunction with the lengthening of cell cycle duration (Figure 2.7B, E).

Moreover, the highest concentration of both CDK2 and CDK1 inhibitors causes a delay in the division phases comparing to the lowest concentration (Figure 2.7D, G). This delay is consistent with the reduction of the period mismatch between the circadian oscillator and the cell cycle occurring at higher dosages of the drugs, in opposition to what we observed for the 40 °C condition, where the increasing of the period mismatch corresponded to a phase advance (Figure 2.7B).

Overall, the interference on cell cycle caused by two different inhibitors strongly indicated and confirmed that cell cycle progression has an influence on the circadian oscillator, as suggested by the impact of the lengthening of cell cycle duration on circadian intervals and circadian phases at division (Figure 2.7B, D, E, G).

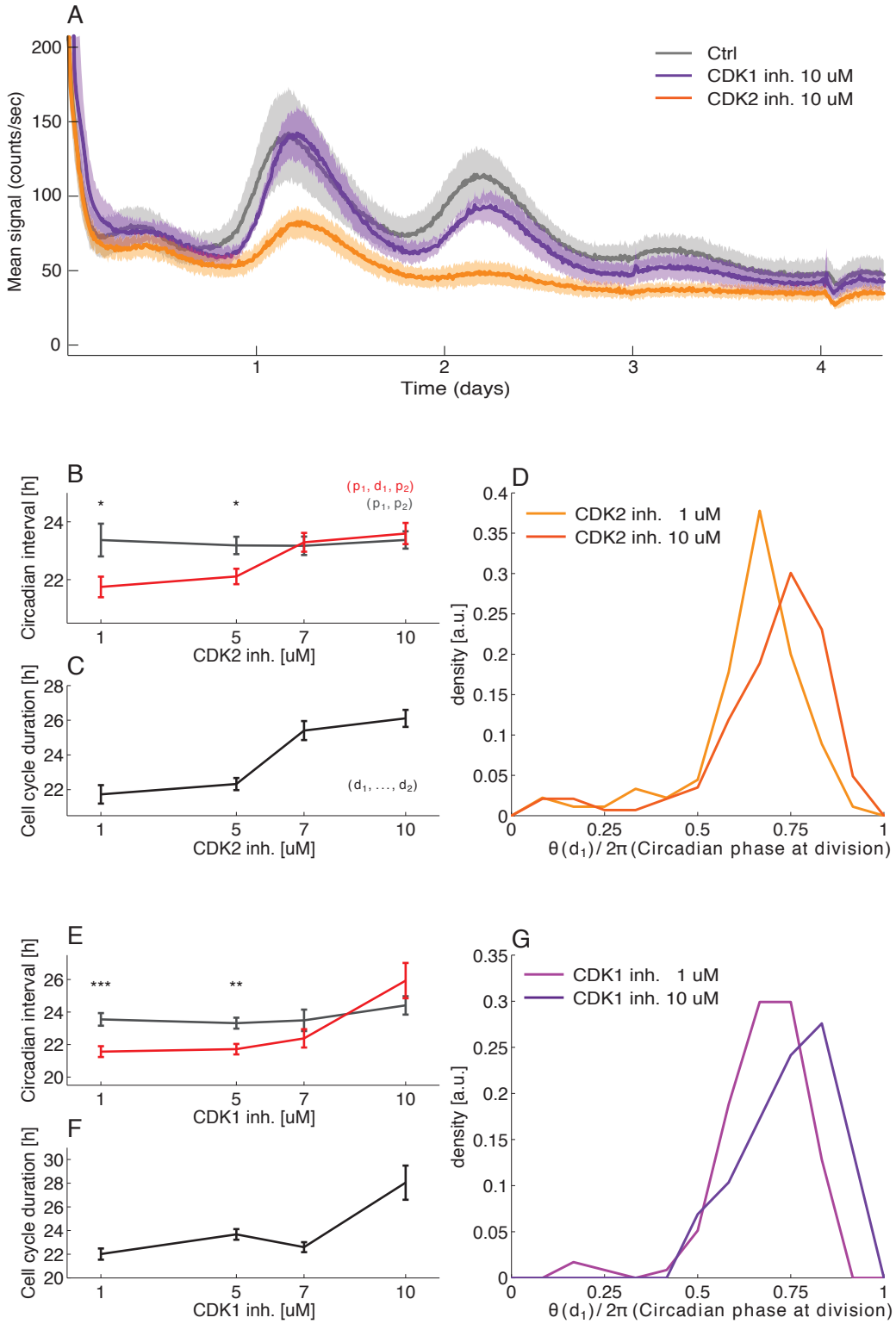

Figure 2.7 – Effects of cell cycle lengthening via CDK inhibitors.

Figure 2.7 – Effects of cell cycle lengthening via CDK inhibitors.
Inhibition of the cell cycle progression with increasing concentrations of CDK2 and inhibitors lengthens circadian intervals and delays division phase.
A. Circadian oscillations of DBP-Luc reporter in synchronized population of DBP-Luc NIH3T3 cells, in absence (grey line) or presence of 10 uM CDKs inhibitors (purple and orange lines). In both CDK1 (purple) and CDK2 (orange) inhibitions there is a shift of the DBP-Luc peak together with a decrease in the mean signal compared to the DMSO ctrl (grey), suggesting a decreasing total number of cells in presence of both 10 uM CDKs inhibitors.
B. Mean circadian intervals without (grey) and with (red) divisions as a function of CDK2 inhibitor NU-6102 concentrations. Circadian intervals with divisions lengthen in a dose dependent manner, together with the lengthening of cell cycle duration (C). A significant difference (*= $p<0.05$, t-test) between circadian intervals with divisions (p1-d1-p2) and without divisions (p1-p2) is observed at 1 uM and 5 uM concentrations.
C. Mean cell cycle duration increases as a function of CDK2 inhibitor concentration, spanning from about 22 hours at the lowest concentration of the drug (1 uM) to about 26 hours at the highest concentration (10 uM).
D. Distributions of circadian phases at divisions at 1 uM (light orange) and 10 uM (dark orange) CDK2 inhibitor. At the highest concentration (10 uM) there is a significant phase delay compared to the 1 uM condition ($p<1.2 \times 10^{-5}$, Kolmogorov-Smirnov test).
E. Mean circadian intervals without (grey) and with (red) divisions as a function of CDK1 inhibitor RO-3306 concentrations. As for the CDK2 inhibitor (B) circadian intervals with divisions lengthen in a dose dependent manner, together with the lengthening of cell cycle duration (F). A significant difference (***= $p<0.001$, **= $p<0.01$, t-test) between circadian intervals with divisions (p1-d1-p2) and without divisions (p1-p2) is observed at 1 uM and 5 uM concentrations.
F. As for the CDK2 inhibitor (C) the mean cell cycle duration increases as a function of CDK1 inhibitor concentration, spanning from about 22 hours at the lowest concentration of the drug (1 uM) to about 28 hours at the highest concentration (10 uM).
G. Distributions of circadian phases at divisions at 1 uM (light purple) and 10 uM (dark purple) CDK1 inhibitor. At the highest concentration (10 uM) there is a significant phase delay compared to the 1 uM condition ($p<0.003$, Kolmogorov-Smirnov test).
B, C, E, F. The number of analyzed cells treated with either CDK2 (n=812 cells) or CDK1 (n=711) inhibitors is nearly equally distributed across the different concentrations tested (1, 5, 7 and 10 uM).

2.8 Longdaysin treatment causes a simultaneous lengthening of both circadian and cell cycle periods

So far, the experiments performed aimed at perturbing cell cycle durations and indicated a strong influence of cell cycle on circadian clock.

In order to investigate the opposite directionality, we next intended to perturb the circadian oscillator. For this purpose, we treated cells with increased concentration of Longdaysin, a compound that lengthen the circadian period in a dose dependent manner [Hirota et al., 2010]. This drug regulates circadian period by inhibiting CK1δ, casein kinases controlling the stability of PER proteins [Etchegaray et al., 2009].

We tested first the effect of Longdaysin treatments at increasing concentrations (0, 1, 3 and 5 uM) in the DBP-Luc NIH3T3 cell line by recording luminescence intensity of confluent populations. As expected, we observed a dose-dependent increase of the circadian period (Figure 2.8A).

We next performed fluorescent time-lapse microscopy on NIH3T3-Venus cells treated with the same Longdaysin concentrations and analyzed the corresponding single-cell traces. Under Longdaysin treatment, the circadian period without division (p1-p2) progressively increases from about 24 hours to about 32 hours (Figure 2.8B), consistently with the observation at the population level (Figure 2.8A). As observed for the previous condition tested, in all concentrations of Longdaysin, the presence of division (p1-d1-p2) systematically shortens the circadian intervals compare to circadian intervals without division (p1-p2).

Interestingly, the cell cycle duration increased in a dose-dependent manner. In principle, this effect could reflect the influence of the circadian clock on cell cycle. However, since Longdaysin has an inhibitory effect on other kinases, notably on ERK2 kinase, crucial for regulating cell cycle progression at different checkpoints in NIH3T3 and in other cell lines [Hirota et al., 2010, Wright et al., 1999, Chambard et al., 2007], we hypothesized that the lengthening of cell cycle period upon Longdaysin treatment might be generated by a direct effect of the drug on cell cycle.

To test this hypothesis, we incubated populations of NIH3T3 cells and HeLa cells, the latter cell line lacking circadian oscillations, in presence or absence of 5 uM Longdaysin for 48 hours. Cell count of the Longdaysin treated samples indicated a reduced proliferation compared with the untreated control (Figure 2.8C) of both cell lines, suggesting a direct effect of Longdaysin on cell cycle lengthening, independently of a possible circadian gating. Thus, this experiment indicated that Longdaysin causes a simultaneous lengthening of both circadian and cell cycle periods.

Importantly, the distribution of division times with regard to the next circadian peak also showed a unimodal peak centered around -5h at all the conditions tested, with no detectable differences from the control (Figure 2.8D). This observation is remarkable considering the

increased variability observed upon Longdaysin treatment in circadian intervals (Figure 2.8B, inset).

However, in Longdaysin treated cells, normalized division times displayed a proportion of cells dividing early in the circadian phase (Figure 2.8E). effect suggests a potential destabilization of the 1:1 mode-lock state in presence of increasing doses of Longdaysin.

Lastly, the comparison of the average signal of cell traces treated with either 1 uM or 5 uM Longdaysin shows that the waveform of the circadian oscillation is unaffected around the peak, whereas it is stretched in the low phase of the *Rev-Erbα* reporter expression (Figure 2.8F). This observation is consistent with the effect of CK1δ inhibition on stabilization of PERs due to Longdaysin treatment, that, in turn causes a lengthening of the repression phase [Etchegaray et al., 2009]. Overall, these results are in line with a scenario in which the cell cycle and the circadian clock are in synchrony and coupled with a predominant influence from the cell cycle on the circadian oscillator.

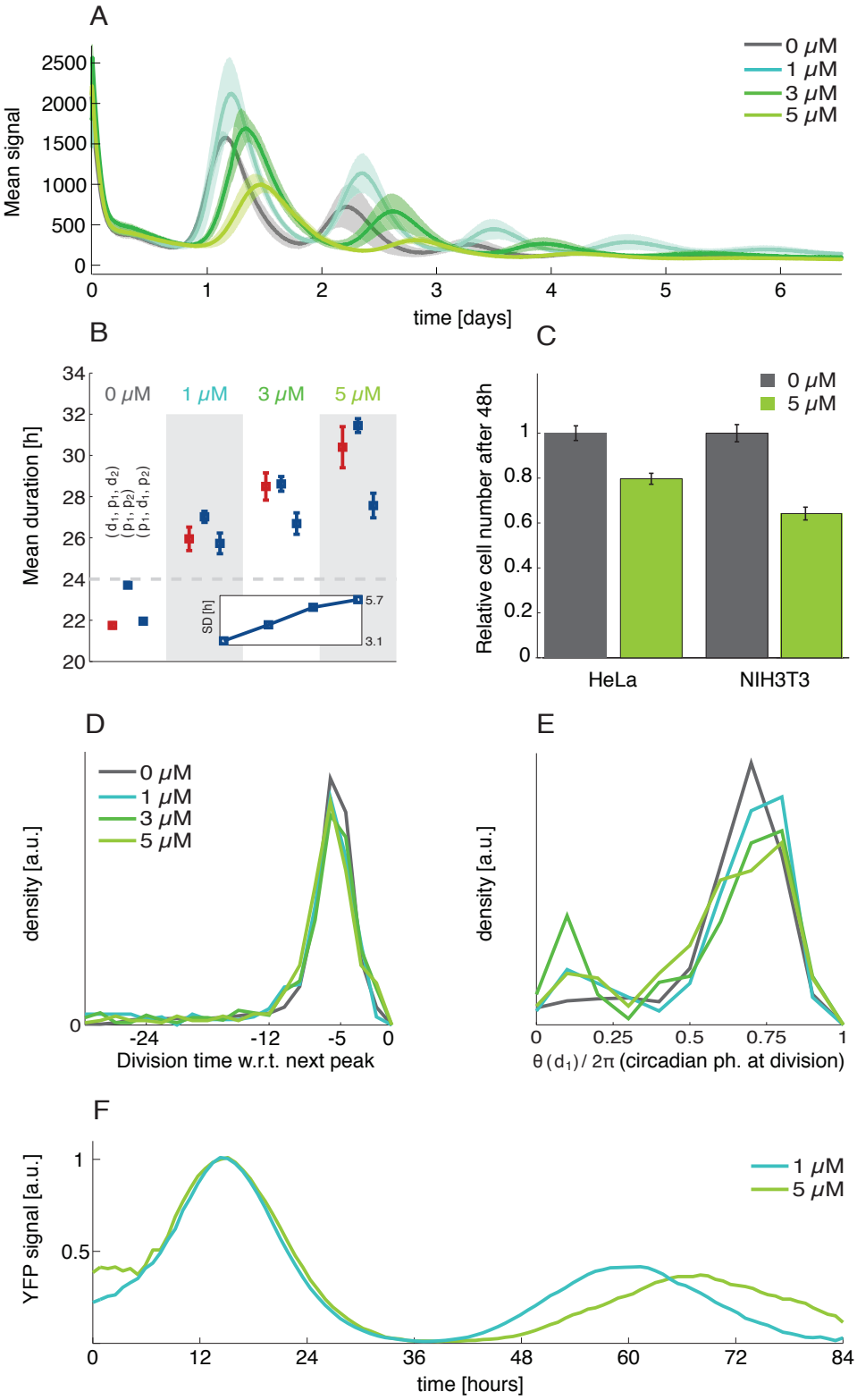

Figure 2.8 – Effects of cell cycle lengthening via Longdaysin treatment on circadian intervals and division phase.

2.8. Longdaysin treatment causes a simultaneous lengthening of both circadian and cell cycle periods

Figure 2.8 – Effects of cell cycle lengthening via Longdaysin treatment on circadian intervals and division phase.
A. Increasing circadian period in DBP-Luc cells dependent on Longdaysin concentrations (0, 1, 3 and 5 uM).
B. Mean duration of cell-cycle intervals (d1-p2-d2), circadian intervals without division (p1-p2) and with division (p1-d1-p2) as a function of increasing concentration of Longdaysin (0, 1, 3 and 5 uM). Both cell cycle and circadian intervals lengthen in a dose dependent manner. Cell cycle duration span from about 22 h to 31.5 h, whereas circadian intervals without division span from 24 h to about 32 h. As for the other condition tested, there is a systematic shortening of circadian periods in presence of division. The inset shows the dose dependency of the standard deviation of circadian intervals (p1-p2).
C. HeLa or NIH3T3 cell count after 48h of growth in presence or absence of Longdaysin 5 uM. Cell numbers are normalized to the untreated DMSO condition (grey bars) and the error bars indicate the standard error on the mean. The number of analyzed samples is equal to 18, 11, 18 and 18 for the four conditions tested (HeLa 0 uM, Hela 5 uM, NIH3T3 0 uM, NIH3T3 5 uM). Cell count indicated a significantly reduced number in both cell lines with a $p<1.4 \times 10^{-4}$ in HeLa cells and $p<10^{-8}$ in NIH3T3 (t-tests).
D. Division times with regard to the next circadian peak show the typical unimodal distribution centered about -5 h for all the conditions tested.
E. Normalized division times in Longdaysin treated cells show distributions with a main peak toward late phases and a smaller peak toward early phases indicating that Longdaysin treated cells have an increased number of early divisions compared to control.
F. Average of cell traces treated with 1 uM (light blue) and 5 uM (greenyellow) Longdaysin shows that the waveform is unaffected around the circadian peak but is stretched in the repression phase of the *Rev-Erbα* reporter expression.

2.9 Longer circadian periods in *Cry2*-deficient cells do not affect the cell cycle duration but shift divisions

We wanted to further test the directionality of the coupling using a more direct perturbation of the circadian clock. For this purpose, we choose a genetic approach and further engineered NIH3T3-Venus cells with the stable expression of a previously validated shRNA targeting the *Cry2* transcript [Moffat et al., 2006].

shCry2 cells show the expected lengthening of the mean circadian period [Maier et al., 2009, Zhang et al., 2009],that increased up to 26.3 ±4 hours hours compared to the scramble shRNA control and the wild type control dataset for which the mean circadian period is about 24 hours (Figure 2.9A). In contrast, cell cycle duration is not affected in shCry2 cells (Figure 2.9B, E), indicating that circadian clock does not strongly impact on cell cycle. Interestingly, both division-to-peak intervals (Figure 2.9C) and normalized division phases (Figure 2.9D) unimodal distributions displaying a significant increase of advanced divisions in shCry2 cells compared to the controls.

As already stated for the temperature (Section 2.6) and CDKs (Section 2.7) experiments, this result is consistent with the property of phase responses in entrained oscillators, in which an increased period mismatch corresponds to a phase advance.

As observed for the previously tested conditions, the shCry2 cells showed a decrease in the mean circadian duration in presence of divisions. Indeed, the mean circadian intervals shorten from 26 hours in p-p intervals to 23.75 in p-d-p intervals (Figure 2.9E).

This experiment using an shRNA against *Cry2* further supported the hypothesis that, in NIH3T3 cells, there is a unidirectional coupling from the cell cycle onto the circadian clock. The results indicated as well that CRY2 protein does not play a key role in mediating this coupling.

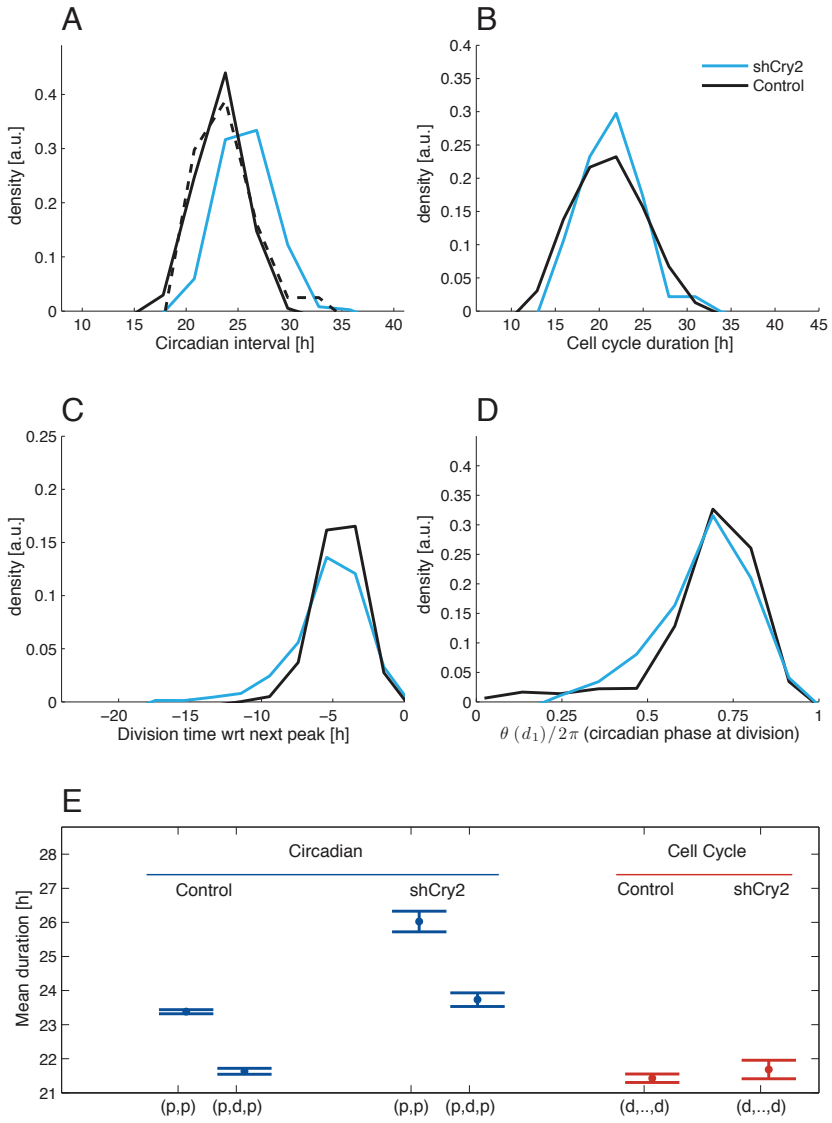

Figure 2.9 – Synchronization of circadian clock and cell cycle in *Cry2* deficient cells.
A. Circadian intervals (p1-p2) in shCry2 cells (cyan) are longer than in control cells (black). Scramble shRNA cells are indicated in dashed black whereas the 37 °C dataset is indicated in solid black. shCry2 cells are significantly longer than both control datasets ($p< 0.02$ for scramble shRNA and $p< 10^{-16}$ for the 37 °C , t-test). Mean circadian intervals are 26.3 ±4 in shCry2 and 23.7 ±3.1 hours in the controls.
B. The cell cycle duration is not affected in shCry2 cells compared to the control cells ($p<0.19$, t-test).
C. The intervals from divisions to the next circadian peaks (d,p) are slightly lengthened in the shCry2 cell line ($p<4.8 \times 10^{-5}$, Kolmogorov–Smirnov test).
D. Circadian phases at division are slightly advanced in shCry2 cells compared to controls ($p<0.008$, bootstrapped two-sample Kuiper test).
E. Mean circadian intervals with divisions are significantly shorter than intervals without divisions in both control ($p<10^{-16}$, t-test) and shCry2 cells ($p< 1.3 \times 10^{-10}$, t-test). Mean cell cycle duration is shown in red. The error bars show the standard error on the mean. The total number of shCry2 cell traces analyzed is n=549.

2.10 Fbxl3-deficient cells with longer circadian periods have longer cell cycle durations

In order to have an additional cell line exhibiting a lengthened circadian period, we generated a NIH3T3-Venus shRNA cell line stably expressing an Fbxl3-targeting shRNA.

These cells showed a mean period lengthening of 2.2 hours, with a period of 25.9 ±6.3 hours (Figure 2.10A). The observed effect was comparable to the results obtained from a recent high-throughput RNAi-based genetic screen [Maier et al., 2009] in U2OS cells, in which three different siRNAs against Fblx3 induced a mean period lengthening spanning from about 2 to 5 hours.

The obtained results were similar to the ones obtained from the shCry2 cell line (confront with Figure 2.9).

In the shFbxl3 condition, however, the cell cycle duration was about one hour longer than in the controls (Figure 2.10B),), whereas in the *Cry2* shRNA cell line the cell cycle duration was unaffected (Figure 2.9B). Moreover, Fbxl3 deficient cells have longer division-to-peak intervals compared to controls (Figure 2.10C) and a narrower peak of distribution of circadian phases at division (Figure 2.10D).

Although the increase in cell cycle duration in shFbxl3 cells indicates a reduced synchrony between the two oscillators, properties such as the shortening of circadian intervals with divisions (Figure 2.10E) were consistent with the previous observations indicating a dominant effect of the cell cycle on the circadian cycle.

Beside from his role in decreasing the stability of CRY proteins [Godinho et al., 2007] [Busino et al., 2007], FBXL3 have been linked with putative cell cycle regulators, as also shown for other FBXs [Cardozo and Pagano, 2004]. Protein interactions of FBXL3 have been shown for CDC34, part of the multiprotein complex required for the degradation of G1 phase regulators, CUL1 and SPK1, essential components of the SCF ubiquitin ligase complex mediating the ubiquitination of proteins involved in cell cycle progression [Cenciarelli et al., 1999]. We thus hypothesize that the observed lengthening of the mean cell cycle duration in shFbxl3 cell line can be due to a possible involvement of FBXL3 in cell cycle regulation.

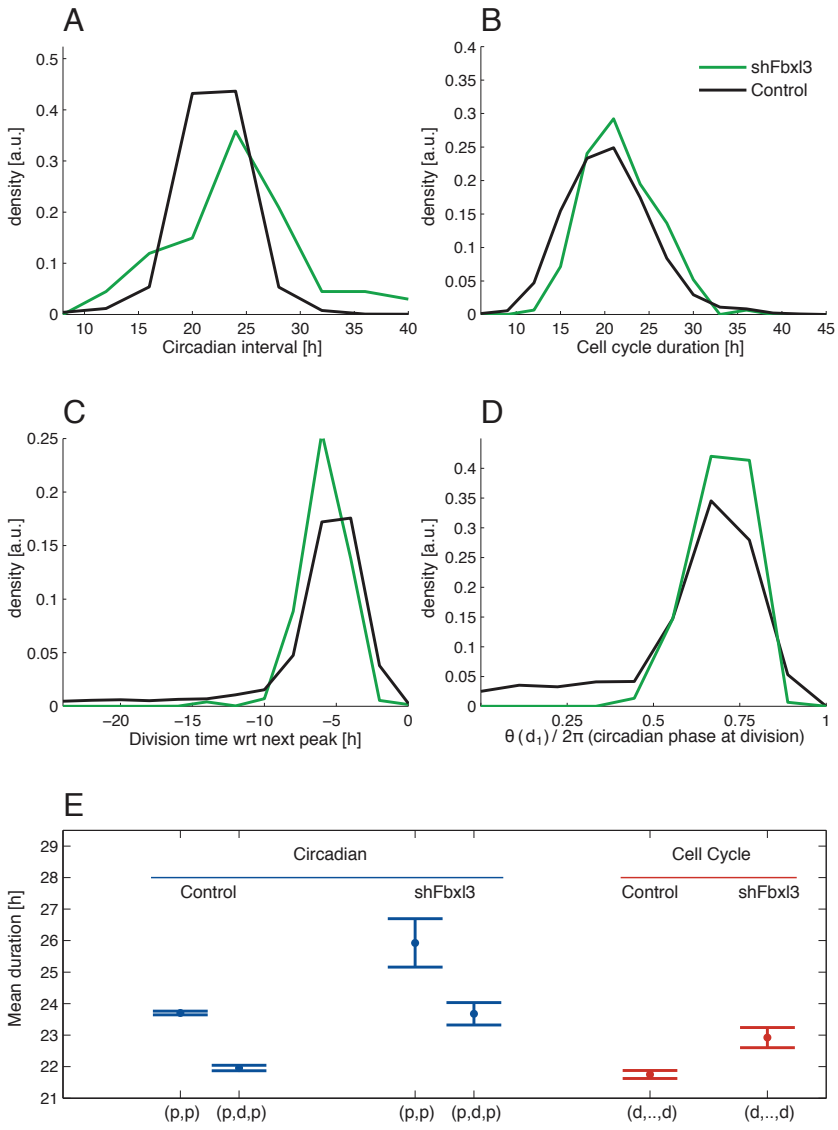

Figure 2.10 – Synchronization of circadian clock and cell cycle in Fblx3 deficient cells.
A. Circadian intervals (p1-p2) in shFbxl3 cells (green) are significantly longer than control cells (37 °C dataset, black, $p< 2 \times 10^{-8}$, t-test). Means are 25.9 ±6.3 (SD) in shFbxl3 and 23.7 ±3.1 hours in the controls.
B. The cell cycle duration is significantly longer in the shFbxl3 cells (p<0.0036, t-test).
C. The intervals from divisions to the next circadian peaks (d,p) are slightly lengthened in the shFbxl3 cell line ($p<5 \times 10^{-6}$, Kolmogorov–Smirnov test).
D. The circadian phases at division are slightly more peaked in shFbxl3 cells compared to controls ($p<5.9 \times 10^{-5}$, Kolmogorov–Smirnov test).
E. Mean circadian intervals with divisions are significantly shorter than intervals without divisions in both control ($p<10^{-16}$, t-test) and shFbxl3 cells (p< 0.0027, t-test). Mean cell cycle duration is shown in red. The error bars show the standard error on the mean. The total number of shFbxl3 cell traces analyzed is n=340.

2.11 Circadian phase resetting does not influence cell divisions but transiently perturbs synchronization of circadian and cell cycles

Finally, we wanted to complement the previous experiments aiming at perturbing the circadian oscillator by transiently resetting the clock with well-established synchronization protocols.

We thus treated cells with either Dexamethasone or Forskolin. In both cases, the treatment showed the expected alignment of the circadian phases (Figure 2.11A, B). Interestingly, the timing at which divisions occur is uniform along time and does not show any dependence on the resetting treatments. The same division time pattern is also observed in the untreated control (Figure 2.11C). Moreover, the sorting of cells according to the first division reveals that circadian peaks following divisions occur after the typical interval of about 5 hours, being in the same range than the untreated control, whereas in cells without divisions the second circadian peak remains aligned to the synchronization treatment.

By estimating the circadian phase of cell traces in the first hour of the recordings we show that the distributions of circadian phases are indeed more peaked in the Dexamethasone and Forskolin treated cells compared to the untreated ones (Figure 2.11A-C, left panels).

We furthermore quantified the difference in synchronizations between treated and untreated samples as a function of time via several synchronization indices. This confirmed that the treated cells have synchronized circadian rhythms and that this synchrony decays along the recording time (data can be found in Figure 7B-D of Bieler et al., 2014, Section A.1.2). Treatment with Dexamethasone or Forskolin thus suggests a transient uncoupling of the two oscillators that is reestablished when divisions occur.

This experiment, while allowing a transient destabilization of synchronization, confirmed once again that, in our cell line, the circadian clock does not have a strong impact on cell cycle, whereas cell division seems to determine the timing of the following circadian peak. Indeed, if the circadian oscillator would have a strong influence on cell cycle progression we would expect cells to divide at specific time windows upon cell cycle synchronization rather than having the observed uniform distribution of cell divisions.

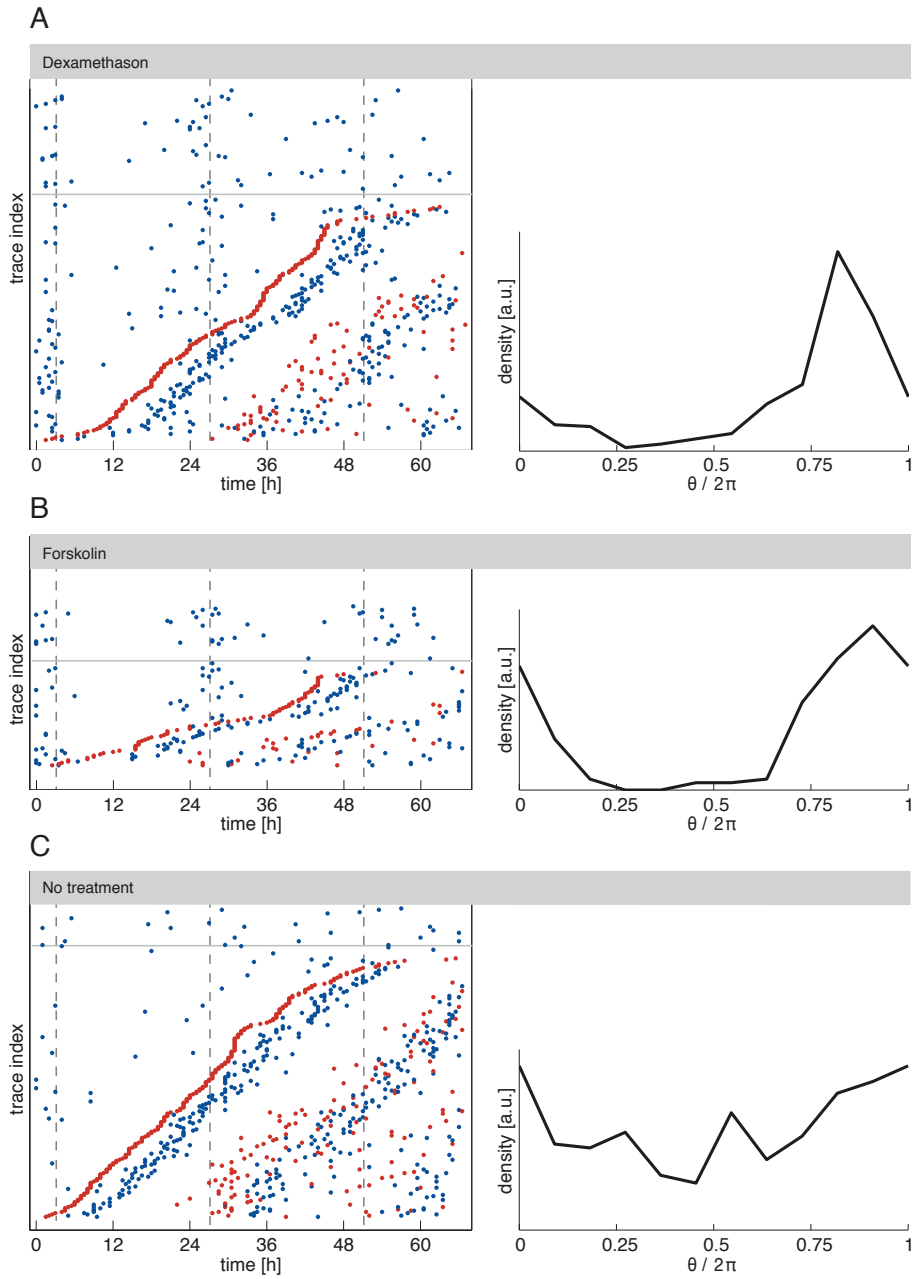

Figure 2.11 – Effects of circadian phase resetting on synchronization.
A-C, left panels: Raster plots for cell treated with Dexamethasone (A), Forskolin (B) and untreated controls (C). Each line represents a cell trace, where circadian peaks are indicated as blue spot whereas divisions are in red. Traces without divisions (p-p) are shown above the grey line in the upper part of the plot. In the lower part of the plot, cell traces are sorted according to the time of the first division, from bottom to top. For cells treated with either Dexamethasone or Forskolin (A, B), divisions occur homogenously along time and the second circadian peak follows division with the expected interval (p-d) as it happens for the untreated control (C).
A-C, right panels: Initial phase distribution in Dexamethasone, Forskolin and control conditions. The estimation of circadian phases in the first hour after the start of the recordings shows how the these distributions are more peaked in the Dexamethasone and Forskolin treatments than in control.

2.12 Main conclusions

The work presented in this chapter aimed at investigating the interaction between circadian clock and cell cycle at the single-cell level in mammalian NIH3T3 mouse fibroblast. This goal was achieved with the analysis of a large dataset from fluorescent time-lapse imaging by monitoring the expression of a circadian reporter under the control of *Rev-Erbα* promoter.

Our large-scale experimental setup allowed us to record single cell traces over several days, and to probe several conditions aiming at altering either the circadian or the cell cycle durations. By quantifying the fluorescent signal, we could extract simultaneously information about the circadian phase and cell division events. Our analysis pipeline led to the collection of thousands of single-cell traces. This allowed us to extract overall about 20'000 circadian peaks and 13'000 cell divisions, gaining information about cell cycle durations and circadian intervals at the single-cell level. The analysis of our dataset showed that the circadian and cell cycle oscillators are coupled in 1:1 mode-locked state, with one oscillator completing one cycle while one cycle of the other oscillator occurs. Remarkably, cell divisions tend to occur, on average, five hours before the circadian peak of the *Rev-Erbα* reporter. We could highlight the influence of the cell cycle on the circadian clock as revealed by the systematic shortening of circadian periods in dividing cells compared to non-dividing ones. Moreover, when incubating cells at different temperatures, the circadian clock's capability of temperature compensation was affected in presence of cell division. These observations, together with additional experiments including genetic and chemical perturbations provided additional signs of the cell cycle impact on the circadian oscillator. Our results also indicated that the circadian clock, in contrast, does not have a strong influence on the cell cycle. Finally, when transiently resetting the clock with synchronization protocols we observed that divisions occurred uniformly along time and did not show dependence on the resetting treatment.

Overall, our experiments made us conclude that, in our cell line, the synchronization between the circadian and cell cycle oscillators is driven by the predominant coupling from the cell cycle to the circadian clock and that this synchronization is highly robust and resilient to perturbations.

3 Results (II)
Reconstructing the phase dynamics of interacting cell cycle and circadian clock

"To raise new questions, new possibilities,
to regard old problems from a new angle,
requires creative imagination and
marks real advance in science."
Albert Einstein

3.0.1 Context and statement of author contributions

In Chapter 2 I described the analysis of a large dataset from time-lapse imaging of mouse fibroblasts showing that the two periodic processes, circadian and cell cycle, are robustly synchronized at the single-cell level. This synchronized state was observed over a wide range of experimental conditions tested, resulting from a predominant influence of the cell cycle on the circadian cycle.

In the current chapter, I will introduce the continuation work aiming at further analyzing the identified synchronization with the use of mathematical modeling. This purpose was already pursued in the published manuscript ([Bieler et al., 2014], Section A.1). In this follow up study we reconstructed a non-parametric model of the phase dynamics, identifying potential interactions between the two processes. This allowed us to make predictions on cell cycle events that could influence the circadian clock and testing those predictions with additional experiments.

As for the work presented in Chapter 2, this study represents a collaborative work combining experiments, statistical analysis and mathematical modeling. The main results of this chapter are generated by mathematical modeling on the dataset introduced in Chapter 2. Jonathan Bieler performed most of the analysis, with a contribution from Nicolas Villa and myself, and he entirely developed the mathematical models. The additional experimental work presented in Section 3.2 and in Section 3.6 including the generation of new stable reporter cells lines was designed and performed by myself, in collaboration with Cedric Deluz for the lentivirus generation and transduction. Microscopy experiments and signal processing tasks were also performed by myself.

3.1 Mathematical modeling describing two interacting oscillators

In the previous chapter (Chapter 2) we demonstrated that circadian and cell cycle oscillators are synchronized and their coupling is unidirectional with a predominant influence of the cell cycle onto the circadian clock.

These observations were supported by mathematical modeling in the published manuscript ([Bieler et al., 2014], Section A.1).Briefly, we fitted a mathematical model describing two interacting cycles, in which the circadian and cell cycle oscillators are described by noisy phase variables denoted as θ and ϕ, respectively.

The two phases are defined so that $\theta = 2\pi$ corresponds to the circadian peaks of our reporter whereas $\phi = 2\pi$ corresponds to cell divisions (cytokinesis). Moreover, the coupling between the two oscillators is modeled via two functions, $F_1(\theta, \phi)$ and $F_2(\theta, \phi)$, where F_1 defines the influence of cell cycle onto the circadian phase velocity and F_2 defines the influence of the circadian clock onto the cell cycle.

These two functions add up with the intrinsic frequencies of the oscillator (frequency in the absence of coupling, $2\pi/T_i$) tto give the velocity of each phase. The model (here written without the noise terms) reads:

$$\mathrm{d}\theta/\mathrm{d}t = 2\pi/T_1 + F_1(\theta,\phi) \tag{3.1}$$

$$\mathrm{d}\phi/\mathrm{d}t = 2\pi/T_2 + F_2(\theta,\phi) \tag{3.2}$$

Assuming that each oscillator's phase could either accelerate or speedup the other oscillator, the model incorporates three main possibilities:

1. The circadian clock influences the cell cycle unidirectionally (F_1=0, F_2 non zero)
2. The cell cycle influences the circadian clock unidirectionally (F_2=0, F_1 non zero)
3. There is a bidirectional influence of the two oscillators (both F_1 and F_2 are non zero).

In Bieler et al., 2014 the functions F_1 and F_2 were determined using detected peaks and divisions. Thus, the model learned the two functions F_1 and F_2 by taking into account only data measured on the boundaries of the phase space.

Despite this indirect way of estimating the two functions, this model was able to reproduce the data, to predict the directionality of the coupling and to reveal the main features of the coupling functions. More specifically, data such as the distributions of circadian intervals or cell cycle durations, and the later division times associated with longer circadian intervals, were accurately reproduced. Moreover, the model predicted an acceleration of the cell cycle

around the division time as the most robust property and a lesser slowdown early in the circadian phase, whereas the influence of circadian clock on cell cycle appeared to be much weaker.

Additional information on the functions estimation and the stochastic model can be found in Bieler et al., 2014 (Section A.1). In particular, representations of the coupling functions are shown in Figure 3 E-F, Figure 4 E-F, Figure 6D (Section A.1.1) and Figure S6 (Section A.1.2), whereas the estimated parameters can be found in Supplementary Tables M1-M5 (Section A.1.2). Moreover, comparisons of the model fit and the data are shown in Figure 3B-C, Figure 4A-D (Section A.1 and Figure S7 of the manuscript (Section A.1.2).

3.2 Instantaneous phase estimation of circadian and cell cycle oscillators

Although the mathematical modeling based on indirect estimations of F_1 and F_2 was able to describe the dynamics of the coupled cell and circadian cycles, we aimed next at obtaining a more detailed picture of this interaction by analyzing the phase dynamics in a more direct manner. To this end, instead of relying just on peaks and divisions, we analyzed the full time traces for the estimation of the two instantaneous phases and their instantaneous velocities.

For the circadian oscillator, the phase θ was inferred from the temporal profile of the fluorescent *Rev-Erbα*-YFP signal with a Hidden Markov Model (HMM) [Bieler et al., 2014], (Figure 3.1A). For the cell cycle, we adapted this approach but used nuclear area measurements as a continuous variable to determine the phase ϕ. This method was based on previous observations that the nuclear area shows a typical and consistent size variation along cell cycle progression from a division to another [Fidorra et al., 1981, Bieler et al., 2014]), (Figure 3.1B). More specifically, the estimation of circadian and cell cycle phases is based on the assumption that both the YFP-signal and the nuclear area data are linked to the phases via a 2π-periodic waveform, allowing to detect deformations of the phase progressions (Figure 3.1).

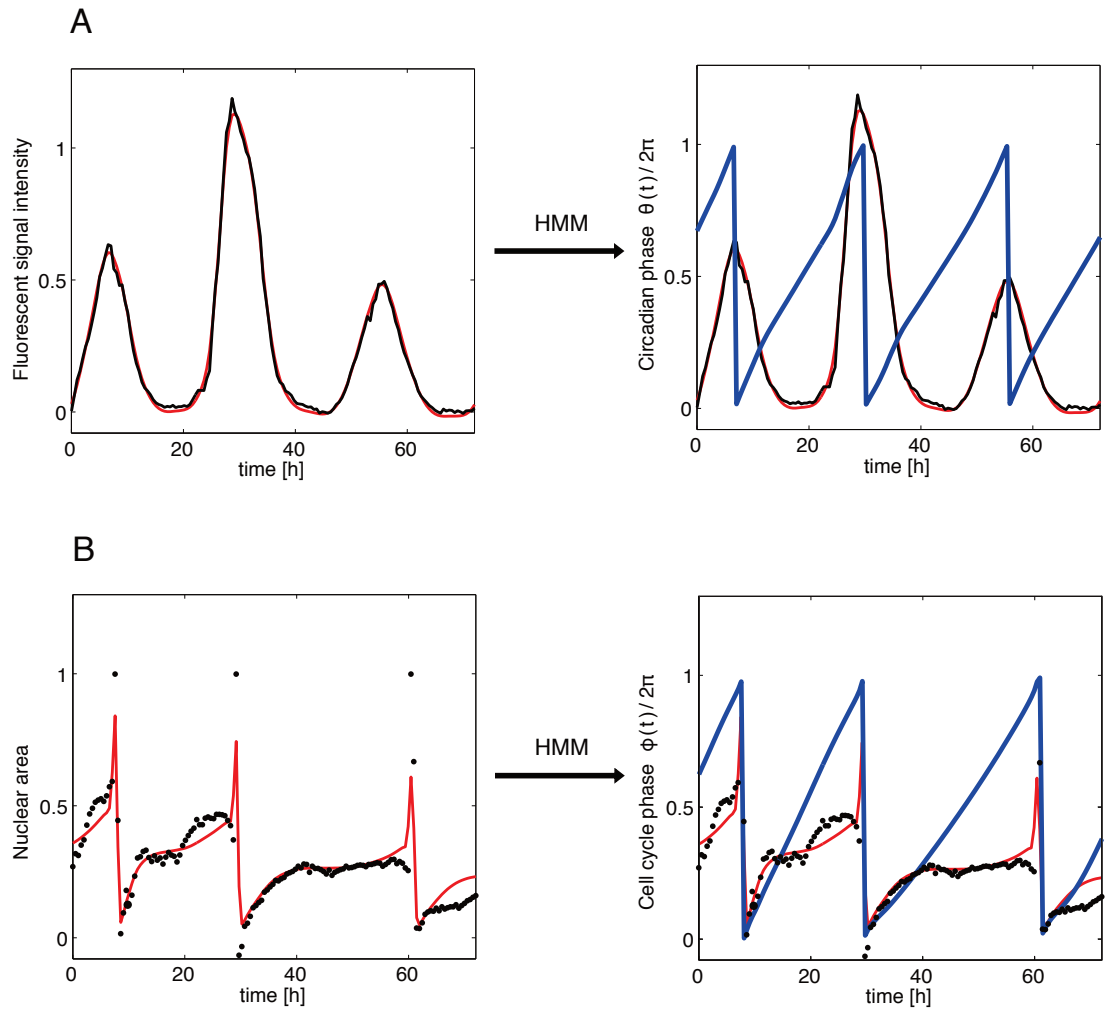

Figure 3.1 – Phases inference from the data.
A. Estimation of the circadian phase. On the left panel, the black line corresponds to the raw *Rev-Erbα*-YFP signal from an example trace, whereas the red line shows the model. On the right panel, in blue is shown the expected circadian phase, inferred from the *Rev-Erbα* -signal with Hidden Markov Models (HMM).
B. Estimation of the cell cycle phase. On the left panel, the black dots correspond to the detected nuclear area from an example trace, showing the characteristic trajectory along the cell cycle, with a rapid increase after division followed by a much slower increase until the following division. As for (A), the model is represented by the red line. On the right panel, in blue is displayed the mean cell cycle phase inferred from the nuclear area data with HMM.

In order to validate the use of the nuclear area to infer the cell cycle phases we imaged NIH3T3 fibroblasts engineered with the Fucci system, a two colors fluorescent reporter that allows to distinguish G1 phase from S/G2/M phase [Sakaue-Sawano et al., 2008].

As already described in Section 1.1.2.2, nuclei of cells in G1 will appear in red because of the presence of the fluorescent protein mKO2 fused with a fragment of the CDT1 protein. The corresponding red signal will thus start to appear right after division and will increase until the end of G1 phase, when the CDT1 protein will start to be degraded, causing a progressive decrease of the fluorescent signal. In contrast, cells in S/G2/M will appear in green due to the fluorescent protein mAG fused with a portion of the Geminin protein. Therefore, the green signal will appear at the end of the G1 phase and will increase up to cell division, when it will abruptly decrease to zero (Figure 3.2A).

We then adjusted our HMM to infer the cell cycle phase from the Fucci signal (denoted as ϕ_F) by multiplying the emission probabilities of both fluorescent reporters (Figure 3.2A) and we independently inferred the cell cycle phase from the nuclear area, denoted as ϕ_N (Figure 3.2B). The comparison between the two inferred phases ϕ_F and ϕ_N indicated a good agreement, with a synchronization index R(ϕ_N-ϕ_F) equal to 0.83 (Figure 3.2C). As expected, the two methods are most accurate close to divisions, because of the abrupt change in both the fluorescent green signal and nuclear area occurring at mitosis. However, the two approaches show more variability in the middle of the cycle, as indicated in Figure 3.2C from the decrease in the data density showed between two consecutive divisions (corresponding to cell cycle phases 0 and 1 in the scatter plot). To further assess the precision of our inferences we estimated the durations of the G1 and S/G2/M cell cycle discrete phases from both ϕ_F and ϕ_N phases. The G1 phase durations inferred from the Fucci signal were predicted from the nuclear area with a mean duration of 10.3 ± 2.3h (Figure 3.2D), whereas the S/G2/M durations were predicted with a mean duration of 14.4h ± 2.0h (Figure 3.2E).

Once the estimated circadian (θ) and cell cycle (ϕ)) phases are inferred at each time step, the temporal trajectory can be plotted in the phase plane (θ, ϕ) and the velocity in both directions can be estimated [Rosenblum and Pikovsky, 2001] using finite differences, which leads to the so called vector field (the collection of arrows on the square). We applied these procedures on more than 4000 single-cell traces from our dataset. Such a large collection of traces allowed us to estimate the velocity on the whole (θ, ϕ) plane and to reconstruct the dynamics of the system directly form the estimated vector fields.

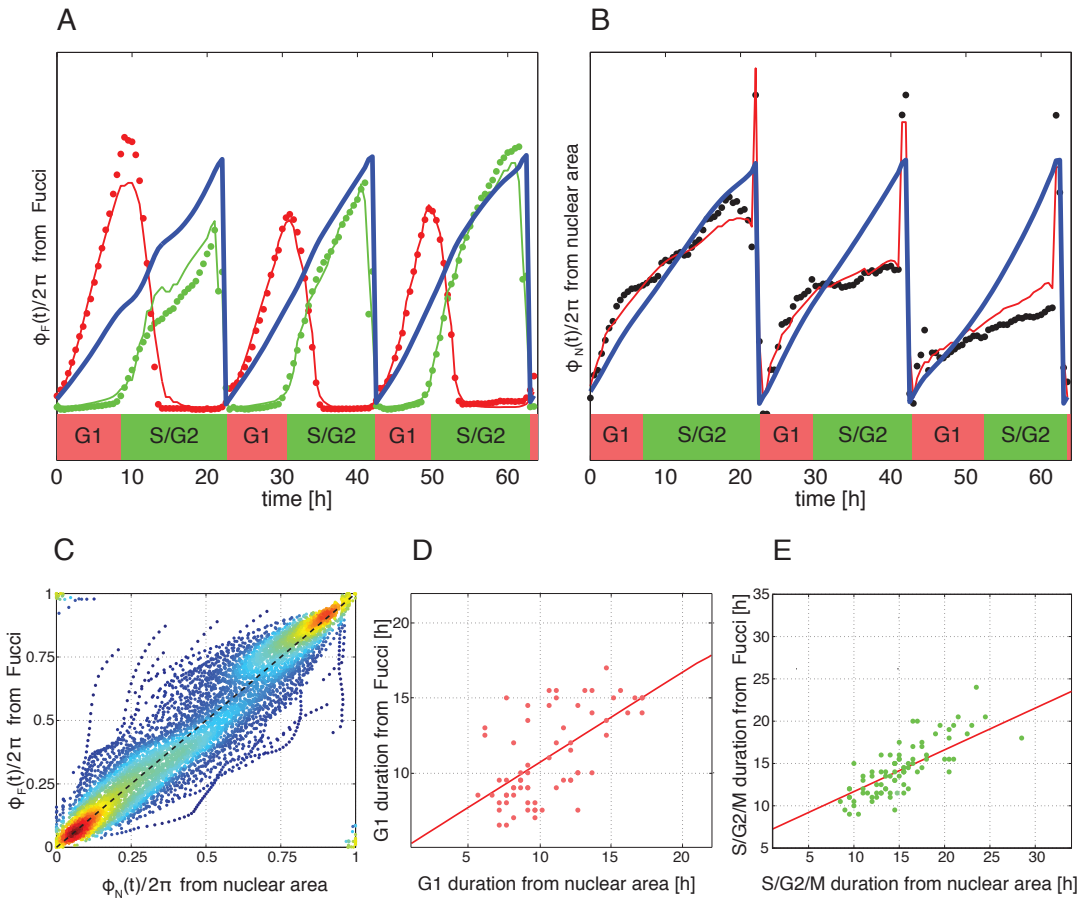

Figure 3.2 – Comparison between the Fucci system and the nuclear area for inference of cell cycle phase.
A. Cell cycle phase inference from the Fucci signal. The red and green dots correspond to the mKO-Cdt1 and mAG-hGem fluorescent signal, respectively. The solid red and green lines correspond to the model for the corresponding signal. The cell cycle phase ϕ_F inferred from the Fucci signal is shown as a solid blue line. The inferred G1 and S/G2/M discrete cell cycle phases are highlighted below the trace. Note that the transition between G1 and S phase corresponds to the rise of the green signal.
B. Cell cycle phase inference from the Nuclear area. The black dots correspond to the detected nuclear area whereas the red line shows the model. The cell cycle phase ϕ_N inferred from the Nuclear area measurements is shown as a solid blue line. As in panel (A), the inferred G1 and S/G2/M discrete cell cycle phases are highlighted below the trace.
C. Scatter plot showing the cell cycle phase inferred from nuclear area (ϕ_N) versus the phase inferred from the Fucci system (ϕ_F) in our dataset. The synchronization index R (ϕ_N-ϕ_F) is equal to 0.83 and the color map shows the data density. Note that the density is high at 0 and 1, i.e. around divisions, indicating that the Hidden Markov Model accurately detects divisions in both cases.
D. Scatter plot showing G1 durations inferred from Nuclear Area (ϕ_N) versus G1 durations inferred from the Fucci system (ϕ_F). The correlation coefficient R^2= 0.37 and mean duration 10.3 hours.
E. Scatter plot showing S/G2/M durations inferred from Nuclear Area (ϕ_N) versus S/G2/M durations inferred from the Fucci system (ϕ_F). The correlation coefficient R^2=0.57 and mean duration 14.4 hours.

3.3 Reconstructed coupling functions identify new interactions between the circadian and cell cycle oscillators

After having inferred the θ and ϕ phases with our HMM, we estimated the coupling functions F_1 and $F_2$by computing the instantaneous phase velocities vθ and vϕ in the (θ,ϕ) plane from the time derivative of the phases (Δt equal to 0.5h). For this analysis, we selected 2'753 time traces from our dataset with a minimum duration of 24h and at least two divisions. After verifying that the distribution of velocities at every position in the phase plane was unimodal, the functions were estimated on a 40 by 40 grid. This gave 208'762 velocities and positions for each function. After smoothing, the two coupling functions (Figure 3.3) clearly indicated that the inferred coupling occurs with a predominant influence of the cell cycle onto the circadian clock, confirming what we had previously described [Bieler et al., 2014]. Indeed, the function F_1 showed three interaction regions (Figure 3.3A). An acceleration of the circadian clock was detected just after the division when the division take place in a circadian phase window between 0.5 and 0.75×2π (Figure 3.3A, yellow), which corresponds to the phase at which most of divisions occur in our dataset (Figure 2.4A, Figure 2.5B). This acceleration region identified with the new inference method is consistent with our previous report [Bieler et al., 2014].

In addition, we found two interaction regions where the circadian clock is slowed down by the cell cycle (Figure 3.3, blue). A first deceleration region was detected when divisions occur early in the circadian phase in a circadian phase window between 0 and 0.25×2π. This region was already identified by our previous inference method [Bieler et al., 2014] even if, its position in the phase plane was quite variable depending on how the fit was seeded.

Interestingly, a previously unidentified deceleration region was revealed with the new model, which was positioned late in the circadian phase (between 0.5 and 0.75×2π) before divisions, in a cell cycle phase window between 0.75 and 0.95×2π. As expected from our previous observation, the function F_2 did not reveal defined interacting regions, as no significant deceleration or acceleration was detected (Figure 3.3B). Altogether, this analysis allowed us to confirm the directionality of the coupling previously observed and to identify new interaction points between circadian and cell cycle oscillators.

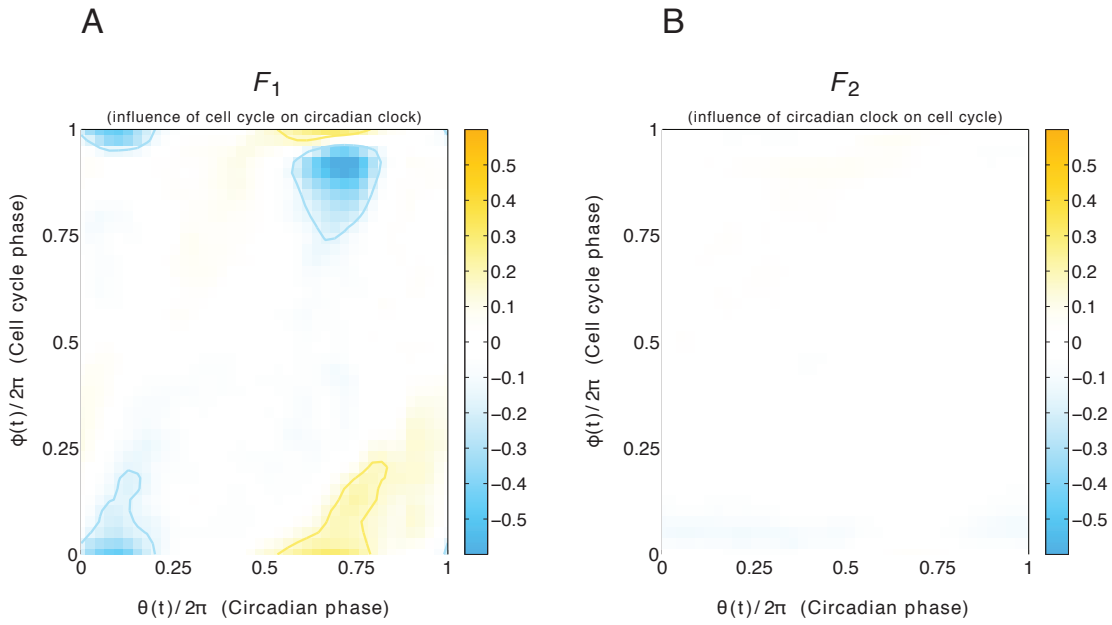

Figure 3.3 – Estimated coupling functions.
A. Estimated function F_1 describing the influence of cell cycle on the circadian clock. Yellow or blue regions correspond to an acceleration or deceleration of the circadian phase, expressed in radians per hour. It is possible to observe two blue deceleration regions, one (bottom left/top left) around division early in the circadian phase, the other (top right) late in the circadian phase before cell division, plus a yellow acceleration region around division (bottom right/top right) later in the circadian phase.
B. Estimated function F_2 describing the influence of circadian clock on the cell cycle. No significant deceleration or acceleration regions are found.

3.4 The phase portrait of the reconstructed dynamical system shows an attracting 1:1 mode locked state

When the trajectories of the system are plotted in the phase plane, the resulting phase portrait reveal features of the dynamical system such as *attractors*, namely trajectories toward which other trajectories converge, and *repellers*, curves "repelling" the surrounding trajectories. curves "repelling" the surrounding trajectories. The phase portrait resulting from the estimated vector field (F_1 and F_2), depicted as arrows in Figure 3.4A, revealed a deterministic attractor (blue curve, Figure 3.4A) corresponding to the 1:1 mode locked state, with a circadian phase at division of about 0.75x2π.

As the interaction regions are quite localized in the phase plane, the attractor attracts trajectories mainly around two regions. The first region is centered around (0.75,1×2π) and shows a slowdown of the circadian phase before the divisions, followed by a speed up just after divisions. Both effects occurred only around a window in which the circadian clock seems sensitive to perturbations. The second region is located nearly at the origin of the phase plane and corresponds to divisions occurring early in the circadian phase, i.e., right after a circadian peak. However, since the deterministic attractor do not pass through this region, traces rarely explore this interaction.

Two trajectories showing the effect of the upper deceleration region are shown in Figure 3.4B-E. To verify that this slowdown was not an artifact of the phase inference we selected traces passing through the deceleration region and compared the length of their encompassing circadian intervals (peak to peak times) to the ones of traces skipping that region. More specifically, we defined the first group of traces by taking the circadian phase at cell cycle phase equal to 0.75×2π included between 0.5 and 0.75×2π, (gray rectangle in Figure 3.4B), while the second group was defined by a circadian phase included between 0.25 and 0.5×2π (gray rectangle in Figure 3.4D).

The mean circadian interval was indeed longer (24.7 hours) in the first group than in the second one (21.8h, p< 10^{-16}, t-test). This suggest that the circadian cycle is only slowed down by cell-cycle progression in a specific region in the phase plane, and that our inference method is able to capture this effect.

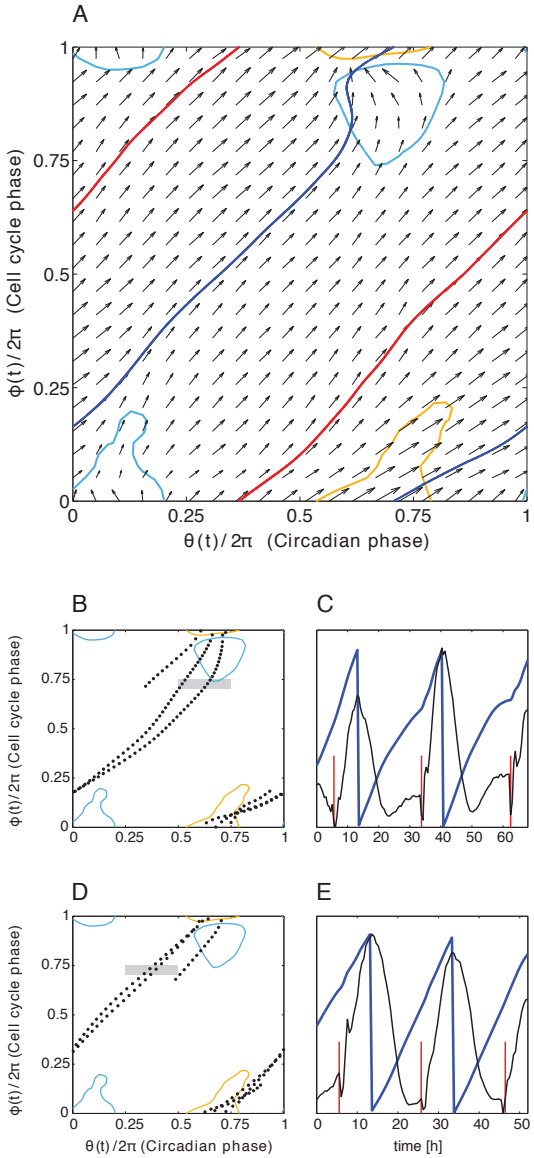

Figure 3.4 – Phase portrait of the reconstructed system.
A. In this phase portrait, the blue curves represent the attractor and the red curves represent the repeller. The trajectories are marked with arrows showing the direction of increasing time. Regions inside orange and light blue curves represent the influence of the cell cycle on circadian phase identified with function F_1 (Figure 3.3). A significant speed up of the circadian phase occurs close to, or shortly after, cell division (orange), while slow-down occurs for earlier circadian and cell cycle phases (light blue edged region at the origin of the the phase plane)and for late circadian and cell cycle phases (light blue edged region on the top left side of the portrait).
B-E. Phase specific effect of cell cycle progression on circadian phase from two example trajectories.
B. Phase portrait with a trajectory passing through the upper deceleration region, corresponding to the trace shown in panel (C).
C. Black: *Rev-Erbα* signal. Blue: Circadian phase. Red: divisions. Note the slow down in the circadian phase before the divisions, corresponding to a plateau in the ascending *Rev-Erbα* signal.
D. Phase portrait with a trajectory skipping the deceleration region, corresponding to the trace shown in panel (E).
E. Curves are indicated as in panel (C).

3.5 Different mode locked states: a fraction of cells adopts a 2:1 mode locking

As explained in the previous section and earlier in Chapter 2, the synchrony between circadian and cell cycles in our system results in a 1:1 mode lock-state, such that, in dividing cells, one cycle of the circadian oscillator is completed while the completion of one round of the cell cycle occurs. In principle, however, phase locking could occur for any rational number *p:q*, with one oscillator completing *p* cycles whereas the other completes *q*. We thus wanted to explore whether our measured interactions F_1 and F_2 could lead to mode-locked states other than the 1:1, when the frequency relationship of the two cycle was modified. For this purpose, we varied the period of the cell-cycle while keeping F_1 and F_2 fixed, and established computationally which stable *p:q* states occur. Then, we estimated different *p:q* attractors and computed the average distance to the attractor for each single-cell trace from our dataset.

Thanks to this analysis we found that a small fraction of cells tightly follows a 2:1 attractor (blue line in left panels, Figure 3.5) with the circadian clock running twice as fast as the cell cycle. Indeed, about the 7% of our cell traces showed to be closer to the 2:1 attractor than to the 1:1, indicating that cells having long cell cycle durations can adopt a different mode locked state with division occurring every two circadian peaks. In Figure 3.5, four traces adopting the 2:1 mode locking state are shown. Note that, in the last trace, the trajectory of the second circadian interval (black dots in the left panel) might represent an example of the "phase slip" phenomena, occurring when the trajectory transiently deviates from the attractor (stable manifold), crosses the unstable manifold before reaching the stable attractor again [Boccaletti et al., 2002, Pikovsky and Rosenblum, 2007].

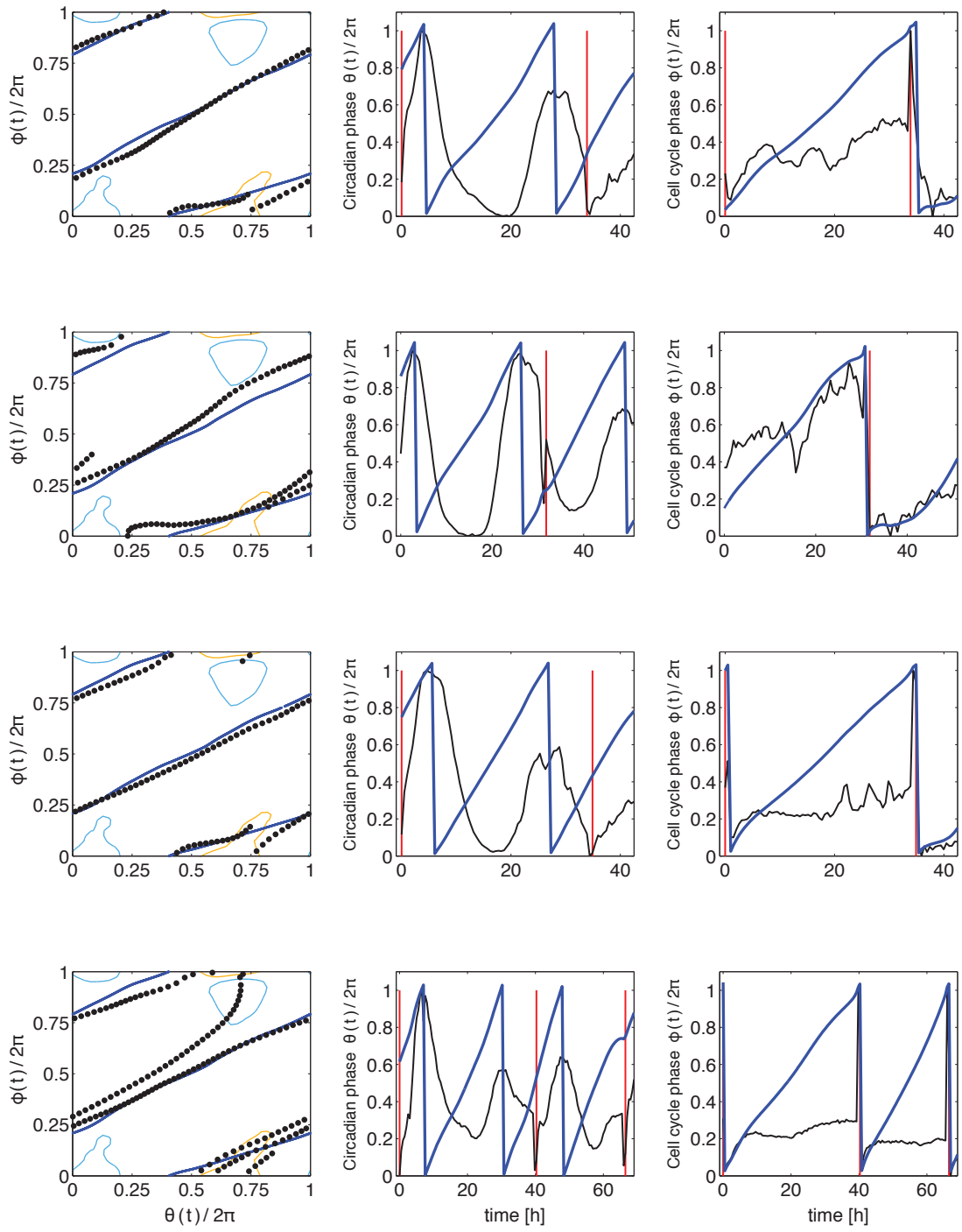

Figure 3.5 – Traces close to the 2:1 attractor.
Each row corresponds to a single cell trace.
Left. Phase portrait with deterministic 2:1 stable manifold (blue) and the measured trajectory (black).
Center. Inferred circadian phase (ϕ) (blue) and the*Rev-Erbα*-YFP signal (black) for the cell shown on the left. Vertical red bars show the annotated divisions.
Right. Inferred cell cycle phase (θ) (blue) from the nuclear area (black) for the cell shown on the right. Vertical red lines indicate the annotated divisions.

3.6 Mitotic phases and circadian phase velocity close to division: onset of prophase might coincide with the slowdown of the circadian clock

As described in Section 3.3 and Section 3.4, the reconstructed model allowed us to identify new interaction points between our the circadian and cell cycle oscillators. More specifically, a previously unidentified deceleration region was detected right before divisions (cell cycle phase between 0.75 and 0.95×2π) and late in the circadian phase (between 0.5 and 0.75×2π).

Since this region corresponds to the rising phase of the *Rev-Erbα*-YFP signal, we hypothesized that the observed slowdown of the circadian clock just before division could be due to transcriptional shutdown during M phase. To test this hypothesis, we needed a reporter allowing us to monitor the G2/M transition, since cell cycle phases between 0.75 and 0.95×2π should approximately correspond to an interval between late G2 and beginning of M phase [Fidorra et al., 1981]. In order to temporally mark the beginning of M phase, we further engineered the NIH3T3-Venus cell line with stable transduction of a construct expressing a Histone 2B-mCherry fusion protein. This reporter allows to follow the chromosome condensation marking the onset of prophase [Sumner, 1991], which is thought to underlie the observed shutdown of transcription at division [Gottesfeld and Forbes, 1997].

We imaged this cell line by simultaneously recording the *Rev-Erbα*-YFP and the Histone 2B-mCherry signals with either 20x or 60x magnification with 10 minutes or 5 intervals, respectively. After segmentation and tracking, we then manually annotated prophase, metaphase and cytokinesis on individual cell traces (Figure 3.6). We marked the onset of prophase as the first frame at which the texture of the chromatin became granular, the metaphase as the frame where the Histone 2B-mCherry reporter shows all condensed chromosomes aligned on the equatorial plate, and the cytokinesis as the first frame where the separation of the two sets of chromosomes is complete and the generation of two separate objects in the *Rev-Erbα*-YFP channel is clearly visible.

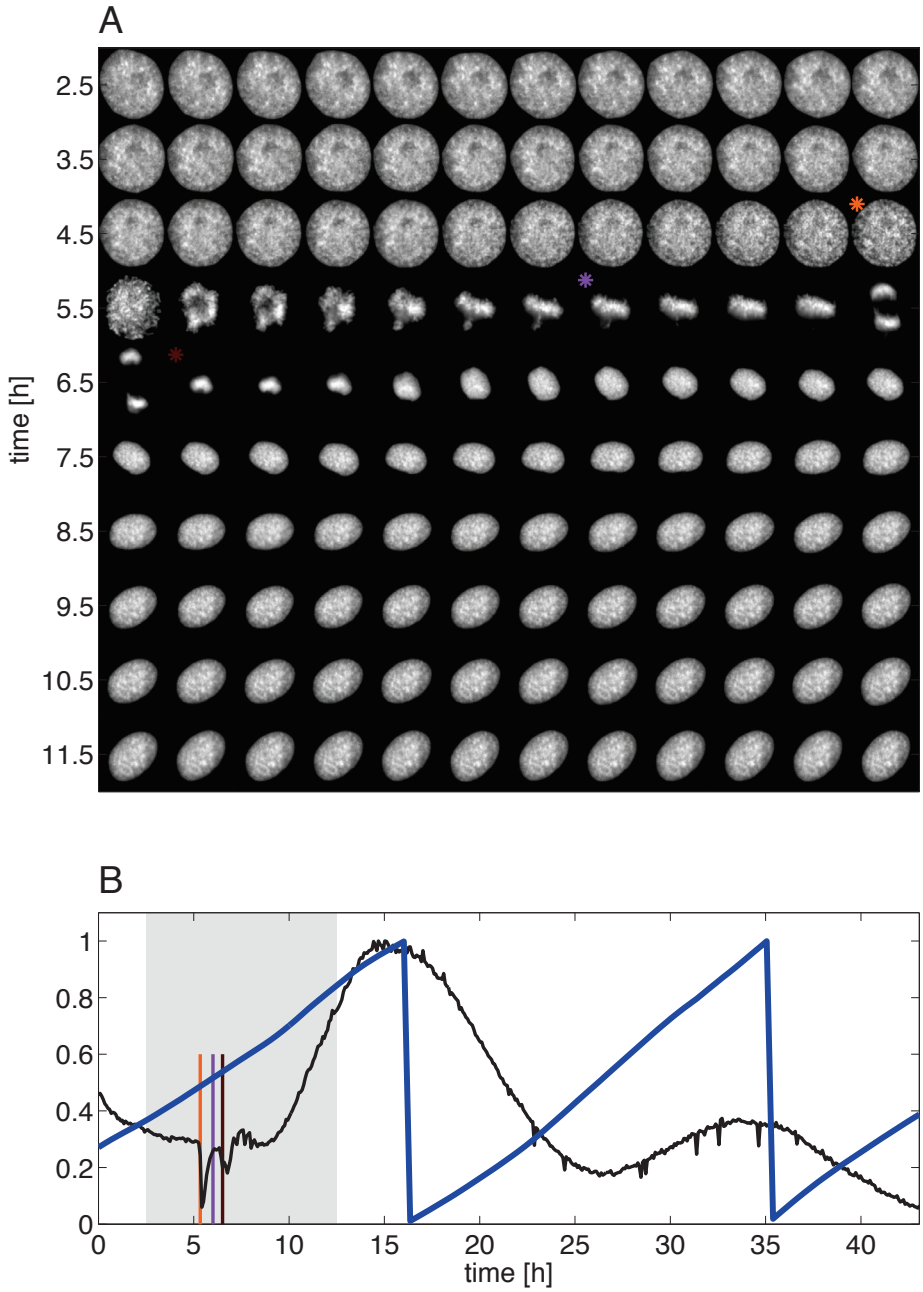

Figure 3.6 – Time series of Histone 2B-mCherry and circadian *Rev-Erbα*-YFP signals in a single cell.
A. Single-frame images showing the Histone 2B-mCherry signal for a tracked cell along the recordings. The cell shown was imaged at 60x magnification with a time resolution of 5 minutes. Time runs from top left to bottom right. Timing of prophase, metaphase and cytokinesis are indicated with orange, purple and brown stars.
B. *Rev-Erbα*-YFP signal (black) corresponding to the cell shown in panel (A). The circadian phase is shown in blue and the annotated prophase, metaphase and cytokinesis are indicated by the orange, purple and brown vertical bars. The grey region of the plot corresponds to the time range of the recordings (2.5h-12.5h) shown in (A). Note that prophase onset coincides with the nuclear envelop breakdown, as reflected by the dip of the *Rev-Erbα* signal.

3.6. Mitotic phases and circadian phase velocity close to division: onset of prophase might coincide with the slowdown of the circadian clock

We then inferred the circadian and cell cycle phases using the HMMs and plotted the timing of the different mitotic phases on the phase portrait (Figure 3.7A). We could see that, when divisions occurs late in the circadian phase (between 0.5 and 0.75×2π), the onset of prophase locates in the upper part of the region associated with a deceleration of the circadian phase, although the full extent of the region covers a broader area of the (θ, ϕ) plane (confront with Figure 3.3A and Figure 3.4A).

To test whether this result was not due to a resolution limit of our recordings, we compared the recordings performed with 20x magnification at 10-minutes interval with recordings generated with 60x magnification and five-minutes time resolution (shown as dots and crosses, respectively, in Figure 3.7A). The two types of recordings produced similar results. As shown in panel B of Figure 3.7, the phase distribution of cytokinesis is centered around 1×π. However, cytokinesis and metaphase phases show a narrow distribution, prophase distribution, centered around 0.965×2π, has a bigger variability than the one observed for the other two mitotic phases.

To better quantify the relationship between circadian phase and prophase onset, we computed the mean circadian velocity for all traces passing through the deceleration region (Figure 3.7A, blue rectangle) while taking, as a comparison, the traces that avoid that region (green rectangle), (compare with gray rectangles in Figure 3.4B, D). As shown in Figure 3.7C, the minimum velocity of the circadian phase coincides with the mean onset of prophase (orange vertical bar).

However, the observed slowdown seems to progressively start before chromosome condensation, which would exclude a direct causality of this mitotic event on the deceleration of the circadian phase.

This result suggests that other processes taking place earlier in the cell cycle might influence the expression of our *Rev-Erbα*-YFP reporter, causing the observed phase deceleration. However, it has to be mentioned that our cell cycle phase inference has a limited precision. As shown in Figure 3.2, the use of the nuclear area measurements showed modest errors in the prediction of cell cycle phases (±2 h on 14.4 h for S/G2/M and ±2.3 h on 10.3 h for G1) compared to the gold standard FUCCI system for monitoring cell cycle progression. The limitations affecting the precision of the inference might thus smear the edge of the deceleration region in the phase plane.

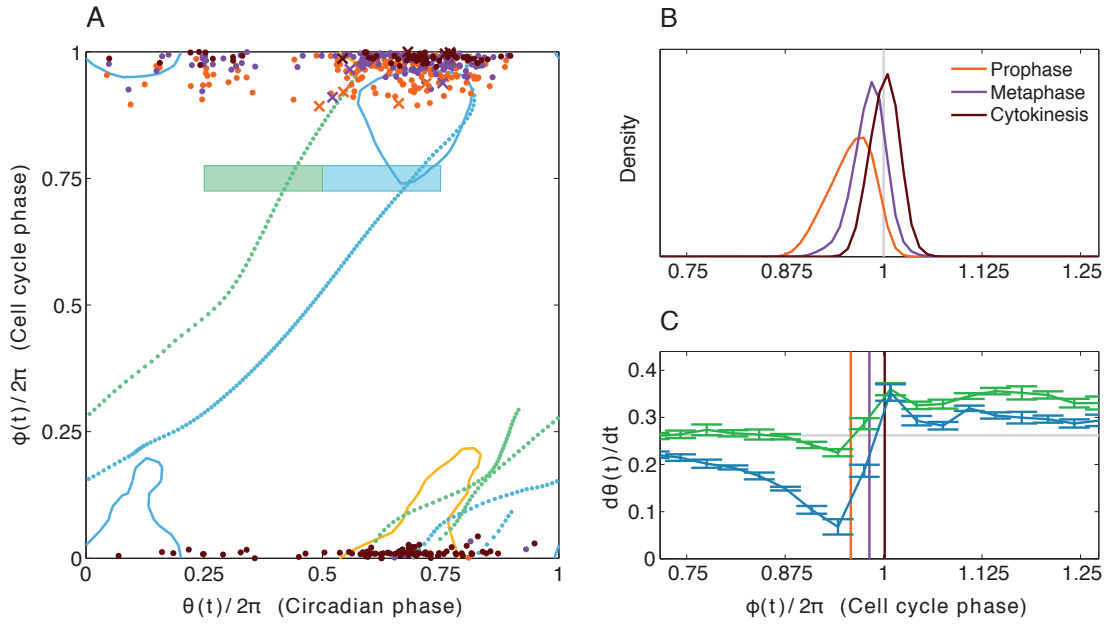

Figure 3.7 – Mitotic phases and circadian phase velocity close to division.
A. The location of 144 prophases (orange) metaphases (purple) and cytokinesis (brown) are shown in the (θ, ϕ) plane. Dots correspond to 20X magnification and the crosses to 60x magnification. The local velocity of traces passing trough the light green (or light blue) rectangle is shown in panel (C). One typical trace from each group is shown.
B. Estimated distribution of prophase, metaphase and cytokinesis. The gray line indicates $2\pi/24$ cell cycle phase.
C. The mean phase velocity in the θ direction is plotted for the two groups of traces as defined in panel (A). Error bars represent the standard error on the mean (n=60 in each group). The first mean phase velocity (light blue) passes through the deceleration region around (0.75, 0.8) and thus shows a significant slow down compared to the second one (light green). Vertical orange, purple and brown bars indicate the mean phase of prophase, metaphase and cytokinesis.

3.7 Main conclusions

The work presented in this chapter aimed at generating a more detailed picture of the interaction between cell cycle and circadian oscillators by analyzing the dynamics of the system with mathematical modeling via direct estimation of the circadian and cell cycle phases θ and ϕ. For this purpose, we analyzed the full time traces for the estimation of the instantaneous circadian and cell cycle phases and estimated the coupling functions F_1 (influence of the cell cycle on the circadian clock) and F_2 (influence of the circadian clock on the cell cycle). The reconstructed model of the phase dynamics allowed us to confirm the predominant influence of the cell cycle on the circadian oscillator previously observed (Chapter 2, [Bieler et al., 2014]). Moreover, this analysis identified new interaction points between the two oscillators.

The resulting phase portrait in the generic conditions revealed a deterministic a 1:1 mode locked state. This attractor attracts trajectories mainly due to a region inducing a slowdown of the circadian phase before division, followed by a speed up region just after division (occurring late in the circadian phase). We also found a small fraction (7%) of cells adopting a 2:1 mode lock state with the circadian clock running twice as fast as the cell cycle.

The identified interaction regions between the cell cycle and the circadian oscillators allowed us to make more specific hypotheses on cell cycle events that could influence the circadian clock, such as the condensation of chromosomes coinciding with transcriptional shutdown. We subsequently tested this prediction using a histone marker allowing the identification of mitotic phases. While showing that the onset of prophase locates in the deceleration region before division, this experiment indicated that the slowdown of the circadian phase likely starts before chromosome condensation, hinting that other cellular events taking place earlier in the cell cycle might affect the circadian phase progression.

Lastly, the results presented in this chapter indicated that our novel method of inferring phases from data using Hidden Markov Models is adequate to decode single cell trace from biological oscillators, highlighting the supporting role of mathematical models in deepening the understanding of the interaction between two important cellular processes such as the circadian clock and the cell cycle.

4 Materials and methods

"Science is fun. Science is curiosity.
Science is a process of investigating.
It's posing questions and coming
up with a method. It's delving in."
Sally Ride

4.1 Materials and methods for Chapter 2

4.1.1 Cell culture

4.1.1.1 *Incubation of NIH3T3 with different serum concentrations*

NIH3T3-Rev-VNP1-cells (abbreviated NIH3T3-Venus), were seeded two days before the start of the time lapse-fluorescent recordings in 12-well glass bottom dishes Poly-D-Lysine coated (MatTek's Glass Bottom Culture Dishes, Cat. No. P12GC-1.5-14-C) at ~12.5% confluence and maintained DMEM (Gibco-Thermo Fisher, 41966029) supplemented with 10% Fetal Bovine Serum (FBS), (Sigma, Cat. No. F7524) and 1% L-Glutamine–Penicillin–Streptomycin (PSG) antibiotics (Sigma, Cat. No. G6784). One day before the recordings, the medium was replaced by phenol red-free DMEM (Gibco-Thermo Fisher, Cat. No. 21063029) supplemented with 1% PSG and different serum concentrations for each well, spanning from 1% to 13%.

4.1.1.2 *Incubation of NIH3T3 cells at different temperatures*

NIH3T3-Venus were seeded two days before the start of the recordings in 12-well glass bottom dishes at 12.5% confluence and maintained in complete cell culture media (DMEM supplemented with 10% FBS and 1% PSG). One day before the recordings, the medium was replaced by phenol red-free DMEM complete media. In three different rounds of experiment, 2-4 hours before the start of recordings, cells previously maintained at 37 °C were incubated either at 34 °C , 37 °C or 40 °C in the microscope humidified chamber. For the recordings performed at 34 °C or 40 °C were allowed to adapt to the lower or higher temperature for 4 hours.

4.1.1.3 *Treatment of NIH3T3 with CDK1 and CDK2 inhibitors*

For the luminescence recordings, NIH3T3-DBP-Luc cells (Stratmann, 2012) were seeded at 70-80% confluence in 35mm dishes (Falcon, Cat. No. 353001) one day before the recordings. Synchronization with Dexamethasone (Sigma-Aldrich, Cat. No. D4902) was performed with 30 min 100 nM Dexamethasone-shock right before recordings. After synchronization, the medium was replaced with phenol red-free DMEM with and 100 uM D- Luciferin (NanoLight, Cat. No. 306). Cells were thus treated with either the CDK1 inhibitor RO-3306 (Sigma-Aldrich, Cat. No. SML0569) or the CDK1/2 inhibitor NU-6102 (Calbiochem, Cat. No. 217713) both resuspended in DMSO (Applichem, Cat. No. A3006), at either 1 or 1uM. As controls, cells were incubated with 0.1% DMSO. Three replicates for each conditions were used. Treatments with different uM concentrations spanning from 1 to 20 uM for each of the compound were performed in preliminary experiments in order to test the viability of the cells after several days of recordings. Considering the high toxicity of both drugs inducing significant cell death after 24 hours of incubations at concentrations higher than 10uM, we further treated cells with a range concentrations spanning from 1 to 10 uM for both inhibitors. For the fluorescence recordings, NIH3T3-Venus were seeded two days before the start of the time lapse-fluorescent

recordings 12-well glass bottom dishes at ~12.5% confluence and maintained in complete DMEM. One day before the recordings, the medium was replaced by complete phenol red-free DMEM and 2 hours before the recordings, either 0.1% DMSO, RO-3306 or NU-6102 at the concentrations of 1, 5, 7, and 10 uM was added to the medium.

4.1.1.4 *Treatment of NIH3T3 with increasing Longdaysin concentrations*

For the luminescence recordings, NIH3T3-DBP-Luc cells [Stratmann et al., 2012] were seeded at 70-80% confluence in 35mm dishes one day before the recordings. Synchronization with Dexamethasone was performed as indicated in the previous section. After synchronization, the medium was replaced with complete phenol red-free DMEM supplemented with 100 uM D- Luciferin. Cells were thus incubated with 1, 3, and 5 uM Longdaysin (Sigma-Aldrich, Cat. No. 438075) or 0.1% DMSO as controls. Three replicates for each conditions were used. Treatments with different uM concentrations spanning from 1 to 10 uM for each of the compound were performed in preliminary experiments (data not shown) in order to test the extent of the circadian period lengthening. Considering the significant lengthening of the period already occurring at the lowest concentrations, for further experiments we reduced the number of conditions to treatments with 1, 3, and 5 uM. For the fluorescence recordings, NIH3T3-Venus were seeded two days before the start of the time lapse-fluorescent recordings 12-well glass bottom dishes at 12.5% confluence and maintained in complete DMEM media. One day before the recordings, the medium was replaced by complete phenol red-free DMEM and 2 hours before the recordings either 0.1% DMSO or 1, 3, and 5 uM Longdaysin was added to the medium.

4.1.1.5 *Setup for NIH3T3 Cry1 and shFbxl3 deficient cells recordings*

Three different cell lines being shScramble-NIH3T3-Venus, shCry2-NIH3T3-Venus and shFbxl3-NIH3T3-Venus cells, were seeded two days before the start of the time lapse-fluorescent recordings 12-well glass bottom dishes at ~12.5% confluence and maintained in complete DMEM media. One day before the recordings, the medium was replaced by phenol red-free complete DMEM media.

4.1.1.6 *Treatments with Dexamethasone and Forskolin*

NIH3T3-Venus were seeded one day before the start of the time lapse-fluorescent recordings 12-well glass bottom dishes at 25% confluence and maintained in complete DMEM media. Circadian phase resetting with Dexamethasone was performed with 30 min 100 nM Dexamethasone-shock right before recordings. After synchronization, the medium was washed out and replaced with complete phenol red-free DMEM media. Phase resetting with Forskolin (Biotrend, Cat. No. BS0080) was performed right before recordings by replacing the medium with complete phenol red-free DMEM supplemented with 10uM Forskolin at the

same time than the wash of Dexamethasone-shocked cells.

4.1.2 Plasmids, lentiviral production, and viral transduction

The generation of shScramble-NIH3T3-Venus, shCry2-NIH3T3-Venus and shFbxl3-NIH3T3-Venus cells was performed via lentiviral transduction. The lentiviral shRNAs in vector backbone pLKO.1 [Moffat et al., 2006] were: Scramble shRNA (addgene #1864; DNA barcode CCTAAGGTTAAGTCGCCCTCG), Cry2-targeting shRNA (Sigma-Aldrich, clone TRCN0000194121; DNA barcode GCTCAACATTGAACGAATGAA) and Fbxl3-targeting shRNA. (Sigma-Aldrich, clone TRCN0000126948). Lentiviral particles were produced in HEK293T cells using envelope vector pMD2.G and packaging plasmid psPAX2 as previously described [Salmon and Trono, 2007]. NIH3T3-Venus cells were transduced with viral particle-containing supernatants according to standard procedures, and transduced cells were selected on 5 mg/ml Puromycin.

4.1.3 Luminescence recordings

NIH3T3-DBP-Luc cells were seeded one day before the start of the recordings in 35mm dishes (Falcon). Synchronization with Dexamethasone (described in Section 4.1.1.3), was performed right before the start of the recordings on confluent cells. After Dexamethasone shock, the medium was replaced with complete red-free DMEM supplemented with 100 uM D-Luciferin. Cells were thus treated with either 10 uM CDK1/CDK2 inhibitors (for the experiment described in Section 2.7) or 1, 3, 5 uM Longdaysin (for the experiment described in Section 2.8). Control conditions included untreated samples (data not shown) and samples treated with 0.1% DMSO, the latter showing no significant difference from the untreated conditions. Right upon treatments, dishes were sealed with Parafilm (Sigma-Aldrich, BR701605) in order to prevent evaporation of the medium along the recordings. Sealed dishes were placed on the turntable device of the luminomiter LumiCycle-32 (ActiMetrics) located in a standard incubator at 37 °C with 0.5% CO_2 at ambient humidity. The luciferase activity of the circadian reporter could be monitored by means of the four photon-counting photomultipliers of the luminomiter allowing for high sensitivity detection of luciferase light emission. The recordings had a total duration of 4-6 days with time intervals equal to 6 minutes, and the collection of data was performed with the LumiCycle Data Collection software (Version 4) while the analysis was performed with the use of a customized script developed with the "R" programming language.

4.1.4 Proliferation assay

Proliferation assays (presented in Section 2.8) were performed by counting cells using the automated cell counter Luna (Logos biosystems). HeLa or NIH3T3-Venus cells were seeded with complete DMEM in 12-well plates at the initial number of 0.1 x 10^6 and treated with either 0.1% DMSO or 5 uM Longdaysin for 48 h. The treatment was performed in triplicate for each condition. For the counts, the medium was removed, cells were washed with 1x PBS and

trypsinized with addition of the TrypLe Select Enzyme (ThermoFisher, Cat. No. 12563029) for 5 minutes. After resuspension in the growing medium, cells were spun down with 5-minutes with centrifugation at 1000 rpm and resuspended in DMEM. The cell resuspension was diluted 1:1 with Trypan blue stain 0.2% (Logos Biosystem) and introduced in counting slides. The image-based cell count was performed by setting two different protocols on the cell counter software for HeLa and NIH3T3 cells, taking into account different features of the cells such us roundness and cell size. The magnification of the incorporated camera was set at 2x. For each biological replicate, 4-6 counts were performed. Extraction of the data from the counts output files and the following statistical analysis was performed with use of a customized script developed with the "R" programming language.

4.1.5 Fluorescence time-lapse microscopy

Cells were plated in 12-well glass bottom dishes coated with Poly-D-Lysine (MatTek's Glass Bottom Culture Dishes, P12GC-1.5-14-C) and treated according to the different experimental setup described in the previous section. Time-lapse microscopy was performed at the EPFL imaging facility (BIOP) with the Olympus Cell Xcellence microscope (inverted Olympus IX81 microscope). In order to allow cells to grow under optimal conditions during the recordings, the dishes were placed on the XY-motorized stage of the microscope in a 37 °C chamber equilibrated with humidified air containing 5% CO2 throughout the microscopy (LIS-system). For the temperature experiments (Section 2.6), temperature in the chamber was modified to either 34 or 40 °C , and dishes were incubated at the respective temperatures for 4 h before starting recordings. Several preliminary experiments were performed in order to to optimize the acquisitions and the viability of the cells along the three days of recordings in the microscope chamber. For the acquisition of the *Rev-Erbα*-YFP signal, NIH3T3-Venus cells were illuminated with the use of an illumination system provided with a xenon lamp and a YFP filter set with excitation wavelength of 500/20 nm and emission at 535/30 nm (Olympus, MT20-E). Time-lapse images were acquired using the Olympus Xcellence software and an EMCCD camera (Andor, Ixon 3). Because of the circadian time dependence, the recording of the *Rev-Erbα*-YFP reporter will display a signal spanning from high to low fluorescence intensity throughout the circadian cycle. Moreover, the mean fluorescence intensity shows a significant cell-to-cell variability. As a consequence, in the same image, some cell can be overexposed, causing a saturation of the detector, while other cells can be underexposed and thus undistinguishable from the background. In order to address this issue, we acquired images from the same field at three different exposure times at each time point. More specifically, cells were illuminated for 20, 40 and 60 ms. With this setup it was possible to capture from the same field both, unsaturated images with cells having a high signal and images in which cells having a low signal intensity are clearly detectable. The images with the three different exposures are then combined for the segmentation, as explained in the next section. Images from three to four fields per well were acquired every 30 minutes for a total duration of 72 hours, using a 20x objective (UPL S APO, NA 0.75). Moreover, bright-field images were acquired at each time point, allowing more detailed observations of our cells.

4.1.6 Cell segmentation

The first part of the analysis of the acquired images consists in the segmentation of the cells and is composed of three main steps: preprocessing and combination of images, automatic segmentation and manual validation. All the steps are performed with the use of scripts developed in the MATLAB programming language. Preprocessing and combining of the images is performed as follow. First, the background of the three images from the same microscopic field, obtained with three different exposure times, is corrected with the subtraction of the low frequencies from the images. With this process, it is possible to obtain and even background and reduce the inhomogeneity from the acquisitions. The images are afterwards denoised in order to allow the average of neighboring pixels while keeping the edges sharp. The three denoised images are thus normalized and averaged. The automatic segmentation starts with convolution of images by using a collection of cell-like filters. The filtered images are then averaged, converted to binary masks and eventually cleaned with morphological operations. The cleaned images undergo an automatic correction that allows the splitting of adjacent cells recognized as one single object. The third and last step of the segmentation consists in the manual correction and validation of the automatically segmented images. Indeed, there are several sources of errors that might lead to failures in detection of cells or to erroneous recognition of two separated cells as a single object. These errors occur mostly in the lower phase of the circadian reporter expression, when the signal intensity drops down and could be almost undistinguishable from background, and around cell division. In the latter case, both, the dilution of the reporter due to nuclear breakdown during mitosis and the proximity of the two daughter cells right after the nuclear reassembly can cause inaccuracy in cell detection and in the split of two adjacent objects. As a consequence, division times might be erroneously determined. Therefore, the manual validation is an essential step for the generation of an accurate dataset. Correction and validation of the segmentation is performed with a customized MATLAB tool (Figure 2.1C) allowing the user to modify parameters such us the segmentation quantile or the split threshold, and to execute a series of operation such us manual local segmentation, splitting objects or erasing objects erroneously recognized as cell nuclei.

4.1.7 Cell tracking

The second part of the analysis of time-lapse recordings involves the tracking in time of individual cells. Segmented individual nuclei are tracked using a Single Particle Tracking (SPT) algorithm [Jaqaman et al., 2008] that is able to link objects frame by frame based on distance and fluorescence intensity features while allowing for detection of cell divisions. The tracking algorithm can reliably detect new objects generated by the divisions whereas it is not accurate in the mother-to-daughter assignment. For this reason, we did not include lineages analysis in our study. Notably, the algorithm creates a new independent trace when two daughter cells originate from cell division. Once cells are tracked, it is possible to obtain the corresponding time traces of the fluorescent signal. *Rev-Erbα*-YFP peaks are automatically detected from the

circadian fluorescent signal, whereas the timing of division is identified with a combination of the circadian signal and the tracking data. Eventually, circadian peaks and cell division times that have been automatically detected are validated and corrected. The customized MATLAB tool allows for the validation and correction of circadian peaks and divisions thanks to simultaneous visualization of the segmented individual nucleus previously tracked and the corresponding time trace.

4.2 Materials and methods for Chapter 3

4.2.1 Generation of NIH3T3-Fucci cell line

4.2.1.1 *Production of Lentiviruses*

NIH3T3-Fucci cells were produced starting from lentiviral plasmids CSII-EF-MCS-mAG-Geminin#2 and CSII-EF-MCS-mKO-Cdt1#10 [Sakaue-Sawano et al., 2008]. Lentiviral particles were produced in HEK293T cells using the envelope vector pMD2.G (encoding the VSV G envelope protein) and the packaging plasmid psPAX2 (encoding HIV-1 Gag, Pol, Tat and Rev proteins), both available from the Trono lab (EPFL) with some modification from a previously described protocol [Salmon and Trono, 2007]. Calcium phosphate transfection was performed as follow. One day before transfection, 2.5-2.85 x10^6 HEK293T cells were seeded in 10-cm dish. The plasmids pMD2.G (5 ug) and psPAX2 (15 ug) were mixed with either CSII-EF-MCS-mAG-Geminin#2 (20 ug) or CSII-EF-MCS-mKO-Cdt1#10 (20 ug) and resuspended in 250 uL sterile H2O with 2.5 MM HEPES in 1.5 mL microcentrifuge tubes. To each tube, 250 uL of sterile CaCl2 was added and the mixture was vortexed. A volume of 500 uL of the 2x HeBS solution (0.28 M NaCl, 0.05 M HEPES, 1.5 mM Na_2HPO_4, pH adjusted to 7.0 with NaOH) was added dropwise to each tube while vortexing. The mixture was left at room temperature for 30 minutes and then added dropwise all over the dish containing HEK293T cells. After 24 hours of incubation, the culture medium containing the transfection mixture was replaced with standard growing medium (DMEM-10%FCS-1%PSG). After one additional day, the virus-containing medium was collected and filtered with a syringe connected to a 0.45-uM PVDF disk filter. In order to concentrate the virus stock, the filtered supernatant was put in ultracentrifugation Beckman plastic tubes, in turn placed in metallic ultracentrifugation tubes. The volume was adjusted to 30 mL with addition of fresh medium. The ultracentrifugation was performed at 20'000 rpm for 90 minutes at 4 °C . The supernatant was carefully removed and the virus-containing pellet was resuspended in 250 uL of culture medium and put on ice for 2 hours before transduction of the target cells. The virus-containing medium was then divided in aliquots and stored at -80 °C .

4.2.1.2 *Transduction into cells*

Transduction with viral particle-containing medium was performed as follow. NIH3T3 cells were seeded at a number equal to 50'000 cells/well in 6-well plates (Corning-Costar, Cat. No. CLS3516) the same day of transduction. The two concentrated virus fluids obtained from the mAG-Geminin and mKO-Cdt1 lentiviral plasmids, were thus added simultaneously to the growing medium of adhering NIH3T3 cells (25 uL/well for each of the two viruses). Co-transduced cells were therefore daily monitored with a fluorescent microscope provided with filters for detection of both red and green fluorescent proteins. The emission of fluorescence in both channels was already clearly visible after 24 hours from co-transduction. Four days after infection, confluent cells were trypsinized, plated in 10cm dishes and allowed for replication

for four additional days.

4.2.1.3 *FACS sorting of transduced cells*

The sorting of infected cells expressing red and green fluorescence signals was performed via FACS at the EPFL Flow Cytometry Core Facility (FCCF). For the sorting, cells were prepared as follow. From confluent 10 cm culture dishes, the medium was removed, adherent cells were washed with 1x PBS and detached with 8-mintues TrypLe Select Enzyme incubation at 37 °C . After resuspension in growing medium, cells were spun down with 5-minutes centrifugation at 1000 rpm. The supernatant was removed and the cell pellet was resuspended in 1xPBS supplemented with 2% FCS. The cell resuspension was thus counted in order to adjust the final cell concentration to approximately 1x107 cells/mL. Cells were transferred in FACS tubes (BD Falcon, Cat. No. 352235) provided with a cell strainer cap containing a 35 um nylon mesh allowing for dissociation of cell aggregates. The passage of cells through the strainer was repeated for 8-10 times in order to assure an optimal preparation of the single-cell suspension. Cell sorting was performed with the MoFlo Astrios sorter (Beckman Coulter). Two samples including NIH3T3 infected with Fucci viruses and wild-type NIH3T3 cells, the latter used as negative control, were processed. Simultaneous analysis for two light scatter parameters and with two lasers for detection of fluorescent signals was performed. More specifically, a blue laser provided with a filter (488-526/52 nm) suitable for detection of the monomeric Azam-Green (mAG) fluorescent protein and a green laser provided with a filter (561-586/15 nm) for detection of the monomeric Kusabira-Orange2 (mKO2) fluorescent protein were used. The cytometry identified about 60% of positive cells for either the mKO2 or the mAG fluorescence or for both fluorescent signals. A population of double positive mKO/mAG cells, corresponding to roughly the 5% of the total population, was selected for the final sorting. The Summit Software (version 6.2.7.16492) was used for data acquisition.

4.2.2 Generation of NIH3T3-Venus-H2B cell line

4.2.2.1 *Production of Lentiviruses*

NIH3T3-Venus-Histone2B-mCherry cells (abbreviated NIH3T3-Venus-H2B) were produced starting from the PGK-H2B-mCherry lentiviral plasmid (fromMarkMercola, Addgene plasmid n. 21217) [Kita-Matsuo et al., 2009]. Lentiviral particles were produced in HEK293T cells using envelope vector pMD2.G and packaging plasmid psPAX2 similarly as indicated in the previous section (Section 4.2.1.1). The calcium phosphate transfection was performed starting from a mix of the pMD2.G (5 ug), psPAX2 (15 ug) and PGK-H2B-mCherry plasmid (20 ug). Following steps for the production of the corresponding lentivirus, including transfection and virus collection, were performed as indicated in the previous section (Section 4.2.1.1).

4.2.2.2 *Transduction into cells*

Cells were transduced with viral particle-containing medium according to standard procedures. NIH3T3-Venus cells were seeded at a number equal to 50'000 cells/well in 6-well plates the same day of transduction. The virus fluid obtained from the PGK-H2B-mCherry was added to the growing medium of adhering NIH3T3-Venus cells (50 uL). After 48 hours from infection, cells clearly showed a nuclear localized fluorescent signal when observed with a microscope provided with a filter for detection of red fluorescent proteins. Three days after infection, confluent cells treated with tryspinization were re-plated in 10cm dishes and allowed for replication for four additional days.

4.2.2.3 *FACS sorting of transduced cells*

The sorting of cells expressing the yellow and red fluorescence signals was performed via FACS at the EPFL Flow Cytometry Core Facility (FCCF). Single-cell suspensions containing $1x10^7$ cells/mL were prepared for the downstream processing in the cell sorting machine, as indicated in the previous section. Cell sorting was performed with the MoFlo Astrios sorter (Beckman Coulter) and data acquisition was performed with the Summit Software (version 6.2.7.16492). Two samples, including NIH3T3-Venus cells infected with the H2B-mCherry virus and the negative control represented by NIH3T3-Venus cells, were processed. Simultaneous analysis for two light scatter parameters and with two lasers for detection of fluorescent signals was performed. More specifically, a blue laser provided with a filter (488-526/52 nm) suitable for detection of the yellow fluorescent protein (YFP-Venus) and a green laser provided with a filter (561-620/29 nm) for detection of the mCherry fluorescent protein were used. A population of double positive Venus/mCherry cells, was selected for the final sorting.

4.2.3 Cell culture

NIH3T3-Fucci or NIH3T3-Venus-H2B cells were seeded two days before the start of the time lapse-fluorescent recordings in 12-well glass bottom dishes Poly-D-Lysine coated or in 96-well BD Falcon Imaging plates (Falcon, Cat. No 353219). Cells were maintained in complete cell culture media (DMEM supplemented with 10% FBS and 1% PSG antibiotics). One day before the recordings, the medium was replaced by FluoroBrite DMEM media (ThermoFisher Scientific, Cat. No. A1896701) supplemented with 10% FBS and 1% PSG.

4.2.4 Fluorescence time-lapse microscopy

Time-lapse microscopy was performed with two different instruments. A first set of recordings was performed as previously described (Section 4.1.5, [Bieler et al., 2014]) at the EPFL imaging facility (BIOP) with the Olympus Cell Xcellence microscope using a 20x objective. For NIH3T3-Fucci recordings, the detection of the mAG reporter was performed through illumination for 40 ms with a FITC filter set having excitation wavelength of 485/20 nm and emission

at 525/30 nm (Semrock), whereas illumination for 60 ms with Cy3 filters having excitation wavelength of 560/25 nm and emission at 607/36 nm was performed for detection of the mKO2 fluorescence. NIH3T3-Venus-H2B cells were illuminated with the YFP (excitation at 500/20 nm, emission at 535/30 nm) and the mCherry (excitation at 560/25 nm, emission at 607/36 nm) filter sets, with an exposure time of 40 ms. Images from 2-3 fields/well in 12-well dishes were captured every 30 minutes for 72 hours. An additional recording was performed on one single microscope field-of-view with images acquired every 5 minutes for 48 hours using an oil immersion objective 60x (UPL S APO, NA 1.35). A second set of recordings was performed at the EPFL Biomolecular Screening Facility (BSF) with the InCell Analyzer 2200 machine (GE Healthcare), provided with temperature, humidity and CO2 control system. For NIH3T3-Fucci recordings, cells were illuminated with the installed FITC (excitation at 475/28 nm, emission at 511.5/23 nm) and Cy3 (excitation at 542/27 nm, emission at 597/45 nm) filters for 100 ms each; images were captured with the incorporated 20x objective (NA 0.75) every 30 minutes for 72 hours. NIH3T3-Venus-H2B were imaged with the TexasRed filter (excitation at 575/25 nm, emission at 620/30 nm) for the mCherry fluorescence recording, and with the YFP channel (excitation at 513/17 nm, emission at 548/22 nm) for the YFP-Venus signal. Both illuminations were set with an exposure time of 100 ms. Cells were recorded by acquiring 1 field/well in 96-well imaging dishes incubated in the humidified and CO2 supplied chamber at 37 °C . An additional experiment was performed with the incorporated 60x objective (NA 0.7) every 5 minutes for 48 hours. Moreover, bright-field images were acquired at each time point for all the recordings.

4.2.5 Cell segmentation and tracking

Segmentation of the cells from the acquired images and single nucleus tracking was performed as previously described (Section 4.1.6, Section 4.1.7, [Bieler et al., 2014]) by implementing and adapting the previously developed segmentation tool for the analysis of multi channel recordings (FITC/CY3 for NIH3T3-Fucci cells and YFP/mCherry-TexasRed for NIH3T3-Venus-H2B cells). Parameters of the software were also optimized in order to allow the analysis of different types of images coming from the two instruments used for the recordings.

4.2.6 Computational methods

The computational methods of this work are herein included only for completeness of this manuscript, though, as already clarified in Section 3.0.1, Jonathan Bieler is the author who entirely developed this aspect.

4.2.6.1 *Hidden Markov Models for estimating phases*

In order to infer the circadian phase θ_t from the observed signal, we modeled it as a diffusion-drift process, where the drift term correspond its mean angular frequency and the noise term allow the phase to deviate form its mean to explain variations in the signal.

$$\mathrm{d}\theta_t = \frac{2\pi}{T_1}\mathrm{d}t + \sigma_\theta \mathrm{d}W_t \tag{4.1}$$

We added to the model a multiplicative amplitude term A_t that allows to explain variations in the amplitude of the signal, and is modeled as an Ornstein-Uhlenbeck process λ_t such that $A_t = \exp(\lambda_t)$.

$$\mathrm{d}\lambda_t = -\gamma_\lambda(\lambda_t - \mu_\lambda)\mathrm{d}t + \sigma_\lambda \mathrm{d}W_t \tag{4.2}$$

Similarly, an additive baseline term B_t was added to take into account traces where the signal does not go back to zero. This was necessary to avoid spurious deformation of the phase around the trough of the signal. The baseline term also follows an Ornstein-Uhlenbeck process.

Finally, the model links the observed circadian signal s_t to the circadian phase θ_t through a waveform $w(\theta)$, the amplitude and the baseline:

$$s_t = \exp(\lambda_t)\, w(\theta_t) + B_t + \xi, \tag{4.3}$$

where ξ is a normally distributed random variable with zero mean and variance σ_{em}. The model parameters are given in Section 4.2.6.1.

Given this model we derived the transition and emission probabilities needed to specify a HMM, discretized the hidden states (θ_t, A_t, B_t), optimized the waveform $w(\theta)$ using maximum likelihood and estimated the sequence of hidden states for each trace via the maximum or mean of the posterior distribution, computed via the forward-backward algorithm.

4.2.6.1.1 Circadian clock: The complete HMM for the circadian clock is defined by:

$$\mathrm{d}\theta_t = \frac{2\pi}{T_1}\mathrm{d}t + \sigma_\theta \mathrm{d}W_t \tag{4.4}$$

$$d\lambda_t = -\gamma_\lambda(\lambda_t - \mu_\lambda)dt + \sigma_\lambda dW_t \tag{4.5}$$

$$dB_t = -\gamma_B(B_t - \mu_B)dt + \sigma_B dW_t \tag{4.6}$$

$$s_t = \exp(\lambda_t)w(\theta_t) + B_t + \xi \tag{4.7}$$

For the phase θ we used a mean period T_1 of 24h and a phase diffusion coefficient σ_θ of 0.15 rad $h^{-1/2}$. For the amplitude λ we used a timescale γ_λ^{-1} of 30h, a zero mean value μ_λ and a diffusion coefficient of 0.07. For the baseline B we used a timescale of 30h, a zero mean and a diffusion coefficient of 0.022. These parameters were chosen such that the amplitude and the baseline smoothly follow the maximums and the minimums of the signal, without explaining variations in the shape of the signal, which we aim to capture in the phase. Finally the variance of the noise ξ was set to 0.1.

The transition probability for the phase and the emission probability are given by simple Normal distributions, and the transition probability for the two Ornstein-Uhlenbeck processes is given by a Normal distribution with mean $\mu_\lambda + \exp(-\gamma_\lambda \Delta t)(\lambda_t - \mu_\lambda)$ and variance $\sigma_\lambda^2/(2\gamma_\lambda)(1 - \exp(-2\gamma_\lambda \Delta t))$[Lemons, 2002].

We preprocessed the data by quantile-normalizing each trace, i.e. the signal s_t was rescaled by subtracting it's quantile p and dividing by it's quantile $1-p$ with $p = 0.05$. This is very similar to normalizing the signal between 0 and 1 but is more robust. Because of this all the parameters related to the signal have arbitrary units. We also masked the typical dip in the signal at division to avoid spurious deformation of the circadian phase at division.

4.2.6.1.2 Cell cycle, nuclear area: The HMM for inferring the cell cycle phase ϕ is very similar to the one for the circadian phase. The only difference is that we didn't include a baseline state, as it wasn't needed. The full HMM for the is defined by:

$$d\phi_t = \frac{2\pi}{T_2}dt + \sigma_\phi dW_t \tag{4.8}$$

$$d\alpha_t = -\gamma_\alpha(\alpha_t - \mu_\alpha)dt + \sigma_\alpha dW_t \tag{4.9}$$

$$a_t = \exp(\alpha_t)\, w(\phi_t) + \xi \tag{4.10}$$

We used a mean period T_2 of 22h and a phase diffusion coefficient σ_ϕ of 0.15 rad $h^{-1/2}$. For the amplitude α we used a timescale γ_α^{-1} of 30h a zero mean value μ_α and a diffusion coefficient σ_α of 0.035. The variance of the noise ξ was set to 0.1. The data were quantile-normalized as in previous section.

4.2.6.1.3 Cell cycle, Fucci: The HMM for inferring the cell cycle phase ϕ from the two Fucci signals (s_t^R and s_t^G, for Green and Red) is the same than the one described in the previous section, except that the two signals are related to the phase trough two waveforms and a shared amplitude:

$$s_t^R = \exp(\alpha_t)\, w^R(\phi_t) + \xi \tag{4.11}$$
$$s_t^G = \exp(\alpha_t)\, w^G(\phi_t) + \xi \tag{4.12}$$

We assumed independence and wrote the emission probability as the product of the two terms: $P(s_t^R, s_t^G|\phi_t, \alpha_t) = P(s_t^R|\phi_t, \alpha_t)P(s_t^G|\phi_t, \alpha_t)$.

We used the same parameters and same data preprocessing as in the previous section, except for the variance of the noise ξ that was set to 0.12 for both colors and $\sigma_\alpha = 0.04$.

4.2.6.2 *Stochastic phase model*

The phase model is given by:

$$\mathrm{d}\theta = 2\pi / T_1 \mathrm{d}t + F_1(\theta, \phi)\mathrm{d}t + \sigma_1 \mathrm{d}W_t^1 \tag{4.13}$$

$$\mathrm{d}\phi = 2\pi / T_2 \mathrm{d}t + F_2(\theta, \phi)\mathrm{d}t + \sigma_2 \mathrm{d}W_t^2 \tag{4.14}$$

With the constraint that $\iint F_i(\theta, \phi) = 0$. W_t^1 and W_t^2 are independent Wiener processes.

The best fit parameters are: $T_1 = 22.05$, $T_2 = 23.49$, $\sigma_1 = 0.18$, $\sigma_2 = 0.31$.

In order to simulate the model we used bilinear interpolation on the two coupling functions, and simulated traces with Euler–Maruyama method.

4.2.6.3 *Measuring distances to the attractor*

For given parameters the deterministic attractor of the system is a closed curve in the phase plane, that can be written in parametric form as $(\theta,\phi) = \Gamma(k)$ with $k \in [0,1]$ and $\Gamma(0) = \Gamma(1)$. We measured the distance D between a particular cell trace (θ_t,ϕ_t) and the attractor as :

$$D = 1/N_t \sum_{t=1}^{N_t} \min_k \|\Gamma(k) - (\theta_t,\phi_t)\| \tag{4.15}$$

However, in order to compare the distances from a trace to a $p_1 : 1$ attractor and the distance to another $p_2 : 1$ attractor a correction need to be taken into account. Indeed as a $p_2 : 1$ attractor is dividing the phase plane into $p_2 + 1$ regions the average distance (integrated over the plane) to the attractor is inversely proportional to p_2. For that reason traces will always be closer to higher order mode locked attractors (e.g. $10 : 1$). Thus in order to do meaningful comparison between the distances to our $2 : 1$ and $1 : 1$ attractors we rescaled the distances as $D \to p_2 D$.

5 Discussion and conclusions

"Science is the process that takes us from confusion to understanding in a manner that's precise, predictive and reliable - a transformation, for those lucky enough to experience it, that is empowering and emotional."
Brian Greene

5.1 Effects of cell cycle progression on circadian oscillators

The circadian clock and the cell cycle represent two major biological processes that might interact and influence each other. Given their periodic nature, they constitute an ideal system for studying the interaction between biological oscillators at the single-cell level.

As already mentioned in Section 1.3, many studies attempted to elucidate the interaction between circadian rhythm and cell cycle in mammalian cells. In several cases [Brown, 1991, Matsuo et al., 2003, Kowalska et al., 2013, Bjarnason et al., 2001, Nagoshi et al., 2004], it was reported that cell cycle states fluctuated with the circadian time, indicating a control, or "gating", of the circadian clock on cell cycle progression. Indeed, investigations at the molecular level indicated a circadian control on both, the G1/S transition, via circadian clock regulators such as BMAL1 or NONO [Geyfman et al., 2012, Kowalska et al., 2013], and at the G2/M transition through a direct or indirect regulation of cell-cycle related genes such as *Wee1* [Matsuo et al., 2003] by the circadian clockwork. Moreover, several key cell cycle regulators such as *Cdc2*, *Cyclin-D*, *c-Myc* or $p21^{Waf/CIP1}$ show circadian rhythmicity in either or both their mRNA expression levels or protein activity [Miller et al., 2007, Fu et al., 2002, Grechez-Cassiau et al., 2008].

However, considering the perturbations caused by cell division and the changes occurring along cell cycle progression on transcription levels [Eser et al., 2011, Bertoli et al., 2013], it seems likely that the cell cycle could also have an impact on the circadian clock. More specifically, events such as the partitioning of cellular components and the redistribution of nuclear proteins during cell division [Bergeland et al., 2001, Zaidi et al., 2003], together with the shutdown of transcription during chromosome condensation [Taylor, 1960], [Martinez-Balbas et al., 1995, Gottesfeld and Forbes, 1997], represent temporal and spatial changes that might interfere with the circadian oscillator. Indeed, experiments inducing circadian phase-shifts in mouse fibroblasts suggested that individual cellular oscillators are highly sensitive to perturbations [Nagoshi et al., 2004, Pulivarthy et al., 2007]. Accordingly, it was observed that the circadian phase of daughter cells is perturbed compared to the phase observed before mitosis [Nagoshi et al., 2004] and that continued cell division in populations of rhythmic cells leads to increased intercellular desynchronization compared with populations of non-dividing cells [O'Neill and Hastings, 2008]. The influence of the cell cycle on the circadian clock in mammalian cells is also supported by a study in U2OS cells that identified cell cycle-related genes as an overrepresented category affecting the circadian period [Zhang et al., 2009].

This thesis work aimed at further investigate the interaction between cell cycle and circadian clock by quantifying the dynamics of the two oscillators in single living fibroblasts. To this end, we performed time-lapse microscopy allowing for a large-scale quantitative analysis of individual NIH3T3 mouse fibroblasts carrying a fluorescent circadian phase marker. This approach was already used in a previous study [Nagoshi et al., 2004] and in a work carried out simultaneously to our study [Feillet et al., 2014]. Our microscopy recordings were performed

under various experimental conditions, including altered growth conditions generated by changes in serum concentration or in temperature (Figure 2.3, Figure 2.6), as well as genetic and pharmacological perturbations aiming at altering either the circadian or the cell cycle durations (Figure 2.7 - Figure 2.11).

The most prominent observation was that, in untreated cells, circadian and cell cycle oscillators are coupled and tick in a 1:1 mode-locked state. The experimental conditions probed pointed out how the observed synchronization is resilient to perturbations, as revealed by division times consistently occurring 5 h before the peak of the *Rev-Erbα*-YFP reporter. Moreover, we observed a shift of circadian phases at division that occurs according to the period mismatches of the two oscillators found in the different experimental conditions. This feature is consistent with the properties of forced oscillators [Pikovsky et al., 2003], (Section 1.2.3). We furthermore highlighted the influence of the cell cycle on the circadian clock as revealed by the systematic shortening of circadian periods in dividing cells compared to non-dividing ones (Figure 2.4). This shortening still occurred when cells were incubated at different temperatures (Figure 2.6). As expected, lower (34 °C) and higher (40 °C) temperatures induced longer and shorter cell cycle intervals, respectively. Interestingly, while circadian intervals with divisions decreased gradually with the increasing of temperature, circadian intervals without divisions did not show significant differences across the different temperatures. These observations provided an additional signature of the cell cycle impact on the circadian oscillator, since the circadian clock's capability of temperature compensation is affected in presence of cell division.

While we could not fully exclude the possibility of a circadian gating of the cell cycle in our system, our experiments, together with mathematical modeling, indicated a predominant influence of the cell cycle on the circadian clock. As will be discussed later, this property might depend on the cell type, as well as on the model organism or the experimental conditions tested.

5.2 Possible mechanisms mediating the influence of the cell cycle on circadian phase

This thesis work provided quantitative evidence demonstrating that in individual mouse NIH3T3 cells, the coupling between cell cycle and circadian clock occurs with a predominant influence of the former to the latter. The estimation of the coupling functions F_1 and F_2 (where F_1 defines the influence of cell cycle onto the circadian clock and F_2 defines the reverse interaction) and the phase portrait resulting from the estimated vector field identified specific temporal windows in which the circadian clock seems sensitive to perturbation (Figure 3.3, Figure 3.4). Indeed, for the case of divisions occurring late in the circadian phase (around 0.75x2π) an acceleration of the circadian clock just after cell division and a deceleration region before division were detected. In contrast, a deceleration region is identified when divisions occur early in the circadian phase. Based on our findings, we hypothesized possible

mechanisms that could mediate the observed influence of cell cycle progression on the circadian phase.

5.2.1 The influence of cell division on the circadian phase

The results from our analysis suggested that cell divisions might explain the impact on the circadian phase, causing a shortening of circadian intervals. As already mentioned (Section 5.1), one of the effects caused by mitosis is the redistribution of nuclear proteins after the nuclear breakdown into the two daughter cells. In our dataset, the majority of divisions occurred toward the end of the low phase of expression of the *Rev-Erbα*-YFP reporter. In terms of circadian time (CT), the *Rev-Erbα* peak occurs at CT6, therefore, most divisions occur at CT1, consistent with previous findings in rodent epidermis and mouse liver [Brown, 1991, Matsuo et al., 2003]. At this phase, the promoter of *Rev-Erbα* is in a repressed state because of the binding of the nuclear CRY1 proteins inhibiting the activity of the BMAL/-CLOCK heterodimers [Stratmann et al., 2010, Ye et al., 2011]. We can thus speculate that the dilution or relocation of CRY1 proteins upon mitosis might induce a faster derepression of the *Rev-Erbα* promoter. This, in turn, would allow the dividing cells to start a new activation round mediated by BMAL1/CLOCK earlier than in cells that do not divide. This hypothesis is compatible with the mathematical modeling findings indicating that most of the acceleration of the circadian phase occurs just after division (Figures 3E, 4E and 6D from Bieler et al., Section A.1.1). The hypothesis envisaging the dilution or relocation of CRY1 as a mechanism causing the shortening of the circadian intervals would be also compatible with the observation of the opposite effect, i.e. the slowdown of the circadian phase progression in case of early divisions (Figure 2D of Bieler et al., Section A.1.1). Indeed, it is conceivable that when divisions occur at early phases of the *Rev-Erbα* reporter, phase at which the PER and CRY proteins are in their production phase, their dilutions will lead to delay in their accumulation that in turn would lead to a lengthening of the circadian intervals.

While our analysis did not allow us to make further hypotheses on the molecular mechanisms explaining the coupling between circadian and cell cycle oscillators, we could exclude CRY2 as a putative key player that might have a role in the shortening of the circadian intervals upon division. In fact, our data showed that in *Cry2*-depleted cells the synchronization is maintained and the shortening of the circadian phase in circadian intervals with divisions still occurs. Moreover, *Cry2*-depleted cells having the expected longer circadian period, only show a modest tendency towards advanced division phases. Similarly, also Fbxl3-depleted cells with lengthened circadian periods show a shortening of circadian intervals in presence of divisions (Figure 2.10). As discussed in Section 2.10, the shFbxl3 cell line showed an increase in cell cycle duration compared to the control cells, probably due to FBXL3 possible link to cell cycle regulators [Cenciarelli et al., 1999, Cardozo and Pagano, 2004]. Even though the lengthening of cell cycle duration indicates a reduced synchrony between cell cycle and circadian oscillators, we can exclude FBXL3 as a key player explaining the cell division influence on the circadian phase.

5.2.2 The circadian phase slows down before cell division

The phase portrait resulting from the reconstructed coupling functions (Figure 3.4) highlighted a previously unidentified interacting region on the phase plane, indicating a deceleration of the circadian phase before division. This region is centered on the attractor at a circadian phase corresponding to the rising of *Rev-Erbα* expression. Based on the hypothesis that this effect could be caused by transcription inhibition occurring during chromosome condensation, we used the histone H2B reporter as a marker of mitosis, and located the timing of prophase, metaphase and cytokinesis on the phase plane. The estimation of the mean circadian phase velocity of traces passing through the deceleration region indicated that the detected slow down starts earlier than the onset of prophase.

Since our method yields a limited precision in the estimation of the cell cycle phase, we cannot however exclude that chromosome condensation might be the direct cause of the deceleration of the circadian phase. At the same time, we cannot exclude that other mechanisms occurring earlier in the cell cycle (during late G2) can play a role in determining the identified slowdown. More precise estimations with additional specific markers of cell cycle phases or direct analysis on transcriptional dynamics during the cell cycle might provide further insights in the understanding of the observed changes in circadian phase velocity.

5.3 Dynamics of the coupling between cell cycle and circadian oscillators

5.3.1 Mode-locked states

As introduced in Section 1.2.3, if two non-identical oscillators with different periods are coupled, they can adjust their rhythm so that they start to oscillate with a common period. This phenomenon is known as *frequency entrainment* or *mode-locking*. The synchronization will occur depending on two main factors: the coupling strength between the two oscillators (K) and the frequency mismatch, i.e. the difference between the periods of the uncoupled oscillators. If the period mismatch is small and the coupling strength is large enough, synchronization can take place [Pikovsky et al., 2003]. Locking can occur with a winding number p:q so that one oscillator runs p cycles while the other completes q cycles [Glass, 2001, Pikovsky et al., 2003]. For example, in the 1:1 mode-locked state, one cycle of the first oscillator is completed while the second oscillator does one full revolution, whereas in a 2:1 mode-locked state, the first oscillator will run exactly twice as fast as the second one. The system can switch from a mode-locked state to another by changing parameters such as the intrinsic frequency of the oscillators or the coupling functions.

Overall, our experiments indicated that the synchronization between the two oscillators is highly robust across the conditions probed, since we almost exclusively observed a 1:1 mode-locked state even under strongly perturbed conditions. The 1:1 mode-locked state led to the

observed unimodal distribution of division times (Figure 2.4). In case of a weak synchronization we would observe, instead, a much broader and unstructured distribution. Moreover, in case of coexistence of different *p:q* mode-locked states we would observe multimodal distributions. An example highlighting the strength of the coupling is provided by the Longdaysin experiment (Section 2.8) in which the treated conditions showed undistinguishable distributions of division times compared to the untreated control (Figure 2.8D), even if the variability of circadian intervals is significantly increased (Figure 2.8B, inset). However, we observed an increased proportion of early divisions in the Longdaysin treated conditions (Figure 2.8E) suggesting that the 1:1 mode-locked state can be challenged in case of very strong perturbations. Furthermore, a small fraction (7%) of our cells having very long cell cycle durations adopts a 2:1 mode-locked state with the circadian oscillator running twice as fast as the cell cycle, meaning that only one division occurs during two consecutive circadian intervals (Section 3.5, Figure 3.5). Importantly, in [Nagoshi et al., 2004] a multimodal distribution of division times was found in cells treated with Dexamethasone, suggesting the presence of more complex mode-locked solutions [Zámborszky et al., 2007]. Likewise, in Feillet et al. [Feillet et al., 2014], the presence of different mode-locked states was detected.

Another signature of entrained oscillators is that an increase of the period mismatch leads to phase advance whereas a decrease of the period mismatch leads to a phase delay. In our study, divisions consistently occurred 5 hours before the *Rev-Erbα*-YFP peak in all the conditions tested, while the circadian phases at division shifted according to the period mismatches. More specifically, the phase advance of division observed at 40 °C (Section 2.6, Figure 2.6E) and in shCry2 cells (Section 2.9, Figure 2.9D) is consistent with the increasing of the period mismatch in these conditions, as well as the phase delay at the highest concentrations of both CDK2 and CDK1 (Section 2.7, Figure 2.7D,G) is consistent with a reduction of period mismatch between the circadian oscillator and the cell cycle.

5.3.2 Dynamical mechanism leading to synchronization

From a dynamical point of view, the mechanism leading to synchronization can be explained by the fact that, in the condition tested, the cell cycle duration was overall shorter than the circadian period. The synchronization mainly resulted from the transient acceleration of the circadian phase shortly before and right after mitosis leading to a stable attractor in the coupled system (Figure 3.4). This acceleration around divisions was also detected with the estimation of the instantaneous circadian phase velocity as a function of the circadian phase showed in Figure 2D of Bieler et al., (Section A.1.1). In cells with early divisions, the circadian phase progression was slowed down around mitosis, whereas cells with late divisions have a shifted velocity with a speedup around division.

Our results suggested that cell division can strongly reset the circadian oscillator when it occurs in a specific circadian phase window (Figure 2.5B, Figure 2.11, left panels). In particular, if divisions occur in the rising phase of the *Rev-Erbα* reporter, when PERs and CRYs are pre-

sumably in their nuclear accumulation phase, the circadian phase would be reset and generate the observed 5-hours delay in the following *Rev-Erbα* peak. As mentioned in Section 5.2.1, this phase resetting could be explained by the derepression of the *Rev-Erbα* promoter and it is consistent with the observed positive slope of circadian intervals in cells dividing late in the circadian phase (Figure 2.5B). This hypothesis would as well justify the lengthening of circadian intervals in early divisions, when the dilution of the repressors caused by the nuclear breakdown would delay their accumulation and, in turn, will defer the rising phase of *Rev-Erbα* expression.

5.3.3 Directionality of the coupling

Our data, together with the model described in Chapter 3, indicated that the coupling occurs predominantly from the cell cycle toward the circadian clock. Indeed, when function F_2 (describing the influence of the circadian clock on the cell cycle) was set to zero in the model, the dynamics remained almost unchanged.

In order to detect potential signatures of the influence of the circadian oscillator on the cell cycle progression in all the conditions tested, we performed the Granger causality test, a statistical approach able to detect causality in time series analysis. This test is described in detail in Supplementary data from Bieler et al., Section A.1.2. The analysis detected about 12% of cells from our entire data set that favored the reverse interaction, i.e., the influence of the circadian clock on cell cycle (Figure S8 of Supplementary data from Bieler et al., Section A.1.2).

The fact that we did not clearly reveal a circadian gating of the cell cycle and that we predominantly detected a signature of the cell cycle influence on the circadian clock could originate from several factors. First of all, this observation might reflect a real lack of control of the cell cycle progression by the circadian clock in NIH3T3. It might indeed be possible that gating is not active or strong enough in our cultured cell line and under the conditions tested, as it was concluded in other studies analyzing different cell types such as tumor-driven Lewis lung carcinoma (LLC) cells [Pendergast et al., 2010] or immortalized Rat-1 fibroblasts [Yeom et al., 2010]. However, the observed directionality of the coupling could also be due to inherent limitations in the experimental design or in the inference methods. For example, an experimental limitation of our approach might originate from the fact that we observed both circadian and cell cycle phases only at certain snapshots. In order to understand the impact of this possible experimental limitation, simulations have been performed. This analysis revealed that our experimental settings do not represent a strong limitation. Details of the simulations can be found in the Supplementary information from Bieler et al. (Section A.1.2). On the other hand, we cannot exclude that errors on the cell cycle phase inference might affect the precision in its velocity estimation, albeit these errors equally affect the estimation of a trajectory position in the (θ, ϕ)-plane for F_1 and F_2. Moreover, we note that our data showed about two times more variations in the cell cycle durations than in the circadian intervals (Figure 2.3). Thus, we could presume that the significant intrinsic variability in the periods of the cycles might

also have an impact in impeding the inference of the coupling from the circadian clock to the cell cycle.

5.3.4 A phase model for the coupling between the circadian and cell cycles

The model developed in this work for inferring phases from data is based on Hidden Markov models (HMM) (Chapter 3). Overall, our phase model was able to recapitulate most of the features present in the data. Remarkably, the model was already able to reproduce the data and to reveal the main characteristics of the coupling when the estimation of the two coupling functions F_1 and F_2 was performed in an indirect way, i.e. by learning the the functions only from the boundaries (Section 3.1).

By analyzing the full time traces for the estimation of the two instantaneous phases and velocities, we could obtain a more detailed pictures of the dynamics of the coupling (Section 3.2). This method inferred the circadian (θ) phase from the *Rev-Erbα*-YFP signal and the cell cycle (ϕ) phase from nuclear area measurements. Since the waveform was determined by linking the phase to the data coming from a very large collection of time traces, we can assume that the inferred phases are robust to transformations of the data. This analysis allowed us to confirm the directionality of the coupling previously observed and to identify new interaction points between circadian and cell cycle oscillators (Section 3.3, Section 3.4). The synchrony in the data, explained by the F_1 coupling function, led to a mean circadian phase at division around $0.75 \times 2\pi$.

Moreover, the model predicted the existence and estimated the position of higher order attractors. While we found signs of 2:1 mode-locking in our dataset (Section 3.5), we assume that it would be difficult to assess other mode-locked states with recording durations of about three days. Indeed, the presence of noise in the dynamics renders it difficult distinguish between a temporary excursion away from the 1:1 attractor and real phase locking around a different one. However, it is remarkable that with this approach we were able to observe the phase shifts between the two oscillators in function of the intrinsic period difference, which represents a clear mark that the two oscillators are in resonance.

5.4 Comparison of this thesis work with the Feillet et al. paper

The publication by Feillet and collaborators [Feillet et al., 2014] is central as the authors essentially addressed the same questions, and further used nearly identical tools than ours. The authors tested experimental conditions similar, but not exactly identical, to the ones presented in this thesis work. The two studies are in agreement on the main conclusion, namely that, in unsynchronized conditions, the circadian and cell cycle oscillators robustly phase-lock each other in a 1:1 mode-locking state.

In our study, we first estimated the cell cycle length using only division times, and we subsequently made use of the nuclear size as a continuous marker of cell cycle progression. One significant advantage of the work from Feillet et al., was the addition of the FUCCI system in the NIH3T3-Venus cell line. Although the authors did not exploit that fully in their analysis, this allowed them to extract the time of G1/S transition. This analysis hence provided further information on the cell cycle progression and would allow detecting phenomenon such as the circadian gating of G1/S transition.

In both studies, several serum concentrations were used to alter the standard growing conditions of the cells. We employed 12 different FCS concentrations spanning from 2% to 13%. In this range, (as shown in Section 2.3) serum concentration affected mainly the fraction of mitotic cells but did not have a large effect either on cell cycle duration or on the circadian period. Feillet et al. in contrast, tested, in addition to the 10%, two concentrations above of our probed range, namely 15% and 20%. Under these conditions, they indeed observed a significant decrease of the cell cycle length going together with the decrease of the clock period. More specifically, while the 10% serum concentration led to a cell cycle duration of 21.3 ±1.3 h and a circadian period of 21.9 ±1.1 h, the 15% serum concentration showed cell cycle duration of 18.6 ±0.6 h and a circadian period of 19.4 ±0.5 h21.9 h. The 20% concentration was only tested in presence of a Dexamethasone pulse. Also in these conditions, a decrease of the cell cycle length (from 20.1 +/- 0.9 h to 19.1 +/- 0.7 h) going together with a decrease of the circadian period (from 24.2 +/- 0.5 h to 23.1 +/- 0.9 h) was observed in the 20% condition compared to the 10%.

Both studies used Dexamethasone to reset the circadian rhythm. However, a slight difference in the method has to be mentioned: in our study we treated cells for 30 minutes, a duration that, in our hands, is enough to elicit good resetting of the clock, whereas in the study from Feillet et al. the treatment was performed for 2 hours. When cells proliferating under higher serum concentrations (20%) were treated with Dexamethasone, (conditions tested only in Feillet et al.) a coexistence of different mode-locking states, notably 1:1, 3:2 was revealed. They also performed stochastic simulations for 5:4 coupling but they found that the system does not lock in a stable fashion as the 5:4 locking region is very small. In our first analysis, we detected only a 1:1 mode-locking. This result could be due to differences in the experimental conditions. For example, the different durations of the Dexamethasone treatment, known to induce a high level of *Per1* mRNA and inhibition of other clock genes, might lead to different

responses in the stabilization of the circadian phase after the transient perturbation. This might, in turn, perturb the coupling. Importantly, as shown in Section 3.5, we were later able to detect a previously undetected 2:1 mode-locking state, with two divisions occurring during one circadian cycle, and we assumed that identifying additional potential mode-locked states would be difficult due to intrinsic limitations of our experimental and computational approach.

In both studies, mathematical models supported the experimental data indicating different directionalities of the coupling: in our study we concluded a unidirectionality of the coupling, with a dominant influence of the cell cycle on the circadian clock, whereas Feillet and collaborators indicated a bidirectional coupling. We can attribute this dissimilar conclusion to the differences in the experimental conditions and analysis methods.

However, both studies converged on one important and unexpected statement, namely the absence of clear signatures of gating of the cell cycle by the circadian clock in NIH3T3 mouse fibroblasts (reviewed in [Feillet et al., 2015]).

5.5 The circadian gating of the cell cycle

As introduced in Section 1.3.1, the circadian gating of the cell cycle appeared to be conserved across evolution. A proposed hypothesis about the importance of this mechanism suggests that it might minimize genotoxic stress during DNA synthesis and replication constraining this cell cycle phase to times of the day when the solar irradiation is low and the metabolic oxidative stress is little [Destici et al., 2011]. Kowalska and collaborators [Kowalska et al., 2013], showed a circadian gating of divisions in wound healing, suggesting a role of the circadian clock in segregating in a temporal fashion cell proliferation from tissue organization. More generally, the circadian gating could represent an additional control of cell cycle progression, providing the advantage of reducing the exposure of dividing cells to potentially hazardous environmental conditions.

Surprisingly, the results from this thesis work did not lead to detection of a circadian gating in proliferating cultures of NIH3T3 mouse fibroblasts. This discrepancy with previous observations could be due to several reasons. First of all, as already explained in Section 5.3.3, we cannot exclude that our analysis might not be able to detect gating because of experimental and analysis methods limitations. For example, our first analysis did not allow us to obtain estimations of the cell cycle phase. We attempted to improve this aspect by the use of nuclear area measurements as a continuous variable of cell cycle progression (Section 3.2). This method allowed us to gain more information on the cell cycle. When comparing the use of the FUCCI system with the use of nuclear area measurements for cell cycle phase estimations we found a good agreement between the two approaches (synchronization index equal to 0.83, Figure 3.2C). However, while with both methods divisions were detected with high accuracy, there was more variation in the phase estimation in the middle of the cell cycle. As a consequence, the estimations of S/G2/M durations (mean of 14.4 h) and G1 (mean of 10.3 h)

durations determined with the FUCCI system was predicted from the nuclear area method with an error of ± 2.0 and ± 2.3 hours, respectively Figure 3.2. This imprecision might have an impact on the coupling estimation that might, in turn, prevent predicting potential gating.

On the other hand, it is also conceivable that gating is not occurring in our system. Indeed, it is highly likely that in mammalian organs or tissues, circadian systemic cues such as feeding cycles, rhythms in body temperature or glucocorticoid hormones, might play a dominant role in synchronizing cell cycle oscillations. This hypothesis is coherent with the observations of Destici and collaborators [Destici et al., 2011] that highlighted a circadian lack of control on the cell cycle at the cell-autonomous level in cultured fibroblast. They thus suggested that systemic mechanisms might be responsible for the observed circadian control on cell cycle *in vivo*. Since cell division represents a large perturbation event for the cell, we can speculate that extracellular circadian systemic cues might represent a solution for the cell to escape the period alterations induced by the cell cycle. These signals may thus override or even invert the entrainment that we detected in our cultured proliferating cells.

5.6 Significance of this thesis for chronobiology, cancer and chronotherapeutics

The findings of this thesis are particularly relevant for the field of chronobiology, since it has been recently demonstrated that the circadian clock has important timing functions in actively proliferating tissues such as epidermis, hair follicles, intestinal epithelium or immune cells [Janich et al., 2011, Janich et al., 2013, Geyfman et al., 2012, Plikus et al., 2013, Mukherji et al., 2013, Cermakian et al., 2013, Scheiermann et al., 2013]. These findings, together with additional observations from several studies [Matsuo et al., 2003, Levi et al., 2007, Bouchard-Cannon et al., 2013, Kowalska et al., 2013] led to the hypothesis that the interplay between circadian clock and cell cycle could represent a way to provide an optimal temporal organization of cell proliferation [Feillet et al., 2015].

In addition to the implications that our findings can have for chronobiology in proliferating tissues, understanding the consequences of coupling between cell cycle and circadian clock also appears to be very important in the context of cancer development and progression. Indeed, dysfunctions of each of the two oscillators could lead to diseases such as cancer. As reviewed in [Feillet et al., 2015], it has been shown that cancer cells frequently have dysregulation or mutations of circadian clock genes that might lead, in turn, to abnormal proliferation [Fu et al., 2002, Lee et al., 2010, Fu and Kettner, 2013]. However, it is still unclear whether the mutations of clock genes would be a direct primary cause of tumorigenesis. Nevertheless, strong environmental perturbations of the circadian functions, such as the ones induced by chronic jetlag, have been associated with augmented carcinogenesis in rodents [van den Heiligenberg et al., 1999, Filipski et al., 2009] and increased risk of cancer development in humans [Fu and Kettner, 2013]. On the other hand, several human cancer cell lines exhibit deregulated expression of circadian genes. Thus, it seems very difficult to distinguish

between the primary cause and the consequence of the observed alteration in both oscillators.

In conclusion, considering the beneficial effects of chronotherapeutics for cancer treatments, consisting of reduced toxicity and increased efficacy of the drug [Levi et al., 2007], the findings highlighted in this thesis work can have an impact in the design of more effective cancer treatments.

5.7 Future directions

5.7.1 Additional circadian reporters

In our system, we used only one circadian reporter for the estimation of the circadian phase. While our experimental design allowed us to reliably estimate the *Rev-Erbα* reporter signal and to simultaneously detect cell divisions and estimate the circadian phase at divisions, our analysis could be more fruitful with the generation of cell lines harboring additional circadian reporters. It would be ideal to use additional reporters having different circadian phases than *Rev-Erbα* . Transcriptome profiling around the clock via RNA-sequencing performed by myself indicated that the peak of *Rev-Erbα* expression occurs at CT1 in NIH3T3 cells. Therefore, the use of circadian reporter such as *Cry1* and *Bmal1*, peaking at CT9 and CT18 respectively, would allow to have a more detailed and precise estimation of the circadian phase progression.

This goal could be achieved by designing constructs expressing fluorescent proteins with distinct excitation/emission spectra than the YFP-Venus. Towards this goal, we designed lentiviral plasmid expressing either the mCherry or the Cerulean fluorescent proteins under the control of *Bmal1* or *Cry1* promoter. These constructs are currently tested.

5.7.2 Different mammalian cell lines

Because of the importance of our findings in the context of cancer and chronotherapeutics (Section 5.6), a further step in this work would be to extend the analysis in cancer tissues, starting, for example, with the human osteosarcoma U2OS cell line, widely used as a circadian cell line model, since it displays a very good rhythmicity [Zhang et al., 2009].

I thus recently generated a stable U2OS cell line expressing the same *Rev-Erbα*-YFP construct used for generating the NIH3T3-Venus cell line. As shown in Figure 5.1, preliminary results on a relatively small number of cell traces indicated that U2OS cells display similar features of synchronization compared to the ones observed in NIH3T3 fibroblasts. The mean cell cycle and the circadian periods are 21h ±6.54h and 21.44h ±6.81h, respectively (Figure 5.1A). Impressively, when plotting traces with at least two circadian peaks aligning them to the second circadian peak, we can observe that divisions show a clear tendency to occur right before the circadian peaks, showing a unimodal distributions centered at -5 hours, very similarly to what was observed in NIH3T3 cells (Figure 5.1B, C).

In addition to the *Rev-Erbα*-YFP construct, the U2OS cells were further engineered with a *Bmal1*-Luciferase reporter that allows luminescence recordings at single-cell and population level. This will represent an advantage since it will allow combining bioluminescence with fluorescence single-cell imaging analysis and provide a tool for investigations on cell populations. As shown in Figure 5.1D The *Bmal1*-Luciferase population signal showed a very good circadian rhythmicity of this U2OS cell line after Dexamethasone synchronization.

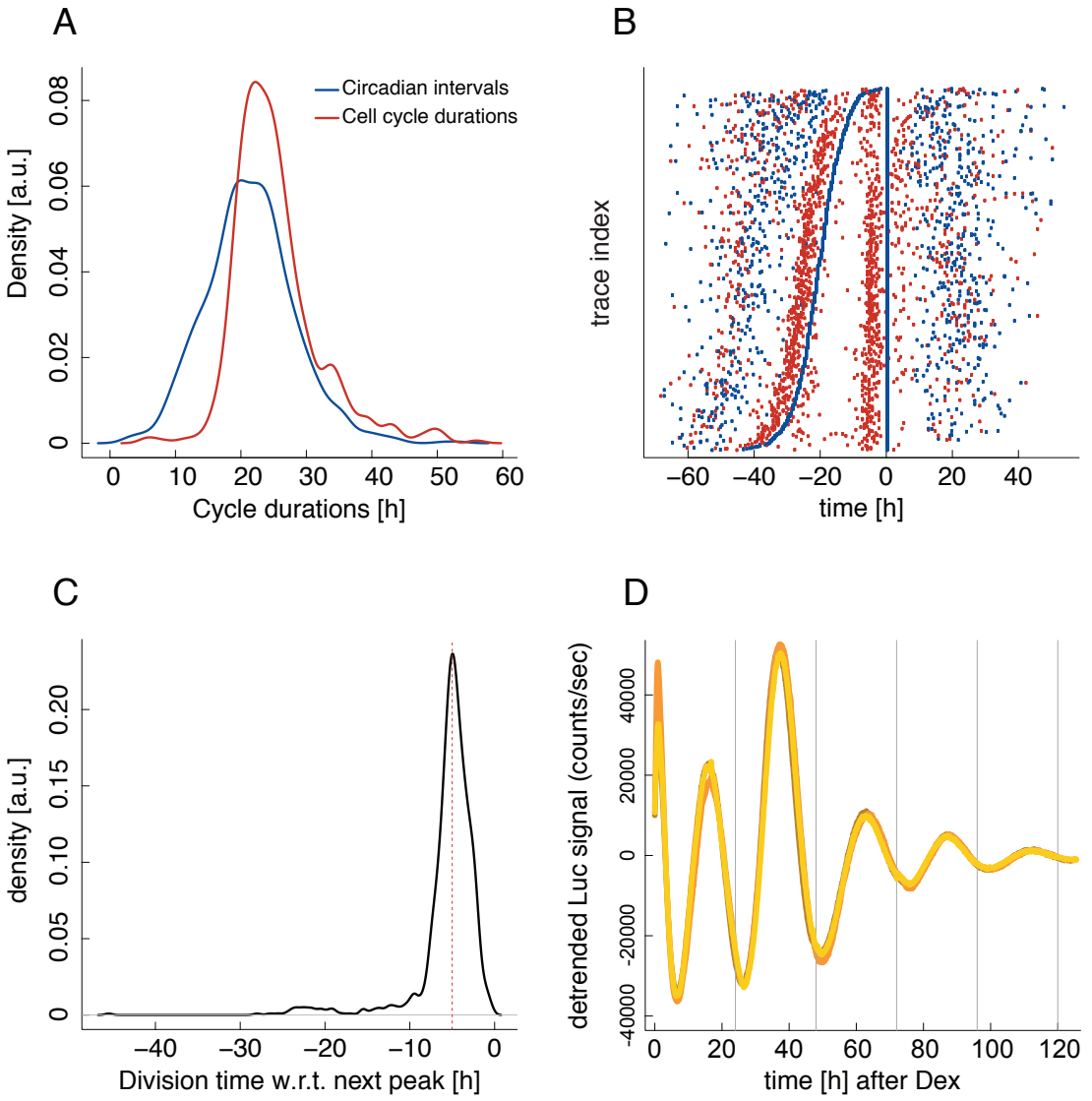

Figure 5.1 – U2OS cells show features of synchronization between the circadian clock and the cell cycle.
A. Circadian (blue) and cell cycle (red) periods distribution in U2OS cells. The mean circadian duration (n=962) is 21.44h ±6.81h whereas the cell cycle mean duration (n=514) is 21h ±6.54h.
B. Raster plot showing 962 time traces (with at least two circadian peaks) aligned on the second circadian peak (blue), and sorted according to the interval between the first and the second circadian peak. Divisions (red) show a tendency to occur on average 5hours before the circadian peaks.
C. Division times (n=986) measures with respect to the subsequent circadian peak show a unimodal distribution centered at about -5 h (median= -5 h, sd= 3.88)
D. *Bmal1*-Luciferase signal from U2OS cell populations after Dexamethasone treatment. The luminescence signal (counts/sec) from the Bmal1-Luc reporter from three different superimposed replicates is plotted after baseline subtraction.

The analysis of a large scale dataset in U2OS cell line, including perturbation experiments similar to the ones performed in NIH3T3 cells will allow us to make comparisons between the two different cell lines and to investigate the impact of cell-type specificity on the synchronization between circadian clock and cell cycle.

5.7.3 Alternative approaches for inferring cell-cycle state

In our study we were able to easily and unambiguously detect cell divisions thanks to the nuclear breakdown causing an abrupt drop in the *Rev-Erbα*-YFP signal. We later made use of the nuclear area measurements as a continuous variable of cell cycle progression, and further engineered our NIH3T3-Venus cell line with a H2B reporter as a mark for M-phase. However, the addition of cell cycle reporters for G1, S and G2 phases would provide a useful advantage in order to gain more insight into cell cycle progression and to improve the precision of the cell cycle phase inference. This will allow, in turn, a more precise quantification of the coupling between the two oscillators.

An interesting approach for the determination of trajectories of cell-cycle progression has recently been developed by Gut and collaborators [Gut et al., 2015]. The methods they developed, named *Cycler*, is able to infer trajectories of cell-cycle progression from populations of fixed cells from image-based datasets. By taking into account features from the microenvironment such as local cell crowding, Cycler allows the identification of the main sources of cell-to-cell variability. Therefore, it allows for the simultaneous analysis of different cellular processes along the cell cycle at the single cell level without the need of transgenic markers. A similar approach could represent an alternative for inferring cell-cycle trajectories in the NIH3T3 cell line, perhaps in combination with genetic perturbation screens. This approach could thus represent a mean for the identification of direct cell cycle-dependent perturbations on the circadian clock.

5.7.4 Cell lineage analysis

Another potential extension of this work would be to analyze cell lineages in order to investigate cell-to-cell variability from mother-to-daughter and progeny cells in both, the circadian period and the cell cycle duration.

A limitation of our current experimental approach originates from the total length of the recordings (72 hours) that does not allow the collections of a significant amount of cell lineages. Moreover, the software developed for segmentation and tracking used for the analysis of our dataset did not allow us to reliably provide automatic mother-to-daughter assignments. However, the current implementation of our software will allow us to investigate this yet unexplored aspect of the project. An example of cell lineage from our dataset is shown in Figure 5.2.

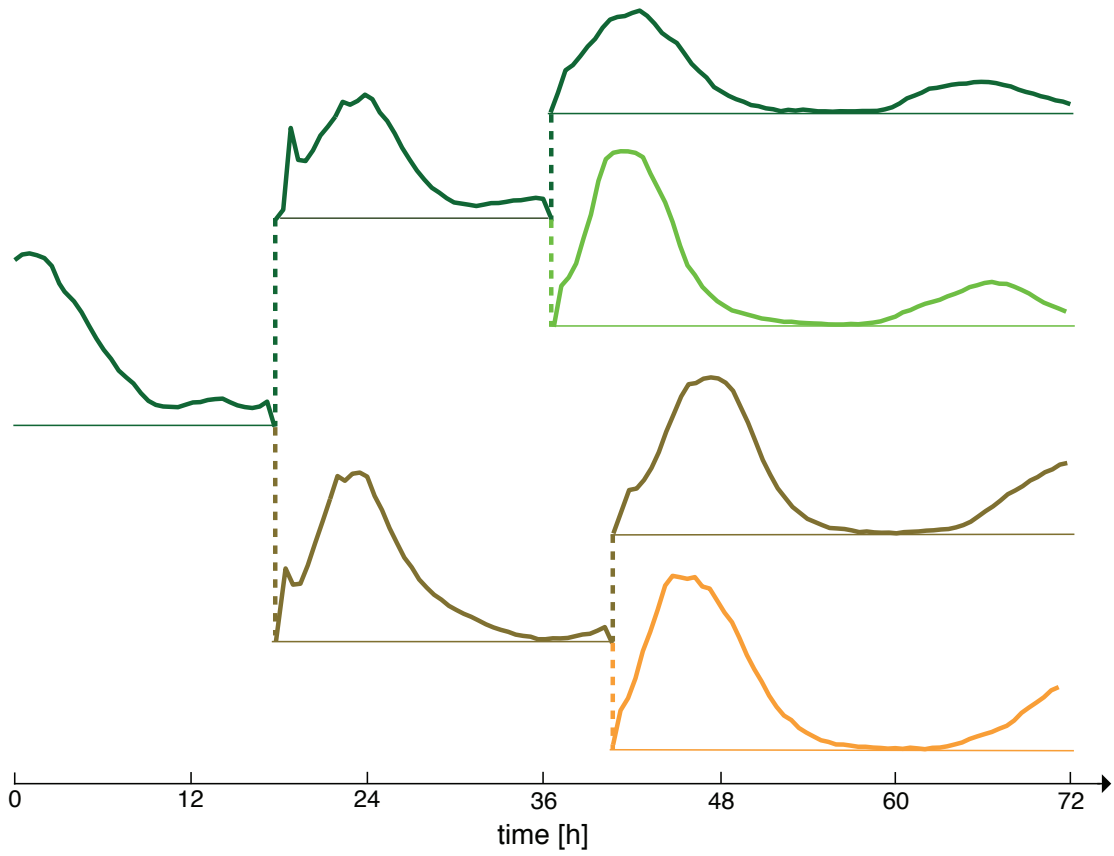

Figure 5.2 – Example of cell lineage.
The normalized signal of the *Rev-Erbα*-YFP reporter is plotted along time for the mother cells and its progeny. The dashed lines correspond to the time of division and connect two daughter cells originating from the same mother cell. Cells corresponding to a unique trace along the recordings are indicated with the same color.

5.8 Final conclusions

In conclusion, this thesis work elucidated previously understudied aspects of the coupling between circadian and cell cycles in mammalian cells, namely that of the influence of the cell cycle on the circadian phase dynamics. While the hypothesis of a gating of cell cycle progression by the circadian cycle has been heretofore the most proposed, our study showed that in NIH3T3 cells grown under standard conditions, the cell cycle has a predominant influence on the circadian cycle (Figure 5.3). This coupling led to a striking robust synchronization of the two cycles in our cell line. Our findings provide thus a valuable piece of knowledge that has important implications for chronobiology in proliferating tissue and might, eventually, have an impact on cancer chronotherapeutics.

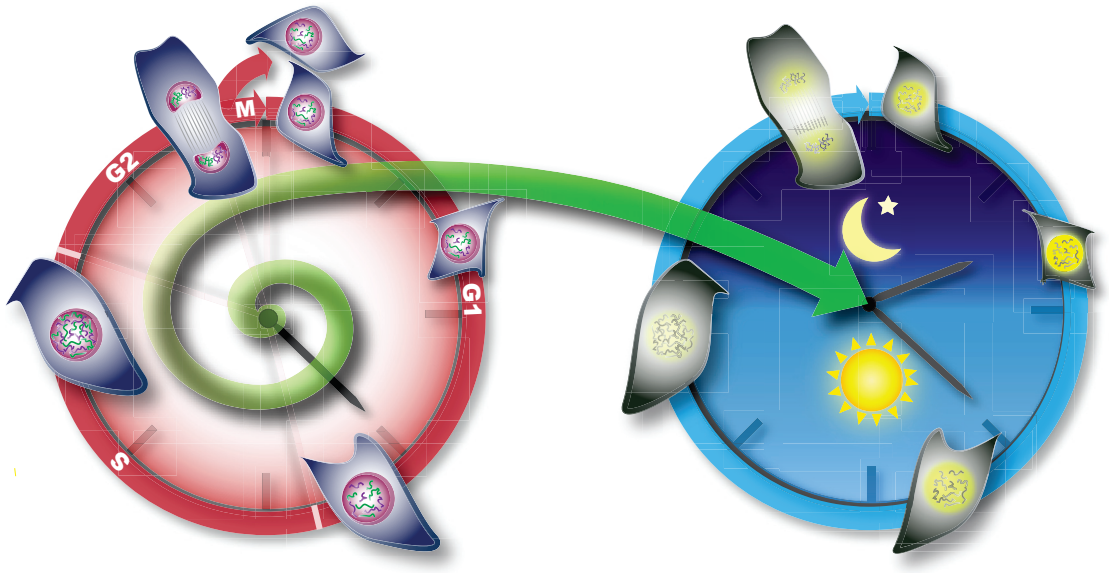

Figure 5.3 – llustration highlighting the coupling between cell cycle and circadian clock in mouse fibroblast cells, with a predominant influence of the cell cycle on the circadian cycle.

A Appendix

A.1 Robust synchronization of coupled circadian and cell cycle oscillators in single mammalian cells

A.1.1 Manuscript

Article

TRANSPARENT PROCESS OPEN ACCESS

molecular systems biology

Robust synchronization of coupled circadian and cell cycle oscillators in single mammalian cells

Jonathan Bieler[1,†], Rosamaria Cannavo[1,†], Kyle Gustafson[1], Cedric Gobet[1], David Gatfield[2] & Felix Naef[1,*]

Abstract

Circadian cycles and cell cycles are two fundamental periodic processes with a period in the range of 1 day. Consequently, coupling between such cycles can lead to synchronization. Here, we estimated the mutual interactions between the two oscillators by time-lapse imaging of single mammalian NIH3T3 fibroblasts during several days. The analysis of thousands of circadian cycles in dividing cells clearly indicated that both oscillators tick in a 1:1 mode-locked state, with cell divisions occurring tightly 5 h before the peak in circadian *Rev-Erbα*-YFP reporter expression. In principle, such synchrony may be caused by either unidirectional or bidirectional coupling. While gating of cell division by the circadian cycle has been most studied, our data combined with stochastic modeling unambiguously show that the reverse coupling is predominant in NIH3T3 cells. Moreover, temperature, genetic, and pharmacological perturbations showed that the two interacting cellular oscillators adopt a synchronized state that is highly robust over a wide range of parameters. These findings have implications for circadian function in proliferative tissues, including epidermis, immune cells, and cancer.

Keywords cell cycle; circadian cycle; single cells; synchronization; time-lapse imaging
Subject Categories Quantitative Biology & Dynamical Systems; Cell Cycle
DOI 10.15252/msb.20145218 | Received 20 February 2014 | Revised 5 June 2014 | Accepted 5 June 2014
Mol Syst Biol. (2014) 10: 739

Introduction

Understanding how cellular processes interact on multiple levels is of fundamental importance in systems biology. In this context, the interconnection between circadian and cell cycle oscillators presents an ideal system that can be analyzed in single prokaryotic (Yang *et al*, 2010) and eukaryotic cells (Nagoshi *et al*, 2004; Welsh *et al*, 2004). Interactions between the circadian oscillator and the cell cycle link two fundamentally recurrent cellular processes (Reddy & O'Neill, 2010; Masri *et al*, 2013). The circadian clock is a cell-autonomous and self-sustained oscillator with a period of about 24 h and thought to function as a cellular metronome that temporally controls key aspects of cell physiology, including metabolism, redox balance, chromatin landscapes and transcriptional states, and cell signaling (Dibner *et al*, 2010; O'Neill *et al*, 2013). In growth conditions, successive divisions and progression through the cell cycle can also be considered as a periodic process. The cell cycle duration in mammalian cells typically also lasts on the order of 1 day (Hahn *et al*, 2009). An immediate theoretical consequence is that coupling between two such oscillators may lead to synchronization, which is also called mode-locking. In fact, depending on the relationships between the intrinsic periods of the oscillators and the strength of their coupling, the system may stabilize into a steady state in which the two cycles advance together, similar to a resonance phenomenon. More generally, the system may switch from asynchrony (quasi-periodicity) to synchronization characterized by a rational winding number (p:q) such that exactly p cycles of the first oscillator are completed while the second completes q cycles (Glass, 2001).

Studies in cyanobacteria (Mori *et al*, 1996; Yang *et al*, 2010), fungi (Hong *et al*, 2014), zebrafish (Tamai *et al*, 2012), and mammalian cells (Brown, 1991; Matsuo *et al*, 2003; Nagoshi *et al*, 2004; Kowalska *et al*, 2013) reported that cell cycle states fluctuate with circadian time. Notably, mitotic indices are known to exhibit clock-dependent daily variations (Brown, 1991; Bjarnason *et al*, 2001; Reddy *et al*, 2005; Masri *et al*, 2013). This has led to a model whereby the circadian clock may establish temporal windows in which certain cell cycle transitions are favored or suppressed, a phenomenon referred to as circadian gating of the cell cycle. Since this gating appears to be recurrent across evolution, it was proposed to reflect an adaptation, for example, to minimize genotoxic stress during DNA synthesis and replication by directing these events to time intervals of low solar irradiation and low metabolically generated oxidative stress (Destici *et al*, 2011). Improved understanding of conditions that synchronize cell and circadian cycles is of great interest for cancer chronotherapeutics, as it might help optimize the timing of anti-proliferative drug treatments (Levi *et al*, 2007).

Regulation of the cell cycle by the circadian clock involves both the G1/S and G2/M transitions. Seminal work in the regenerating

1 The Institute of Bioengineering, School of Life Sciences, Ecole Polytechnique Fédérale de Lausanne (EPFL), Lausanne, Switzerland
2 Center for Integrative Genomics, Génopode, University of Lausanne, Lausanne, Switzerland
*Corresponding author. Tel: +41 21 693 1621; E-mail: felix.naef@epfl.ch
†These authors contributed equally to this work

mouse liver suggested that WEE1 kinase, which limits the kinase activity of CDK1 and thereby prevents entry into mitosis, is controlled at the transcriptional level through BMAL1/CLOCK and shows circadian activity, thereby functioning as a clock-dependent cell cycle gate (Matsuo *et al*, 2003). In a single-cell study, we previously observed circadian gating of mitosis in dexamethasone-synchronized NIH3T3 fibroblasts, showing multiple windows permitting mitosis (Nagoshi *et al*, 2004). However, studies in Rat-1 fibroblasts (Yeom *et al*, 2010) and cancer cell lines (Pendergast *et al*, 2010) concluded that circadian gating of mitosis was absent. A recent breakthrough showed that NONO, an interaction partner of PER protein (Brown *et al*, 2005), gates S-phase to specific circadian times in primary fibroblasts (Kowalska *et al*, 2013). The consequences of these multiple interactions along the cell-division cycle were investigated with mathematical models, showing conditions under which the cell cycle can mode-lock to the circadian oscillator (Zámborszky *et al*, 2007; Gérard & Goldbeter, 2012). In addition, several core clock regulators including CRY proteins (Destici *et al*, 2011) and BMAL1 (Geyfman *et al*, 2012; Lin *et al*, 2013) have been shown to influence cell proliferation, although the directionality of the effects seems to be condition-specific.

Less is known about the reverse interaction, or how the cell cycle influences the circadian cycle. However, a signature thereof is the dependency of circadian period on the time of mitosis (Nagoshi *et al*, 2004). Since the circadian oscillator is based on transcriptional–translational feedback loops, it is plausible that alteration of transcription rates during cell cycle progression (Zopf *et al*, 2013), transcriptional shutdown during mitosis (Gottesfeld & Forbes, 1997), or the transient reduction in the concentration of circadian regulators following division may indeed shift the circadian phase (Nagoshi *et al*, 2004), a phenomenon that is further supported by modeling (Yang *et al*, 2008). In addition, the activation of cell cycle checkpoints, notably via the induction of DNA damage, produces a circadian phase advance (Oklejewicz *et al*, 2008; Gamsby *et al*, 2009), which is thought to involve the interactions of several circadian oscillator proteins with the CHK1,2 checkpoint kinases (Masri *et al*, 2013).

Even though the molecular interactions between the cell cycle and circadian clock are emerging, it is not clear under which conditions these lead to entrainment of one cycle by the other, or possibly synchronization between the two cycles in mammalian cells. Here, we performed a systematic analysis of the coupling between the cell cycle and the circadian clock using time-lapse imaging of mouse fibroblasts containing a fluorescent reporter under the control of the circadian clock. Semi-automatic single-cell segmentation, tracking of circadian rhythms in single cells, and estimation of the timing of divisions allowed us to gather sufficient statistics to quantitatively probe interdependencies of the two processes under a wide set of conditions, including several serum concentrations, different temperatures, treatment with pharmacological compounds to perturb one or both of the cycles, and shRNA-mediated knockdown of circadian regulator. We found that the two oscillators showed a clear signature of mutual synchronization, with cell divisions occurring very tightly 5 h before the peak of expression of the BMAL1/CLOCK-controlled circadian *Rev-Erbα*-YFP reporter. While coupling in either direction may cause such synchrony, mathematical modeling of our data unambiguously showed that the influence of the cell cycle on the circadian clock dominated in NIH3T3 cells and that this interaction was highly robust across the many conditions tested.

Results

Circadian and cell cycle oscillators are tightly synchronized in NIH3T3 cells

A universal property of interacting oscillators is the emergence of synchronized states, also called mode-locking (Glass, 2001). Since the cell cycle duration in many mammalian cells lines is in the range of the period of the circadian oscillator (about 24 h), this leads to the possibility that the two cycles could synchronize. To quantitatively investigate this possibility in single cells, we used the well-established mouse NIH3T3 cell line as a model of the circadian oscillator, previously engineered with a destabilized and nuclear-localized YFP circadian fluorescent reporter driven by the *Rev-Erbα* promoter (Nagoshi *et al*, 2004). *Rev-Erbα* is a direct target of the circadian activator complex CLOCK/BMAL1, and is thus maximally expressed at midday, or at the circadian time (CT) CT6 in mouse liver (Preitner *et al*, 2002; Rey *et al*, 2011).

To monitor individual cells, we designed large-scale time-lapse microscopy experiments, in which we optimized imaging conditions for reliable cell segmentation and cell tracking. Quantification of the YFP signal intensity in individual cell nuclei allowed us to monitor circadian phase and cell division events, marked by a characteristic and short (30–60 min) dip in signal intensity due to breakdown of the nuclear envelope (Fig 1A and Supplementary Fig S1). Across several conditions, these experiments collectively produced over 10,000 cell traces, totaling 20,000 circadian peaks and 13,000 cell divisions (Materials and Methods and Supplementary Movie S1). We chose as our default condition to monitor the system at steady state and thus used unstimulated cells to reduce possible transient effects. Recordings were acquired for 72 h at 30-min intervals under a variety of conditions.

We first considered cells grown at 37°C at several serum concentrations (in the range of 2–13% FCS), with the initial aim to probe a range of cell cycle durations. However, while serum concentration affected the fraction of mitotic cells, it had only a small effect on cell cycle duration (defined as the intervals between successive mitoses), and it showed no effect on the circadian period (Supplementary Fig S2A, B and D). The most prominent observation was that the two oscillators showed a clear signature of synchronization such that cell divisions occurred, on average, 5 h before the peak of circadian *Rev-Erbα*-YFP reporter expression, independently of serum concentration (Supplementary Fig S2C). For simplicity, we thus combined the datasets for all serum concentrations in our first analysis (Fig 1). An important property of circadian oscillations in individual cells is their inherent stochasticity, which yields successive peak-to-peak times in *Rev-Erbα*-YFP signals (hereafter referred to as circadian intervals) varying by about 10% around their mean (Nagoshi *et al*, 2004; Welsh *et al*, 2004; Rougemont & Naef, 2007). Similarly, cell cycle entry and progression through the cell cycle phases also exhibit stochasticity (Hahn *et al*, 2009). These fluctuations are clearly apparent in the timings

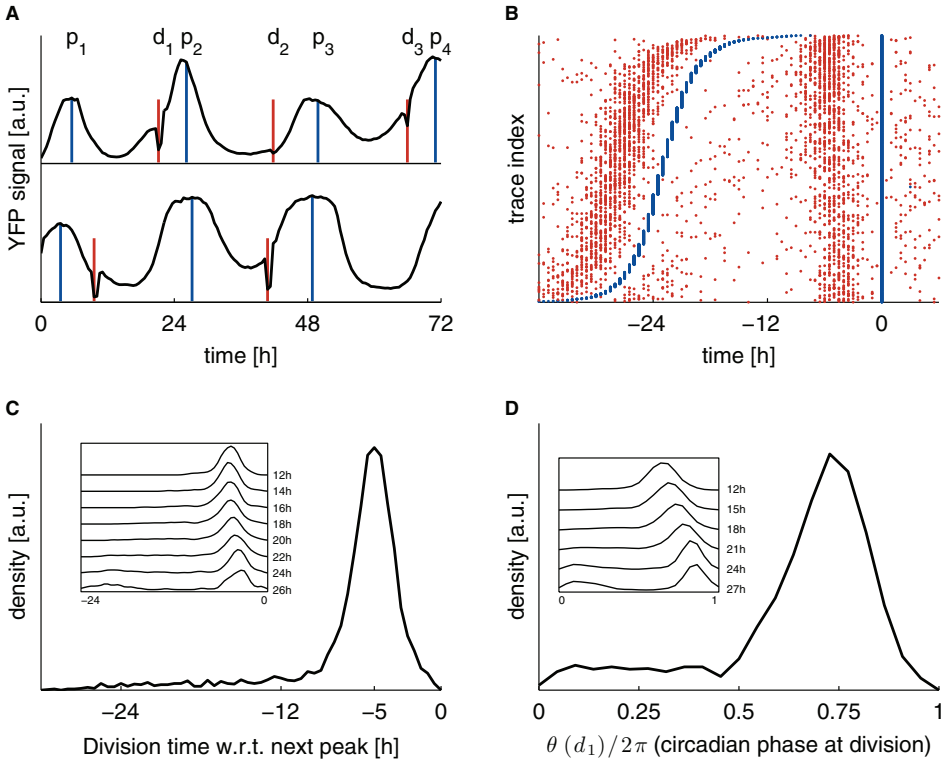

Figure 1. Circadian and cell cycle oscillators are tightly synchronized in NIH3T3 cells.

A Single-cell time traces showing the circadian YFP signal (black, identified maxima in blue denoted as p), together with cell division events (nuclear envelope breakdown, red, denoted as d). The top trace is typical and shows three divisions before the circadian peaks, the second trace shows an early first division.

B Raster plot showing 3,160 traces (with at least two circadian peaks) aligned on the second circadian peak (blue), and sorted according to the interval between the first and second circadian peaks. Divisions (red) show a clear tendency to occur, on average, 5 h before the circadian peaks. A sparse group of early division events associated usually with longer circadian intervals is also visible.

C Division times measured with respect to the subsequent circadian peak show a unimodal distribution centered at −5 h. Inset: longer circadian intervals correlate with mitosis occurring, on average, closer to the next peak (also visible in B).

D Circadian phases at division (normalized division times) show a unimodal distribution. Inset: longer circadian intervals correlate with mitosis occurring at later circadian phases.

of circadian peaks and cell divisions (Fig 1A and B). It is therefore remarkable that the intervals, denoted by (d,p), between divisions (d) and following circadian *Rev-Erbα*-YFP peaks (p) show a strongly peaked and unimodal distribution centered around -5 ± 2 h (Fig 1B and C). Moreover, it was apparent that longer circadian intervals tended to include divisions that occurred closer to the next circadian peak (Fig 1B and C). The variability of (d,p) intervals was significantly smaller than that of the intervals, denoted by (p,d), from the previous peaks to the divisions (Supplementary Fig S3A). As a consequence, (d,p) intervals were also less variable compared to the circadian phases at division (division times normalized to the enclosing circadian interval, also referred to as division phases, Fig 1D). Part of this variability came from the inclusion of circadian intervals of variable duration (due to the noise), with shorter circadian intervals associated with advanced division phases, and longer circadian intervals associated with delayed division phases (Fig 1D, inset).

The significant variability in each of the cycles clearly ruled out that this tight synchrony could reflect independently running, initially synchronized cycles. In fact, the synchrony of the circadian and cell cycles was equal for events in the first and second half of the recordings (Supplementary Fig S3B). Instead, the peaked and unimodal distribution must reflect the interaction of the two oscillators within each cell, resulting in a 1:1 mode-locked state. Furthermore, while the large majority of cells divided late in the circadian interval, a minority of cells, owing to the stochastic nature of the coupled system, divided early. This occurrence was more frequent for long circadian intervals (Fig 1A and B; see modeling below). Overall, the observed synchronization was highly robust to fluctuations. Indeed, the successive circadian intervals and cell cycle durations, measured on events (p_1,d_1,p_2,d_2) or (d_1,p_1,d_2,p_2), were highly correlated, although the individual circadian and cell cycle intervals varied by more than 30% (Supplementary Fig S3C, $R^2 = 0.52$, $n = 1{,}230$, $P < 10^{-16}$).

Thus, our data showed that circadian and cell cycles proceeded in tight synchrony in NIH3T3 cells. Translated to CT, taking the *Rev-Erbα*-YFP transcription peak as a reference (CT6), our divisions occurred near CT1, consistent with earlier observations

in mouse liver (Matsuo *et al*, 2003) and rodent epidermis (Brown, 1991). However, evidence of synchronization does not yet inform on the directionality of the interactions, as such a state could be established if either of the cycles entrained the other, or both.

The cell cycle influences circadian phase progression

To further investigate the directionality of the interactions, we first exploited the fact that stochastic exit from the cell cycle also produces circadian intervals in which no divisions occur between two successive circadian peaks. Comparing circadian intervals with division, denoted by (p_1,d_1,p_2), and those without divisions, (p_1,p_2), we observed a clear shortening of the circadian interval in the presence of divisions (Fig 2A). While circadian intervals without division (n = 2,748) lasted 23.7 ± 3.1 h, as expected for free-running circadian oscillators, the intervals with one division (n = 1,926) lasted 21.9 ± 3.8 h ($P < 10^{-16}$, t-test), which provides an unambiguous signature that cell cycle progression influences the circadian cycle. Also, these durations were nearly identical for events from the first and second half of the recordings, thus excluding the possibility that this correlation could have originated from temporal biases in the recordings (Supplementary Fig S4). Moreover, although the majority of cell division events occurred late in the circadian interval, the duration of the circadian interval varied depending on the circadian phase at cell division (Fig 2B, an alternative representation is shown in Supplementary Fig S5A), as already reported in cells stimulated with dexamethasone (Nagoshi *et al*, 2004). Indeed, the circadian intervals were shortest (18 h on average) when mitosis occurred about halfway into the interval, while being longest (27 h) for early divisions. To investigate this further, we estimated the instantaneous circadian phase from the *Rev-Erbα*-YFP signal using a hidden Markov model (Fig 2C, Materials and Methods). This showed that compared to circadian intervals without divisions, the circadian phase progression was distorted both for cells with early and later divisions (Fig 2C and D), thus providing further evidence of a directional interaction. Indeed, cells with early divisions showed a transient slowing down of the circadian phase progression after division, while cells dividing about halfway through the circadian interval showed a speedup near and following division (Fig 2D).

This finding naturally begged the question of whether the reverse interaction, by which the circadian cycle gates the cell cycle, was evident as well. Surprisingly, the characteristics of (d_1,p_1,d_2) events did not require such an interaction (compare Supplementary Fig S5A and B). Indeed, while (p_1,p_2) intervals negatively correlate with (p_2,d_1), (d_1,d_2) positively correlate with (p_1,d_1), and this positive correlation can be explained by assuming that (d_1,d_2) intervals and normalized peak times $(p_1–d_1)/(d_2–d_1)$ independently vary around their means, the latter being a consequence of the entrainment of the circadian cycle by the cell cycle. No similar argument can be made to explain the negative correlation in Supplementary Fig S5A. While this suggests that no gating mechanism needs to be invoked to explain the data, further quantitative arguments will be presented in the next section. Thus, while gating of cell division by the circadian cycle in mouse cells, established in the liver (Matsuo *et al*, 2003) and in primary fibroblasts (Kowalska *et al*, 2013), has attracted the most attention, our data suggest that the influence of the cell cycle on the circadian oscillator is predominant in NIH3T3 cells under standard culture conditions.

A stochastic model of two coupled phase oscillators shows the dominant influence of the cell cycle on the circadian oscillator

In order to characterize the possibly reciprocal interactions more rigorously, we implemented and calibrated a mathematical model describing two interacting, noisy cycles (Equation 1 in Materials and Methods). As previously done for circadian oscillations (Rougemont & Naef, 2007; d'Eysmond *et al*, 2013) and the coupled system (Yang *et al*, 2010), we describe the two cycles by noisy phase variables (θ for the circadian and ϕ for the cell cycles) that are subject, in the absence of influences from the other oscillator, to a mean frequency modulated by prescribed noise (phase diffusion). For non-dividing cells, this model thus accounts for variable circadian intervals (for example Fig 2A, black). In addition, to encompass the three scenarios of a circadian clock gating the cell cycle, of the cell cycle influencing the circadian clock, or both, we used generic forms for the coupling function in either direction, in which each phase could slowdown and/or speedup the other phase for some combinations of phases (Supplementary Fig S6; Materials and Methods). Briefly, a function $F_1(\theta, \phi)$ represents the influence of the cell cycle phase on the circadian phase, where positive regions of F_1 (in yellow, Supplementary Fig S6) accelerate the circadian phase, while negative ones (in blue) slow it down. Likewise, F_2 represents the action of the circadian clock on the cell cycle. In order to allow for different scenarios and to keep the model complexity manageable, we parameterized F_1 and F_2 as a mixture of two weighted two-dimensional Gaussians with arbitrary means and diagonal covariance matrices (represented as ellipses in Figs 3, 4 and 6, and Supplementary Fig S6).

To fit the model to data, we computed the likelihood of the time traces by decomposing the probability of a trace as a product of causally independent factors, and approximated the probabilities of these by numerical simulations (Materials and Methods). Parameters were then estimated by maximizing the total likelihood using a genetic optimization algorithm (Hansen & Ostermeier, 2001). We used simulations to validate our fitting and assess identifiability of the parameters (Supplementary Information), which showed that the model was able to predict the directionality of the coupling and recovered the prominent features of the coupling functions.

We applied this method first to the 37°C dataset (Fig 3). The best-fit model was able to reproduce the data accurately (estimated parameters in Supplementary Tables M1–M5), as indicated by comparing data and best fit for several features: the distributions of circadian intervals, those of cell cycle durations, those of the intervals from divisions to the next circadian peaks, and those of the interval between the previous peaks and the divisions (Supplementary Fig S7). In particular, the model was able to capture the later division time observed in longer circadian intervals (Fig 3A and B). The most important features of the model are the coupling functions F_1 and F_2. Strikingly, the best-fit model predicted an acceleration of the circadian phase right around or slightly after division as the strongest interaction, when the circadian phase just passed its trough, and a weaker slowdown earlier in the circadian cycle (Fig 3C). On the contrary, the effects of the

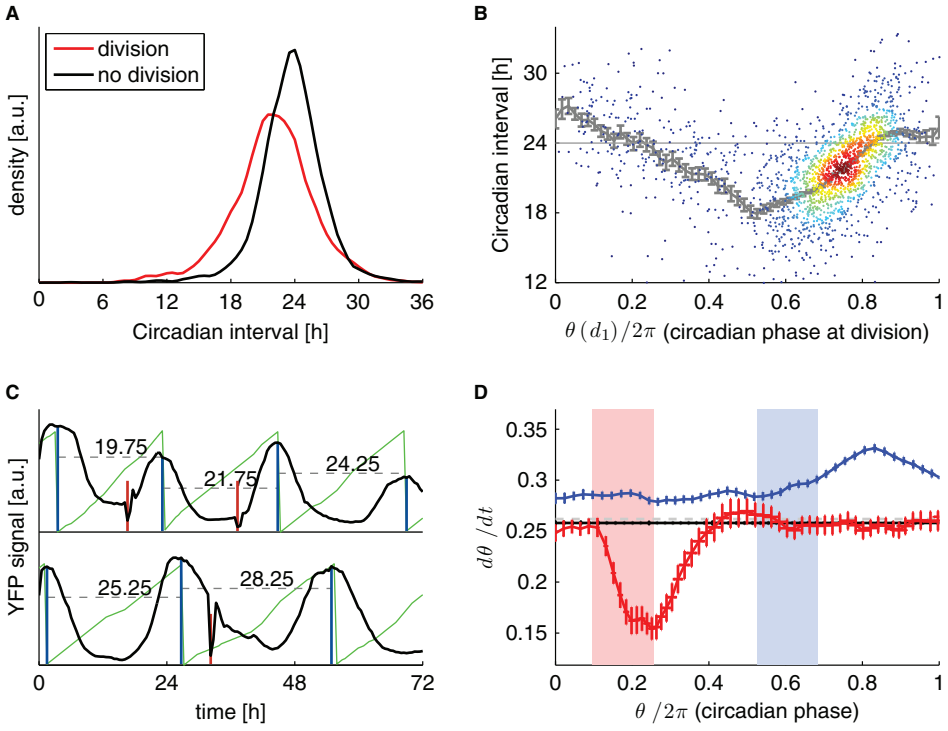

Figure 2. The cell cycle influences circadian phase progression.

A Circadian intervals with divisions (p_1,d_1,p_2) last 21.95 ± 3.8 h (n = 1,926) and are significantly shorter ($P < 10^{-16}$, t-test) compared to circadian intervals with no divisions (p_1, p_2) lasting 23.7 ± 3.1 h (n = 2,748).

B Duration of circadian interval as a function of circadian phase (θ) at division. The latter is estimated from interpolating between the two maxima. Running mean and standard errors are indicated in gray.

C Estimation of the instantaneous circadian phase from the wave forms using a hidden Markov model (Supplementary Information). The instantaneous phase (thin green lines, zero phase is defined as the maximum of the waveform) shows a distortion when comparing short circadian intervals (top trace) with longer ones. Note also the slowdown of the phase progression after an early division (shown in red, bottom).

D Instantaneous circadian phase velocity as a function of the circadian phase for intervals without divisions (black) shows that in cells with early divisions (within the pink interval, n = 103), the circadian phase progression is slowed down around and after the division (red), compared to circadian intervals with no divisions (n = 2,748, horizontal black line). In contrast, cells with late divisions within the light blue interval (n = 234) show a globally shifted velocity and a speedup in circadian phase progression after and around the division (blue). Standard error of the mean for the instantaneous frequency at each time is indicated. For better visualization, the three velocity profiles are normalized (centered) by the nearly flat velocity profile (not shown) in division-free intervals. The gray line corresponds to 2π/24.

circadian cycle on the cell cycle were much weaker. The resulting (deterministic) phase portrait shows an attracting 1:1 mode-locked state (Fig 3C), and the tendency of stochastic trajectories to cluster in the phase space according to circadian intervals (Fig 3D) explains the observed shift in division times (Fig 1D). To explore the possibility of multiple solutions among local maxima, we ran multiple optimizations with different initial conditions (parameters obtained in Supplementary Table M1). The obtained solutions indicated that the acceleration of the circadian phase close to mitosis was a robust property, while slowdown was found in some solutions and its location in the phase plane was more variable (Fig 3E). Note that these two effects were consistent with the slowing down and acceleration of circadian phase progression discussed using the instantaneous phase estimation (Fig 2C and D). Finally, while a few solutions indicated that the circadian cycle influenced cell cycle progression, the location of this gating in phase space was not consistent (Fig 3F).

As an alternative and model-independent method to deduce causal relationships among the circadian and cell cycle oscillators, we applied the Granger causality test (Granger, 1969). We used the property that nuclear size conveys information on cell cycle progression in mammalian cells (Fidorra *et al*, 1981), which we validated from time-lapse recordings in HeLa cells (Sakaue-Sawano *et al*, 2008) (Supplementary Information). We then tested whether nuclear size Granger caused the circadian *Rev-Erbα*-YFP signal, and vice versa, and found that a much larger proportion of cells (up to 60%) showed evidence ($P < 0.001$, Granger-Wald test) for a causal influence of cell cycle progression on the circadian signal, compared to the reverse interaction (< 20%) (Supplementary Fig S8). Counting only cases where the evidence was stronger in one direction compared to the other gave 55 and 12%, respectively. Altogether, our quantitative modeling of the time traces strongly suggested that the influence of the cell cycle on the circadian cycle was the dominant effect in our recordings.

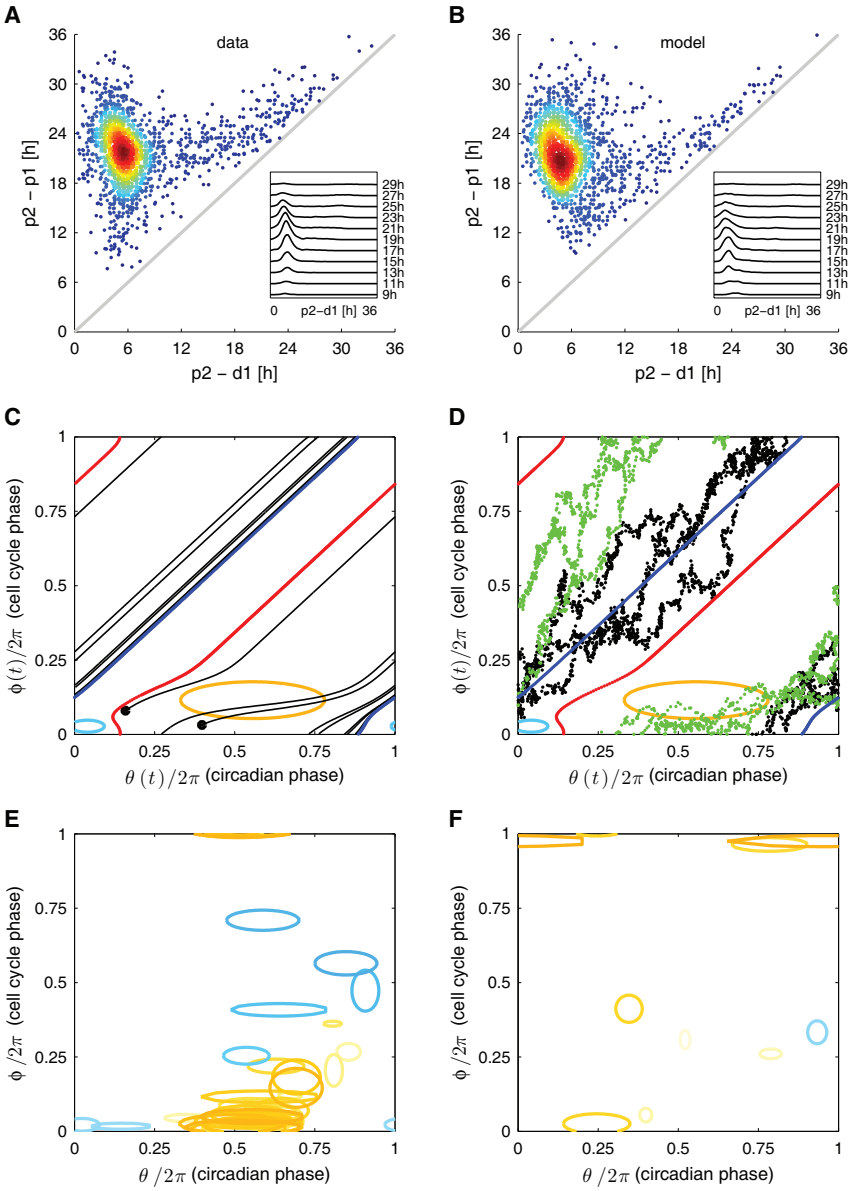

Figure 3. A stochastic model of two coupled-phase oscillators shows that the influence of the cell cycle on the circadian oscillator is predominant.

A, B Data versus model. Circadian intervals with divisions (p_1,d_1,p_2) as a function of the shorter subinterval (d_1,p_2) from the data (A) and well reproduced by the fit (B). Outliers represent a minority of cells dividing early in the circadian cycle, and the tendency of cells to divide nearer the peak for long intervals is also reproduced.

C A generic stochastic model of two interacting phases (θ: circadian phase, θ = 0 is the circadian *Rev-Erbα*-YFP peak; ϕ: cell cycle phase, ϕ = 0 at mitosis) is fit to data, giving an estimate for the coupling functions. Phase portrait (noise terms set to zero) of the best-fit solution shows 1:1 mode locking. The blue (red) curves represent the attractor (repeller), and the black lines are representative trajectories (initial conditions shown as black dots). Regions inside the ellipses represent the influence of the cell cycle on circadian phase: significant speedup of the circadian phase occurs close to, or shortly after, cell division (yellow), while slowdown occurs for earlier circadian phases (light blue). The contours correspond to |K1*G1| or |K2*G1| = 2 [rad/h], and the reverse couplings (K3 and K4) are not shown since they are very small. Estimated parameters are given in Supplementary Tables M1–M5.

D Stochastic simulations explain why longer circadian intervals coincide with later divisions (Figs 1D and 2B). Trajectories with long circadian intervals (black) divide late in the circadian cycle and thus tend to have short (d,p) intervals. Trajectories with short circadian intervals (green) tend to divide early in the circadian cycle and tend to have longer (d,p) intervals.

E Coupling functions obtained describing the influence of the cell cycle phase on the circadian phase for 36 independent optimizations show consistency in the location of the acceleration of circadian phase due to the cell cycle (orange), while the slowdown is more variable and weaker in magnitude (light blue). Here 29 (7) out of 42 (30) positive (negative) Gaussians with values above 2 [rad/h] are plotted.

F Coupling functions describing the influence of the circadian phase on the cell cycle are smaller and not consistently located in phase space. Here 7 (1) out of 38 (34) positive (negative) Gaussians with values above 2 [rad/h] are plotted.

Changing temperature affects cell cycle duration and shortens circadian intervals in dividing cells, but does not disrupt synchronization

The above modeling predicts that modifying cell cycle duration should influence circadian intervals. To test this, we exploited the fact that the circadian oscillator in NIH3T3 cells is temperature compensated (Tsuchiya *et al*, 2003), while the cell cycle duration is not (Watanabe & Okada, 1967; Yeom *et al*, 2010). We thus repeated the experiment at both lower (34°C) and higher (40°C) temperatures, which indeed shifted the mean cell cycle duration by 6 h, from 24.5 ± 4.4 h at 34°C to 18.1 ± 3.5 h at 40°C (Fig 4A). As expected, the circadian intervals (p_1,p_2) without divisions were effectively temperature compensated, in fact slightly overcompensated ($Q_{10} = 0.93$) but less so than reported in population experiments (Tsuchiya *et al*, 2003) (Fig 4B). But importantly, circadian intervals encompassing cell divisions gradually shortened with increasing temperature, thus confirming the prediction (Fig 4B). Interestingly, this means that temperature compensation is less effective in dividing NIH3T3 cells (here $Q_{10} = 1.36$ for intervals with divisions), and in general, temperature compensation will depend on the proliferation status of the cells. Despite these significant changes in cell cycle duration, the synchronization of the two cycles remained tight, showing a virtually indistinguishable distribution of intervals from division to the next peak (d,p) at the three temperatures (Fig 4C). Since the duration of the full intervals (p_1,d_1,p_2) decreased with temperature, the divisions occurred at significantly advanced circadian phases at 40°C (Fig 4D). While we might have expected that the increased period mismatch between the circadian oscillator and the cell cycle at the highest temperature could have either disrupted synchrony or revealed mode-locking different from the 1:1 state (Glass, 2001), as in the case of cyanobacteria (Yang *et al*, 2010), we found that 1:1 locking was resilient to these changes. Moreover, the phase advance in the divisions at 40°C is consistent with the increased period mismatch, as this is a generic property of phase responses in entrained oscillators (Granada *et al*, 2013).

To assess whether our model was able to match the data at these three temperatures, we recalibrated the model to all temperatures jointly (using a single likelihood function), keeping all parameters common except for the cell cycle frequency, which was allowed to take independent values. We also reasoned that fitting more data jointly would help identify the coupling functions better. This constrained model matched the data well (Fig 4A, C and D, and Supplementary Fig S9), and the predicted shared coupling functions were qualitatively similar to the ones obtained with a single temperature (Fig 4E and F, Supplementary Tables M2–M5). The main differences were that the slowing down of circadian phase was more consistently placed toward the center of the phase plane (Fig 4E) and the weak influence of the circadian cycle on cell division seemed to be predominantly negative, as would be predicted by a gating mechanism. Therefore, our extended temperature dataset could be captured well by a model in which only the cell cycle duration was affected. Moreover, the accelerating influence of the cell cycle on the circadian phase was strong enough to maintain 1:1 mode-locking despite the period mismatch.

Inhibition of the cell cycle lengthens circadian intervals and delays division phase

In order to complement the temperature experiments with more direct interventions on the cell cycle, we monitored cells at 37°C in the presence of inhibitors of CDK2, affecting G1/S transitions and CDK1, affecting G2/M transitions. Increasing concentration of the CDK2 inhibitor, NU-6102, did not change the duration of division-free (p_1,p_2) intervals. However, it progressively increased the duration of (p_1,d_1,p_2) intervals from about 22 h as in the unperturbed condition (Fig 2A) to the same duration as (p_1,p_2) intervals (Fig 5A), concomitantly with an expected lengthening of the cell cycle duration (Fig 5B). Interestingly, the highest concentration (10 μM) produced significantly delayed division phases compared to the lowest concentration (1 μM) (Fig 5C). Invoking the same argument as in the 40°C temperature experiment, this delay is now consistent with a reduction of period mismatch at the higher dose. Though it was overall more difficult to record cells for 3 days under the CDK1 inhibitor, RO-3306, presumably due to higher toxicity and arrest in G2, the results were overall very similar with those of the CDK2 inhibitor, including progressive lengthening of (p_1,d_1,p_2) intervals of the cell cycle duration (Fig 5D and E), and significantly phase-delayed divisions (Fig 5F). Thus, interfering with cell cycle progression at two different checkpoints confirmed that cell cycle progression has a clear and predictable influence on the duration of circadian intervals and circadian phases at division.

Cry2-deficient cells with longer circadian periods do not affect the cell cycle but shift divisions

We next aimed at testing conditions in which the circadian cycle was perturbed and first opted for a genetic approach. To this end, we engineered NIH3T3-Rev-VNP1 lines stably expressing a validated shRNA targeting the *Cry2* transcript (Moffat *et al*, 2006), a condition that lengthens circadian period by a few hours (Thresher *et al*, 1998; van der Horst *et al*, 1999; Maier *et al*, 2009; Zhang *et al*, 2009). This produced the expected perturbation on the circadian oscillator (mean period of 26.3 h) but did not affect cell cycle duration (Supplementary Fig S10A, B and E), confirming that the circadian cycle did not have a strong influence on the cell cycle. However, the circadian intervals with divisions were still significantly shorter than those without divisions (Supplementary Fig S10E). In addition, the distribution of both (d,p) intervals and division phases, while still unimodal, showed a modest but significant enrichment of advanced divisions (Supplementary Fig S10C and D), again consistent with the predicted phase advance from an increased period mismatch. Thus, these *Cry2* knockdown experiments are fully consistent with the predictions of unidirectional coupling from the cell cycle onto the circadian cycle. Moreover, these data indicate that CRY2 protein is dispensable for the underlying coupling mechanism.

Treatment with Longdaysin lengthens circadian intervals and cell cycle duration but preserves synchronization

To further probe a condition of longer circadian period, we repeated the experiments at 37°C after treating cells with Longdaysin. This

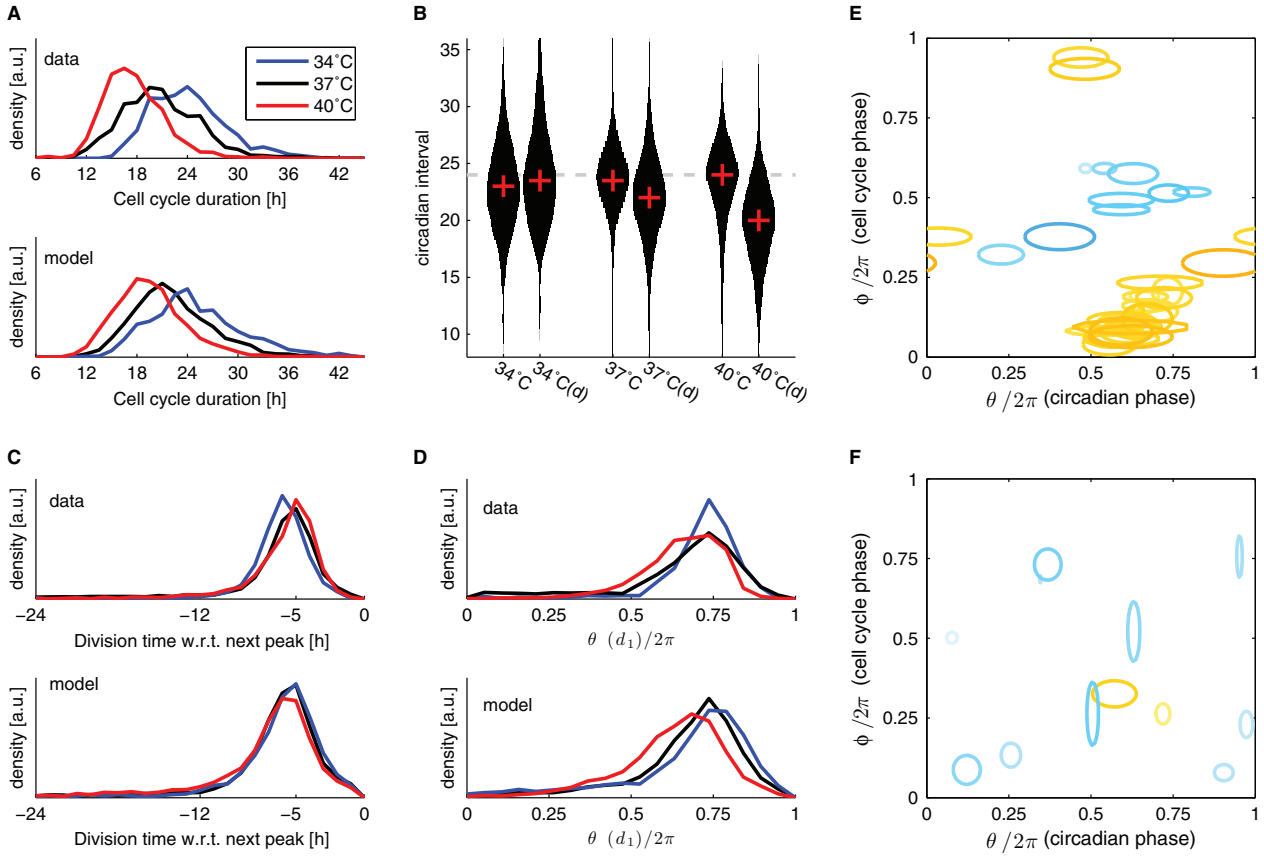

Figure 4. Changing temperature affects cell cycle duration and shortens circadian intervals only in dividing cells.

A The cell cycle duration (interval between divisions) scales with temperature.

B Circadian intervals are temperature compensated (slight overcompensation, Q_{10} = 0.9) in the absence of division (columns labeled 34, 37 and 40°C), and decrease with increasing temperature in presence of divisions (columns labeled 34, 37 and 40°C (d)). Width of the black areas indicates density of traces (histograms); the crosses indicate the median.

C Division times with respect to the next peak are not affected by temperature: divisions occur, on average, 5 h before the circadian YFP peaks at all temperatures.

D Circadian phases at division (normalized division times) show unimodal distributions at all temperatures. Division phases at 40°C are significantly phase advanced compared to 37°C ($P < 10^{-7}$, Kolmogorov–Smirnov test, K–S). Division phases at 34°C show a small but significant ($P < 10^{-9}$, K–S test) phase delay compared to 37°C.

E, F Fitting data from all three temperatures together: only the intrinsic periods of the cell cycle were allowed to change, coupling parameters were shared among the three temperatures (obtained parameters are summarized in Supplementary Table M1). (E) Coupling functions obtained describing the influence of the cell cycle phase onto the circadian phase for 38 independent optimizations show consistency in the location of the acceleration of circadian phase due to the cell cycle (orange), while the slowdown (light blue) is more variable and weaker in magnitude. The contours are as in Fig 3. Here 27 (9) out of 41 (35) positive (negative) Gaussians with values above 2 [rad/h] are plotted. (F) Coupling functions describing the influence of the circadian phase onto the cell cycle are small (only 12 out of the 76 Gaussians are above threshold) and not consistently located in phase space. Here 2 (10) out of 4 (72) positive (negative) Gaussians with values above 2 [rad/h] are plotted.

Data information: The dataset included n = 1,139 cell traces at 34°C, n = 4,207 at 37°C, and n = 1,374 at 40°C.

compound lengthens the circadian period in a dose-dependent manner through inhibition of CK1δ (Hirota *et al*, 2010), a well-known regulator of circadian period that acts by controlling the stability of PER proteins (Etchegaray *et al*, 2009). However, Longdaysin is also known to inhibit additional kinases (Hirota *et al*, 2010), of which in particular ERK2 has been noted for its role in cell cycle progression at several checkpoints in NIH3T3 (Wright *et al*, 1999) and other cells (Chambard *et al*, 2007). Our data showed that compared to control, the circadian period without divisions (p_1,p_2) progressively increased from 24 h to nearly 32 h with increasing Longdaysin concentration (Fig 6A). As in previous conditions, (p_1,d_1,p_2), intervals were systematically shorter compared to (p_1,p_2) intervals at all Longdaysin concentrations. Instantaneous phase analysis showed that the circadian phase progression in treated cells was slowed down in the interval of low *Rev-Erbα*-YFP expression in a dose-dependent manner, consistent with the destabilizing effect on PER proteins of CK1δ inhibition (Etchegaray *et al*, 2009) (Supplementary Fig S11). However, the cell cycle duration also significantly increased in a dose-dependent manner. While this could in principle reflect gating of the cell cycle by the circadian clock, which our

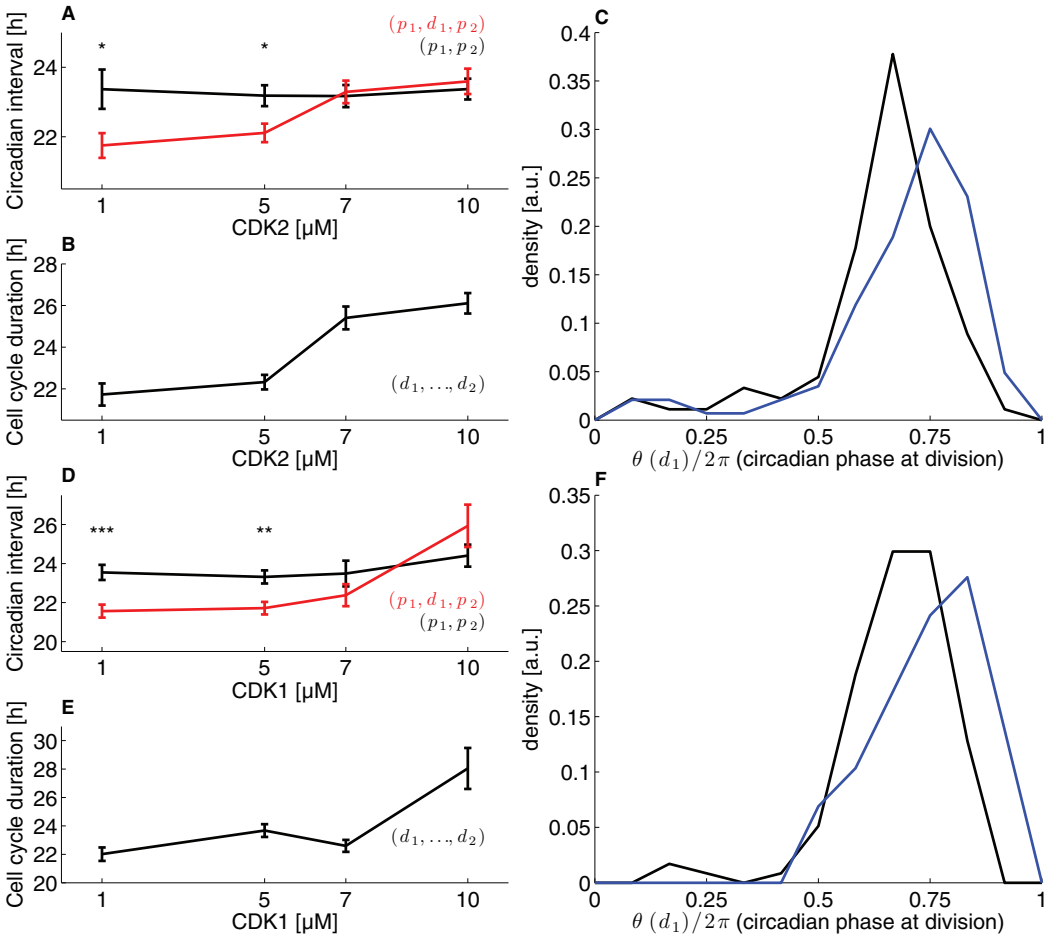

Figure 5. Inhibition of the cell cycle lengthens circadian intervals and delays division phase.

A Mean circadian intervals as a function of CDK2 inhibitor concentration for intervals with division (red) and without (black) show that intervals with division lengthen as the cell cycle duration lengthen. The error bars show the standard error on the mean.

B Mean cell cycle duration as a function of CDK2 inhibitor concentration.

C The distribution of normalized division times (circadian phase at division) at 1 μM CDK2 inhibitor (black) and 10 μM (blue) shows a significant shift ($P < 1.2 \times 10^{-5}$, K–S test) toward later phases.

D As in (A) for the CDK1 inhibitor.

E As in (B) for the CDK1 inhibitor.

F As in (C) for the CDK1 inhibitor ($P < 0.003$, K–S test).

Data information: In (A) and (D), significant difference between (p_1,p_2) and (p_1,d_1,p_2) intervals is indicated (*$P < 0.05$; **$P < 0.01$; ***$P < 0.001$, *t*-tests). The dataset included $n = 812$ cells traces for the CDK2 and $n = 711$ for the CDK1 inhibitors, nearly equally distributed across concentrations.

analysis had not revealed so far, we deemed a direct effect of Longdaysin on cell cycle progression the more likely scenario (Wright *et al*, 1999; Chambard *et al*, 2007).

Using cell counting, we indeed confirmed that Longdaysin treatment reduced the proliferation of NIH3T3-Venus cells, as well as of HeLa cells, which are devoid of circadian oscillators. These experiments thus suggested that the cell cycle period increase observed under Longdaysin treatment did not reflect gating (Supplementary Fig S12) and that Longdaysin rather induced a condition in which both the intrinsic circadian and cell cycle periods were lengthened. Remarkably, the interval lengths from divisions to circadian peaks were sharply peaked at all Longdaysin concentrations and indistinguishable from the control condition (Fig 6B), even though the overall variability in circadian interval had nearly doubled (Fig 6A, inset). The only difference was that upon treatment, a small proportion of cells divided early in the circadian interval (Fig 6C), indicating that the 1:1 state might start to be destabilized at the highest Longdaysin concentration.

Finally, we applied our modeling to all concentrations independently. While indeed the model predicted that both circadian period and cell cycle duration were lengthened in a dose-dependent manner (Supplementary Table M1), the estimated coupling functions were

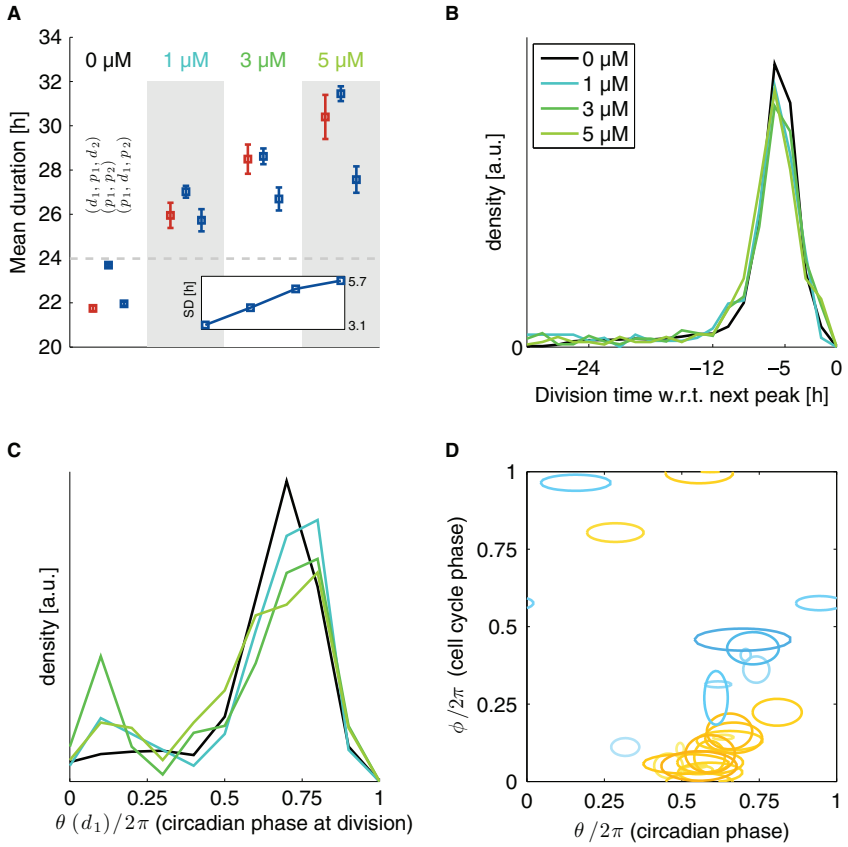

Figure 6. Treatment with Longdaysin lengthens circadian intervals and cell cycle durations but does not disrupt synchronization.

A Dose dependency of cell cycle durations (d_1,p_1,d_2), circadian intervals without division (p_1,p_2) and circadian intervals with divisions (p_1,d_1,p_2). Inset: dose dependency of the standard deviation (SD) of circadian intervals (p_1,p_2).

B Temporal synchronization of the two cycles is equally tight at all Longdaysin concentrations and indistinguishable from the control condition.

C Normalized division times (circadian phase at division) show that Longdaysin-treated cells have more early divisions compared to control.

D Coupling function estimated from the stochastic model (n = 31 independent optimizations) for 1,3 and 5 μM Longdaysin is similar to ones obtained in control (Fig 3). Models for all concentrations are fit independently (obtained parameters are summarized in Supplementary Table M3). Contours are as in Figs 3 and 4. Here 17 (9) out of 35 (27) positive (negative) Gaussians with values above 2 [rad/h] are plotted.

Data information: the dataset included n = 1,435 cells traces nearly equally distributed across concentrations.

similar to the ones obtained in controls, again confirming the absence of clear signs of cell cycle gating by the circadian clock (Fig 6D). Furthermore, rescaling the period parameters of the models obtained for 37°C to match the observed periods in Fig 6A, while keeping other parameters (noise and coupling) fixed, was sufficient to obtain good agreement with the 5 μM Longdaysin data (mean log-likelihood of -2800 ± 50 for rescaled solutions versus -2700 ± 16 for best-fit solutions directly fitted on the Longdaysin dataset, and -4800 ± 760 for original, non-rescaled solutions). Longdaysin decreased the intrinsic frequencies of the two oscillators by a similar factor, but the coupling and noise parameters remained largely unaffected (Supplementary Table M1). After rescaling the frequencies, we obtained an effective phase model (Equation 1, Materials and Methods) in which both coupling and noise became stronger with increasing Longdayin concentrations. This might explain why synchrony was only mildly affected despite significantly increased variability of circadian intervals. Taken together, these results are consistent with a model in which the cell cycle and the circadian clock are coupled phase oscillators, with a coupling that is predominantly from the cell cycle to the circadian clock.

Circadian phase resetting does not influence cell divisions but transiently perturbs synchronization of circadian and cell cycles

Finally, to complement the long-lasting genetic and pharmacological perturbations of the circadian oscillator, we decided to use an approach that is much less invasive. To this end, we transiently perturbed the circadian phases using established phase resetting protocols that are based on brief treatment with dexamethasone and forskolin. While both treatments showed the expected alignment of circadian phases (Fig 7A and Supplementary Fig S13), the timing of cell divisions appeared mostly random and unaffected by the treatment (Fig 7A), indicating that this condition allowed transient uncoupling of the circadian and cell cycles. Remarkably, sorting of

the recorded cell traces according to the first division revealed that subsequent (second) circadian *Rev-Erbα*-YFP peaks tightly followed division by the usual 5 h, while cells without divisions (on the top, above the thin lines) remained aligned with the treatment (Fig 7A). We used different synchronization indices (order parameters, Supplementary Information) to quantify the differences of dexamethasone-treated and control cells as functions of time. This confirmed that circadian cycles were synchronized by the treatment, and this synchrony gradually decayed over the recording time (Fig 7B). Meanwhile, the synchronization of the cell cycle was low throughout the recordings (Fig 7C). However, the relative synchronization of the circadian and cell cycles in the treated cells, while showing a marked reduction at the beginning of the recording, eventually relaxed to identical levels as for the untreated cells after about 40 h (Fig 7D). Thus, by acutely perturbing the circadian but not the cell cycle phases, this minimally invasive perturbation of the circadian clock provided a condition in which the synchronization of the two cycles was transiently disrupted. This confirms that the circadian oscillator does not strongly influence cell division, while cell divisions determine the timing of the consequent circadian peaks.

Discussion

Effects of cell cycle progression on circadian oscillators

Circadian and cell cycle oscillators in individual cells and tissues provide a system in which two fundamental periodic processes may reciprocally influence each other. A number of important cell cycle regulators display 24-h rhythms in expression levels or activity that are aligned with the circadian cycle (Ueda *et al*, 2002; Miller *et al*, 2007; Gréchez-Cassiau *et al*, 2008). Molecular investigations showed that the circadian clock controls cell cycle progression both at the G1/S (Geyfman *et al*, 2012; Kowalska *et al*, 2013) and at G2/M (Matsuo *et al*, 2003; Hong *et al*, 2014) transitions, a phenomenon referred to as circadian gating of the cell cycle. On the other hand, cell cycle progression imposes rather drastic temporal changes notably on the level of transcription, which increases following replication (Zopf *et al*, 2013) and shuts down during chromosome condensation (Gottesfeld & Forbes, 1997), or via partitioning of cellular content during mitosis. Since the circadian oscillator in individual cells is highly sensitive to perturbations, as revealed through phase-shifting experiments (Nagoshi *et al*, 2004; Pulivarthy *et al*, 2007), it was natural to expect that the cell cycle could influence the circadian oscillator. It was reported previously that the time of mitosis correlates with local circadian period (Nagoshi *et al*, 2004) but also that cell proliferation reduces the coherence of circadian cycles in cell populations (O'Neill & Hastings, 2008). Here, we performed a large-scale quantitative analysis of single NIH3T3 cells carrying a fluorescent circadian phase marker under various experimental conditions, including altered growth conditions (serum and temperature), as well as genetic and pharmacological perturbations. A main result was that under steady-state free-running conditions (no entrainment), the coupled oscillators tick in a 1:1 mode-locked state that is highly resilient to perturbations, with divisions consistently occurring 5 h before the *Rev-Erbα*-YFP peak, and circadian phases at division shifting according to period mismatches in the different conditions, reminiscent of generic properties of forced oscillators. Moreover, our modeling showed that the influence of the cell cycle on circadian phase progression quantitatively accounted for the observed mode-locking. Although this finding did not completely exclude that a circadian gating of the cell cycle occurred as well, this effect was clearly subordinate to the much stronger reciprocal interaction described above. In our data, dividing cells thus showed circadian periods that were systematically shorter by several hours, as compared to non-dividing cells (Fig 2). Conceivably, this property may also depend on the model organism or cell types. However, irrespective of possible cell type-specific variations, our findings may have important consequences for downstream circadian functions in proliferating tissues *in vivo*, and also for population measurements in cellular assays, in which circadian period is often used as a phenotype. Interestingly, a genome-wide siRNA screen in U2OS cells identified cell cycle regulators as an enriched functional category affecting circadian period (Zhang *et al*, 2009).

Possible mechanisms mediating influence of the cell cycle on circadian phase

Cell cycle progression could influence the circadian oscillator by a number of plausible mechanisms, but for the moment we can only speculate why cell divisions lead to shortened circadian intervals. Most divisions occur at the equivalent of CT1, toward the end of the low *Rev-Erbα*-YFP expression phase, when the *Rev-Erbα* promoter, activated by the BMAL1/CLOCK complex, is still in a repressed state due to nuclear CRY1 proteins bound to BMAL1/CLOCK on the DNA (Stratmann *et al*, 2010; Ye *et al*, 2011). It is thus conceivable that mitosis, by diluting (Nagoshi *et al*, 2004) or relocating CRY proteins, contributes to derepressing the *Rev-Erbα* promoter more rapidly, such that cells dividing in a CRY-repressed state would be able to initiate a new round of BMAL1/CLOCK activity more rapidly than cells that did not divide. Consistent with this scenario, our modeling found that the acceleration of the circadian phase predominantly took place just after the division (Figs 3E, 4E and 5D). Of note, due to potential inaccuracies in the instantaneous phase estimates, it is not entirely excluded that the acceleration of the circadian phase could be due to an earlier event in the cell cycle, such as during late G2, where transcription rates are higher due to double DNA content (Zopf *et al*, 2013). Concerning molecular players involved, since *Cry2*-depleted cells only showed a modest but predictable tendency toward advanced division phases, though statistically significant, we conclude that CRY2 is not a key player in mediating this coupling. Moreover, as suggested (Nagoshi *et al*, 2004), the slowdown of the circadian phase progression following early divisions (Fig 2D) could also be explained by the dilution argument, since the accumulation of the state variables PER and CRY (Travnickova-Bendova *et al*, 2002), then in their production phase, would be delayed.

Dynamics of two coupled oscillators

Coupled oscillators are not only of great biological interest, but also very interesting from a dynamical systems standpoint. The noise-free (deterministic) dynamical behavior originating from two coupled phase variables representing the state of each oscillator is strongly constrained (since two trajectories cannot cross). Solutions therefore show either irregular (quasiperiodic) behavior

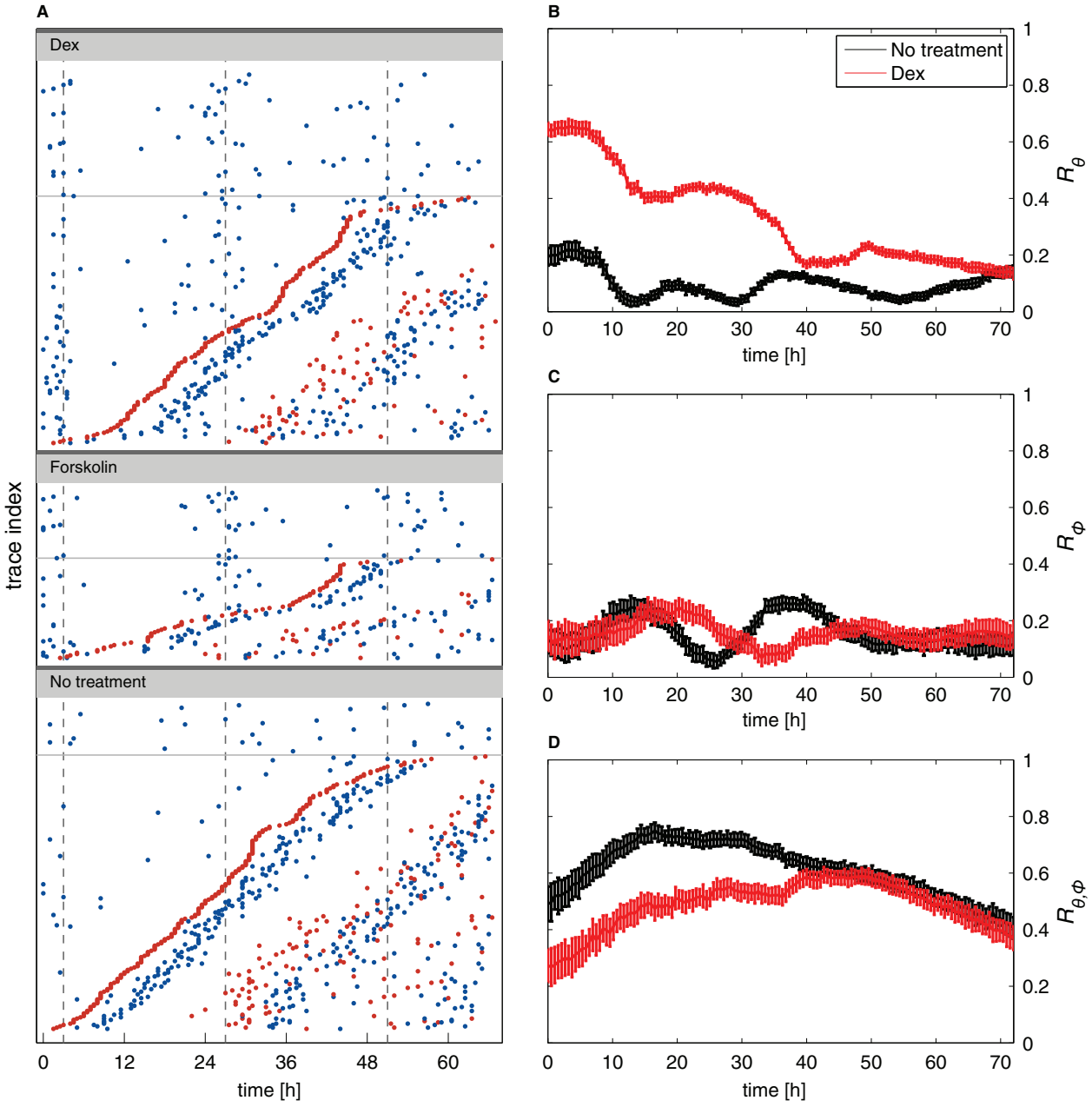

Figure 7. Circadian phase resetting does not influence the cell cycle and transiently perturbs synchronization of circadian and cell cycles.

A Raster plots (each line is a cell trace) for cells treated with dexamethasone (Dex), forskolin, and untreated controls. Circadian peaks are in blue and division in red. Traces without division are in the upper parts of the panels above the thin lines. For cells with divisions, traces are sorted from bottom to top according to the time of the first division. This shows that cell divisions occur uniformly and are not affected by the phase resetting and that the second circadian peaks follow division after both dexamethasone and forskolin.

B–D Synchronization indices over time in dexamethasone-treated cells (red) and controls (black). A value of zero for an index coincides with fully random phases while a value of 1 describes perfect synchronization. The circadian synchronization index R_θ (B) is initially much higher in dex-treated cells, as expected. Synchrony rapidly decays due to divisions (as visible in A, non-dividing cells clearly stay more synchronized). The cell cycle synchronization index (C) $R\phi$ is low throughout the recordings, indicating that dexamethasone treatment, and thus circadian phase synchronization, does not synchronize the cell cycle (also visible in A since the first divisions do not line up vertically). The synchronization index $R_{\theta}\phi$ (D) measuring synchronization of the circadian and cell cycles indicates that dexamethasone treatment transiently reduces synchrony of the two cycles. The initial increase ($t < 15$ h) in both conditions mostly reflects larger uncertainties in the estimated phases for early times (Supplementary Information). Error bars indicate standard deviations.

corresponding to an unsynchronized state or the two phases proceed in synchrony, such that the system exhibits mode-locking. Mode-locked states are characterized by a winding number *p:q*, specifying that *p* cell cycles complete during *q* circadian cycles (Glass, 2001). Changing parameters such as the individual frequencies of the cycles or the coupling functions can drive the systems from one state to another, resulting in qualitatively distinct outcomes. For examples, two cell divisions may occur every circadian cycle (2:1) instead of one (1:1) as described in cyanobacteria (Yang *et al*, 2010). It was suggested that the multimodal distribution of division times found in NIH3T3 cells synchronized by dexamethasone (Nagoshi *et al*, 2004) may be explained by more complex (with higher *p* and *q* integers) mode-locked solutions (Zámborszky *et al*, 2007). Since molecular oscillators are subject to noise, the deterministic scenario is blurred; nevertheless, qualitative differences reminiscent of the different synchronization states remain. The observed stochastic 1:1 mode-locked state still leads to a unimodal distribution of division times, while reduced synchrony generates a significantly broader distribution and other (*p:q*) states produce multimodal distributions (Yang *et al*, 2010). The fact that, by and large, we did not observe such states even under strongly perturbed conditions, for example in the Longdaysin-treated cells, indicates that this synchrony is highly robust over a range of conditions, presumably because it confers selective advantage.

While we have addressed the problem of possible couplings in rather general terms using our inference method (Fig 3), the net dynamical mechanism leading to synchronization is relatively simple: since the cell cycle duration was mostly shorter than the circadian period in the conditions probed, synchrony resulted from the transient acceleration of the circadian phase around mitosis, leading to a stably attracting synchronized state (the attractor) in the coupled system. In fact, our data (in particular Figs 2B, D and 7) point to a scenario in which cell divisions, when occurring after a critical circadian phase (which we can tentatively assign to the nuclear entry of the PER and CRY repressors), act as a strong resetting of the circadian cycle (via derepression of the *Rev-Erbα* promoter). This then produces the tight 5-h delay of the *Rev-Erbα* peak and explains the positive slope of circadian intervals versus division phase for late dividing cells (Fig 2B). As already mentioned, this scenario would also explain why circadian intervals are lengthened when divisions occur early (Fig 2B), since a dilution of the repressors in their accumulation phase would then delay reaching of the critical phase. Note that this stochastic effect is added on top of the deterministic shifting of the peak in division phases as a function of period mismatch, observed in the temperature, the shCry2, and cell cycle inhibition experiments.

While we predominantly detected signature of the influence of the cell cycle on circadian phase progression across all conditions, we note that the Granger causality test detected at most 12% of cells that favored the reverse interaction of the circadian cycle onto the cell cycle (Supplementary Fig S8). There are several reasons why our experiments might not reveal clearer evidence for circadian gating of the cell cycle. This could originate as an experimental limitation since the circadian and cell cycle phases were observed only at certain snapshots. However, simulations suggested that this is not a severe limitation since noise actually renders the coupling functions identifiable to a reasonable extent, provided that the regions of interactions are located in a region of phase space that is explored by the noisy dynamics under the conditions probed (Supplementary Information). Also, it is possible that biologically possible interactions are in effect inactive in certain conditions. This would typically be the case when the attractor does not intersect the regions in phase space where gating is effective. Finally, it is quite possible that gating is simply not strongly active in NIH3T3 cells, as suggested for other cell types including cancer cells (Pendergast *et al*, 2010; Yeom *et al*, 2010).

Circadian oscillator and cell cycle in cyanobacteria

In cyanobacteria, it was reported in population studies (Mori *et al*, 1996) and single cells (Yang *et al*, 2010) that the circadian cycle can gate cell division. Time-lapse microscopy combined with mathematical modeling was thus able to show that the cell cycle is synchronized by the circadian clock, and that increased rates of cell division engender a system transition from a 1:1 to a 2:1 state in which the cells divide twice every circadian cycle (Yang *et al*, 2010). However, the reverse interaction appears to be absent, at least it does not affect the high accuracy (24-h periods) or precision (very low period dispersion) of the circadian phase (Mihalcescu *et al*, 2004). Given the significant perturbations faced by cycling cells, for example changes in cell size, doubling of DNA content, partitioning of cellular components at cell division, it is remarkable that the cyanobacterial clock circuit can buffer such nuisances.

Relevance for circadian rhythms in proliferating mammalian cells and tissues

While most adult tissues such as the liver or the brain show little or no cell division, the interaction described is particularly relevant as recent reports indicate that the circadian clock exerts important timing functions in proliferating tissues such as epidermis (Janich *et al*, 2011, 2013; Geyfman *et al*, 2012), hair follicles (Plikus *et al*, 2013), intestinal epithelium (Mukherji *et al*, 2013), or immune cells (Cermakian *et al*, 2013; Scheiermann *et al*, 2013). The importance of 24-h timing across these systems suggests that these cell types may have found solutions to escape the period alterations induced by the cell cycle, or alternatively that systemic signals with 24-h periodicity may override or even entrain the occurring shortened periods of the cell-autonomous oscillators. This would then lead to the interesting possibility that proliferating cells within a tissue (or proliferating tissues as a whole) might show slight phase advances compared to the non-proliferating ones. An obvious next step relevant in the context of cancer chronotherapeutics (Levi *et al*, 2007) would be to extend our approach to cancer tissues, starting with the human osteosarcoma U2OS cell line, a widely used circadian model (Maier *et al*, 2009; Zhang *et al*, 2009).

In conclusion, our study sheds quantitative light on a hitherto understudied aspect of the coupled circadian and cell cycles in mammalian cells, namely that of the influence of the cell cycle on the circadian phase dynamics. While the gating of cell cycle progression by the circadian cycle has attracted most attention, we showed here that in NIH3T3 cells grown under standard conditions, the cell cycle has a dominant influence on the circadian cycle, leading to exquisitely robust synchronization of the two cycles. This possibility has important implications for chronobiology in proliferating tissues.

Materials and Methods

Cell culture

NIH3T3-Rev-VNP-1 cells (abbreviated NIH3T3-Venus), shScramble-NIH3T3-Rev-VNP-1 cells, shCry2-NIH3T3-Rev-VNP-1 cells, and HeLa cells were maintained in DMEM supplemented with 10% FCS and 1% PSG antibiotics. For time-lapse microscopy of fluorescent cells, the medium was replaced by phenol red-free DMEM. Unless indicated, recording conditions were at 10% FCS. When probing different FCS concentration, NIH3T3-Rev-VNP-1 cells were switched to the new concentration 1 day before starting the recordings. Where indicated, NIH3T3-Rev-VNP-1 cells were incubated with 1, 3, and 5 μM Longdaysin (Sigma-Aldrich) or 0.1% DMSO in 10% FCS phenol red-free DMEM few hours before starting the recording.

Phase resetting of the circadian cycle was performed with either 30 min 100 nM Dexamethasone-shock (Sigma-Aldrich) or by treatment with 10 μM forskolin (Biotrend). Perturbation of cell cycle progression was performed with the use of the CDK1 inhibitor RO-3306 (Sigma-Aldrich) or the CDK1/2 inhibitor II NU-6102 (Calbiochem) at the concentration of 1, 5, 7, and 10 μM.

Fluorescence time-lapse microscopy

Cells were plated in 12-well glass bottom dishes (MatTek's Glass Bottom Culture Dishes, P12GC-1.5-14-C). The dishes were placed on a motorized stage in a 37°C chamber equilibrated with humidified air containing 5% CO_2 throughout the microscopy. For the temperature experiments, temperature in the chamber was modified to either 34 or 40°C, and dishes were incubated at the respective temperatures for 4 h before starting recordings. Time-lapse microscopy was performed at the EPFL imaging facility (BIOP) with an Olympus Cell Xcellence microscope using a 20× objective. The cells were illuminated (excitation at 505 nm) for 20, 40, and 60 ms every 30 min for 72 h. Time-lapse movies were captured with the use of a YFP filter set and an Andor Ixon3 camera. Images from three to four fields per well were acquired using Olympus Xcellence software.

Cell tracking

Individual nuclei from fluorescence images were automatically segmented using a custom method (Supplementary Information, Section I) and tracked in time using a standard algorithm (Jaqaman *et al*, 2008). The timing of circadian *Rev-Erbα*-YFP peaks was automatically detected from the single-cell circadian signal while the division times were detected by using both the tracking data and the fluorescence signal. Each segmented image was manually validated and corrected, and likewise for each circadian peak and division (Supplementary Information, Section I).

Plasmids, lentiviral production, and viral transduction

Lentiviral shRNAs in vector backbone pLKO.1(Moffat *et al*, 2006) were Scramble shRNA (addgene #1864; DNA barcode CCTAAGGT TAAGTCGCCCTCG), Cry2-targeting shRNA (Sigma-Aldrich, clone TRCN0000194121; DNA barcode GCTCAACATTGAACGAATGAA). Lentiviral particles were produced in HEK293T cells using envelope vector pMD2.G and packaging plasmid psPAX2 as previously described (Salmon & Trono, 2007). NIH3T3-Rev-VNP1 cells were transduced with viral particle-containing supernatants according to standard procedures, and transduced cells were selected on 5 mg/ml puromycin.

Proliferation assay

Proliferation assays were performed by counting cells using the automated cell counter Luna (Logos biosystems). HeLa or NIH3T3-Rev-VNP-1 cells were seeded in triplicate for each condition in 12-well plates and counted after 48 h for both 0.1% DMSO and 5 μM Longdaysin. Cells were trypsinized, spun down and resuspended in DMEM diluted with Trypan blue stain 0.2% (Logos Biosystem). For each biological replicate, 4–8 counts were performed.

Instantaneous estimation of circadian phase

We inferred the circadian phase from the fluorescent *Rev-Erbα*-YFP signal using a hidden Markov model (HMM). The model contains two hidden states: the circadian phase and the signal amplitude. As in our stochastic phase model, the phase variable follows a Brownian motion with drift. The amplitude variable, necessary to account for amplitude variations in the data, is modeled as an Ornstein–Uhlenbeck process. The circadian phase is related to the data through a sinusoidal waveform. Finally, the most likely temporal sequence of phases and amplitudes was computed for each trace using the Viterbi algorithm (Supplementary Information, Section III).

Stochastic phase model

The two cycles are modeled by noisy phase oscillators. We use θ to denote the circadian phase and ϕ for the cell cycle phase. θ = 0 corresponds to a *Rev-Erbα*-YFP peak and ϕ = 0 to a mitosis. The stochastic differential equations for the generic coupled model read:

$$\begin{aligned} \mathrm{d}\theta_t &= 2\pi/\mathrm{T}_1\,\mathrm{dt} + \mathrm{F}_1(\theta_t, \varphi_t)\,\mathrm{dt} + \sigma_1\,\mathrm{dW}_t \\ \mathrm{d}\varphi_t &= 2\pi/\mathrm{T}_2\,\mathrm{dt} + \mathrm{F}_2(\theta_t, \varphi_t)\,\mathrm{dt} + \sigma_2\,\mathrm{dY}_t \end{aligned} \quad (1)$$

In the absence of interaction between the two cycles, the phases follow a Brownian motion with drift, with intrinsic periods T_1 and T_2 and phase diffusion coefficients σ_1 and σ_2. dW_t and dY_t are independent Wiener processes. The interaction between the two cycles is captured by the two functions, F_1 and F_2. F_1 represents the influence of the cell cycle onto the circadian clock, where positive regions of F_1 accelerate the circadian phase, while negative ones slow it down. Likewise, F_2 represents the action of the circadian clock on the cell cycle. In order to allow for different scenarios and to keep the model complexity manageable, we chose to parameterize the coupling functions as a mixture of two weighted two-dimensional Gaussians: $F_1 = K_1\ G_1(\theta, \phi) + K_2\ G_2(\theta, \phi)$ where K_1 and K_2 are coupling constants that can be positive or negative, and G_i are Gaussians with arbitrary means and diagonal (but not necessarily isotropic) covariances (Supplementary Fig S6). To calibrate this model from the measured time traces, we factorized the probability of a sequence of measured peaks and divisions into a product of conditional probabilities that can be estimated numerically. We then computed the likelihood for entire datasets and optimized the

parameters using a genetic algorithm (details in Supplementary Information, Section II).

Supplementary information for this article is available online: http://msb.embopress.org

Acknowledgements
We thank Emi Nagoshi for providing the NIH3T3-Rev-VNP-1 cells, the EPFL imaging facility (BIOP) for assistance with the microscopy, Mara de Matos for help with the shRNA cell lines, and Johannes Becker for useful discussions. The Naef Lab was supported by the Swiss National Science Foundation (SNF Grants 31-130714 and 31-153340), the European Research Council (ERC-2010-StG-260667), and the École Polytechnique Fédérale de Lausanne (EPFL). The laboratories of FN and DG received funding by the Fondation Leenaards and StoNets, a grant from the Swiss SystemsX.ch (www.systemsx.ch) initiative evaluated by the Swiss National Science Foundation (SNSF). DG acknowledges funding by SNSF professorship Grant PP00P3_128399.

Author contributions
JB, RC, and FN designed and participated in the study concept. JB and RC acquired the data. JB, RC, KG, CG and FN analyzed and interpreted the data. JB, KG and FN wrote the manuscript. FN obtained the funding. All authors contributed to the preparation of the manuscript.

Conflict of interest
The authors declare that they have no conflict of interest.

References

Bjarnason GA, Jordan RC, Wood PA, Li Q, Lincoln DW, Sothern RB, Hrushesky WJ, Ben-David Y (2001) Circadian expression of clock genes in human oral mucosa and skin: association with specific cell-cycle phases. *Am J Pathol* 158: 1793 – 1801

Brown WR (1991) A review and mathematical analysis of circadian rhythms in cell proliferation in mouse, rat, and human epidermis. *J Invest Dermatol* 97: 273 – 280

Brown SA, Ripperger J, Kadener S, Fleury-Olela F, Vilbois F, Rosbash M, Schibler U (2005) PERIOD1-associated proteins modulate the negative limb of the mammalian circadian oscillator. *Science* 308: 693 – 696

Cermakian N, Lange T, Golombek D, Sarkar D, Nakao A, Shibata S, Mazzoccoli G (2013) Crosstalk between the circadian clock circuitry and the immune system. *Chronobiol Int* 30: 870 – 888

Chambard JC, Lefloch R, Pouyssegur J, Lenormand P (2007) ERK implication in cell cycle regulation. *Biochim Biophys Acta* 1773: 1299 – 1310

Destici E, Oklejewicz M, Saito S, van der Horst GT (2011) Mammalian cryptochromes impinge on cell cycle progression in a circadian clock-independent manner. *Cell Cycle* 10: 3788 – 3797

Dibner C, Schibler U, Albrecht U (2010) The mammalian circadian timing system: organization and coordination of central and peripheral clocks. *Annu Rev Physiol* 72: 517 – 549

Etchegaray JP, Machida KK, Noton E, Constance CM, Dallmann R, Di Napoli MN, DeBruyne JP, Lambert CM, Yu EA, Reppert SM, Weaver DR (2009) Casein kinase 1 delta regulates the pace of the mammalian circadian clock. *Mol Cell Biol* 29: 3853 – 3866

d'Eysmond T, De Simone A, Naef F (2013) Analysis of precision in chemical oscillators: implications for circadian clocks. *Phys Biol* 10: 056005

Fidorra J, Mielke T, Booz J, Feinendegen LE (1981) Cellular and nuclear volume of human-cells during the cell-cycle. *Radiat Environ Bioph* 19: 205 – 214

Gamsby JJ, Loros JJ, Dunlap JC (2009) A phylogenetically conserved DNA damage response resets the circadian clock. *J Biol Rhythms* 24: 193 – 202

Gérard C, Goldbeter A (2012) Entrainment of the mammalian cell cycle by the circadian clock: modeling two coupled cellular rhythms. *PLoS Comput Biol* 8: e1002516

Geyfman M, Kumar V, Liu Q, Ruiz R, Gordon W, Espitia F, Cam E, Millar SE, Smyth P, Ihler A, Takahashi JS, Andersen B (2012) Brain and muscle Arnt-like protein-1 (BMAL1) controls circadian cell proliferation and susceptibility to UVB-induced DNA damage in the epidermis. *Proc Natl Acad Sci USA* 109: 11758 – 11763

Glass L (2001) Synchronization and rhythmic processes in physiology. *Nature* 410: 277 – 284

Gottesfeld JM, Forbes DJ (1997) Mitotic repression of the transcriptional machinery. *Trends Biochem Sci* 22: 197 – 202

Granada AE, Bordyugov G, Kramer A, Herzel H (2013) Human chronotypes from a theoretical perspective. *PLoS ONE* 8: e59464

Granger CWJ (1969) Investigating causal relations by econometric models and cross-spectral methods. *Econometrica* 37: 414

Gréchez-Cassiau A, Rayet B, Guillaumond F, Teboul M, Delaunay F (2008) The circadian clock component BMAL1 is a critical regulator of p21WAF1/CIP1 expression and hepatocyte proliferation. *J Biol Chem* 283: 4535 – 4542

Hahn AT, Jones JT, Meyer T (2009) Quantitative analysis of cell cycle phase durations and PC12 differentiation using fluorescent biosensors. *Cell Cycle* 8: 1044 – 1052

Hansen N, Ostermeier A (2001) Completely derandomized self-adaptation in evolution strategies. *Evol Comput* 9: 159 – 195

Hirota T, Lee JW, Lewis WG, Zhang EE, Breton G, Liu X, Garcia M, Peters EC, Etchegaray J-P, Traver D, Schultz PG, Kay SA (2010) High-throughput chemical screen identifies a novel potent modulator of cellular circadian rhythms and reveals CKIα as a clock regulatory kinase. *PLoS Biol* 8: e1000559

Hong CI, Zamborszky J, Baek M, Labiscsak L, Ju K, Lee H, Larrondo LF, Goity A, Chong HS, Belden WJ, Csikasz-Nagy A (2014) Circadian rhythms synchronize mitosis in *Neurospora crassa*. *Proc Natl Acad Sci USA* 111: 1397 – 1402

van der Horst GT, Muijtjens M, Kobayashi K, Takano R, Kanno S, Takao M, de Wit J, Verkerk A, Eker AP, van Leenen D, Buijs R, Bootsma D, Hoeijmakers JH, Yasui A (1999) Mammalian Cry1 and Cry2 are essential for maintenance of circadian rhythms. *Nature* 398: 627 – 630

Janich P, Pascual G, Merlos-Suarez A, Batlle E, Ripperger J, Albrecht U, Cheng HY, Obrietan K, Di Croce L, Benitah SA (2011) The circadian molecular clock creates epidermal stem cell heterogeneity. *Nature* 480: 209 – 214

Janich P, Toufighi K, Solanas G, Luis NM, Minkwitz S, Serrano L, Lehner B, Benitah SA (2013) Human epidermal stem cell function is regulated by circadian oscillations. *Cell Stem Cell* 13: 745 – 753

Jaqaman K, Loerke D, Mettlen M, Kuwata H, Grinstein S, Schmid SL, Danuser G (2008) Robust single-particle tracking in live-cell time-lapse sequences. *Nat Methods* 5: 695 – 702

Kowalska E, Ripperger JA, Hoegger DC, Bruegger P, Buch T, Birchler T, Mueller A, Albrecht U, Contaldo C, Brown SA (2013) NONO couples the circadian clock to the cell cycle. *Proc Natl Acad Sci USA* 110: 1592 – 1599

Levi F, Filipski E, Iurisci I, Li XM, Innominato P (2007) Cross-talks between circadian timing system and cell division cycle determine cancer

biology and therapeutics. *Cold Spring Harb Symp Quant Biol* 72: 465 – 475

Lin F, Chen Y, Li X, Zhao Q, Tan Z (2013) Over-expression of circadian clock gene BMAL1 affects proliferation and the canonical Wnt pathway in NIH-3T3 cells. *Cell Biochem Funct* 31: 166 – 172

Maier B, Wendt S, Vanselow JT, Wallach T, Reischl S, Oehmke S, Schlosser A, Kramer A (2009) A large-scale functional RNAi screen reveals a role for CK2 in the mammalian circadian clock. *Genes Dev* 23: 708 – 718

Masri S, Cervantes M, Sassone-Corsi P (2013) The circadian clock and cell cycle: interconnected biological circuits. *Curr Opin Cell Biol* 25: 730 – 734

Matsuo T, Yamaguchi S, Mitsui S, Emi A, Shimoda F, Okamura H (2003) Control mechanism of the circadian clock for timing of cell division *in vivo*. *Science* 302: 255 – 259

Mihalcescu I, Hsing W, Leibler S (2004) Resilient circadian oscillator revealed in individual cyanobacteria. *Nature* 430: 81 – 85

Miller BH, McDearmon EL, Panda S, Hayes KR, Zhang J, Andrews JL, Antoch MP, Walker JR, Esser KA, Hogenesch JB, Takahashi JS (2007) Circadian and CLOCK-controlled regulation of the mouse transcriptome and cell proliferation. *Proc Natl Acad Sci USA* 104: 3342 – 3347

Moffat J, Grueneberg DA, Yang X, Kim SY, Kloepfer AM, Hinkle G, Piqani B, Eisenhaure TM, Luo B, Grenier JK, Carpenter AE, Foo SY, Stewart SA, Stockwell BR, Hacohen N, Hahn WC, Lander ES, Sabatini DM, Root DE (2006) A lentiviral RNAi library for human and mouse genes applied to an arrayed viral high-content screen. *Cell* 124: 1283 – 1298

Mori T, Binder B, Johnson CH (1996) Circadian gating of cell division in cyanobacteria growing with average doubling times of less than 24 hours. *Proc Natl Acad Sci USA* 93: 10183 – 10188

Mukherji A, Kobiita A, Ye T, Chambon P (2013) Homeostasis in intestinal epithelium is orchestrated by the circadian clock and microbiota cues transduced by TLRs. *Cell* 153: 812 – 827

Nagoshi E, Saini C, Bauer C, Laroche T, Naef F, Schibler U (2004) Circadian gene expression in individual fibroblasts: cell-autonomous and self-sustained oscillators pass time to daughter cells. *Cell* 119: 693 – 705

Oklejewicz M, Destici E, Tamanini F, Hut RA, Janssens R, van der Horst GT (2008) Phase resetting of the mammalian circadian clock by DNA damage. *Curr Biol* 18: 286 – 291

O'Neill JS, Hastings MH (2008) Increased coherence of circadian rhythms in mature fibroblast cultures. *J Biol Rhythms* 23: 483 – 488

O'Neill JS, Maywood ES, Hastings MH (2013) Cellular mechanisms of circadian pacemaking: beyond transcriptional loops. *Handb Exp Pharmacol* 217: 67 – 103

Pendergast JS, Yeom M, Reyes BA, Ohmiya Y, Yamazaki S (2010) Disconnected circadian and cell cycles in a tumor-driven cell line. *Commun Integr Biol* 3: 536 – 539

Plikus MV, Vollmers C, de la Cruz D, Chaix A, Ramos R, Panda S, Chuong C-M (2013) Local circadian clock gates cell cycle progression of transient amplifying cells during regenerative hair cycling. *Proc Natl Acad Sci USA* 110: E2106 – E2115

Preitner N, Damiola F, Lopez-Molina L, Zakany J, Duboule D, Albrecht U, Schibler U (2002) The orphan nuclear receptor REV-ERBalpha controls circadian transcription within the positive limb of the mammalian circadian oscillator. *Cell* 110: 251 – 260

Pulivarthy SR, Tanaka N, Welsh DK, De Haro L, Verma IM, Panda S (2007) Reciprocity between phase shifts and amplitude changes in the mammalian circadian clock. *Proc Natl Acad Sci USA* 104: 20356 – 20361

Reddy AB, Wong GKY, O'Neill J, Maywood ES, Hastings MH (2005) Circadian clocks: neural and peripheral pacemakers that impact upon the cell division cycle. *Mutat Res* 574: 76 – 91

Reddy AB, O'Neill JS (2010) Healthy clocks, healthy body, healthy mind. *Trends Cell Biol* 20: 36 – 44

Rey G, Cesbron F, Rougemont J, Reinke H, Brunner M, Naef F (2011) Genome-wide and phase-specific DNA-binding rhythms of BMAL1 control circadian output functions in mouse liver. *PLoS Biol* 9: e1000595

Rougemont J, Naef F (2007) Dynamical signatures of cellular fluctuations and oscillator stability in peripheral circadian clocks. *Mol Syst Biol* 3: 93

Salmon P, Trono D (2007) Production and titration of lentiviral vectors. *Curr Protoc Hum Genet*, Chapter 12: Unit 12.10.

Sakaue-Sawano A, Kurokawa H, Morimura T, Hanyu A, Hama H, Osawa H, Kashiwagi S, Fukami K, Miyata T, Miyoshi H, Imamura T, Ogawa M, Masai H, Miyawaki A (2008) Visualizing spatiotemporal dynamics of multicellular cell-cycle progression. *Cell* 132: 487 – 498

Scheiermann C, Kunisaki Y, Frenette PS (2013) Circadian control of the immune system. *Nat Rev Immunol* 13: 190 – 198

Stratmann M, Stadler F, Tamanini F, van der Horst GT, Ripperger JA (2010) Flexible phase adjustment of circadian albumin D site-binding protein (DBP) gene expression by CRYPTOCHROME1. *Genes Dev* 24: 1317 – 1328

Tamai TK, Young LC, Cox CA, Whitmore D (2012) Light acts on the zebrafish circadian clock to suppress rhythmic mitosis and cell proliferation. *J Biol Rhythms* 27: 226 – 236

Thresher RJ, Vitaterna MH, Miyamoto Y, Kazantsev A, Hsu DS, Petit C, Selby CP, Dawut L, Smithies O, Takahashi JS, Sancar A (1998) Role of mouse cryptochrome blue-light photoreceptor in circadian photoresponses. *Science* 282: 1490 – 1494

Travnickova-Bendova Z, Cermakian N, Reppert SM, Sassone-Corsi P (2002) Bimodal regulation of mPeriod promoters by CREB-dependent signaling and CLOCK/BMAL1 activity. *Proc Natl Acad Sci USA* 99: 7728 – 7733

Tsuchiya Y, Akashi M, Nishida E (2003) Temperature compensation and temperature resetting of circadian rhythms in mammalian cultured fibroblasts. *Genes Cells* 8: 713 – 720

Ueda HR, Chen W, Adachi A, Wakamatsu H, Hayashi S, Takasugi T, Nagano M, Nakahama K-I, Suzuki Y, Sugano S, Iino M, Shigeyoshi Y, Hashimoto S (2002) A transcription factor response element for gene expression during circadian night. *Nature* 418: 530 – 534

Watanabe I, Okada S (1967) Effects of temperature on growth rate of cultured mammalian cells (L5178Y). *J Cell Biol* 32: 309 – 323

Welsh DK, Yoo SH, Liu AC, Takahashi JS, Kay SA (2004) Bioluminescence imaging of individual fibroblasts reveals persistent, independently phased circadian rhythms of clock gene expression. *Curr Biol* 14: 2289 – 2295

Wright JH, Munar E, Jameson DR, Andreassen PR, Margolis RL, Seger R, Krebs EG (1999) Mitogen-activated protein kinase kinase activity is required for the G(2)/M transition of the cell cycle in mammalian fibroblasts. *Proc Natl Acad Sci USA* 96: 11335 – 11340

Yang XO, Pappu BP, Nurieva R, Akimzhanov A, Kang HS, Chung Y, Ma L, Shah B, Panopoulos AD, Schluns KS, Watowich SS, Tian Q, Jetten AM, Dong C (2008) T helper 17 lineage differentiation is programmed by orphan nuclear receptors ROR alpha and ROR gamma. *Immunity* 28: 29 – 39

Yang Q, Pando BF, Dong G, Golden SS, van Oudenaarden A (2010) Circadian gating of the cell cycle revealed in single cyanobacterial cells. *Science* 327: 1522 – 1526

Ye R, Selby CP, Ozturk N, Annayev Y, Sancar A (2011) Biochemical analysis of the canonical model for the mammalian circadian clock. *J Biol Chem* 286: 25891 – 25902

Yeom M, Pendergast JS, Ohmiya Y, Yamazaki S (2010) Circadian-independent cell mitosis in immortalized fibroblasts. *Proc Natl Acad Sci USA* 107: 9665 – 9670

Zámborszky J, Hong CI, Csikász Nagy A (2007) Computational analysis of mammalian cell division gated by a circadian clock: quantized cell cycles and cell size control. *J Biol Rhythms* 22: 542 – 553

Zhang EE, Liu AC, Hirota T, Miraglia LJ, Welch G, Pongsawakul PY, Liu X, Atwood A, Huss JW III, Janes J, Su AI, Hogenesch JB, Kay SA (2009) A genome-wide RNAi screen for modifiers of the circadian clock in human cells. *Cell* 139: 199 – 210

Zopf CJ, Quinn K, Zeidman J, Maheshri N (2013) Cell-cycle dependence of transcription dominates noise in gene expression. *PLoS Comput Biol* 9: e1003161

A.1.2 Supplementary data

Supplemental Information

Robust synchronization of coupled circadian and cell cycle oscillators in single mammalian cells

Jonathan Bieler, Rosamaria Cannavo, Kyle Gustafson, Cedric Gobet, David Gatfield, and Felix Naef

The Institute of Bioengineering, School of Life Sciences, Ecole Polytechnique Federale de Lausanne (EPFL), AAB 040 Station 15, Lausanne, CH-1015, Switzerland

Contents

I. CELL SEGMENTATION AND TRACKING

Imaging circadian signal can be challenging as cells will go through high and low fluorescence intensity during the circadian cycle. As a result an image can be overexposed for some cells (saturating the detector) and underexposed (cells being hard to distinguish from background) for other cells. In addition to this time dependent change in the signal, there is also significant cell-to-cell variability in the fluorescence intensity.
In order to mitigate this problem we took three images with different exposure times at each time point. This permits collection of unsaturated images for signal quantification at low exposure time, while being able to segment low intensity cells by combining the different images as explained in the next section.

A. Cell segmentation

The segmentation is an important step in the data analysis, as segmentation errors will lead to short traces and reduce the overall quality of the data. Most segmentation errors occurs either around mitosis due to the very low YFP signal during nuclear envelope breakdown, and during cytokinesis as cells can have dramatic changes in shape and texture. Since we are interested in division times it is important for us to minimize segmentation errors linked to divisions. Another source of error is the phase of the circadian cycle when the YFP signal is low, during which some cells can become hard to detect automatically. In order to minimize these segmentation errors and assure the quality of our dataset we did a manual validation of all automatically segmented frames.
The segmentation is composed of three main steps:

1. Preprocess and combine images
2. Automatic segmentation
3. Manual validation

In the first step the background from the three images obtained using different exposure times (30ms, 50ms, 80ms) is corrected by subtracting the low frequencies from the image. This allows removal of the large scale illumination inhomogeneities and obtains an even

background. Then the images are denoised using a median filter. This allows averaging of neighboring pixels while keeping the edges relatively sharp. Finally the three images are normalized and averaged (Figure M1B).

In the second step the combined images are segmented. The segmentation procedure is straightforward: the image is convolved with a family of cell-like filters (Figure M2B). The resulting images are then averaged (Figure M2C) and converted to binary masks using an adaptive threshold (Figure M2D, left). The binary images are cleaned using morphological operations (Figure M2D, right). Finally an automatic correction is done by splitting adjacent cells that have been recognized as one object. An example of an automatically segmented image is shown in Figure M1C.

In the third step the segmented images are manually corrected and validated using a custom Matlab tool shown in Figure M3. An example of a typical correction is shown in Figure M1D.

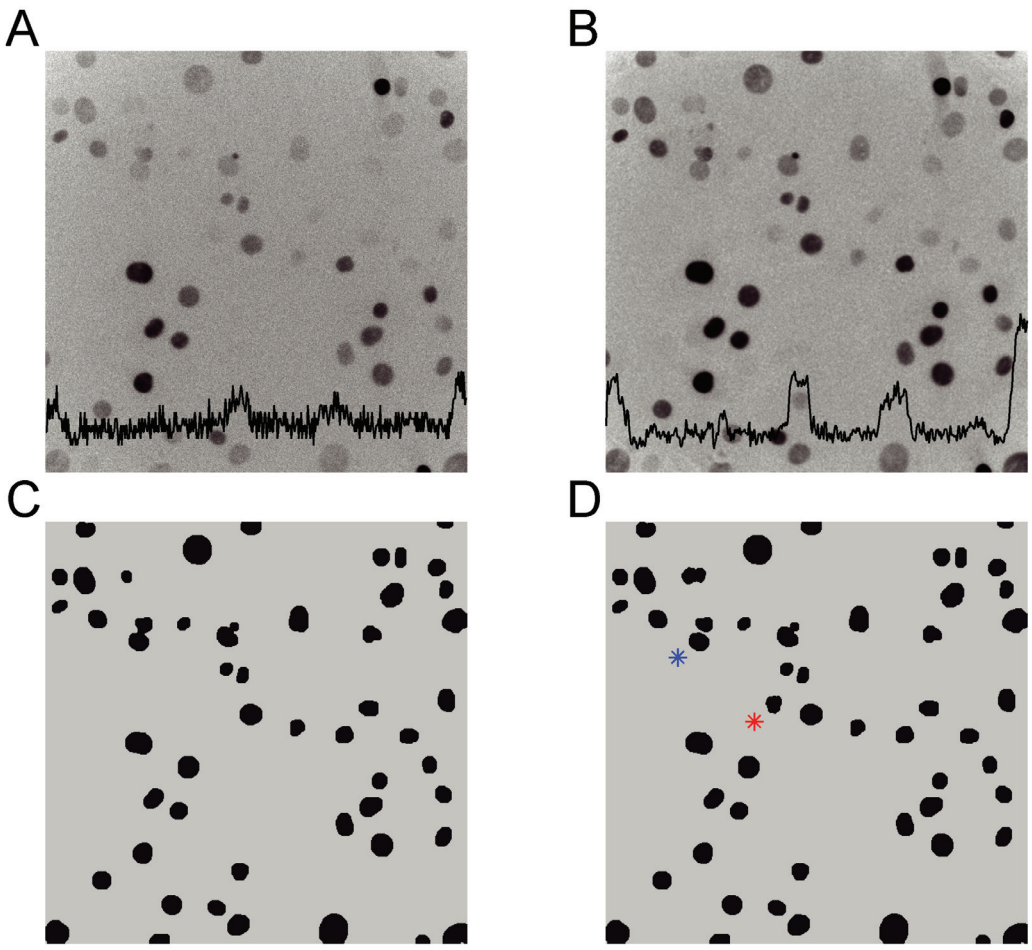

Figure M1: **Cell segmentation overview. A.** Raw image used for quantification. For ease of visualization the image is shown with false color map that enhances contrast. **B.** Preprocessed image ready for segmentation. The black line plot in A and B is the normalized image intensity taken on a single row. **C.** Segmented image after the automatic segmentation. **D.** Segmented image after the manual validation. Two errors were corrected, in blue two adjacent cells that were recognized as one object in panel C were separated, in red a missing cell was added.

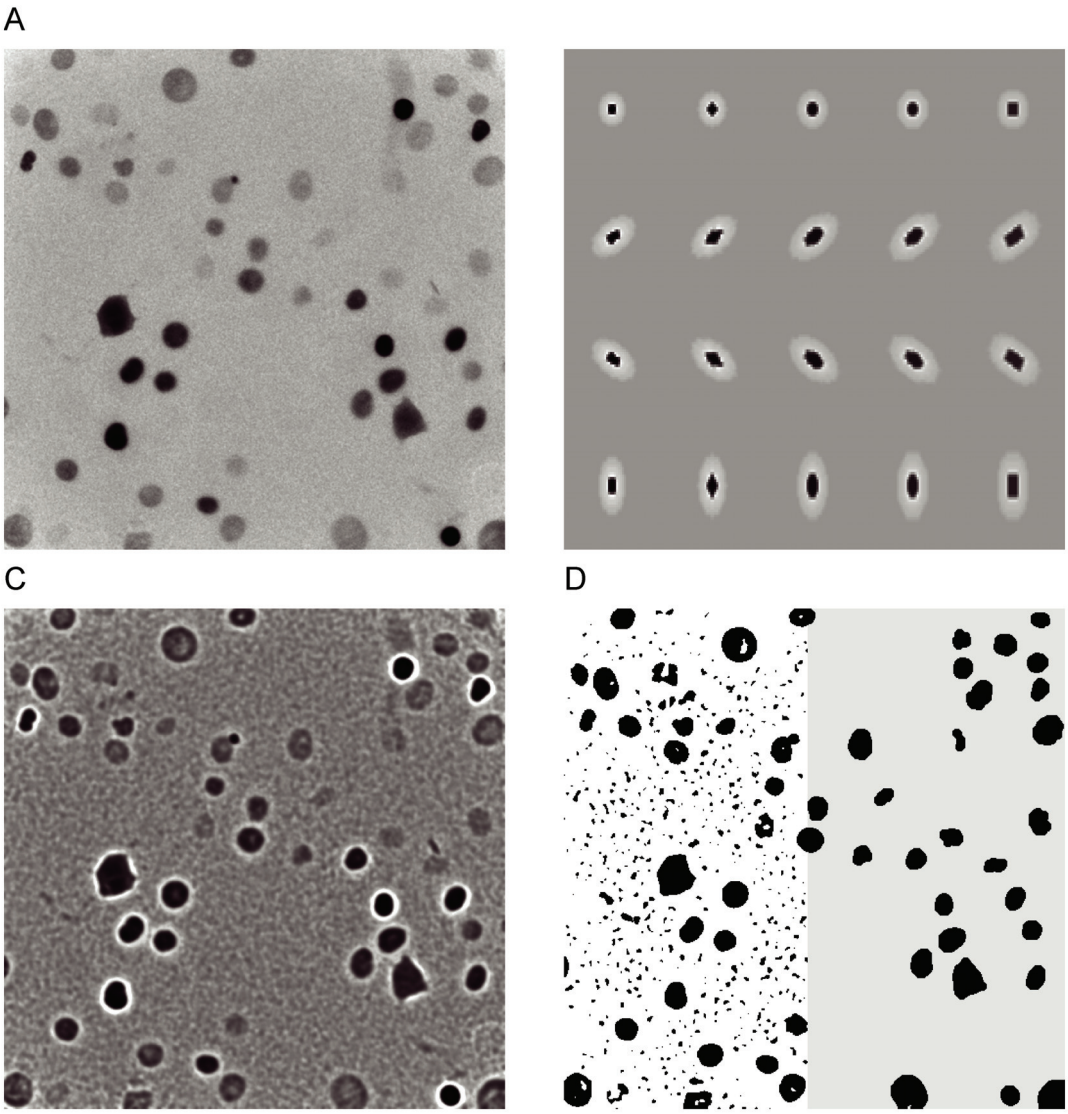

Figure M2: **Segmentation steps A.** Preprocessed image before segmentation. **B.** Small collection of cell-like filters. **C.** Filtered image. **C.** Thresholded image, the left part shows the image before cleaning with morphological operations while the right part shows the cleaned image.

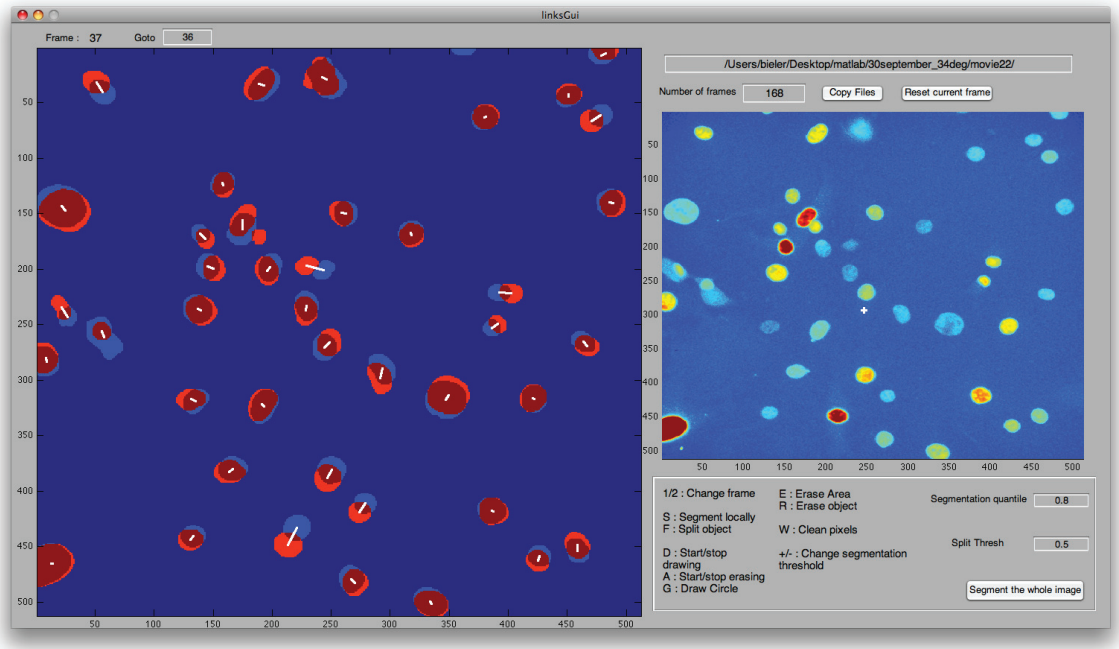

Figure M3: **Segmentation validation tool.** The left panel shows both the current segmented frame and the previous one. Red areas correspond to part of the image that are recognized as objects in the two frames, orange to ones that are only present in the current frame, and light blue to the ones that are only present in the previous frame. The white lines represent which objects are linked by local tracking between the two frames. The left panel shows the image before the segmentation. The user is able to execute a series of operations on the current segmented frames to correct automatic segmentation errors.

B. Cell tracking

Once the images are segmented, detected cells need to be tracked in time in order to obtain time traces. We used a standard tracking algorithm [6] to follow our cells. This algorithm links objects frame by frame based on a certain list of features (here we used distance and fluorescence intensity) before performing a global assignment. Importantly it supports divisions. As our cells enter and leave the camera view and new cells appear with division, we obtained a collection of time traces of different lengths. In our 37 °C dataset we obtained traces of 55 hours on average and about 25% of traces span the whole recording time of 72 hours.

Even if the tracking algorithm can reliably detect new objects generated by divisions, there is a significant error in the mother-to-daughter assignment. For that reason, and in order to simplify our analysis we decided not to use lineage information in our main analysis. More precisely, when a new cell is generated by mitosis, a new independent trace is created at the division time to keep track of the daughter cell.

II. STOCHASTIC PHASE MODEL

The simplest and most general way to model two coupled noisy phase oscillators is to reduce the system to two coupled phase variables. The only underlying assumption is that amplitude fluctuations in these oscillators decouple from the phase dynamics. We can then describe the system as a two dimensional stochastic differential equation (SDE). The phase of the circadian cycle is given by θ. In the absence of coupling (coupling function $F_1 = 0$) the circadian phase is a Brownian motion with drift, where the drift term is given by 2π over the circadian period T_1 and the noise term by $\sigma_1 \mathrm{d}W_t$ where W_t is a Wiener process. The phase of the cell cycle ϕ follows a similar and independent Brownian motion.

$$\mathrm{d}\theta_t = \frac{2\pi}{T_1}\mathrm{d}t + F_1(\theta_t, \phi_t)\mathrm{d}t + \sigma_1 \mathrm{d}W_t \tag{1}$$

$$\mathrm{d}\phi_t = \frac{2\pi}{T_2}\mathrm{d}t + F_2(\theta_t, \phi_t)\mathrm{d}t + \sigma_2 \mathrm{d}Y_t \tag{2}$$

The periodic function $F_1(\theta, \phi)$ represents the influence of the cell cycle on the circadian clock: positive regions of $F_1(\theta, \phi)$ speed up the circadian clock while negative ones slow it down.

Here we used to following parametrization for the coupling function: $F_1 = K_1 G_1(\theta, \phi) + K_2 G_2(\theta, \phi)$ where G_i's are 2D Gaussians with diagonal covariance matrices. This means that the cell cycle can possibly interact with the circadian clock at different phases and have different effects (speed up and slow down) depending on the sign of K_i. The coupling function F_2 is written in the same way: $F_2 = K_3 G_3(\theta, \phi) + K_4 G_4(\theta, \phi)$. An illustration of such functions is shown in Figure S6.

This parametrization allows for flexible coupling functions that can account for different scenarios, while remaining relatively economical in terms of number of parameters.

A. Likelihood function

Our dataset is a collection of sequences of time-ordered events (circadian peaks and divisions) corresponding to individual cell traces.

We denote the successive circadian peaks of a particular trace as $p_1, .. p_N$ where each $p_i \in (0, \Delta t, .. t_{max})$ represents the timing of the circadian peak with respect to the beginning of the trace. Similarly we denote the successive divisions as $d_1, .. d_M$.
For simplicity of notation, when the type of event is unspecified we will denote event i as e_i so that the time ordered sequence of N events corresponding to a particular cell can be written as $S_N = (e_1, .. e_N)$ and its sub-sequence $(e_1, .. e_{N-1})$ as S_{N-1}.
In the context of our phase model we interpret our data as the first-hitting time of the corresponding oscillator:

$$p_i = \inf_{t \geq 0}(t : \theta(t) = 2\pi \mid \theta(p_{i-1}) = 0)$$
$$d_i = \inf_{t \geq 0}(t : \phi(t) = 2\pi \mid \phi(d_{i-1}) = 0)$$

Then the probability of a sequence S_N can be recursively decomposed as:

$$\begin{aligned} P(S_N) &= P(e_1, .. e_N) \\ &= P(e_N | e_{N-1}, .. e_1) P(e_N - 1, .. e_1) \\ &= P(e_N | e_{N-1}, .. e_1) P(S_{N-1}) \end{aligned} \tag{3}$$

Since the phase of the relevant oscillator is by definition known exactly at event time, the probability of the event e_N depends on the last event of the same kind e_j plus all the events of the other kind that happened in-between:
$P(e_N | e_{N-1}, .. e_1) = P(e_N | e_{N-1}, .. e_j)$.
For example the probability of the sequence $S_4 = (d_1, p_1, d_2, p_2)$ is decomposed as:
$P(S_4) = P(p_2 | d_2, p_1, d_1) P(S_3) = P(p_2 | d_2, p_1) P(S_3)$.
As our measurements are invariant under time translation, we can rewrite the conditional probability $P(p_2 | d_2, p_1)$ as $P(p_2 - p_1 | d_2 - p_1, 0) = P(p_2 - p_1 | d_2 - p_1)$.
This quantity represents the probability distribution of a circadian interval $p_2 - p_1$ given that a division took place at time $d_2 - p_1$ after the first circadian peak. Figure M4 shows a scatter plot of theses two quantities measured in mouse fibroblasts. Figure M5 shows the conditional probability estimated from the model in a synchronized regime similar to the one

we observe in the data. For comparison this conditional probability is shown in Figure M6 for the same model with all coupling constants K_i's set to zero. Importantly the structures present in these distributions strongly depend on the coupling functions F_1 and F_2.

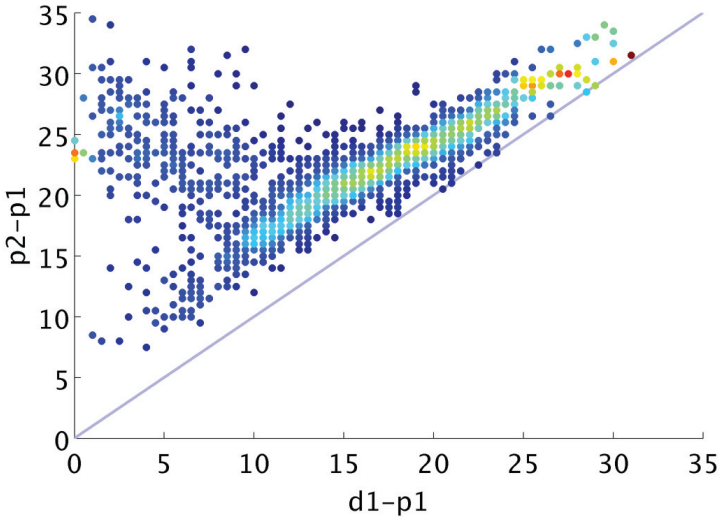

Figure M4: **Distribution of subintervals in** (p_1, d_1, p_2) **events.** The color intensity (blue: lowest, red: highest) represents the estimated conditional density of the data points (the integral on $p_2 - p_1$ is equal to one for each $d_1 - p_1$ values). Since we are plotting events of the type (p_1, d_1, p_2), the quantity $p_2 - p_1$ is by definition always larger than $d_1 - p_1$, so the data are confined above the diagonal. Note that the second peak takes place around 5 hours after the division (the data are shifted above the diagonal), and that this delay depends on the division time (the band is slightly curved). Note also that when the divisions take place early in the circadian cycle ($d_1 - p_1 < 10$ hours) then the 5 hour locking breaks down.

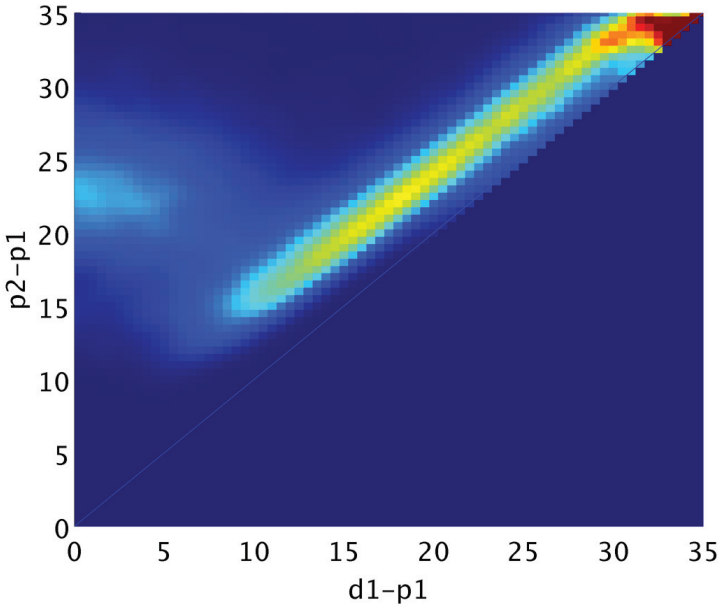

Figure M5: **Conditional probability $P(p_2 - p_1, d_1 - p_1)$ in a synchronized model.** Note that most of the features in Figure M4 are reproduced in the model.

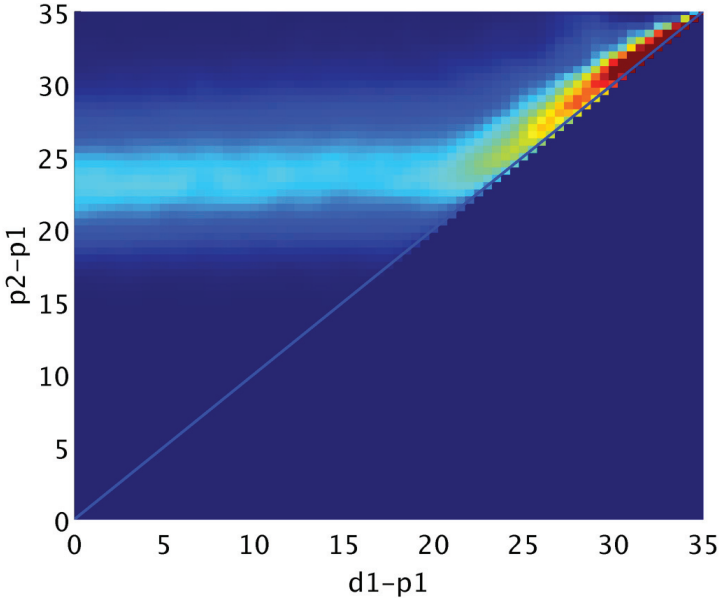

Figure M6: **Conditional probability in a model without coupling.** Note that in the absence of coupling between the two cycles, the circadian interval $p_2 - p_1$ is independent of the division time until the distribution comes close to the diagonal. Then the distribution get squeezed against the diagonal by the selection of time ordered events (p_1, d_1, p_2).

B. Boundary conditions

As we measure only finite time traces, we need to deal with boundary conditions when the recursive decomposition of sequence probability using Equation (3) reaches the end of a sequence.

For example, calculating the probability of the sequence $S_4 = (d_1, p_1, d_2, p_2)$ will eventually lead to the sub-sequence $S_2 = (d_1, p_1)$.

In this particular case we assume that an unobserved circadian peak p_0 took place somewhere before the beginning of the trace (time zero). We can then write the probability $P(S_2)$ as:

$$
\begin{aligned}
&P(d_1, p_1) = \textstyle\int_{-\infty}^{0} P(p_0, d_1, p_1) P(p_0) \mathrm{d}p_0 \\
&= \textstyle\int P(p_1 | d_1, p_0) P(d_1, p_0) P(p_0) \mathrm{d}p_0 \\
&= \textstyle\int P(p_1 - p_0 | d_1 - p_0) P(d_1 - p_0) P(p_0) \mathrm{d}p_0 \\
&= \textstyle\int P(p_1 - p_0, d_1 - p_0) P(p_0) \mathrm{d}p_0
\end{aligned}
$$

A natural distribution to use for $P(p_0)$ is a truncated inverse Gaussian (since it is related to the first passage time in a diffusion-drift process [3]) with mean $p_1 - T_1$ and variance $\sigma_1^2 T_1^3/(2\pi)^2$. Figure M7 shows the distribution $P(S_2)$ estimated from the model.

Other event types - e.g. (p_1, d_1) - are treated in a similar way.

C. Numerical approximation

The estimation of the conditional probability $P(p_2 - p_1 | d_2 - p_1)$ is done by simulation. First we perform stochastic simulations of equation (1) with the initial condition $\theta(0) = 0$ (circadian peak at time zero) and $\phi(0) = \phi_0$, where ϕ_0 is a uniformly distributed random variable between 0 and 2π. The simulation is performed until $\theta(t)$ hits 2π. If $\phi(t)$ passed once through 2π in this interval we record these two hitting times as p_2 and d_2. The joint distribution $P(p_2,d_2)$ is then estimated on a reasonable support from a large number of such events using Gaussian kernel density estimation. The conditional probability $P(p_2|d_2)$ is finally computed from the joined distribution: $P(p_2|d_2) = P(p_2, d_2)/P(d_2)$ with $P(d_2) = \int P(p_2, d_2) \mathrm{d}p_2$.

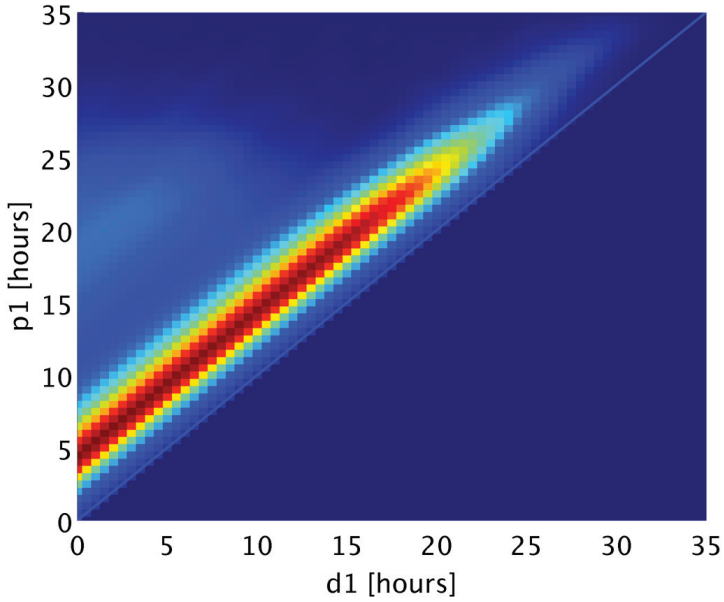

Figure M7: This distribution is similar to the one shown in Figure M5, but has been blurred in the diagonal direction by the integration over the unknown peak p_0. This reflects the lack of knowledge about the precise timing of this non-measured peak.

This conditional probability can then directly be used the evaluate the probability of our dataset. The same procedure is used for other types of events.

Note that our datasets consist mainly of events of the type (p_1, d_1, p_2), (d_1, p_1, d_2) and (p_1, p_2): these event types represent 94% of all our data points. More complicated sequences like (p_1, d_1, d_2, p_2) (two divisions during a circadian interval), represent only 3.5% of all data points. This allows us to neglect some of these rare events.
Finally our likelihood function for a parameter vector p is simply the multiplication of the probability of each sequence S_i:

$$L(\{S\}|p) = \prod_i P(S_i)$$

or more conveniently the sum of the log of the probabilities.
One drawback of using stochastic simulations to estimate our likelihood function is that this function itself is stochastic, but our optimization approach can suitably handle this.

D. Parameter optimization

When using the parametrization for the coupling function described above our model has a total of 24 parameters. The value of some of these parameters is fairly well known (e.g. the circadian period is close to 24 hours), while others are unknown. Thus we bounded our parameter space to constrain our parameters values to realistic intervals.

In order to find the parameters that maximize our likelihood function we used the Covariance Matrix Adaptation Evolution Strategy (CMA-ES) algorithm [4]. This algorithm is well suited for our optimization problem as it has global search properties and can deal with a large numbers of unknown parameters. Unlike some deterministic algorithms, it also performs reasonably well on stochastic likelihood functions.

For each condition we ran several independent optimizations using random initial conditions. A few optimization traces are shown in Figure M8. The parameters values found are shown in Table M1 and the coupling functions are shown in the main text.

As explained in the main text, the 37 °C and the Longdaysin data were fitted separately. The data at different temperatures were fitted together, assuming that the cell cycle period only is affected by the temperature.

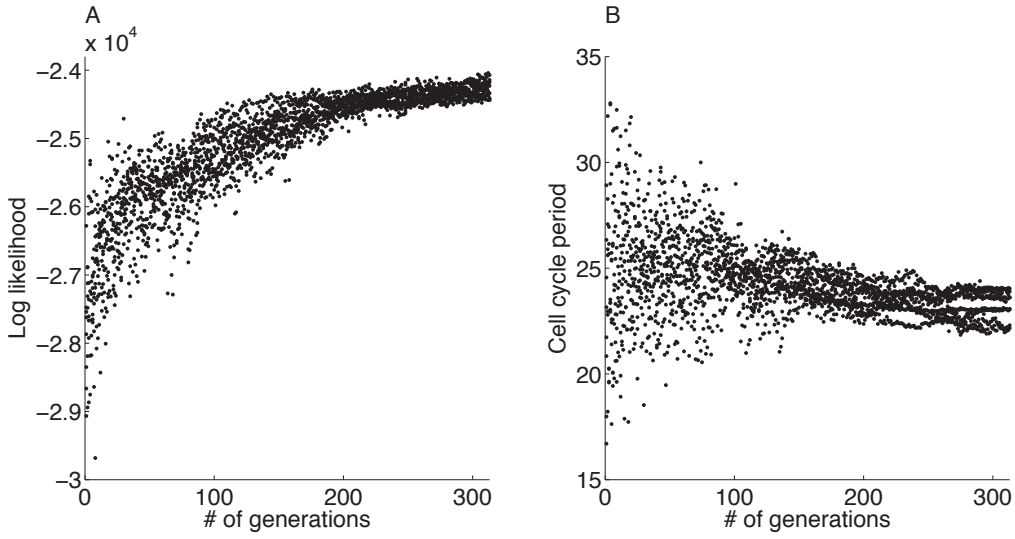

Figure M8: **Optimization traces. A.** The log likelihood is shown for a few different optimizations. **B.** The cell cycle period is shown as a function of the number of generations.

Condition	$T_1[h]$	$T_2[h]$	$\sigma_1[rad \times h^{-1/2}]$	$\sigma_2[rad \times h^{-1/2}]$
37 °C A	24.2 ± 0.5	23.75 ± 1.2	0.13 ± 0.03	0.37 ± 0.05
1 uM LD	27.5 ± 0.37	25.3 ± 1.32	0.18 ± 0.01	0.33 ± 0.02
3 uM LD	29.8 ± 0.79	30.7 ± 2.3	0.18 ± 0.008	0.31 ± 0.03
5 uM LD	32.2 ± 0.6	29.3 ± 2.5	0.18 ± 0.01	0.34 ± 0.03
37 °C	23.9 ± 0.6	20.5 ± 0.4	0.18 ± 0.02	0.33 ± 0.01
34 °C	idem	18.7 ± 1.0	idem	idem
40 °C	idem	24.4 ± 0.8	idem	idem

Table M1: **Estimated periods and noise values.** The values of the circadian period T_1, the cell cycle period T_2 and the respective noise coefficients are shown. The mean and standard deviations are computed on 10 to 30 independent solutions depending on the condition. 37 °C A refers to the 37 °C data that were fitted alone, while the three different temperatures at the end of the table were fitted together.

Condition	$K_1^+[rad \times h^{-1}]$	$\mu_\theta^+[rad]$	$\mu_\phi^+[rad]$	$\Sigma_\theta^+[rad]$	$\Sigma_\phi^+[rad]$
37 °C A	2.53 ± 0.95	3.90 ± 0.82	1.27 ± 1.43	0.70 ± 0.18	0.29 ± 0.13
1 uM LD	1.82 ± 0.57	3.65 ± 0.87	1.82 ± 2.12	0.70 ± 0.22	0.41 ± 0.21
3 uM LD	2.32 ± 1.06	3.36 ± 1.20	1.88 ± 1.97	0.64 ± 0.22	0.29 ± 0.08
5 uM LD	3.50 ± 1.36	3.62 ± 0.33	0.92 ± 1.50	0.70 ± 0.15	0.36 ± 0.16
34-37-40 °C	2.76 ± 0.78	3.90 ± 0.82	1.27 ± 1.43	0.70 ± 0.18	0.29 ± 0.13

Table M2: **Parameters associated with positive region of F_1.** 37 °C A refers to the 37 °C data that were fitted alone, while 34-37-40 °C refers to the three temperatures that were fitted together. K_1^+ is the mean coupling constant that multiply positive Gaussians in F_1, while μ^+ and Σ^+ are the means and the standard deviations of the Gaussians, in the two coordinates θ and ϕ.

Condition	$K_1^-[rad \times h^{-1}]$	$\mu_\theta^-[rad]$	$\mu_\phi^-[rad]$	$\Sigma_\theta^-[rad]$	$\Sigma_\phi^-[rad]$
37 °C A	-1.28 ± 0.95	3.39 ± 1.91	3.32 ± 1.94	0.91 ± 0.72	0.36 ± 0.51
1 uM LD	-2.35 ± 0.96	3.30 ± 1.03	2.22 ± 1.33	0.57 ± 0.21	0.40 ± 0.17
3 uM LD	-1.45 ± 1.17	3.85 ± 2.32	4.20 ± 1.75	0.51 ± 0.22	0.34 ± 0.11
5 uM LD	-1.65 ± 1.12	3.20 ± 1.50	2.09 ± 1.51	0.66 ± 0.27	0.33 ± 0.18
34-37-40 °C	-1.99 ± 1.05	3.25 ± 1.43	3.12 ± 0.96	0.77 ± 0.26	0.31 ± 0.13

Table M3: **Parameters associated with negative region of F_1.** 37 °C A refers to the 37 °C data that were fitted alone, while 34-37-40 °C refers to the three temperatures that were fitted together.

Condition	$K_2^+[rad \times h^{-1}]$	$\mu_\theta^+[rad]$	$\mu_\phi^+[rad]$	$\Sigma_\theta^+[rad]$	$\Sigma_\phi^+[rad]$
37 °C A	1.32 ± 2.40	2.56 ± 1.61	2.35 ± 2.08	0.66 ± 0.60	0.57 ± 0.51
1 uM LD	0.99 ± 0.73	3.94 ± 1.46	2.35 ± 1.70	0.57 ± 0.26	0.43 ± 0.24
3 uM LD	0.84 ± 0.49	3.00 ± 1.05	1.71 ± 2.02	0.42 ± 0.14	0.38 ± 0.17
5 uM LD	0.94 ± 1.02	2.52 ± 1.49	2.64 ± 2.09	0.50 ± 0.25	0.39 ± 0.13
34-37-40 °C	1.48 ± 1.27	3.89 ± 0.43	2.27 ± 1.33	0.39 ± 0.17	0.42 ± 0.14

Table M4: **Parameters associated with position region of F_2.** 37 °C A refers to the 37 °C data that were fitted alone, while 34-37-40 °C refers to the three temperatures that were fitted together.

Condition	$K_2^-[rad \times h^{-1}]$	$\mu_\theta^-[rad]$	$\mu_\phi^-[rad]$	$\Sigma_\theta^-[rad]$	$\Sigma_\phi^-[rad]$
37 °C A	-1.32 ± 2.95	4.34 ± 1.47	3.42 ± 1.51	0.62 ± 0.52	0.81 ± 0.62
1 uM LD	-0.57 ± 0.33	1.16 ± 0.94	2.77 ± 1.61	0.64 ± 0.22	0.63 ± 0.29
3 uM LD	-0.62 ± 0.55	2.44 ± 1.60	2.76 ± 1.17	0.46 ± 0.20	0.52 ± 0.23
5 uM LD	-0.58 ± 0.21	3.22 ± 1.99	3.76 ± 1.62	0.42 ± 0.21	0.51 ± 0.23
34-37-40 °C	-1.07 ± 0.65	3.30 ± 1.84	3.30 ± 1.52	0.49 ± 0.29	0.63 ± 0.32

Table M5: **Parameters associated with negative region of F_2.** 37 °C A refers to the 37 °C data that were fitted alone, while 34-37-40 °C refers to the three temperatures that were fitted together.

E. Validation and parameters identifiability

In order to validate our fitting procedure we generated data from our model using realistic parameters ($T_1 = 24$h, $T_2 = 22$h,$\sigma_1 = 0.15$, $\sigma_1 = 0.2$) and unidirectional coupling functions. We then inferred the parameters, the resulting coupling functions are shown in Figure M9 and Figure M10.

Our fitting procedure is able to predict unambiguously the directionality of the coupling (almost no interactions are predicted in Figure M9C and Figure M9A). It can also predict the position of the interaction relatively precisely, even though there is clearly some soft indeterminacy in the diagonal direction (the interactions are spread along the diagonal in Figure M10C). The deceleration in Figure M9B seems also hard to recover, though this might be due to the fact that this interaction is just behind the other one, in the diagonal direction, and thus might have effectively little impact on the dynamic of the trajectories. The stable manifolds are well predicted (Figure M9E and Figure M10E).

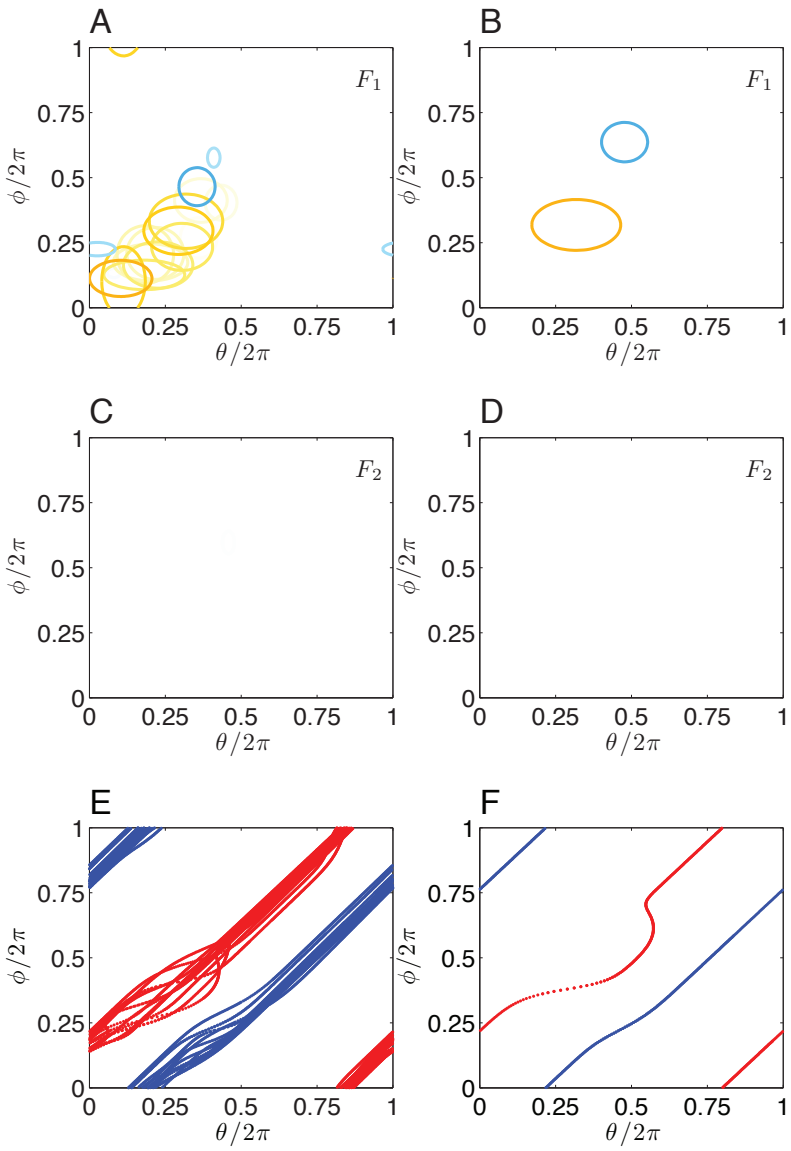

Figure M9: **Validation of model inference** The model was fitted on simulated data with $F_2 = 0$ and F_1 as shown in B ($K_1 = 2.9$, $K_2 = -1.2$). **A.** Inferred coupling function F_1. Orange regions indicate significant acceleration of the circadian phase by the cell cycle, while blue regions indicate a deceleration of the circadian phase. **B.** Coupling function F_1 used to generate the data. **C.** Inferred coupling function F_2. **D.** Coupling function F_2 used to generate the data. **E.** Stable (blue) and unstable (red) manifolds in the fitted models. **F.** Stable (blue) and unstable (red) manifolds in the model used to generate the data.

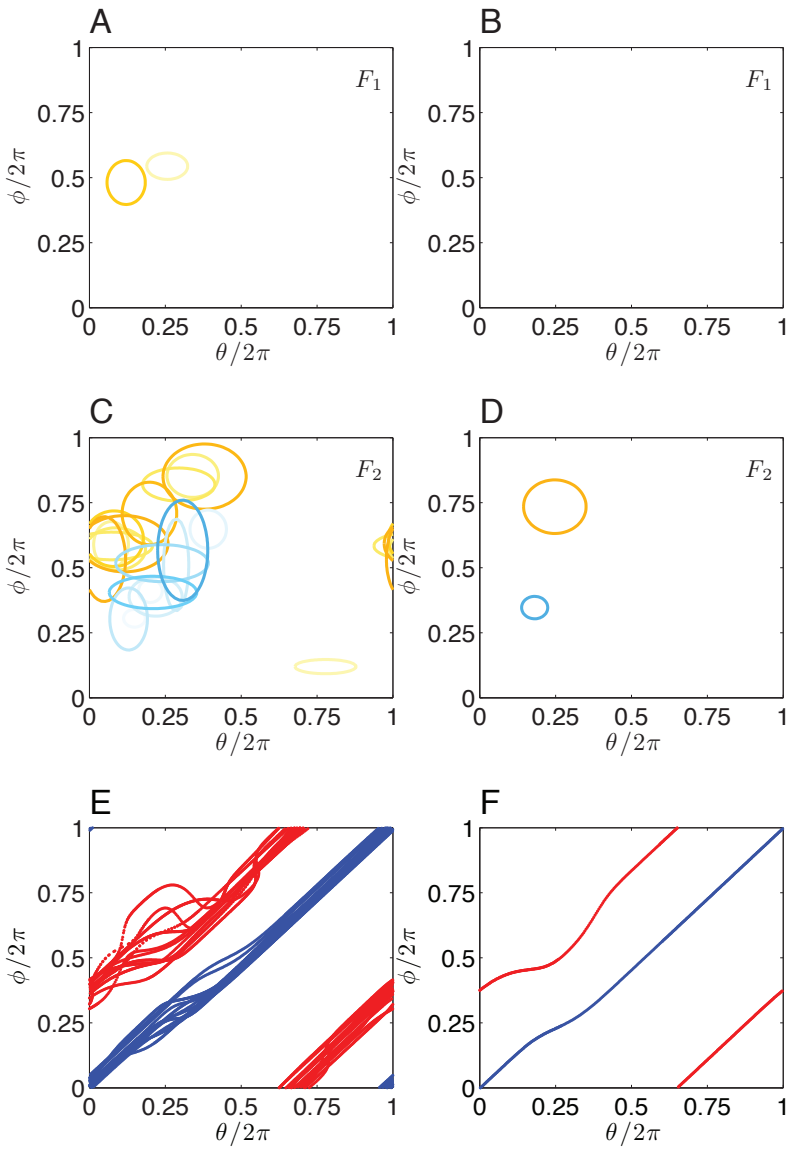

Figure M10: **Validation of model inference** The model was fitted on simulated data with $F_1 = 0$ and F_2 as shown in B ($K_3 = 2.9$, $K_4 = -1.2$). **A.** Inferred coupling function F_1. **B.** Coupling function F_1 used to generate the data. **C.** Inferred coupling function F_2. Orange regions indicate significant acceleration of the cell cycle phase by the circadian clock, while blue regions indicate a deceleration of the cell cycle phase. **D.** Coupling function F_2 used to generate the data. **E.** Stable (blue) and unstable (red) manifolds in the fitted models. **F.** Stable (blue) and unstable (red) manifolds in the model used to generate the data.

III. PHASE INFERENCE USING A HIDDEN MARKOV MODEL

In most analyses we used circadian peak times, corresponding to local maxima of the circadian signal as the time when the circadian phase goes through 2π. However the complete circadian signal contains additional information about the phase progression through the circadian cycle. We used a hidden Markov model (HMM) to infer the phase of the circadian cycle from our recordings.

In addition to the circadian phase, we also need to assume a time varying amplitude as the amplitude of the signal in our data can vary from peak to peak.

The model links the observed circadian signal $s(t)$ to the circadian phase $\theta(t)$ through a waveform $w(\theta)$ and an amplitude $A(t)$:

$$s(t) = A(t)w(\theta(t)) + \xi, \tag{4}$$

where ξ is normally distributed random variable with zero mean. For the waveform we used the function $w(\theta) = (1/2 + 1/2\cos(\theta))^\alpha$ with $\alpha = 1.6$. This simple waveform corresponds reasonably well to the data.

As in our stochastic phase model (Section II), the phase variable is modeled by a diffusion-drift equation, i.e. the phase increments $\theta(t+\Delta t) - \theta(t)$ are normally distributed with mean $\frac{2\pi}{T}\Delta t$ and variance $\sigma^2\Delta t$, where T is the circadian period and σ the circadian phase diffusion coefficient:

$$\mathrm{d}\theta_t = \frac{2\pi}{T}\mathrm{d}t + \sigma\mathrm{d}W_t \tag{5}$$

We used a mean period of 24h and a diffusion coefficient of 0.15, corresponding to a standard deviation on the circadian intervals of 2.8h and consistently with the values found in our stochastic phase model.

The amplitude $A(t)$ is modelled by $\exp(\lambda(t))$ where $\lambda(t)$ is an Ornstein-Uhlenbeck process with zero mean :

$$\mathrm{d}\lambda_t = -\gamma\lambda_t\mathrm{d}t + \sigma_\lambda\mathrm{d}W_t \tag{6}$$

An Ornstein-Uhlenbeck process converges on average to its mean, thus the amplitude $A(t)$ will stay close to unity on average, but is able to fluctuate to compensate for large amplitude

changes in the data. The parameter γ defines the time scale with which the process relaxes to its mean, here we used $1/\gamma = 24$h and $\sigma_\lambda = 0.08$ which gives a standard deviation of the amplitude $A(t)$ of ~ 0.3 around the mean of 1.

The circadian signal was preprocessed by normalizing its amplitude and removing its linear trend. The dip in the signal during the division was also masked to avoid spurious distortion of the phase at mitosis.

Using the standard framework of HMMs [1] in which the joined probability of signal s and hidden states θ and λ factors as $P(s, \theta, \lambda) = P_e(s|\theta, \lambda)Q(\theta, \lambda)$ where P_e is the total emission probability, we computed the most likely sequence of phases and amplitudes for each trace using the Viterbi algorithm.

The emission term was computed using Equation 4 and the probability Q was obtained from solving propagators (transition probabilities) corresponding to Equations 5 and 6.

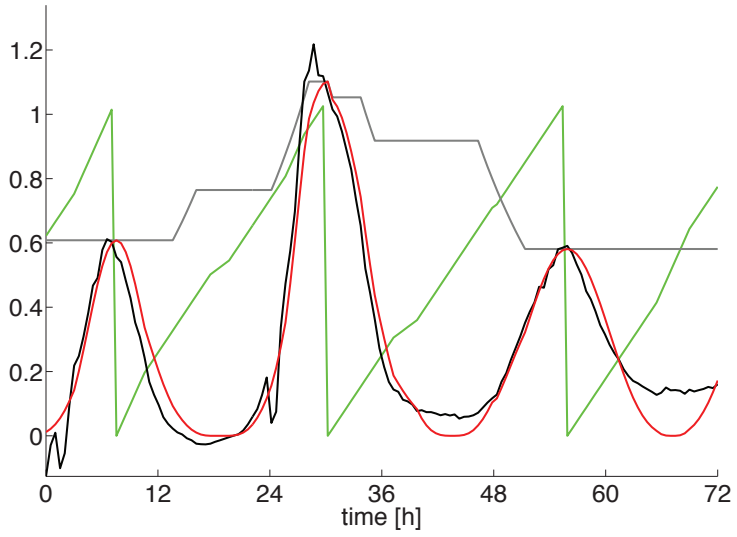

Figure M11: **Example of inferred phase and amplitude.** Black: Circadian trace at 37 °C. Red: inferred signal. Green: inferred phase. Gray: inferred amplitude.

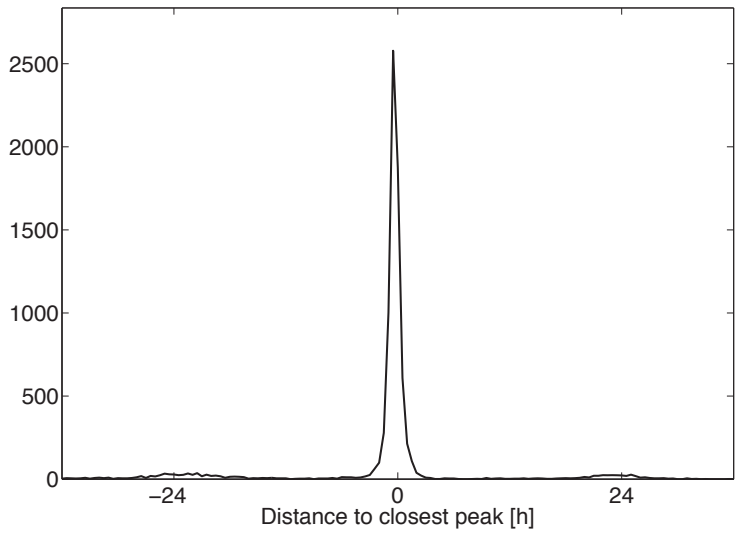

Figure M12: **The HMM recovers the manually validated circadian peak timings.** Distribution of distance from a manually validated peak to the closest peak found by the HMM. Only a small fraction of peaks are not found as indicated by the tiny bumps around -24 and 24h.

A. Validation

In order to validate our inference procedure we simulated data using our stochastic phase model, using reasonable noise values and coupling constants, and inferred back the phase and amplitude using our HMM. Two additional ingredients were necessary to generate realistic signals at shown in Figure M13: a waveform which we took as $w(\theta) = (1/2 + 1/2\cos(\theta))^{\alpha}$ with $\alpha = 1.3$ and an amplitude that we generated by simulating an Ornstein-Uhlenbeck process as described above.

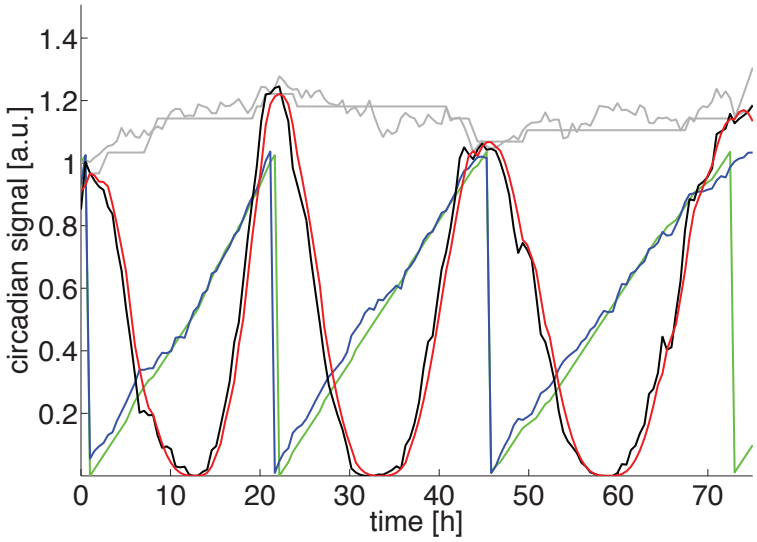

Figure M13: **Simulated signal used for the validation.** Black: Simulated signal. Red: inferred signal. Blue: simulated phase. Green: inferred phase. Gray: simulated and inferred amplitude.

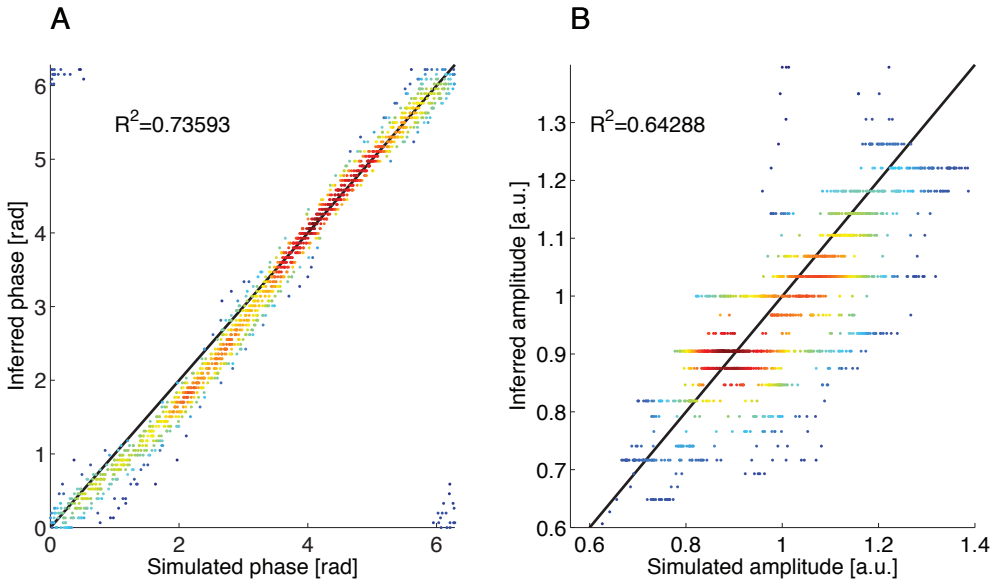

Figure M14: **The HMM infers accurately the phase of the simulated oscillator. A.** The correlation between the simulated phase and the inferred phase is very good. The slight deviation from the diagonal indicates that the waveform used in the model and in the inference procedure is not exactly the same ($\alpha = 1.3$ vs 1.6). The color scale corresponds to the data point density. **B.** The amplitude is well predicted.

IV. SYNCHRONIZATION INDICES

In order to quantify the synchrony of the circadian phase across cells we computed the order parameter R_θ defined by:

$$R_\theta(t)\exp[i\Psi_\theta(t)] = \frac{1}{N}\sum_{k=1}^{N}\exp[i\theta_k(t)]. \tag{7}$$

Where θ_k is the circadian phase of cell k. The order parameter R_θ takes values between zero (no synchrony: the phases are uniformly distributed along the unit circle in the complex plane) and one (complete synchrony). Note that when N is finite, R_θ does not reach exactly zero values for unsynchronized phases (finite size effect, cf. Figure 7). We define the order parameter for the cell cycle (R_ϕ) in a similar way. The synchrony between the cell cycle and the circadian clock ($R_{\theta,\phi}$) is measured by the coherence of phase differences across cells:

$$R_{\theta,\phi}(t)\exp[i\Psi_{\theta,\phi}(t)] = \frac{1}{N}\sum_{k=1}^{N}\exp[i\theta_k(t) - i\phi_k(t)]. \tag{8}$$

Here, we estimated θ_k by assuming that the circadian phase goes linearly from 0 to 2π between two observed peaks. In order to quantify the error on our order parameters we estimated the variance of $\theta_k(t)$ as follows. Because we observe only finite traces we have to deal with two different cases: first we need to estimate the phase at the end (or beginning) of a trace, in which only one peak is available on the left (or right) of the trace. Secondly, we need to estimate the phase between two peaks. In the first case, assuming the phase follows a Brownian motion with drift (Eq. 5), the phase at time t is given by a normal distribution with mean $2\pi/T_1(t - p_M)$ and variance $(t - p_M)\sigma_1$, where p_M is the time of the last peak of the trace, T_1 and σ_1 are the intrinsic period and the the noise parameter of the circadian phase. For the phase at the beginning of a trace we use the same distribution with reversed time.In the second case the phase at time t is given by a normal distribution with mean $2\pi(t - p_1)/(p_2 - p_1)$ and variance $(t - p_1)(p_2 - t)/(p_2 - p_1)\sigma_1$ where p_1 and p_2 are the times of the two peaks encompassing the circadian phase. This distribution is the solution to the diffusion-drift equation with Dirac boundary conditions at p_1 and p_2. Figure M15 shows these quantities for a trace with two peaks.

An analogous procedure is done for the cell cycle phase $\phi_k(t)$. Finally, the means and variances of the order parameters R_θ, R_ϕ and $R_{\theta,\phi}$ are computed by sampling these phase distributions.

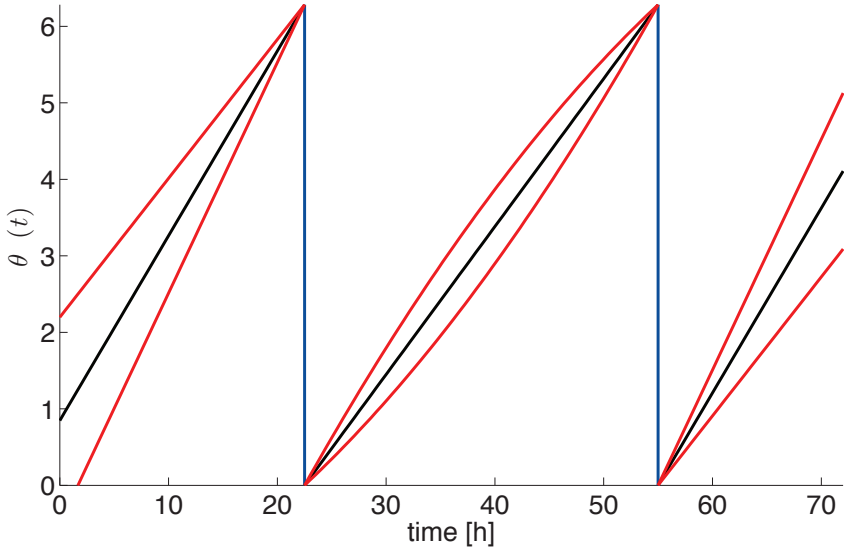

Figure M15: **Illustration of phase estimation.** The mean (black) and variance (red) of the estimated circadian phase between two peaks (blue) is shown. Note that the phase is more constrained between two peaks than at the boundaries.

V. GRANGER CAUSALITY

A. Nuclear area and cell cycle phase

In addition to the fluorescent signal we also measure the area of the nucleus from our segmentation and tracking analysis. It is known [2] that the nucleus volume increases during the cell cycle in mammalian cells. We thus hypothesized that the nucleus area contains information about the cell cycle progression. To test this we first plotted the nuclear area for a few cells, as shown in Figure M16 the nucleus area increases between two divisions with a characteristic pattern, before decreasing by about a factor of two at mitosis. The nuclei seem to regrow rapidly for about 4 to 5 hours after the division and then increase in size at slower pace. This is clearly visible when looking at the nucleus area averaged over many cell cycles (Figure M17), where we find a pattern that is very similar that reported in [2]. We verified that the rapid increase after a division is not due to movement in the z-axis, as nuclei regain focus after about one hour following division in our recordings.

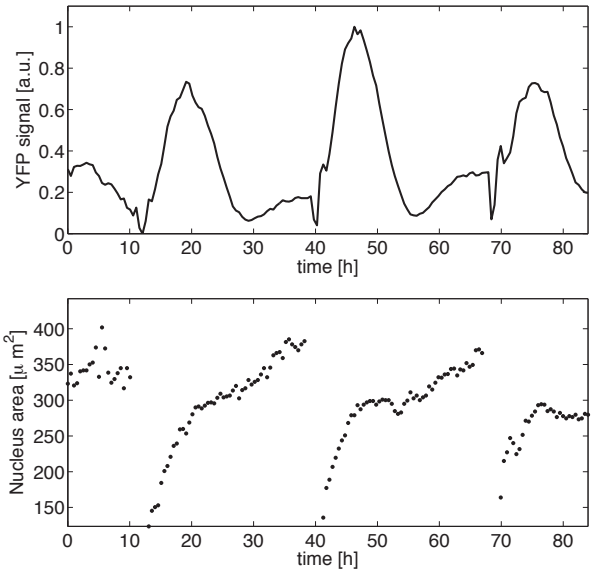

Figure M16: **Circadian signal and nucleus area**

The normalized circadian signal is shown on top, and the nucleus area on the bottom. The area in μm^2 was computed from the objective magnification (20x) and the camera pixel size (16x16 μm). This gives nuclei radii around 5 to 10 μm.

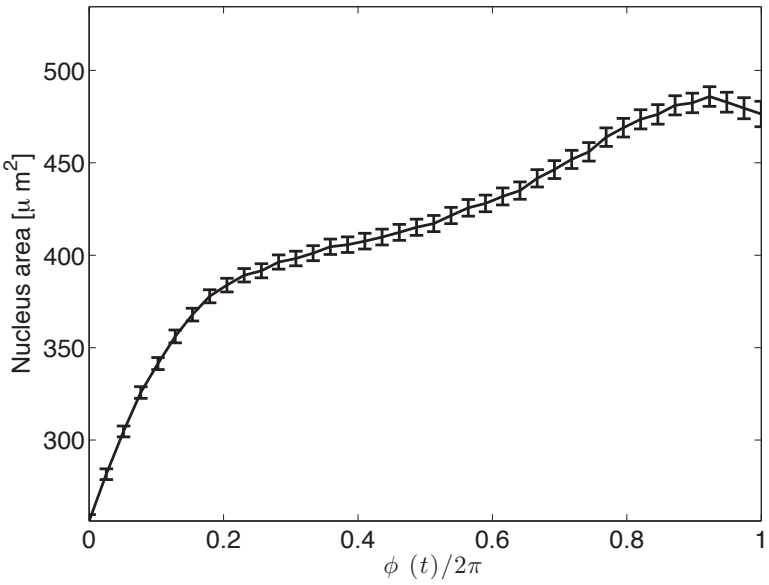

Figure M17: **Mean nucleus area during the cell cycle** The mean (n=836) nucleus area is shown in function of the cell cycle phase. Here we assumed that the cell cycle phase goes linearly from 0 to 2π between two mitosis. The error bars represent the standard error on the mean.

To confirm that nuclear area contains information about the state of the cell cycle we analyzed a previously publish movie of HeLa cells containing the FUCCI system (movie S1 in [7]). After segmentation of the movie this allowed us to estimate the time of onset of S phase in 31 cells. The estimated S phase onset is shown in a single cell in Figure M18 and the average S phase onset is shown alongside the mean nucleus area in Figure M19.
We then aimed at predicting the measured times of S phase onset, denoted t_S, by using only the normalized nucleus area $n(t)$. For a given cell we computed the probability that time t is t_S as:

$$P(t = t_S) = \mathrm{G}(n(t), \dot{n}(t); \mu, \Sigma)$$

Where G is a bivariate Gaussian with mean μ and covariance matrix Σ, while $\dot{n}(t)$ is the time derivative of $n(t)$. We split our data into a training set and a test set, and estimated μ and Σ from the training set. As shown in Figure M20 this simple model is able to predict the onset of S phase with good accuracy, demonstrating that the nuclear size does contain information on the cell cycle progression.

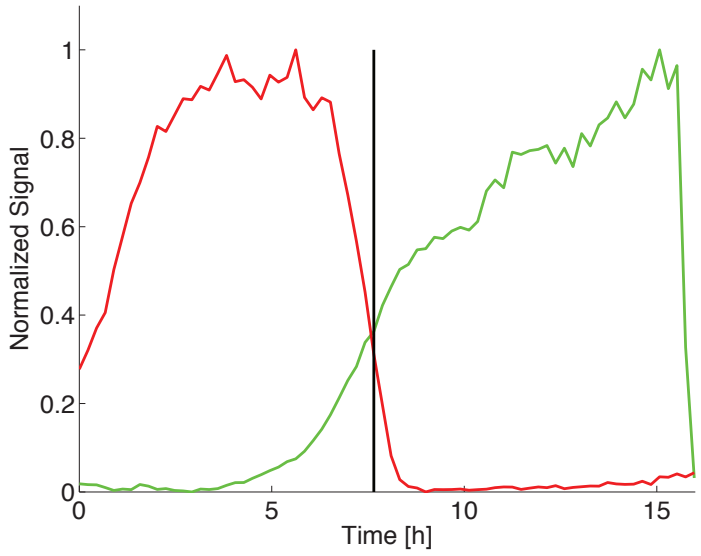

Figure M18: **Measuring S phase onset in HeLa cells.** Red : Measured mKO2-hCdt1 signal in a single cell between two divisions. Green: Measured mAG-hGem signal. The vertical black line represent the estimated S phase (time of crossing of red and green signal).

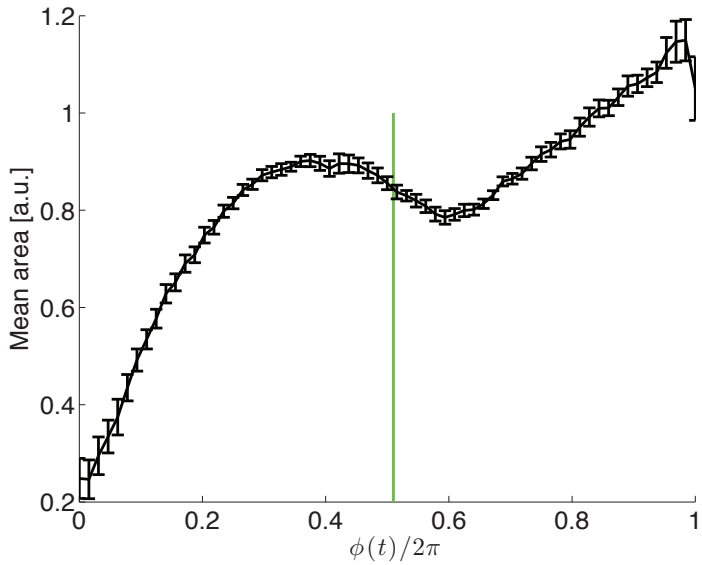

Figure M19: **Mean S phase onset and mean nucleus area in HeLa cells.** The mean normalized nucleus area is shown in black (error bars represent the standard error on the mean) against the cell cycle phase. The mean estimated phase of S phase onset (0.51 ± 0.07) is shown in green.

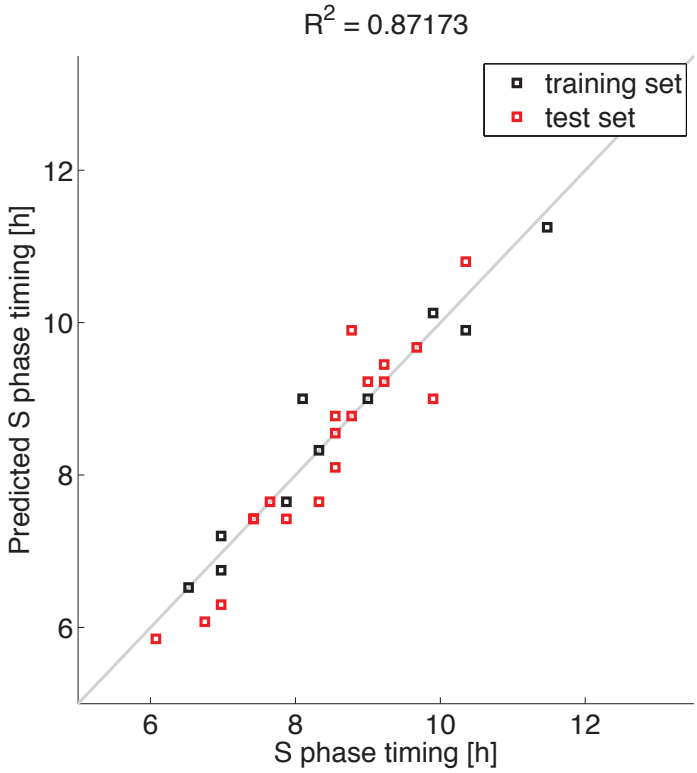

Figure M20: **Nucleus area predicts S phase onset in HeLa cells**

B. Granger Causality

We applied the Granger-Wald causality test as defined in [5] to each trace (we used only traces longer than 60 hours) independently. For a given lag L in the autoregressive model, we applied the test directly to the raw circadian signal and nucleus area, and decided for each trace if the circadian signal was Granger-causing the nucleus area or vice-versa using the Granger-Wald test with a p-value of 10^{-3}. Finally we counted the fraction of traces falling in each category. The results are shown in Figure S8.

[1] Richard Durbin, Sean R. Eddy, Anders Krogh, and Graeme Mitchison. *Biological Sequence Analysis: Probabilistic Models of Proteins and Nucleic Acids*. Cambridge University Press, 1998.

[2] J Fidorra, T Mielke, J Booz, and L E Feinendegen. Cellular and nuclear volume of human cells during the cell cycle. *Radiation and environmental biophysics*, 19(3):205–14, January 1981.

[3] J. L. Folks and R. S. Chhikara. The inverse gaussian distribution and its statistical application–a review. *Journal of the Royal Statistical Society. Series B (Methodological)*, 40(3):pp. 263–289, 1978.

[4] N. Hansen and A. Ostermeier. Completely derandomized self-adaptation in evolution strategies. *Evol Comput*, 9(2):159–95, 2001.

[5] K Hlavackova-Schindler, M Palus, M Vejmelka, and J Bhattacharya. Causality detection based on information-theoretic approaches in time series analysis. *Physics Reports*, 441(1):1–46, March 2007.

[6] Khuloud Jaqaman, Dinah Loerke, Marcel Mettlen, Hirotaka Kuwata, Sergio Grinstein, Sandra L Schmid, and Gaudenz Danuser. Robust single-particle tracking in live-cell time-lapse sequences. *Nature methods*, 5(8):695–702, August 2008.

[7] Asako Sakaue-Sawano, Hiroshi Kurokawa, Toshifumi Morimura, Aki Hanyu, Hiroshi Hama, Hatsuki Osawa, Saori Kashiwagi, Kiyoko Fukami, Takaki Miyata, Hiroyuki Miyoshi, Takeshi Imamura, Masaharu Ogawa, Hisao Masai, and Atsushi Miyawaki. Visualizing spatiotemporal dynamics of multicellular cell-cycle progression. *Cell*, 132(3):487–98, March 2008.

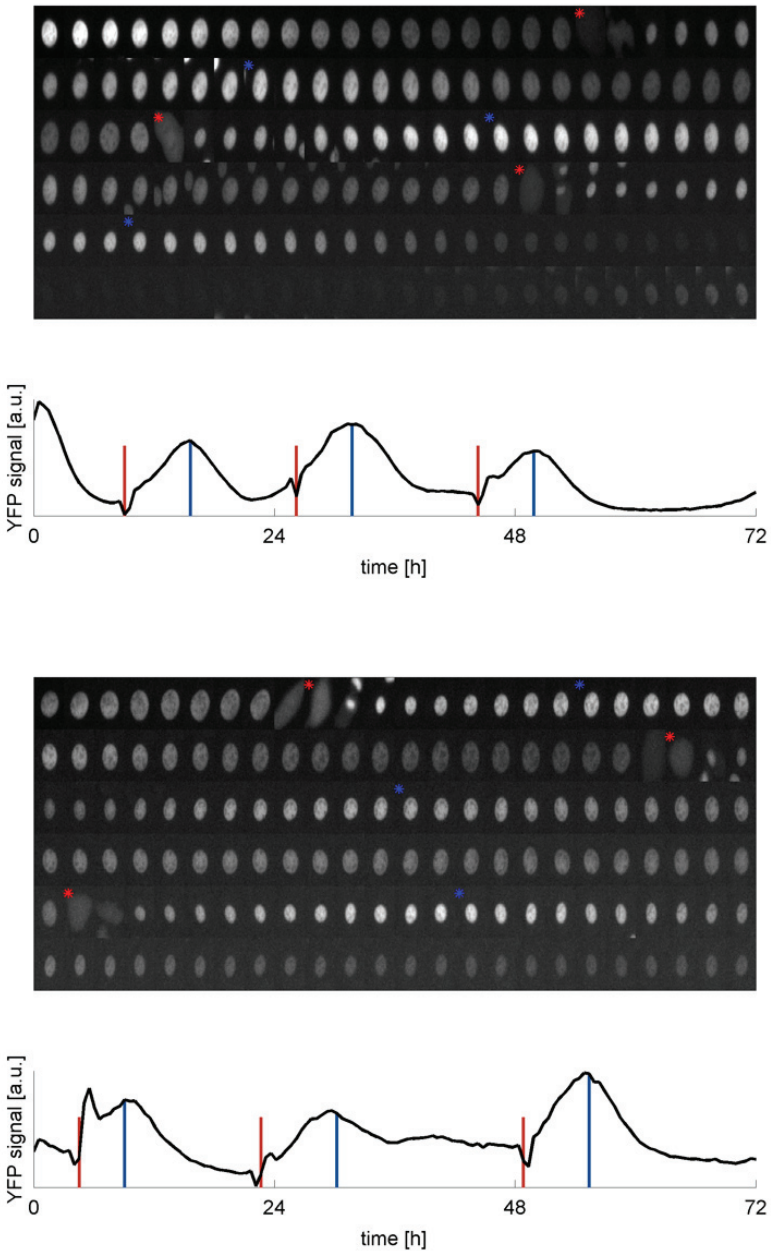

Figure S1. Time series of circadian *Rev-Erb*α-YFP signals in tracked nuclei.

Two time series of tracked nuclei are shown along with YFP signals underneath. Time goes from top left to bottom right, each of the six rows represent 12 hours. Images are taken every 30 minutes for a total of 72 hours. Stars indicate frames with circadian peaks (blue) or divisions (red). Below the images, the circadian signal (black) is shown with detected peaks (blue) and divisions (red).

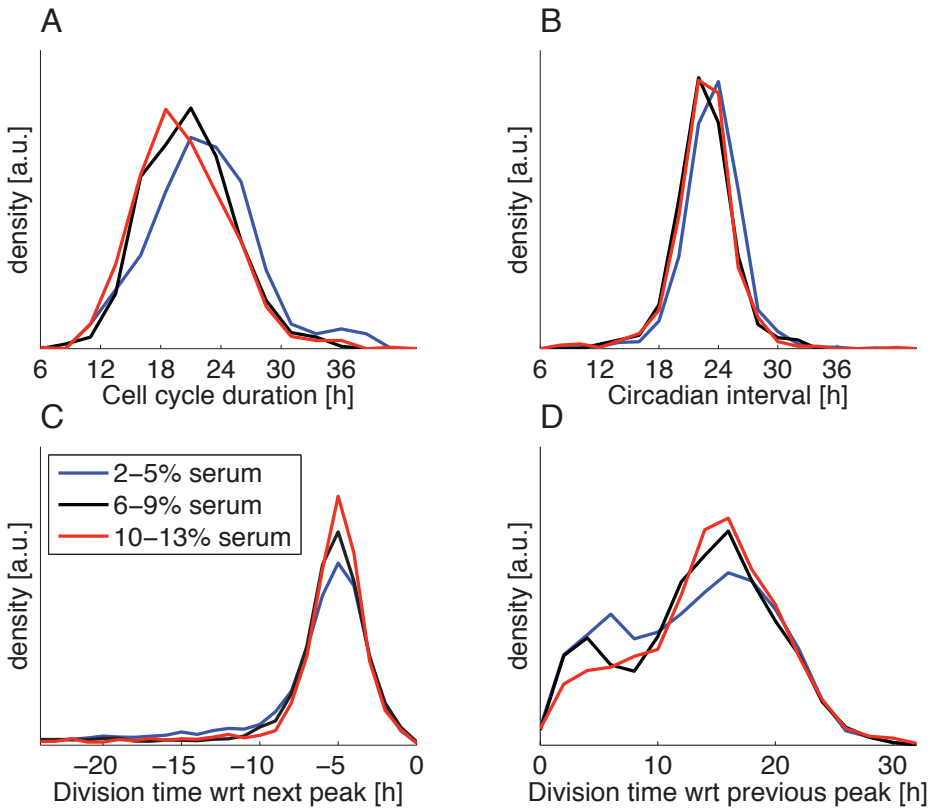

Figure S2. Effect of serum concentration on circadian intervals and cell cycle durations.

A. The distribution of cell-cycle duration shows a small dependence on serum concentration (the distribution is shown for 2-5%, 6-9% and 10-13% serum). B. Distribution of circadian intervals does not vary much with serum concentration. C. The distribution of division time is similar for all serum concentrations. D. The distribution of division time w.r.t. previous circadian peak shows a minor dependence on serum concentration. The number of traces analyzed here were n=1465, n=1288 and n=3967 in the low, medium and high concentration range, respectively.

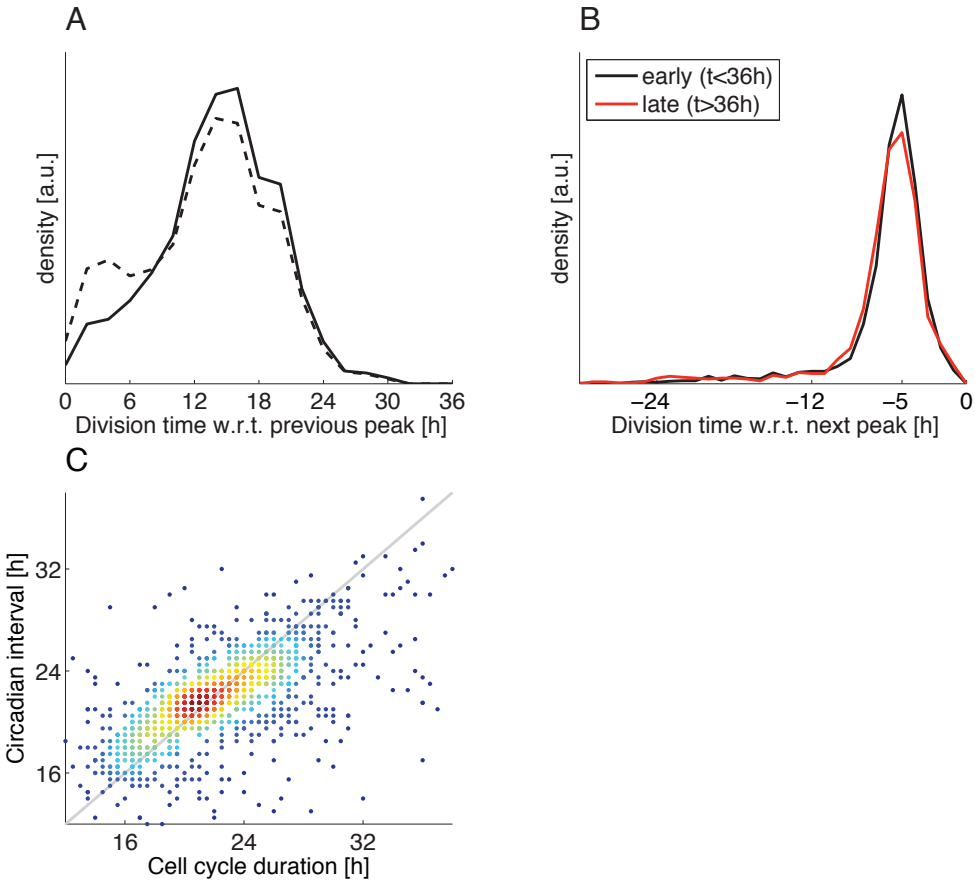

Figure S3. Circadian and cell cycle oscillators are tightly synchronized at 37 ºC.

A. The interval length from the previous circadian peak to the division time (p,d) is less constrained than (d,p) interval length (Figure 1C). Solid line: histogram of (p_1,d_1) subintervals from (p_1,d_1,p_2) events; dashed line: all (p,d) intervals. The population of short (p,d) intervals is reduced among (p_1,d_1,p_2) events. B. The distribution of (d,p) intervals is homogenous in time: events in the first half (black) of the recordings are no different than during the second half (red). C. Circadian intervals (peak-to-peak times) and cell cycle durations are tightly correlated. Color indicates density of measurements.

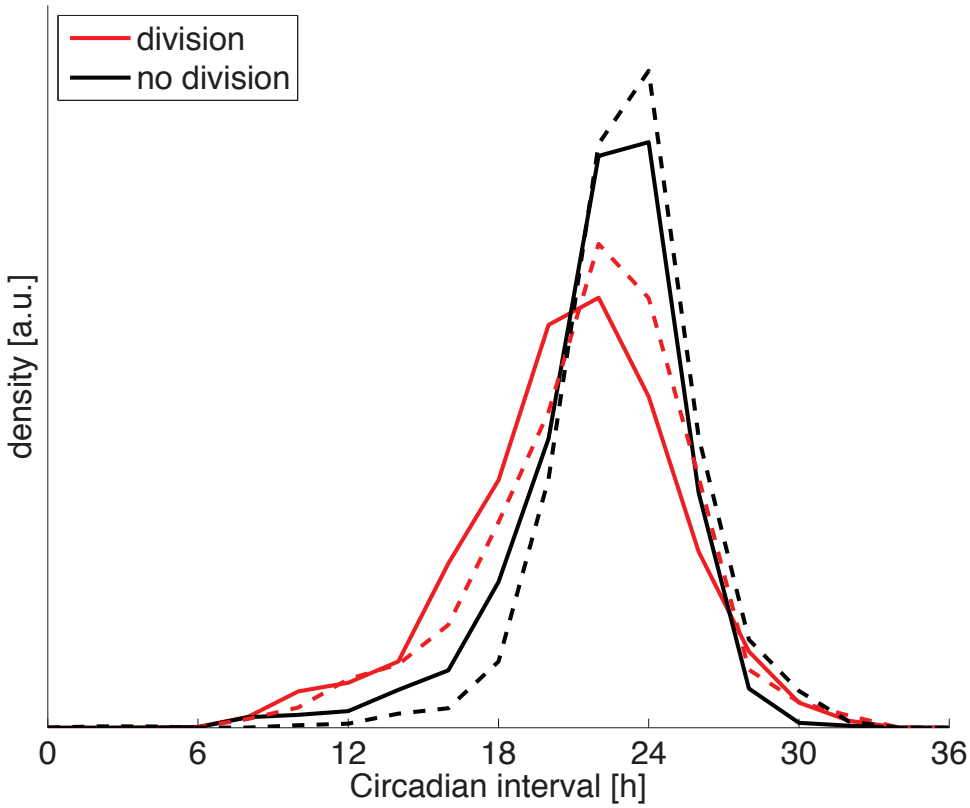

Figure S4. The influence of cell-cycle time on circadian phase progression is homogenous in time. Circadian intervals with (black) and without (red) divisions in the first (solid) and second (dashed) halves of the recordings show significant shifts (first half, $p<10^{-7}$, t-test; second half, $p<10^{-9}$, t-test).

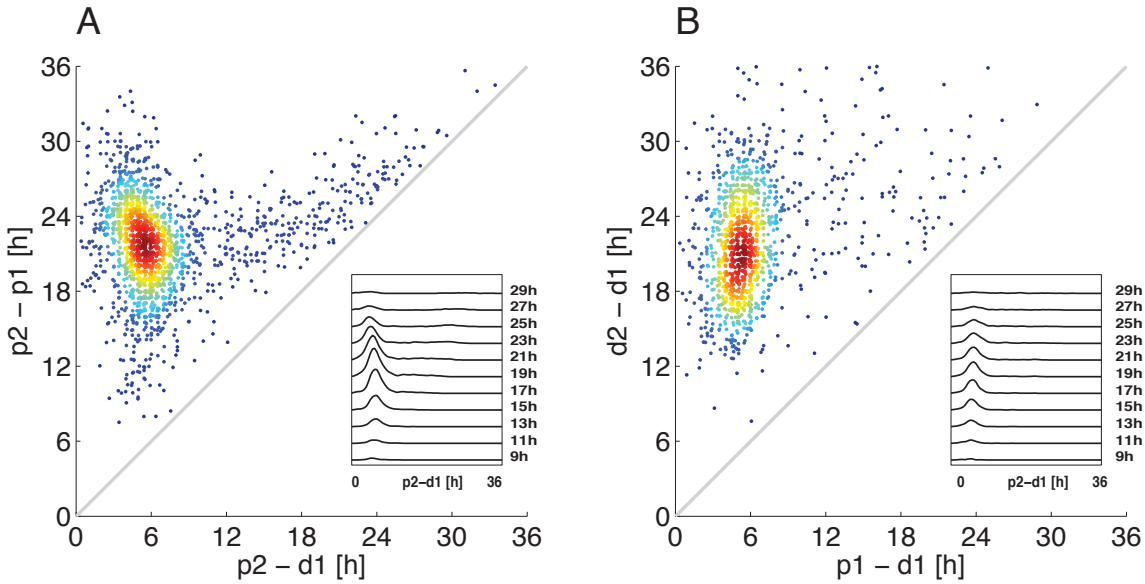

Figure S5. Signature of unidirectional coupling from the cell cycle onto the circadian phase for normally growing cells at 37 ºC.

A. Full circadian intervals (p_1,p_2) in (p_1,d_1,p_2) events compared to the second subinterval (d_1,p_2) shows early division events as outliers along the diagonal. The negative correlation of (p_1,p_2) vs. (d_1,p_2) in the center of the distribution coincides with the positive correlation centered on phases ~0.8 in Figure 2B and is a property of the fitted stochastic model in which the influence of the cell cycle onto the circadian oscillator dominates (cf. Figure 3). Insets show the marginal distributions (times on the x-axis stratified according to the y-axis), shifting towards smaller times. B. Similar representation for (d_1,p_1,d_2) to probe the reverse interaction of the circadian cycle onto the cell cycle. Unlike A), the distribution shows a positive correlation that is consistent with a proportional stretching of the (d_1,p_1) subintervals as the enclosing (d_1,d_2) duration lengthens (see main text).

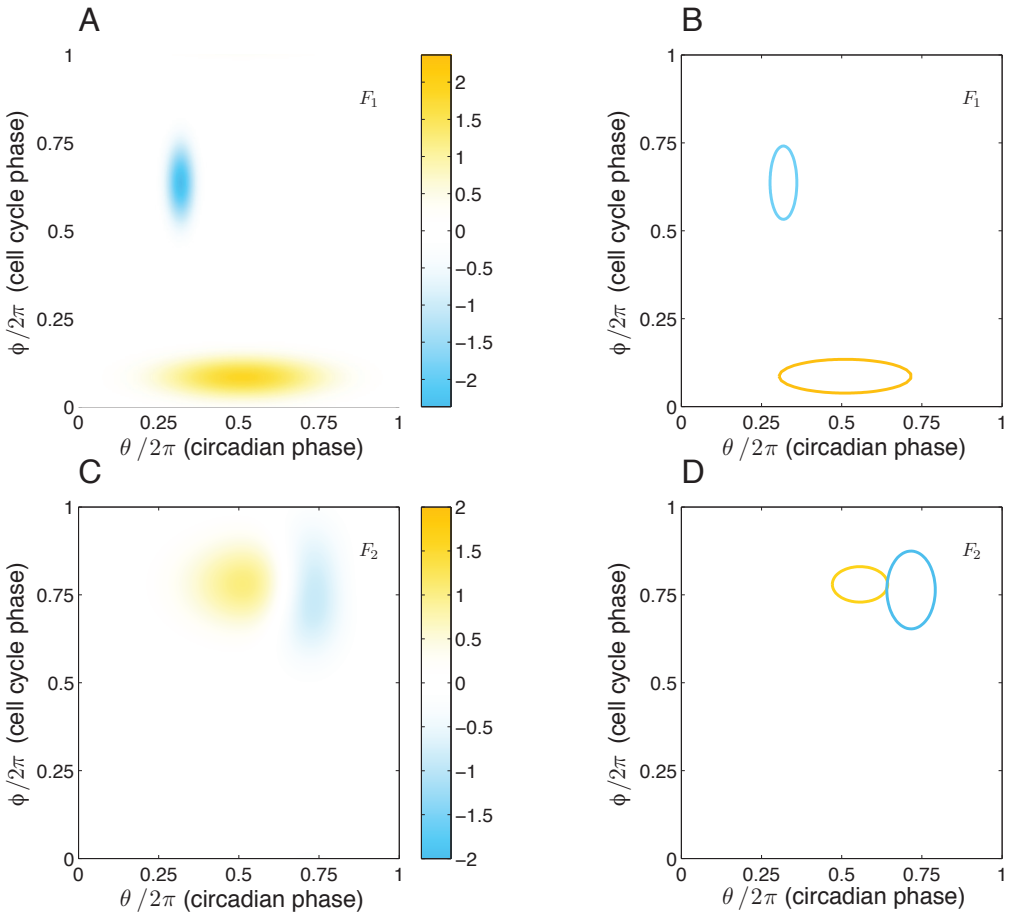

Figure S6. Representation of coupling functions in the generic model used to fit the data.

A-B. The influence of the cell-cycle on the circadian clock can be described by two Gaussian functions arbitrarily placed and sized, which can either accelerate (yellow) or decelerate (blue) the circadian phase progression. Covariance is diagonal in the coordinates used. A: the density of the elliptical function; B: the contours correspond to a fixed (absolute) value of the function, as shown in the main figures. C-D. Idem for the coupling functions describing the influence of the circadian cycle on cell division. The functions shown here were chosen arbitrarily for illustration purpose.

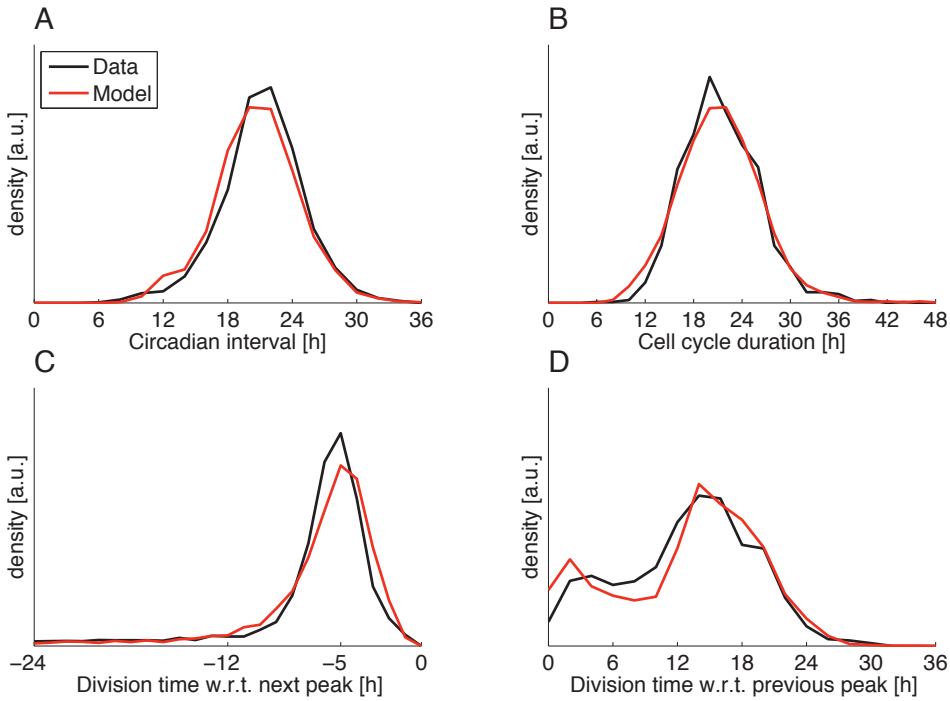

Figure S7. Comparison of fit and data at 37 ºC for the best-fit model.

A. The distributions of circadian intervals (p_1,d_1,p_2).

B. The distributions of cell-cycle durations (d_1,p_1,d_2).

C. The interval from divisions to the next circadian peaks (d,p).

D. The interval between the previous peaks and the divisions (p,d).

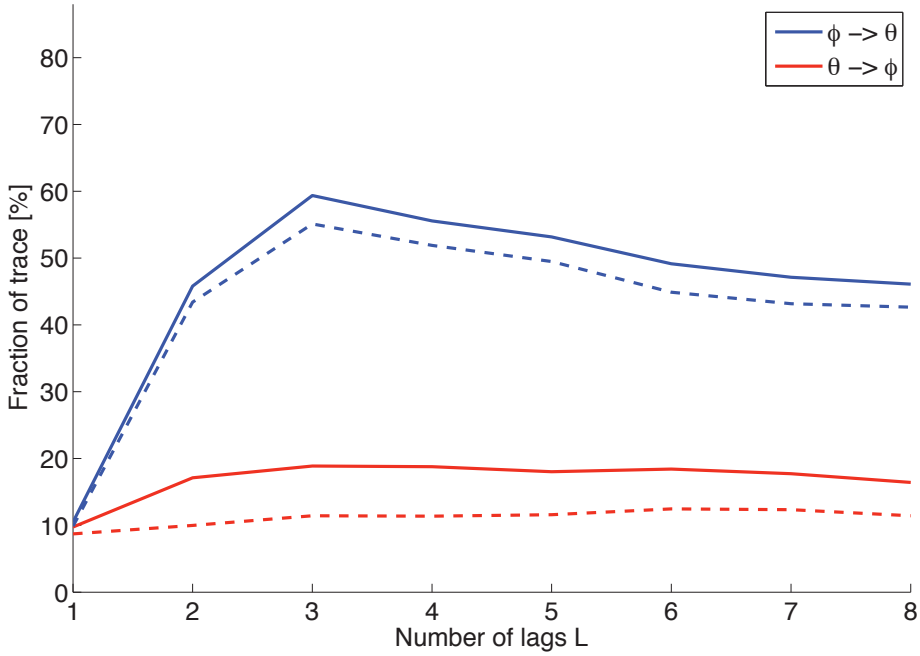

Figure S8. Testing for Granger causality. Proportion of cells showing significant evidence ($p<0.001$, Granger-Wald test) that cell cycle progression (assessed via the nuclear size, Supplementary Information section VA) predicts the circadian *Rev-Erbα*–YFP signal (solid blue), or vice versa (solid red), in function of the number of lags used in the autoregressive models. Dashed lines show the proportion of cells for which the detected causality ($p<0.001$) is more significant than that of the reverse direction.

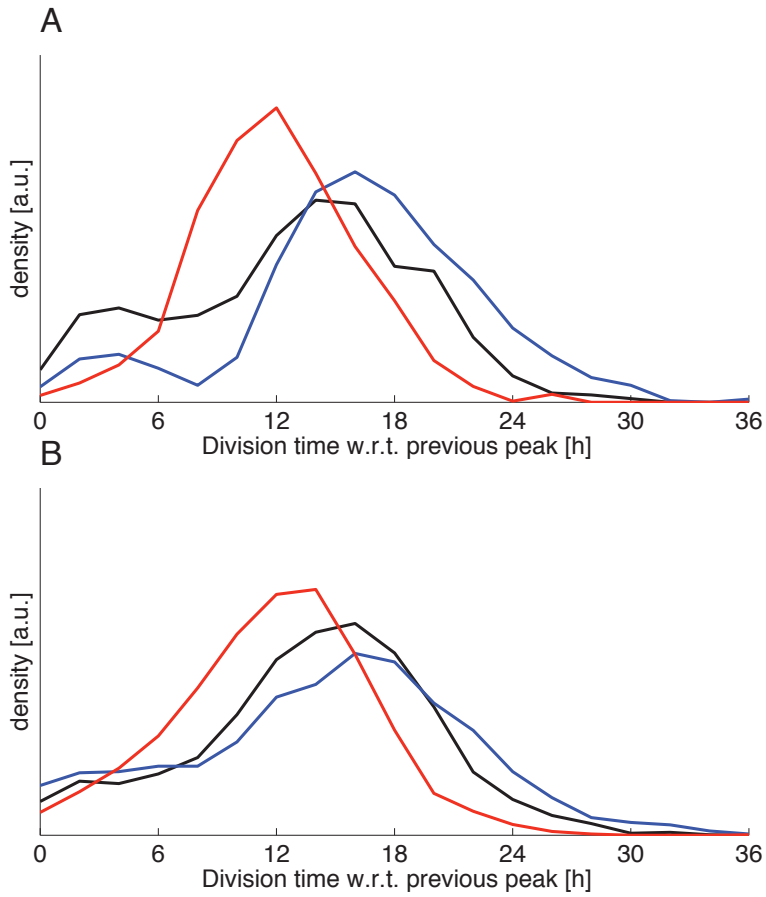

Figure S9. Distributions of division times measured with respect to the previous circadian peak in temperature experiments.

A. Division times measured with respect to the previous circadian peak are strongly affected by temperature (blue: 34 ºC, black 37 ºC, red: 40 ºC). B. Division times measured with respect to the previous circadian peaks in the model.

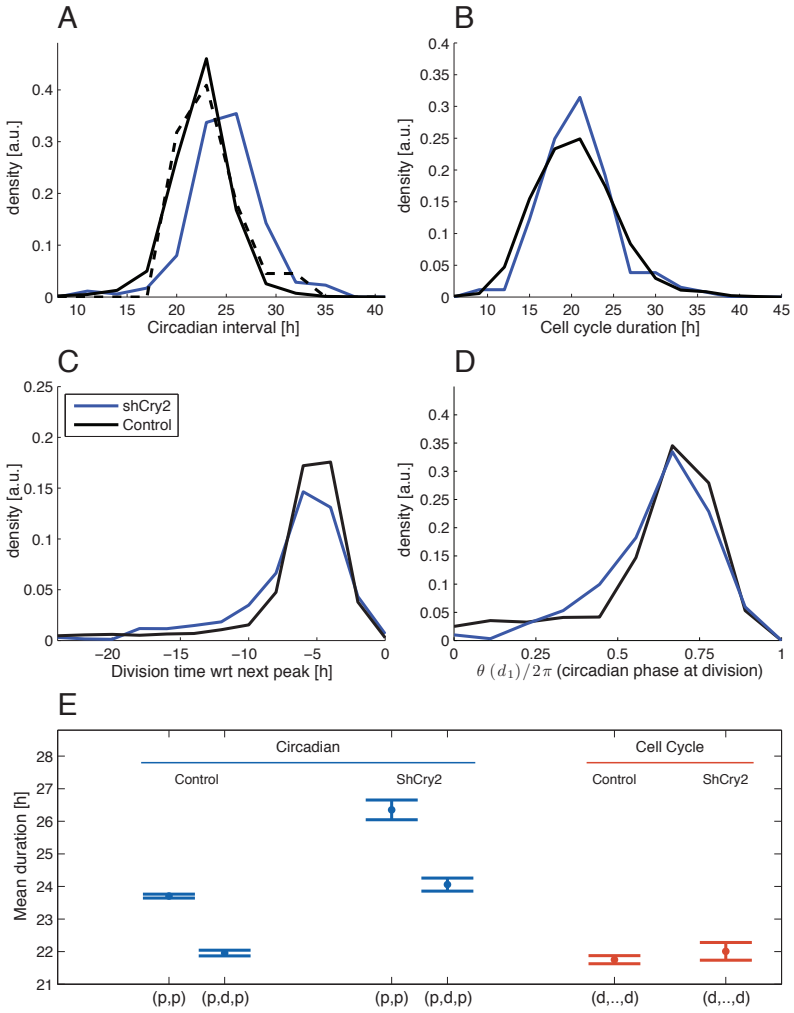

Figure S10. Cry2 deficient cells with longer circadian periods.

A. Circadian intervals (p_1,p_2) in shCry2 cells are significantly longer than controls ($p<0.02$ for Scramble shRNA cells in dashed black and $p<10^{-16}$ for the 37 ºC dataset in solid black, t-tests). Means are 26.3 +/- 4 in shCry2 and 23.7 +/- 3.1 in the controls. B. The cell cycle duration is unaffected in shCry2 cell line ($p<0.19$, t-test). C. The intervals from divisions to the next circadian peaks (d,p) are slightly lengthened in shCry2 cell line ($p<4.8\times10^{-5}$, Kolmogorov–Smirnov test, K-S). D. The circadian phases at division are slightly advanced in shCry2 cells compared to controls (while the K-S test is not significant; $p<0.008$, bootstrapped two-sample Kuiper test). E. Mean circadian intervals with divisions are significantly shorter than intervals without divisions in both control ($p<10^{-16}$, t-test) and shCry2 cells ($p<1.3\times10^{-10}$, t-test). Mean cell cycle durations is shown in red ($p<0.19$, cf. panel B). The error bars show the standard error on the mean. The total number of shCry2 cell traces analyzed is n=549.

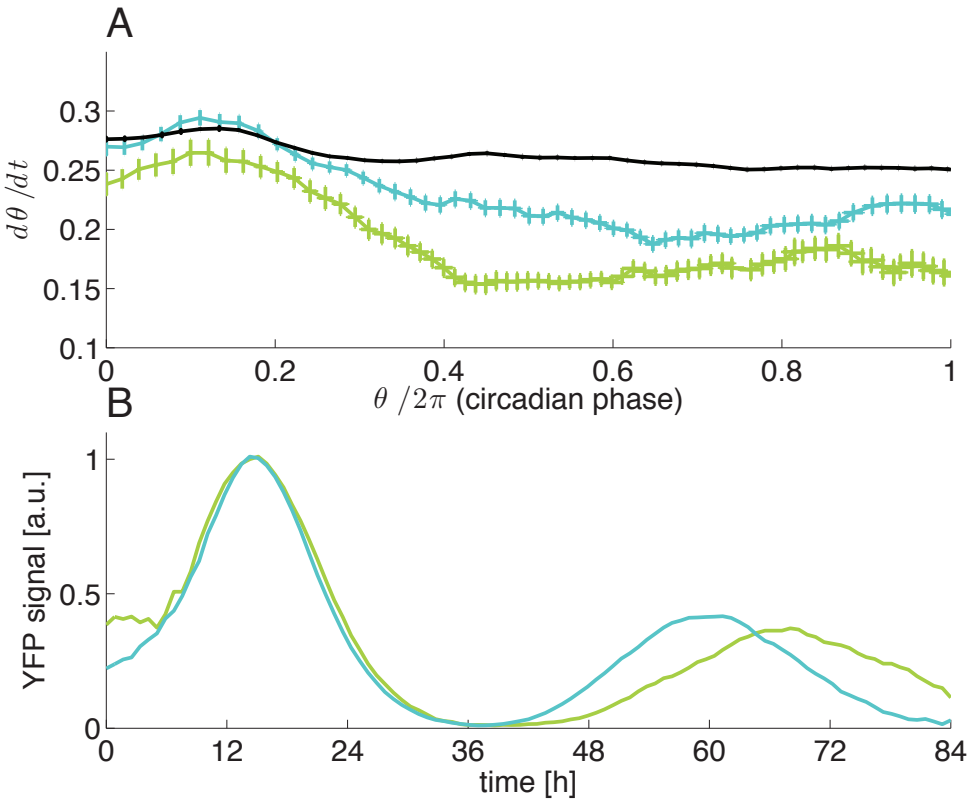

Figure S11: Instantaneous circadian phase progression under Longdaysin treatment

A. Instantaneous circadian phase velocity in intervals without divisions (p_1,p_2) is slowed down predominantly in the interval of low *Rev-Erb*α-YFP expression in dose dependent manner (Black: 37 ºC 0 μM Longdaysin, Blue: 1 μM Longdaysin, Green: 5 μM Longdaysin). B. Average of traces show that the waveform around the peak is unaffected but the 'off' interval is stretched. Standard errors on the estimated phase are shown, but are very small.

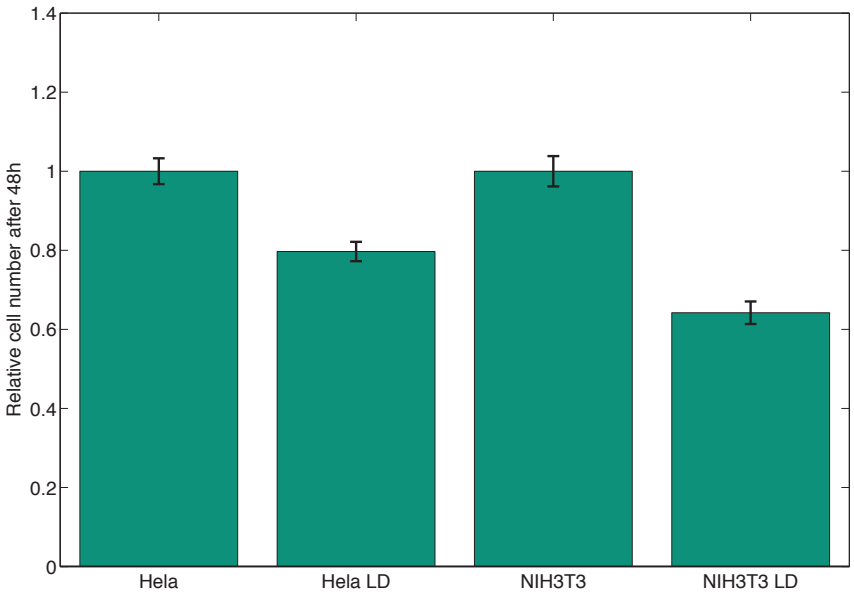

Figure S12. Longdaysin reduces cell cycle duration in NIH3T3-Venus and HeLa cells

Cell count normalized to the untreated condition after 48h of growth in presence of 5μM Longdaysin (LD) or DMSO controls. The error bars show standard error on the mean (SEM) from n=18 (HeLa DMSO), n=11 (HeLa + LD), n=18 (NIH3T3-Venus), n=18 (NIH3T3-Venus + LD) samples. The number of Longdaysin cells is significantly reduced in both cell lines ($p<1.4\ 10^{-4}$ in HeLa cells, and $p<10^{-8}$ in NIH3T3-Venus, t-tests).

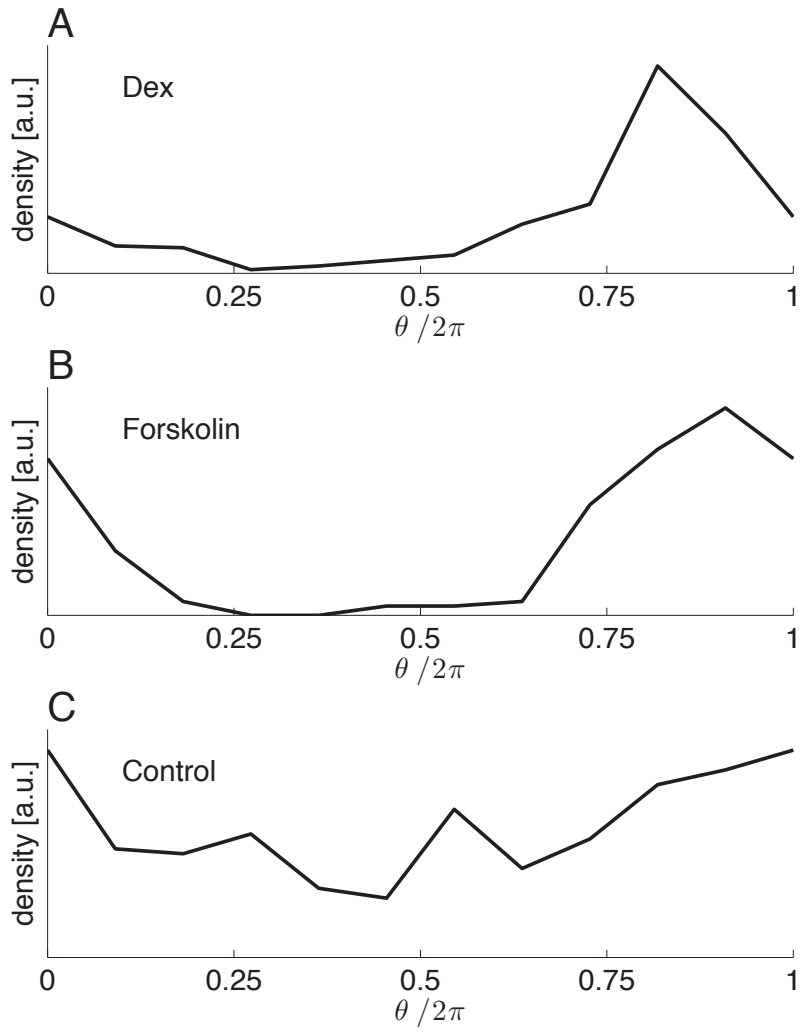

Figure S13. Initial phase distribution in dexamethasone, forskolin and control conditions.

A-C. Circadian phase distribution during the first hour after the start of the recordings. The phases were estimated as explained in Supplementary Information section IV. These distributions are clearly more peaked in the dexamethasone and forskolin treatments than in control, as expected. Synchronization indices used in Figure 7 can be computed from these distributions.

A.2 Stimulus-induced modulation of transcriptional bursting in a single mammalian gene.

A.2.1 Context

During my thesis work I had the opportunity to collaborate to the realization of a work entitled "Stimulus-induced modulation of transcriptional bursting in a single mammalian gene" published in the PNAS Journal in 2013, from the following authors: Nacho Molina, David M. Suter (equally contributing), Rosamaria Cannavo, Benjamin Zoller, Ivana Gotic and Felix Naef [Molina et al., 2013].

This work aimed at understanding how transcriptional bursting is modulated upon different types of stimulations. More specifically, transcriptional responses of the endogenous connective tissue growth factor gene (CTGF) gene were monitored upon two different physiological stimuli in NIH3T3 cells. The *ctgf* gene encodes a secreted protein involved in wound healing and response to shear stress, and its expression can be stimulated by shear stress, serum shock, or TGF-β1. The NIH3T3 gt:ctgf cell line used in this study, generated by gene trap insertion of a short-lived luciferase in exon 5 of CTGF, was monitored via single-cell time-lapse luminescence imaging and luminescence recordings at the population level. The two different responses to serum and TGF-β1 were analyzed using stochastic modeling. The analysis showed that both stimuli cause acute increase in transcriptional activation characterized by transiently modified gene activities. However, whereas the TGF-β1 showed prolonged transcriptional activation mediated by an increase of transcription rate, serum stimulation induced a large and peaked first transcriptional burst, followed by a refractory period in the range of hours. Overall, this study provided insights on the understanding of transcriptional bursting kinetics upon different physiological stimulations.

My contribution to this work consisted in the design and realization of the experiments concerning the stimulation with both, serum and TGF-β1 at the population level, with the use of luminescence recordings. These experiments, summarized in Figure 5 and Figures S2, S3, S4 and S5 of the manuscript, allowed identifying several characteristics of the transcriptional responses. With these experiments it was possible to highlight: i) the existence of a 3 hours refractory period occurring after the first transcriptional upon serum stimulation; ii) the lack of contribution of post-transcriptional mechanisms in the observed responses; iii) a very little contribution of increased translational efficiency in the responses, confirming that induction of transcription is the dominating cause of the observed response.

A.2.2 Manuscript

Stimulus-induced modulation of transcriptional bursting in a single mammalian gene

Nacho Molina[a,1], David M. Suter[b,1,2,3], Rosamaria Cannavo[a], Benjamin Zoller[a], Ivana Gotic[b], and Félix Naef[a,3]

[a]Institute of Bioengineering, School of Life Sciences, Swiss Institute of Bioinformatics, Ecole Polytechnique Fédérale de Lausanne, CH-1015 Lausanne, Switzerland; and [b]Department of Molecular Biology, Sciences III, National Centre of Competence in Research Frontiers in Genetics, University of Geneva, CH-1211 Geneva, Switzerland

Edited by Charles S. Peskin, New York University, New York, NY, and approved November 11, 2013 (received for review June 28, 2013)

Mammalian genes are often transcribed discontinuously as short bursts of RNA synthesis followed by longer silent periods. However, how these "on" and "off" transitions, together with the burst sizes, are modulated in single cells to increase gene expression upon stimulation is poorly characterized. By combining single-cell time-lapse luminescence imaging with stochastic modeling of the time traces, we quantified the transcriptional responses of the endogenous connective tissue growth factor gene to different physiological stimuli: serum and TGF-β1. Both stimuli caused a rapid and acute increase in burst sizes. Whereas TGF-β1 showed prolonged transcriptional activation mediated by an increase of transcription rate, serum stimulation resulted in a large and temporally tight first transcriptional burst, followed by a refractory period in the range of hours. Our study thus reveals how different physiological stimuli can trigger kinetically distinct transcriptional responses of the same gene.

stochastic gene expression | single-cell dynamics | computational modeling

Cells have evolved to respond to temporally varying signals and stresses. Such responses typically involve tuning the expression of few to thousands of genes, reflecting a dynamic interplay between epigenetic, transcriptional, and posttranscriptional processes that collectively determine temporal profiles of mRNA and protein numbers in individual cells (1). In particular, kinetic studies in mammalian cell populations showed that the synthesis and degradation rates of mRNA can be quickly regulated upon stimulation (2, 3). For instance, in stimulated dendritic cells, the majority of changes in mRNA levels reflected regulation at the transcriptional level, whereas regulated mRNA degradation was essential for shaping fast and peaked responses (2).

At the level of single eukaryotic cells, several studies shed light on how processes upstream of transcription respond to stimulation, such as mechanisms that influence the nuclear accumulation of specific transcription factors, or their DNA binding kinetics after stimulation. In yeast, the timing of transcriptional bursts in target genes of calcineurin-responsive zinc finger 1 (Crz1) follows the nucleocytoplasmic shuttling frequency of the Crz1 transcription factor (4). Also, the binding of the transcription activator Ace1p onto a specific gene promoter showed fast and slow cycling dynamics upon copper induction (5). In mammalian cells, the nuclear shuttling kinetics (6), DNA residence time, and DNA-bound fractions of the ligand-bound glucocorticoid receptor were measured (7, 8). Other examples of stimulus-regulated transcription factor activity include the modulation of nucleocytoplasmic shuttling of p53 after irradiation (9, 10) and the dose-responsive nuclear accumulation and shuttling frequency of NF-κB (11, 12). However, much less is known about how such activities eventually modulate the transcriptional output in single cells.

Although many studies of stochastic gene expression relied on modeling population heterogeneity from temporal snapshots (13–16), real-time imaging of transcriptional bursting in single cells opened the possibility to develop temporal stochastic modeling as a powerful framework to extract kinetic parameters on the bursting process in individual cells (17–20). In this context, monitoring transcriptional output of native mammalian gene promoters in single cells (under constant environmental conditions) showed that transcription typically occurs during short windows of activity interspersed with silent periods (17, 18, 21). In particular, by using a single copy of a short-lived transcriptional reporter, we showed that the bursting patterns are gene-specific (18), and identified a refractory period in the range of hours characterizing intervals of gene inactivity, a finding that was confirmed by others (17). Perturbation experiments to increase the permissivity of chromatin for transcription showed that elevated histone acetylation levels do not dramatically influence the bursting characteristics on short time scales (18), and stimulation of a signaling pathway involved in the expression of a particular gene with small molecules led to an increase in average bursting frequency (17). However, how transcriptional bursting in individual cells responds dynamically to physiological stimuli remains largely unexplored.

Here, we used single-cell monitoring of transcription at high temporal resolution to quantify the transcriptional response of a single endogenous allele of the connective tissue growth factor (*ctgf*) gene to two different physiological stimuli. *Ctgf* encodes a secreted protein that plays an important role in wound healing

Significance

Recent single-cell studies showed that gene transcription in mammals is fundamentally stochastic, occurring in short and intense transcriptional bursts. However, less is known on how transcriptional bursting is modulated upon stimulation. Here, we monitor the transcriptional response of a single allele of the endogenous *connective tissue growth factor* gene, encoding a secreted protein involved in wound healing and response to shear stress, to two different physiological stimuli in single cells. Analysis using stochastic modeling shows that both stimuli cause acute transcriptional responses characterized by transiently modified gene activities, and increased transcription rates that may last longer depending on the stimulus. These results provide insights on how transcriptional bursting kinetics can be adjusted to increase gene expression upon physiological stimulations.

Author contributions: N.M., D.M.S., and F.N. designed research; N.M., D.M.S., R.C., B.Z., and I.G. performed research; R.C. and B.Z. contributed new reagents/analytic tools; F.N. supervised research; N.M. and D.M.S. analyzed data; and N.M., D.M.S., and F.N. wrote the paper.

The authors declare no conflict of interest.

This article is a PNAS Direct Submission.

Freely available online through the PNAS open access option.

[1]N.M. and D.M.S. contributed equally to this work.

[2]Present address: Institute of Bioengineering, School of Life Sciences, Ecole Polytechnique Fédérale de Lausanne CH-1015 Lausanne, Switzerland.

[3]To whom correspondence may be addressed. E-mail: david.suter@epfl.ch or felix.naef@epfl.ch.

This article contains supporting information online at www.pnas.org/lookup/suppl/doi:10.1073/pnas.1312310110/-/DCSupplemental.

and response to shear stress, and its expression can be stimulated by shear stress, serum shock, or TGF-β1 in cultured fibroblasts (22). We show that serum treatment rapidly induces an intense window of transcriptional activity, followed by a period refractory to restimulation. In contrast, TGF-β1 stimulation resulted mainly in a prolonged increase in transcription rate (k_m) without affecting "on–off" switching kinetics. Thus, different physiological stimuli can trigger kinetically distinct transcriptional responses of the same gene, suggesting that switching kinetics in gene activity is transiently modulated whereas k_m values dominate the longer-term adjustment of transcriptional output.

Results

Serum or TGF-β1 Stimulation of *ctgf* Induce Qualitatively Different Transcriptional Responses. In principle, the modulation of transcriptional bursting in response to a physiological stimulus could exhibit a large spectrum of behaviors depending on the stimulation modalities, promoter architecture, and wiring of the signaling pathways. In terms of a commonly used model of transcriptional bursting (Fig. 1*A*), the stimulation could increase the frequency of bursts by shrinking the duration of inactive periods, or it may increase burst sizes by lengthening the duration of active periods or up-regulating the k_m (Fig. 1*B*). All three scenarios cause a higher effective synthesis rate of mRNA molecules. To test which scenario(s) occur in mammalian cells, we focused on the response of the endogenous *ctgf* gene. Among different inducers of *ctgf* expression, we chose to study serum stimulation, acting through the Rho/Mal/SRF pathway (23), and TGF-β1, acting through the TGF-β receptor/SMAD signaling pathway (22). We monitored transcriptional activity by using our previously engineered destabilized luciferase reporter with a 1-min time resolution for approximately 12 h. Briefly, this reporter consists of a short-lived luciferase inserted into exon 5 of the *ctgf* gene, allowing luciferase expression to be strictly controlled by the endogenous *ctgf* regulatory sequences. Luciferase expression can be monitored by luminescence microscopy in single cells at high temporal resolution, and used to infer the temporal sequence of gene activity windows and the k_m of *ctgf* as described previously (18). Compared with mock induction, serum shock at two different concentrations rapidly induced a large peak of luminescence lasting several hours, followed by a fast decay of the signal to its basal level (Fig. 1*C* and *SI Appendix*, Fig. S1). In contrast, TGF-β1 stimulation induced a longer-lasting response (Fig. 1*C*), typically manifesting itself as a succession of distinct bursts.

We then assessed whether the observed responses to both stimuli could be caused by posttranscriptional mechanisms altering protein stability, mRNA stability, or translational efficiency of the reporter. First, we measured protein and mRNA half-life by quantifying the decay in bulk luciferase activity after blocking translation or transcription with cycloheximide or actinomycin D treatments, respectively. We performed experiments before induction, at 1 or 10 h after serum stimulation, and at 2 or 10 h after TGF-β1 stimulation (*SI Appendix*). The luciferase protein half-life was not affected by the stimulation (*SI Appendix*, Figs. S2 and S3), and the mRNA half-life was also similar across conditions (*SI Appendix*, Figs. S4 and S5). Next, we investigated whether the induction could reflect an increase in translational efficiency upon stimulation, rather than increased transcription. We stimulated cells with serum or TGF-β1 and simultaneously blocked transcription with actinomycin D. The absence of response

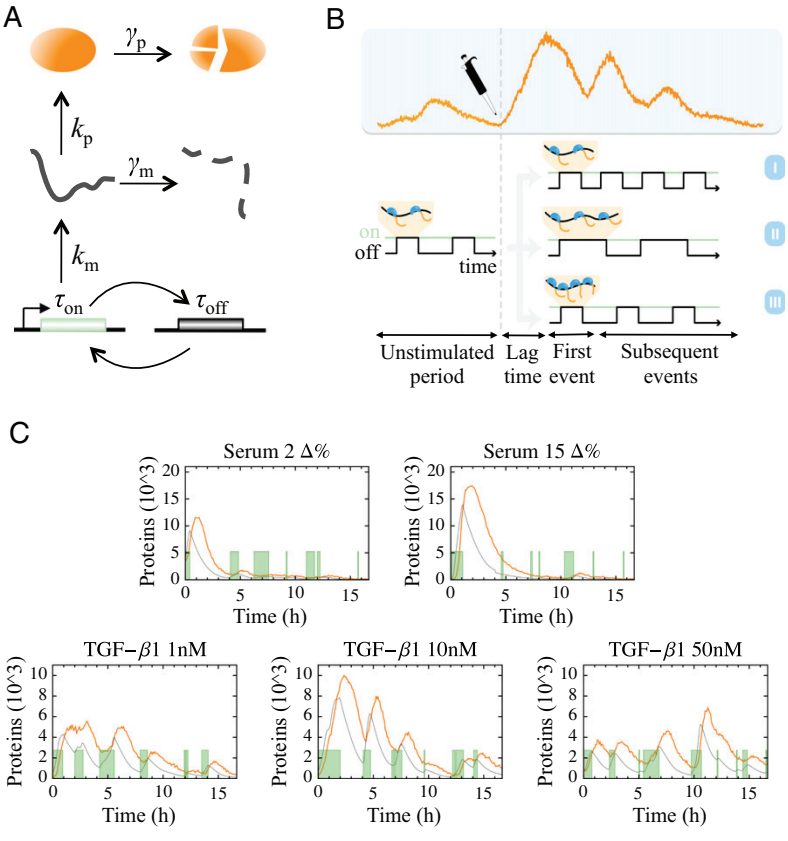

Fig. 1. Transcriptional bursting of the *ctgf* gene after serum or TGF-β1 stimulation. (*A*) Two-state prior model of gene expression: the gene promoter can switch between active (on) and inactive (off) states, and this stochastic process is characterized by the time scales τ_{on} and τ_{off}. During the "on" state, transcription can occur at constant rate k_m. Protein translation is described by the rate k_p. mRNA and protein degradation are modeled as Poissonian processes with rates γ_m and γ_p, respectively. All rates can, in principle, be changed upon gene stimulation, either transiently or in a sustained manner. (*B*) Inducing gene transcription can, in principle, be achieved by modifying the frequency (*I*) or the duration (*II*) of transcriptional bursts, as well as by increasing the k_m (*III*). (*C*) Sample single-cell luminescence traces (orange) showing responses to different stimuli as well as inferred times traces of the number of mRNA molecules (black) and gene states (green).

(*SI Appendix*, Fig. S6) suggested that induction of transcription is the dominating cause for the response, as translational efficiency was not strongly up-regulated after serum or TGF-β1 stimulation. Thus, stimulation of the same gene with different physiological stimuli can trigger qualitatively distinct transcriptional responses in single cells.

Serum and TGF-β1 Induce Dose-Dependent Increase in k_m Values. To further investigate which parameters underlie the responses in function of stimulation strength, we first assessed whether the responses were homogenous across the cell population, as stimulations in other systems can lead to digital response across cell populations (12, 24–26). Over the range of tested inducer concentrations, we observed that nearly all cells responded to both stimuli (Fig. 2*A* and *SI Appendix*, Fig. S7).

Next, we quantified how *ctgf* transcriptional kinetics changes in function of stimulus type and strength by analyzing the time traces using stochastic modeling of gene expression, as described previously (18). Briefly, the method includes two steps (*SI Appendix*). First, we compute the likelihood of the time traces according to a minimal model of gene expression, hereafter called the prior. To keep the number of parameters low, this prior models protein and mRNA numbers as birth–death processes controlled by an underlying two-state promoter model, and all rates are constant in time (Fig. 1*A*). Following our analyses (*SI Appendix*, Figs. S2–S6), we fixed mRNA and protein $t_{1/2}$s, as well as translation rates, to be the same in all tested conditions. The remaining transcriptional parameters ["on" time (τ_{on}), "off" time (τ_{off}), and k_m] are then calibrated via Markov chain Monte Carlo (MCMC) sampling. The second, and key, step is to estimate (by using Gibbs sampling) mRNA numbers and promoter state at each time point along the traces (Fig. 1*C*). Importantly, we showed previously that this allows to reliably identify bursting statistics that deviate form those of the prior itself (18) (*SI Appendix*).

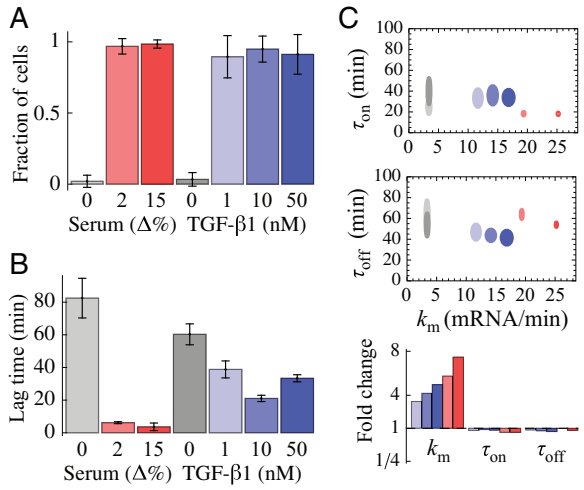

Fig. 2. Nearly all cells respond to both stimuli by changing the k_m in a dose-dependent manner. (*A*) Percentage of cells responding to each stimulus (*SI Appendix*, Fig. S7). (*B*) Response lag time to serum and TGF-β1. Cells responded after a short (~5 min) lag time in the case of serum stimulation and longer (~30 min) in the case of TGF-β1 stimulation. (*C*) Transcriptional parameters estimated from the model (*SI Appendix*, Table S1). k_m is correlated with stimulus concentration, whereas mean τ_{on} and τ_{off} values remain unchanged across all conditions. Control conditions are shown in gray, and colors are as in *A* and *B*. Ellipses indicate posterior SDs. In total, 458 cells were analyzed (*SI Appendix*).

Applying this methodology, we found that stimulation with serum or TGF-β1 resulted in a rapidly occurring first transcriptional burst. Remarkably, serum stimulation induced a transcriptional response within a few minutes, approximately 10 times faster than TGF-β1 stimulation (Fig. 2*B*), and these response times did not vary much with the stimulus dose. Similarly, the durations of τ_{on} and τ_{off} were comparable to control conditions (Fig. 2*C*). In contrast, k_m values were positively correlated with serum or TGF-β1 concentration (Fig. 2*C* and *SI Appendix*, Table S1). Thus, although the vast majority of cells responded to all doses of the stimuli (Fig. 2*A*), the graded k_m values indicated that the concentrations used did not simply saturate the response. In summary this shows that, independently of the activation pathway, the bulk transcriptional response reflected predominantly a dose-dependent increase in the k_m (Fig. 2*C*).

Transient (Serum) or Sustained (TGF-β1) Increase in k_m Values Distinguishes the Two Responses. We next determined how the transcriptional kinetics changed over time in response to the stimulations. By using Gibbs sampling to reconstruct temporal profiles of gene activity and mRNA number (*SI Appendix*), we computed the duration of each τ_{on}, the effective k_m associated with it, and the duration of the following τ_{off} in each cell (*SI Appendix*). We then summarized those quantities across all cells (Fig. 3). Upon serum induction, the duration of the first transcriptional burst (i.e., τ_{on}) was approximately two times longer than in control conditions (Fig. 3*A*). The k_m in the same time interval was increased by more than fivefold compared with baseline levels (Fig. 3*B*), showing values close to 40 mRNA molecules per minute [65% of the maximal possible k_m reached when elongation becomes limiting for initiation (27)]. Remarkably, the corresponding burst size (b; i.e., $k_m \cdot \tau_{on}$) was approximately 1,700 mRNA molecules, two orders of magnitude larger than the typical values observed in unperturbed cells (18). In addition, the period of gene inactivity immediately following this first transcriptional event was clearly prolonged by more than threefold compared with the subsequent events or control conditions (Fig. 3*C*). Then, within a few hours, transcriptional parameters relaxed to values close to steady-state activity (Fig. 3 *A*–*C*).

Similarly to serum induction, TGF-β1 induced a two- to threefold increase in the duration of the first transcriptional interval (Fig. 3*D*) and also increased k_m values by three- to fourfold, producing burst sizes as large as 1,200 mRNA molecules. However, this effect was much more prolonged compared with serum, lasting throughout the whole recording (Fig. 3*E*, compare with Fig. 3*B*). Unlike we found for serum induction, TGF-β1 did not affect the duration of gene inactivity intervals after stimulation (Fig. 3*F*, compare with Fig. 3*C*).

To verify that the estimated temporally varying parameters were not biased (as a result of a too-rigid prior model), we performed simulations mimicking a situation similar to the serum case, in which τ_{on}, τ_{off}, and k_m values are increased following stimulation before relaxing to the baseline. Analyzing those simulations (by using the exact same methodology) clearly showed that all three quantities can be accurately estimated (*SI Appendix*, Fig. S10*A*). This indicates that the two-state prior model is flexible enough, and the data sufficiently informative, to reliably identify the parameters underlying temporally nonhomogenous transcriptional bursting.

Thus, the transcriptional response of the same gene to two different stimuli exhibits qualitatively distinct temporal characteristics. Most importantly, the first activity period after serum stimulation is followed by a long refractory period in the range of several hours, which is not the case for TGF-β1. In addition, most parameters relaxed to their control values in less than 4 h, except for the k_m following TGF-β1 stimulation. It also appears that the acute transcriptional response reflects mainly increased

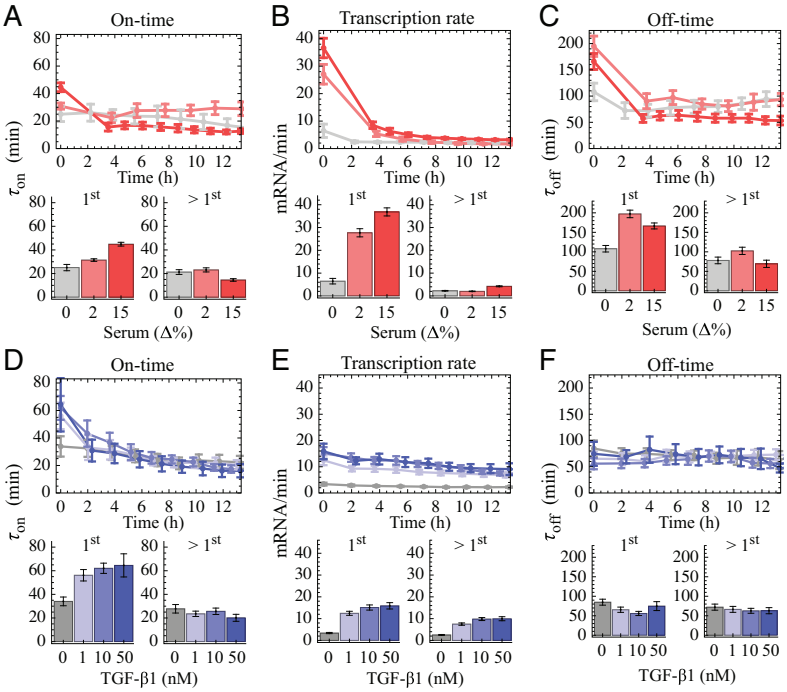

Fig. 3. Temporal analysis shows that the response is mediated by increased k_m values transiently (serum) or in a sustained manner (TGF-β1). (*A* and *D*) Temporal behavior of τ_{on}, (*B* and *E*), k_m, and (*C* and *F*) τ_{on} and τ_{off} values. (*Upper*) Variations of parameters in function of time. Temporal analysis of transcriptional events was obtained with Gibbs sampling (*SI Appendix*). Mean ± 2SEM over the individual cells are indicated. Bar plots show data separately for the first transcriptional event (*Left*, "1st"), and grouped subsequent transcriptional events (*Right*, ">1st").

k_m values (and burst sizes), and not increased bursting frequency (Fig. 1*B*).

The Duration of the First Transcriptional Burst Is Tightly Regulated After Serum Stimulation. We previously reported that, at steady state, transcription bursts of many genes, including *ctgf*, are switched off in a single rate-limiting step, resulting in exponentially distributed τ_{on} values. In contrast, most genes showed peaked τ_{off} values, suggesting that the transition from "off" to "on" involves several regulatory steps. However, *ctgf* was atypical, as τ_{on} and τ_{off} values were distributed exponentially (18). Here we found that, following a shortened inactivity period after stimulation (Fig. 2*B*), the duration of the first transcriptional event (τ_{on}) showed a clear maximum around 20 to 40 min after induction with serum (Fig. 4*A*), and a reduced coefficient of variation (Fig. 4*A*, *Inset*). TGF-β1 showed a similar, although less pronounced, behavior (Fig. 4*B*). In contrast, the subsequent τ_{on} values were exponentially distributed independently of the stimulus (*SI Appendix*, Fig. S8*A*). This suggests that regulatory mechanisms exert a tight control on the first transcriptional event, preventing *ctgf* from switching off for a certain amount of time, resulting in peaked, nonexponentially distributed, τ_{on} values. We verified, by using simulations, that the computational methodology based on a two-state prior can reliably distinguish between peaked τ_{on} values after stimulation, followed by relaxation to exponentially distributed τ_{on} values (*SI Appendix*, Figs. S9 and S10*B*).

A 3-h-Long Refractory Period Occurs Following the First Transcriptional Event After Serum Stimulation. Upon serum induction, we observed an inactivity period after the first transcriptional event lasting, on average, twice as long (Fig. 3*C*), and whose distribution was more peaked (Fig. 5*A*), compared with the unstimulated control and the subsequent inactivity periods (*SI Appendix*, Fig. S8*B*). Neither effect occurred in the case of TGF-β1 stimulation (Figs. 3*F* and 5*B* and *SI Appendix*, Fig. S8*B*). Simulations indicated that the computational analysis could efficiently distinguish between peaked and exponentially distributed τ_{off} values (*SI Appendix*, Figs. S9 and 10*B*). Moreover, a model selection technique (reversible jump MCMC; *SI Appendix*, Fig. S11) allowing us to automatically choose between exponential and peaked distributions, for both the τ_{on} and τ_{off} values, confirmed that the first transcriptional event and following τ_{off} favor models with peaked τ_{on} and τ_{off} values after serum stimulation, whereas the exponential models are preferred for the subsequent transcriptional events in all cases (*SI Appendix*, Fig. S12 and Table S2). Together with the other simulations (*SI Appendix*, Figs. S9 and S10), this shows that the simpler and computationally much more tractable two-state prior leads to quantitatively accurate inference in temporally nonhomogenous situations characterized by changing parameters and/or distribution types.

To further investigate whether the prolonged inactivity period after serum stimulation reflected a state that was refractory to transcription, we restimulated cells with serum after varying delays relative to the first stimulation. We observed a response to the second stimulation only when the time interval between the two stimulations was at least 4 h (Fig. 5 *C*–*F*). Therefore, serum stimulation of the *ctgf* gene induced an acute transcriptional burst followed by a period of inactivity that is refractory to serum restimulation.

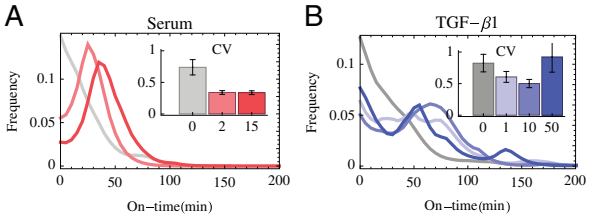

Fig. 4. The duration of the first transcriptional event is tightly regulated after serum stimulation. Distributions of τ_{on} values for the first transcriptional burst after serum stimulation (*A*) and TGF-β1 stimulation (*B*). (*Insets*) Coefficients of variation (CV; SD over mean) of plotted distributions.

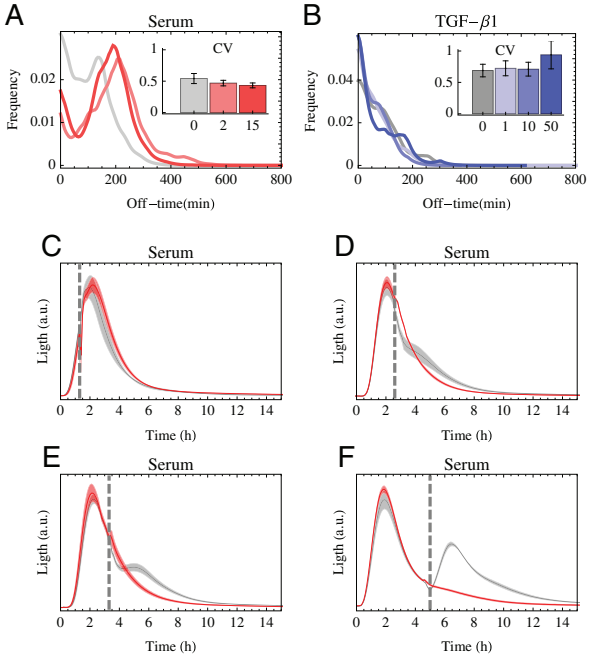

Fig. 5. A 3-h refractory period occurs following the first transcriptional event after serum stimulation. The τ_{off} distributions of the first inactivity period after serum stimulation (*A*) or after TGF-β1 stimulation (*B*). (*Insets*) CVs. (*C*–*F*) Cell population responses to serum restimulation with fresh medium (red) or after removal and addition of the same medium (control, gray). Initial stimulation is at time 0 and restimulation (gray dashed lines) after 70 min (*C*), 130 min (*D*), 210 min (*E*), and 270 min (*F*). Cells do not respond during the refractory period lasting ~200 min.

Discussion

Previous quantitative analysis of single mammalian cells at steady state have shown that gene expression is governed by stochastic episodes of gene activity resulting in asynchronous transcriptional bursts (28). These studies prompted us to investigate how transcriptional bursting might be temporally modulated in response to physiological stimulations.

Monitoring an Acute Transcriptional Response in Single Mammalian Cells. We used high temporal resolution microscopy in single mammalian cells to quantify how a single allele of the *ctgf* gene responds to two different external stimuli, serum and TGF-β1, acting via distinct pathways. Although both rapidly triggered transcriptional bursts (within minutes), as is typical for primary response genes (9, 29), the response induced by serum occurred significantly faster compared with TGF-β1 (Fig. 2*B*). Moreover, the longer-term response (up to 8 h after stimulation) showed interesting differences. Serum essentially triggered one large and tightly controlled response, after which the transcriptional activity relaxed to steady state. This single response was characterized by a refractory period, lasting approximately 3 h, during which cells were insensitive to restimulation. Although the underlying molecular mechanisms are unknown, several negative feedback loops in the MRTF/SRF pathway involving decreased SRF activity by actin expression (30) or decreased SRF expression by miR-133 induction (31) might contribute to establish and maintain this refractory period. Although the properties of "on" and "off" switching after TGF-β1 stimulation also rapidly relaxed to steady state, this stimulus induced a longer lasting series of transcriptional events characterized by an increased k_m. Interestingly, this suggests that some stimuli can increase k_m values (and hence burst size) in a sustained manner, without altered promoter switching kinetics.

Challenges for Stochastic Modeling of Gene Expression. Regarding the model-based quantification of transcriptional bursting, the stimulated situation is significantly more complex than at steady state, as the transcriptional parameters (including parameter values and statistics of τ_{on} and τ_{off}) may change during the acquisition time in a way that is not a priori known. Here, we have taken the first steps to generalize the methodology, by using the reversible jump MCMC model selection technique. This explicitly allows for peaked τ_{on} and τ_{off} in the prior models (in addition to the exponential ones) and lets the data select the optimal model. This confirmed that, indeed, the first transcriptional events after serum stimulation show preference for nonexponentially distributed "on" and "off" states (*SI Appendix*, Fig. S12). However, we also emphasized that the simple two-state prior model (when used in combination with Gibbs sampling) is flexible enough for a quantitatively correct inference.

Implications for *ctgf* Function. Although the biological significance of the stimulus-dependent temporal profiles of *ctgf* induction remains puzzling, the physiological contexts in which different stimuli act may provide some clues. TGF-β is an important mediator of wound healing, and acts in part by stimulating *ctgf* expression that induces fibroblast proliferation and production of extracellular matrix (22). As this process typically occurs over a period of several days, a sustained TGF-β–mediated CTGF up-regulation might be necessary for completion of wound repair. The strong and transient response to serum stimulation is harder to interpret, as the nature of the serum molecule(s) inducing up-regulation of *ctgf* is not known. However, like serum stimulation, mechanical stress also induces *ctgf* expression via the RhoA/MRTF/SRF signaling pathway (22, 32) and might thus generate similar temporal responses of *ctgf* induction. In endothelial cells lining blood vessels, *ctgf* expression is induced by shear stress (22) and regulates endothelial cell adhesion, migration, and the production of basal lamina (33–35). As shear stress in blood vessels can change on very short time scales, the rapid up-regulation of *ctgf* might allow for fast adjustment of the cytoskeleton and the adhesive properties of endothelial cells, and its rapid shutdown after a first period of activity might be necessary to avoid undesired tissue remodeling as observed during wound repair.

In conclusion, single-cell recordings of transcriptional activity in combination with computational modeling, as presented here, provides a powerful tool to shed light on how the kinetics of transcriptional bursting adjusts to modulate gene expression output upon physiological stimulation.

Materials and Methods

Detailed descriptions of the experimental and computational methods can be found in *SI Appendix*.

Cell Culture and Luminescence Imaging. The NIH 3T3 gt:ctgf cell line was generated by gene trap insertion of a short-lived luciferase in exon 5 of the connective tissue growth factor gene, as described earlier (18). Luminescence microscopy was performed by using an LV200 Luminoview microscope (Olympus) equipped with an EM-CCD cooled camera (EM-CCD C9100-13; Hamamatsu Photonics) as described previously (18), with an exposure time and time resolution of 1 min. For serum stimulation experiments, cells were cultured in 5% (vol/vol) FBS for at least 24 h before imaging, and induced by increasing serum concentration by 2% or 15%. For TGF-β1 (eBiosciences) induction, cells were continuously cultured in 10% serum. Stimulation with serum or TGF-β1 was performed 60 to 120 min after initial baseline recording by adding FBS or TGF-β1 to the cell culture dish without disturbing the imaging field. Analysis of time-lapse imaging was performed by manual tracking of single cells to quantify luminescence signals as previously described (18). Numbers of cells analyzed in each condition were as follows: control

serum ($n = 47$), serum +2% ($n = 90$), serum +15% ($n = 96$), TGF-β1 control ($n = 56$), TGF-β1 1 nM ($n = 47$), TGF-β1 10 nM ($n = 52$), and TGF-β1 50 nM ($n = 33$).

Fraction of Cells That Respond. To estimate the fraction of cells that respond to different stimuli, we computed the mean protein level for each cell measured within a window of 3 h after the addition of the stimulus. We first fitted a Gamma distribution to the mean expression levels obtained from the control cells. Then, we modeled the protein levels observed after gene induction by a two Gamma mixture model. The first Gamma distribution represents nonresponding cells, and therefore its parameters were fixed to the ones obtained from the control cells. The second γ-distribution represents the responding cells. The mixture coefficient is then the fraction of the cells that respond. We fitted the free parameters by using MCMC sampling.

Parameter Estimation. To estimate the transcriptional parameters, we used the computational method developed previously (18). Briefly, we computed the likelihood that the time traces of luciferase activity were generated by a simple stochastic gene expression model, whereby the gene can switch between and active and inactive state and transcription occurs in bursts only during the active periods (Fig. 1*A*). For this study, we introduced two modifications. First, to reduce the computation load, which was prohibitive given the high protein levels, we fixed the protein levels (instead of summing over all protein numbers) to their expected values from the established calibration curves, and filtered experimental noise on a (fast) time scale of 5 min. This procedure did not interfere with the longer time scales (i.e., τ_{on} and τ_{off}) estimated. Second, after stimulation, cells may not be in steady state anymore, and parameters could vary over time. We modeled this (extrinsic) variability, assuming that the k_m can take values between a lower bound of 0.2 molecule per minute to an upper bound of 1 mRNA per second (27) from a rescaled Beta distribution (*SI Appendix*). MCMC sampling from the posterior distribution was performed to estimate the two parameters of the β-distribution and the two time scales of the gene activation process τ_{on} and τ_{off} (*SI Appendix*).

Temporal Profiles of the Transcriptional Parameters. We used Gibbs sampling to draw mRNA accumulation and gene activity time traces from the corresponding posterior probability (*SI Appendix*). For each instance and each transcriptional event, we computed the length of the transcriptional active window and the length of the following inactive window. We estimated the burst size in each time interval as $b = \gamma t(m_f - m_o e^{-\gamma t})/(1 - e^{-\gamma t})$, where m_o and m_f are the initial and final amounts of mRNAs, and γ is the mRNA degradation rate. Then, we calculated the total burst size as the sum of the burst sizes in each time interval within an active window and the k_m as the total burst size divided by the duration of the active window (*SI Appendix*). Finally, we computed the response time as the time from the addition of the stimulus to the first active window of transcription.

ACKNOWLEDGMENTS. We thank Ueli Schibler for his support and scientific input, and Laura Symul for help with Fig. 1. The computations were performed at Vital-IT (www.vital-it.ch). The work in the laboratory of F.N. was supported by Swiss National Science Foundation Grant 31-130714 and European Research Council ERC-2010-StG-260667, and by the Ecole Polytechnique de Lausanne.

1. Orphanides G, Reinberg D (2002) A unified theory of gene expression. *Cell* 108(4): 439–451.
2. Rabani M, et al. (2011) Metabolic labeling of RNA uncovers principles of RNA production and degradation dynamics in mammalian cells. *Nat Biotechnol* 29(5):436–442.
3. Zeisel A, et al. (2011) Coupled pre-mRNA and mRNA dynamics unveil operational strategies underlying transcriptional responses to stimuli. *Mol Syst Biol* 7:529.
4. Cai L, Dalal CK, Elowitz MB (2008) Frequency-modulated nuclear localization bursts coordinate gene regulation. *Nature* 455(7212):485–490.
5. Karpova TS, et al. (2008) Concurrent fast and slow cycling of a transcriptional activator at an endogenous promoter. *Science* 319(5862):466–469.
6. Htun H, Barsony J, Renyi I, Gould DL, Hager GL (1996) Visualization of glucocorticoid receptor translocation and intranuclear organization in living cells with a green fluorescent protein chimera. *Proc Natl Acad Sci USA* 93(10):4845–4850.
7. McNally JG, Müller WG, Walker D, Wolford R, Hager GL (2000) The glucocorticoid receptor: Rapid exchange with regulatory sites in living cells. *Science* 287(5456): 1262–1265.
8. Gebhardt JCM, et al. (2013) Single-molecule imaging of transcription factor binding to DNA in live mammalian cells. *Nat Methods* 10(5):421–426.
9. Lahav G, et al. (2004) Dynamics of the p53-Mdm2 feedback loop in individual cells. *Nat Genet* 36(2):147–150.
10. Geva-Zatorsky N, et al. (2006) Oscillations and variability in the p53 system. *Mol Syst Biol* 2:0033.
11. Ashall L, et al. (2009) Pulsatile stimulation determines timing and specificity of NF-kappaB-dependent transcription. *Science* 324(5924):242–246.
12. Tay S, et al. (2010) Single-cell NF-kappaB dynamics reveal digital activation and analogue information processing. *Nature* 466(7303):267–271.
13. Raj A, Peskin CS, Tranchina D, Vargas DY, Tyagi S (2006) Stochastic mRNA synthesis in mammalian cells. *PLoS Biol* 4(10):e309.
14. Zenklusen D, Larson DR, Singer RH (2008) Single-RNA counting reveals alternative modes of gene expression in yeast. *Nat Struct Mol Biol* 15(12):1263–1271.
15. Octavio LM, Gedeon K, Maheshri N (2009) Epigenetic and conventional regulation is distributed among activators of FLO11 allowing tuning of population-level heterogeneity in its expression. *PLoS Genet* 5(10):e1000673.
16. Neuert G, et al. (2013) Systematic identification of signal-activated stochastic gene regulation. *Science* 339(6119):584–587.
17. Harper CV, et al. (2011) Dynamic analysis of stochastic transcription cycles. *PLoS Biol* 9(4):e1000607.
18. Suter DM, et al. (2011) Mammalian genes are transcribed with widely different bursting kinetics. *Science* 332(6028):472–474.
19. Larson DR, Zenklusen D, Wu B, Chao JA, Singer RH (2011) Real-time observation of transcription initiation and elongation on an endogenous yeast gene. *Science* 332(6028):475–478.
20. Stratmann M, Suter DM, Molina N, Naef F, Schibler U (2012) Circadian Dbp transcription relies on highly dynamic BMAL1-CLOCK interaction with E boxes and requires the proteasome. *Mol Cell* 48(2):277–287.
21. Muramoto T, et al. (2012) Live imaging of nascent RNA dynamics reveals distinct types of transcriptional pulse regulation. *Proc Natl Acad Sci USA* 109(19):7350–7355.
22. Samarakoon R, Goppelt-Struebe M, Higgins PJ (2010) Linking cell structure to gene regulation: signaling events and expression controls on the model genes PAI-1 and CTGF. *Cell Signal* 22(10):1413–1419.
23. Philippar U, et al. (2004) The SRF target gene Fhl2 antagonizes RhoA/MAL-dependent activation of SRF. *Mol Cell* 16(6):867–880.
24. Ko MS, Nakauchi H, Takahashi N (1990) The dose dependence of glucocorticoid-inducible gene expression results from changes in the number of transcriptionally active templates. *EMBO J* 9(9):2835–2842.
25. Podtschaske M, et al. (2007) Digital NFATc2 activation per cell transforms graded T cell receptor activation into an all-or-none IL-2 expression. *PLoS ONE* 2(9):e935.
26. Kar P, Nelson C, Parekh AB (2012) CRAC channels drive digital activation and provide analog control and synergy to Ca(2+)-dependent gene regulation. *Curr Biol* 22(3): 242–247.
27. Suter DM, Molina N, Naef F, Schibler U (2011) Origins and consequences of transcriptional discontinuity. *Curr Opin Cell Biol* 23(6):657–662.
28. Coulon A, Chow CC, Singer RH, Larson DR (2013) Eukaryotic transcriptional dynamics: from single molecules to cell populations. *Nat Rev Genet* 14(8):572–584.
29. Fowler T, Sen R, Roy AL (2011) Regulation of primary response genes. *Mol Cell* 44(3): 348–360.
30. Kuwahara K, Barrientos T, Pipes GCT, Li S, Olson EN (2005) Muscle-specific signaling mechanism that links actin dynamics to serum response factor. *Mol Cell Biol* 25(8): 3173–3181.
31. Niu Z, Li A, Zhang SX, Schwartz RJ (2007) Serum response factor micromanaging cardiogenesis. *Curr Opin Cell Biol* 19(6):618–627.
32. Barry ST, Critchley DR (1994) The RhoA-dependent assembly of focal adhesions in Swiss 3T3 cells is associated with increased tyrosine phosphorylation and the recruitment of both pp125FAK and protein kinase C-delta to focal adhesions. *J Cell Sci* 107(Pt 7):2033–2045.
33. Babic AM, Chen C-C, Lau LF (1999) Fisp12/mouse connective tissue growth factor mediates endothelial cell adhesion and migration through integrin alphavbeta3, promotes endothelial cell survival, and induces angiogenesis in vivo. *Mol Cell Biol* 19(4):2958–2966.
34. Shimo T, et al. (1999) Connective tissue growth factor induces the proliferation, migration, and tube formation of vascular endothelial cells in vitro, and angiogenesis in vivo. *J Biochem* 126(1):137–145.
35. Hall-Glenn F, et al. (2012) CCN2/connective tissue growth factor is essential for pericyte adhesion and endothelial basement membrane formation during angiogenesis. *PLoS ONE* 7(2):e30562.

A.2.3 Supplementary information

Supporting information: Stimulus-induced modulation of transcriptional bursting in a single mammalian gene

Nacho Molina[*1], David M. Suter[*†2,3],
Rosamaria Cannavo[1], Benjamin Zoller[1], Ivana Gotic[2] and Félix Naef[†1]

[1]Computational Systems Biology Group, Ecole Polytechnique Fédérale de Lausanne, Swiss Institute for Experimental Cancer Research and Swiss Institute of Bioinformatics, AAB 021 Station 15, CH-1015 Lausanne, Switzerland. [2]Department of Molecular Biology, Sciences III, University of Geneva, and National Centre of Competence in Research Frontiers in Genetics, 30 Quai Ernest Ansermet, 1211 Geneva, Switzerland. [3]Present address: The Institute of Bioengineering, School of life sciences, Ecole Polytechnique Fédérale de Lausanne (EPFL) AI 1241 Station 15, CH-1015 Lausanne, Switzerland.

[*]These authors contributed equally to this work.
[†]To whom correspondence should be addressed (david.suter@epfl.ch, felix.naef@epfl.ch).

Contents

1 Experimental methods

1.1 Cell culture and luminescence imaging

The NIH-3T3 gt:ctgf cell line was generated by gene trap insertion of a short-lived luciferase in exon 5 of the connective tissue growth factor gene, as described earlier [1]. Luminescence microscopy was performed using a LV200 luminoview microscope (Olympus) equipped with an EM-CCD cooled camera (Hamamatsu photonics, EM-CCD C9100-13) as described before [1], with an exposure time and time resolution of one minute. For serum stimulation experiments, cells were cultured in 5% fetal bovine serum for at least 24 hours before imaging, and induced by increasing serum concentration by 2% or 15%. For TGF-β1 (eBiosciences) induction, cells were continuously cultured in 10% serum. Stimulation with serum or TGF-β1 was performed 60-120 minutes after initial baseline recording by adding fetal bovine serum (FBS) or TGF-β1 to the cell culture dish without disturbing the imaging field. Analysis of time lapse imaging was performed by manual tracking of single cells to quantify luminescence signals as previously described [1]. Number of cells analyzed in each condition: control serum (n=47), serum +2% (n=90), serum +15% (n=96), TGF-β1 control (n=56), TGF-β1 1nM (n=47), TGF-β1 10nM (n=52), TGF-β1 50nM (n=33).

1.2 Fraction of cells that respond upon stimulation

To estimate the fraction of cells that responded to different stimuli we computed the mean light signal for each cell measured within a window of three hours after the addition of the stimulus. We first fitted a Gamma distribution to the mean expression levels obtained from the control cells. Then, we modeled the mean protein levels $\bar{p}$ observed after gene induction by a two-Gamma mixture model:

$$P(\bar{p}|\pi_r) = P_0(\bar{p}|\theta_0\alpha_0)(1-\pi_r) + P_r(\bar{p}|\theta_r\alpha_r)\pi_r$$

where the first Gamma distribution $P_0(\bar{p}|\theta_0\alpha_0)$ characterizes the probability to obtain the observed mean protein level if the cell did not respond to the stimulus. On the contrary $P_r(\bar{p}|\theta_r\alpha_r)$ describes the mean protein levels if the cell did respond. The variable π_r stands for the fraction cells that respond to the stimulus and it is the parameter of interest. Finally, the likelihood of the mean protein levels $\{\bar{p}_n\}$ of a population of cells is:

$$L(\{\bar{p}_n\}|\pi_r) = \prod_i P(\bar{p}_i|\pi_r)$$

The scale parameter θ_0 and the shape parameter α_0 were fixed to the ones obtained from the fits to single Gamma distributions of cells from the control experiments. We fitted the free parameters π_r, θ_r and α_r using Markov Chain Monte Carlo sampling.

1.3 Protein and mRNA half-lives before and after stimulation

In principle, we expect that neither the stability of the mRNA that codes for the luciferase nor the stability of the luciferase itself are specifically affected upon serum or TGF-β1 stimulation. Luciferase is an exogenous protein and therefore should not be affected by the active regulation of protein degradation of specific proteins. The mRNA, although it contains the first part of the endogenous *ctgf* gene (see [1]), lacks the 3'UTR which is very often an essential component for post-transcriptional regulation. Possible changes on the global cellular state after stimulation, however, may indirectly modify the protein or the mRNA half-lives. To confirm that indeed half-lives are not affected upon stimulation we recorded luminescence activity decays, before and after adding serum or TGF-β1, from cell populations when translation or transcription were blocked by Cycloheximide or Actinomycin D treatments respectively.

Cells were cultured in 5% or 10% fetal calf serum (FCS) medium for at least 18 hours before imaging. For serum stimulation, cells were induced by increasing serum concentration from 5% to 20%. For TGF-β1 (eBiosciences) induction, cells were continuously cultured in 10% serum. Stimulation with serum or TGF-β1 was performed 60 minutes after initial baseline recording. Translation or transcription were blocked by adding Actinomycin D [5 ug/mL] (Sigma) or Cycloheximide [10 ug/mL] (Axon Lab) respectively at 1 or 10 h after serum stimulation and 2 or 10 h after TGF-β1 stimulation. Luciferase activity was then recorded on the LumiCycle-32 (ActiMetrics).

Similarly as in [1], we first fitted the decay experiments after translation inhibition to a simple exponential function:

$$p(t) = p_0 e^{-\gamma_p t}$$

and thus estimating the protein degradation rate γ_p. Then, knowing γ_p , we estimated the mRNA degradation rate γ_m by fitting the function,

$$p(t) = \left(p_0 - \frac{k_p}{\gamma_p - \gamma_m}\right) e^{-\gamma_p t} + \left(\frac{k_p}{\gamma_p - \gamma_m}\right) e^{-\gamma_m t}$$

to the decays measured after transcription inhibition. Both functions are easily obtained from the deterministic differential equation of the protein and mRNA dynamics once the translation rate k_p and the transcription rate k_m are set to zero respectively (see [1]).

1.4 Serum/TGF-β1 stimulation and transcription inhibition

Luciferase translation is initiated from an IRES sequence. Therefore, we also expect that the translational efficiency might not be strongly affected by serum or TGF-β1 stimulation. To confirm this we designed experiments where serum or TGF-β1 stimulations are performed at the same time that transcription blockage by Actinomycin D treatment. The rational is as follows: if the measured signal increase upon induction is mainly due to an increase in the translational efficiency we should observe a similar behavior even if transcription is inhibited. Stimulations with either serum or TGF-β1 were performed as indicated above. Transcription was inhibited by adding 5 ug/ml Actinomycin D (Sigma) simultaneously to the stimulations

with either serum or TGF-β1. Luciferase activity was then recorded on the LumiCycle-32 (ActiMetrics).

1.5 Double serum stimulation and the refractory period

Upon serum induction, we observed a refractory period after the first transcriptional event 2-fold longer than in control condition. This suggests that gene activation is restricted during this period by a yet uncharacterized negative feedback mechanism. Therefore, we expect that, when cells are exposed to a double stimulation, the second stimulation will not induce gene expression if the time interval between the two stimulations is shorter than ~ 240 minutes. To test this experimentally we performed two consecutive serum stimulations on cell populations with time separation of 120, 210 and 270 minutes from the first stimulation (time 0). In control dishes we removed and immediately replaced the same medium, in order to evaluate the mechanical stress caused by the medium change. Luciferase activity was recorded on the LumiCycle-32 (ActiMetrics).

2 Computational methods

2.1 Parameter estimation from single cell recordings

To estimate the transcriptional parameters we used the computational method that we developed previously [1]. Specifically, we computed the probability that the time traces of luciferase activity were generated by a simple stochastic gene expression model where the gene can switch between and active and inactive state and transcription occurs in bursts only during the the active periods. The stochastic model is parametrized by six constant rates: the two switching rate k_0 and k_1, the transcription rate k_m, the translation rate k_p and the mRNA and protein degradation rates γ_p and γ_m. Thanks to the Markovian nature of the stochastic model the likelihood of a time trace $D = \{s_i\}$, given the above set of parameters denoted by Θ, can be written as

$$P(D|\Theta) = \sum_{\Lambda} \prod_{i} P_e(s_i|p_i) P_t(p_i m_i g_i | p_{i-1} m_{i-1} g_{i-1} \Theta) \tag{1}$$

where $P_e(s_i|p_i)$ is the emission probability of observing the signal s_i given the amount of protein p_i at time i and $P_t(p_i m_i g_i | p_{i-1} m_{i-1} g_{i-1} \Theta)$ is the transition probability that the system changes from the previous state $p_{i-1} m_{i-1} g_{i-1}$, i.e. p_{i-1} proteins, m_{i-1} mRNA copies and gene state g_{i-i}, at time $i-1$ to a new state $p_i m_i g_i$ at time i. The emission probabilities are characterized by calibrating the experimental set up and the transition probabilities are approximated analytically (see for details [1]). The sum in equation (1) run over all hidden (unobserved) state trajectories $\Lambda = \{p_i m_i g_i\}$.

For this study, we introduced two modifications. First, to reduce computation which was prohibitive given the high protein levels, we fixed the protein amount at each time point (instead of summing over all protein numbers) to their expected values from the calibration relationship already established in [1], and filtered experimental noise on a (fast) time scale of 5 minutes. This procedure did not interfere with the longer times scales ('on' and 'off'

times) estimated. Second, after stimulation, cells may not be in steady state anymore, and parameters could vary over time. We incorporated this (extrinsic) variability, assuming that the transcription rate can take values between a lower bound of 0.2 molecules/min to an upper bound of 60 molecules/min [3]. The variability on the transcription rate k_m is then modeled as a rescaled beta distribution,

$$P(k_m|\alpha\beta) = q(k_m)^{\alpha-1}(1-q(k_m))^{\beta-1}/B(\alpha,\beta)$$

where $B(\alpha,\beta)$ is the beta function and $q(k_m) = (k_m - 0.2)/(60 - 0.2)$. Therefore the transition probability of the mRNA states (supplemental Eq. 4 in [1]) takes the new form:

$$P(m_i|m_{i-1}\alpha\beta\gamma_p) = \int P(m_i|m_{i-1}k_m\gamma_m)P(k_m|\alpha\beta)\mathrm{d}k_m$$

The two parameters of the beta distribution α and β, and the two time scales of the gene activation process $\tau_{\mathrm{on}} = 1/k_{\mathrm{off}}$ and $\tau_{\mathrm{off}} = 1/k_{\mathrm{on}}$ are estimated from the posterior probability $P(\Theta|D)$. The actual estimation was done using Markov Chain Monte Carlo sampling.

2.2 Temporal profiles of transcriptional parameters

We used Gibbs sampling to draw mRNA accumulation and gene activity time traces from the corresponding posterior probability $P(\Lambda|D\Theta)$. In particular, at every iteration we chose randomly a time point i and we resampled the state of the system $\lambda_i = p_i m_i g_i$ from the marginal distribution,

$$P(\lambda_i|\lambda_{i-1}\lambda_{i+1}) \propto P_e(s_i|p_i)P_t(\lambda_{i+1}|\lambda_i\Theta)P_t(\lambda_i|\lambda_{i-1}\Theta)$$

We recorded a hidden state trajectory $\Lambda = \{p_i m_i g_i\}$ every 10000 iteration which ensures that every time point was chosen and resampled approximately 30 times on average. The process was run until 100 trajectories were recorded. For each transcriptional event in each Gibbs sample, we computed the length of the transcriptional active window $\hat{\tau}_{\mathrm{on}}$ and the length of the following inactive window $\hat{\tau}_{\mathrm{off}}$. We estimated the burst size in each time interval as

$$\hat{b} = \frac{\gamma_m \Delta t(m_f - m_0 e^{-\gamma_m \Delta t})}{(1 - e^{-\gamma_m \Delta t})}$$

which follows easily from the expression of the expected number of final mRNA molecules after an interval of time Δt. We calculated the total burst size $\hat{B}$ as the sum of the burst sizes in each time interval within an active window. The transcription rate was then estimated as the total burst size divided by the duration of the active window: $\hat{k}_m = \hat{B}/\hat{\tau}_{\mathrm{on}}$. Finally, we computed the lag time $\hat{\tau}_{\mathrm{lag}}$ as the time since the addition of the stimulus until the first active window of transcription. In summary, for each transcriptional event k in each sampled trajectory i of each cell n we estimated the transcription rate, the duration of the active period and the duration of the following inactive period which in general are denoted as $\{x_i^n\}_k$.

To estimate how the transcriptional parameters change over time we carried out two type

of averages over the Gibbs trajectories. For each transcriptional event we first averaged over all Gibbs samples of one cell. Then, to obtain the final expected on-time, off-time and transcription rate, we averaged over the results of each cell. Formally, we can write the likelihood of obtaining the transcriptional values $\{x_i^n\}_k$ as the convolution of two normal distributions:

$$P(\{x_i^n\}_k|M_k\Sigma_k) = \prod_n^{N_c}\prod_i^{N_t}\int N(\{x_i^n\}_k|\mu_n^k\sigma_n^k)N(\mu_n^k|M_k\Sigma_k)\mathrm{d}\mu_n\mathrm{d}\sigma_n$$

where N_c and N_t are the number of cells and the number of Gibbs samples respectively. The parameter μ_n^k is the mean of the transcriptional variable at the kth transcriptional event for the cell n. The standard deviations σ_n^k measure the precision of the estimate taking into account the uncertainty on the deconvolution process. Finally, M_k and Σ_k are the total mean and the standard deviation of the transcriptional variable at the kth transcriptional event. The standard deviations Σ_k represent in this case the cell-to-cell variability of the transcriptional variable at the $k$the transcriptional event. After integrating out the parameters μ_n^k and, if the standard deviations are known, the maximum likelihood solution for the total mean M_k is:

$$\hat{M}_k = \frac{\sum_n \frac{\bar{x}_n^k}{(\sigma_n^k)^2/N_g+\Sigma_k^2}}{\sum_n \frac{1}{(\sigma_n^k)^2/N_g+\Sigma_k^2}} \pm \left(\frac{1}{\sum_n \frac{1}{(\sigma_n^k)^2/N_g+\Sigma_k^2}}\right)^{-1/2}$$

We instead used MCMC to sample both the mean M_k and the standard deviation Σ_k which allowed us to also compute the coefficient of variation $C_k = M_k/\Sigma_k$. To constrain the sampling space we set the standard deviation σ_n^k to the squared root of the observed variance, i.e $\sigma_n^k = (\sum_i(\{x_i^n\}_k - \bar{x}_n^k)^2)^{-1/2}$. In addition, the MCMC algorithm naturally produces errors for the estimated parameters as the standard deviation of the posterior probabilities for each parameter.

2.3 Validation of the algorithm using simulated data

We showed, using Gibbs sampling, that upon serum stimulation, the duration of the first transcriptional burst as well as the following off-time are non-exponentially distributed. In addition, we reported that the transcriptional parameters changed over time indicating that the stimulation of cells leads to an non-stationary process. The two features deviate from the simple two-state model used to impose a prior probability over the space of hidden (unobserved) trajectories. While this may appear counter-intuitive, it is important to notice that in equation (1), which defines the probability of the data, there are two competing factors: the emission probabilities and the transition probabilities. The former is fully driven by the data and the latter by the prior model. Therefore, it is possible to obtain trajectories (by Gibbs sampling) that deviate from the prior model if the data outcompete the prior expectations. Importantly, we showed previously that this allows to reliably identify bursting statistics that deviate form those of the prior itself [1], for example we identified that 'off' intervals show peaked distributions, characteristic of a refractory time before gene re-activation. To further illustrate that our algorithm based on the two-state prior model is flexible enough to correctly

identify non-exponential distributions, as well as variations of the parameters over time, we applied it to two sets of simulated data.

First, we simulated data from a toy model where a gene bursts at regular intervals drawing 'on' and the 'off' times from sharply peaked Gamma distributions with shape parameter equal to 400 (coefficient of variation of 5%) and mean of 40 minutes and 200 minutes respectively. The estimated effective parameters of the simple telegraph prior model are 27 minutes and 180 minutes, slightly underestimated. However the 'on' and 'off' time distributions that we obtained by Gibbs sampling resemble the true distributions (Fig. S9). Notice, that in this case the prior distributions (thin gray lines) are extremely different from the target ones (dashed lines) yet the algorithm is able to significantly deviate from the prior expectation.

Next, we simulated data reproducing the features observed upon serum stimulation: first, the first on-time as well as the following off-time were drawn from peaked distributions; second, the subsequent times were drawn from exponential distributions; and third, two different set of transcriptional parameters (k_{m}, τ_{on} and τ_{off}) were used to simulate the first transcriptional burst and the subsequent bursts (dashed lines in Fig. S10). Applying the same procedure than with real data we obtained temporal profiles of the transcriptional parameters as well as on-time and off-times distributions (solid lines in Fig. S10) that reproduced the ones we used to simulate the data (dashed lines).

2.4 Inference with exponential and non-exponential models

To further validate our results on serum stimulation, namely the observation of a tightly regulated first transcriptional burst and a refractory period following it, we performed model selection among gene models that *explicitly* incorporate Gamma distributed 'on' and 'off' times. In order to generate Gamma shaped distributions we extended the gene switch model by considering an irreversible cycle of n sequential 'on' and m sequential 'off' states. Fixing the transition rates to n/τ_{on} and m/τ_{off}, the 'on' and 'off' times are then Gamma distributed with mean τ_{on} and τ_{off} and shape parameter n and m respectively. For the sake of simplicity, we only considered models for which the values of n and m are either one (exponentially distributed times with coefficient of variation $CV = 1$) or three (peaked times, $CV = 0.58$) , i.e. the original switch model ($n = 1$,$m = 1$) and three irreversible cycles ($n = 1$,$m = 3$), ($n = 3$,$m = 1$) and ($n = 3$,$m = 3$). This setting gave us enough flexibility to assess whether the 'on' or 'off' times are non-exponentially distributed while keeping the inference computationally feasible.

The model selection and the parameters estimation, were based on the joint posterior distribution:

$$P(M, \Theta_M|D) = \frac{\mathcal{L}(D|M, \Theta_M)P(M, \Theta_M)}{\sum_M \int \mathcal{L}(D|M, \Theta_M)P(M, \Theta_M)d\Theta_M}$$

where $M \equiv (n, m)$ is the model indicator, Θ_M the parameters of the model, D the signal time traces and $P(M, \Theta_M)$ the prior distribution. We chose a uniform prior for the model indicator M and log uniform for α,β,τ_{on} and τ_{off}. The likelihood $\mathcal{L}(D|M, \Theta_M)$ was computed following the modifications described in section 2.1, with the addition that the gene transition probability$P(g_i|g_{i-1}, \tau_{\mathrm{on}}, \tau_{\mathrm{off}}, M)$ needs to be computed according to the new topology of the

different gene models:

$$P(g_i|g_{i-1}, \tau_{\text{on}}, \tau_{\text{off}}, M) = e^{K_M(\tau_{\text{on}},\tau_{\text{off}})\Delta t}$$

where $K_M(\tau_{\text{on}}, \tau_{\text{off}})$ is the rate matrix of the model, which contains the propensity functions of the different reactions.

We sampled the posterior distribution $P(M, \Theta_M|D)$ with a Reversible Jump Markov Chain Monte Carlo (RJ-MCMC) algorithm [2]. As shown schematically in Fig S11, the jump between models consisted in changing either the 'on' or the 'off' time distribution to an exponential (n=1) or a Gamma distribution (n=3). Note that, although the models share the same parameters (α, β, τ_{on} and τ_{off}), building an efficient (in terms of sampling acceptance probabilities) mapping between the respective parameter spaces is not necessarily trivial. Indeed, choosing the parameters of the new proposed model equal to the parameters of the current model resulted in an inefficient sampler. Thus, we modified the mapping by setting the new time scale τ'_{on} or τ'_{off} to minimizes the squared error between the means plus the squared error between the standard deviations of the exponential and the Gamma distributions, which improved the acceptance rates of the moves (jumps) across models. We validated our inference framework on four sets of 48 simulated traces of two days generated from each gene model with kinetic parameters matching those of Serum Δ2% (Table S1). Our procedure successfully recovered the right model and parameters.

Since our primarily aim was to validate the non-exponential nature of the 'on' and 'off' times of the first transcriptional event after serum stimulation, as opposed to the subsequent events, we split the signal time traces at the first protein copy number minimum following the first maximum. We then applied our model selection framework on each partition for the different serum conditions. The favored model and the mean parameters are reported in Table S2. For the first part of the traces the fully non-exponential model (3,3) is consistently favored with estimated posterior probability equal one, except for the control condition at 5% serum for which $P((1,3)|D) = 0.95$ and $P((1,1)|D) = 0.05$. This reflects that the medium change at the start of the recording, even if serum was not increased, slightly induced transcription, as can also be seen in Figs. 3C or 5A. For the second part of the traces the fully exponential model (1,1) is preferred for all conditions. Therefore, we recovered the peaked on-time and off-time distributions for the first transcriptional event after serum stimulation as well as the exponential distributions for the subsequent events confirming our previous finding with a simple gene switch model. In addition, we reconstructed the on and off-time distributions using Gibbs sampling as described in section 5, using the favored model for the different conditions and partitions. The resulting distributions (Fig. S12) are very close to the ones obtained in Figures 4,5 and S8 with the two-state prior. Together with the simulations (Figs. S9-10), this generalized analysis in which the optimal prior is automatically selected, confirms that the two-state prior model, used in combination with Gibbs sampling, is actually flexible enough for accurate inference also in conditions where parameters and statistical properties are not homogeneous in time.

3 Supplementary Tables

Condition:	k_p(1/min)	γ_p (1/min)	k_m (1/min)	γ_m (1/min)	τ_{on} (min)	τ_{off} (min)
Control (5%)	0.21	0.0212	3.38	0.01	24.9	63.8
Serum Δ2%	0.21	0.0212	19.4	0.01	18.2	63.4
Serum Δ15%	0.21	0.0212	25.2	0.01	18.2	53.9
Control (10%)	0.21	0.0212	3.39	0.01	39.9	53.7
TGF-β1 1 nM	0.21	0.0212	11.6	0.01	33.3	46.9
TGF-β1 10 nM	0.21	0.0212	14.2	0.01	35.9	43.7
TGF-β1 50 nM	0.21	0.0212	16.8	0.01	33.9	41.5

Table S1: Model parameters. Translation efficiency (k_p) was estimated by measuring average protein and mRNA levels in cell populations (see [1]). Protein and mRNA degradation rates (γ_p and γ_m) were obtained from Cycloheximide and Actinomycin D experiments (see section 1.3). Transcriptional parameters (k_m, τ_{on} and τ_{off}) were inferred from single-cell recordings.

Condition:	Model	k_m (1/min)	τ_{on} (min)	τ_{off} (min)
Control 5% (first part)	(1,3)	6.7	25.2	128.4
Serum Δ2% (first part)	(3,3)	30.0	44.8	339.4
Serum Δ15% (first part)	(3,3)	30.1	50.4	172.4
Control 5% (second part)	(1,1)	1.9	28.4	81.7
Serum Δ2% (second part)	(1,1)	1.9	25.9	78.3
Serum Δ15% (second part)	(1,1)	3.0	18.1	53.2

Table S2: Inferred model and transcriptional parameters using a RJ-MCMC algorithm on the first part of the traces (from induction time up to the first minimum after the first maximum) and the second part of the traces (the rest).

4 Supplementary figures

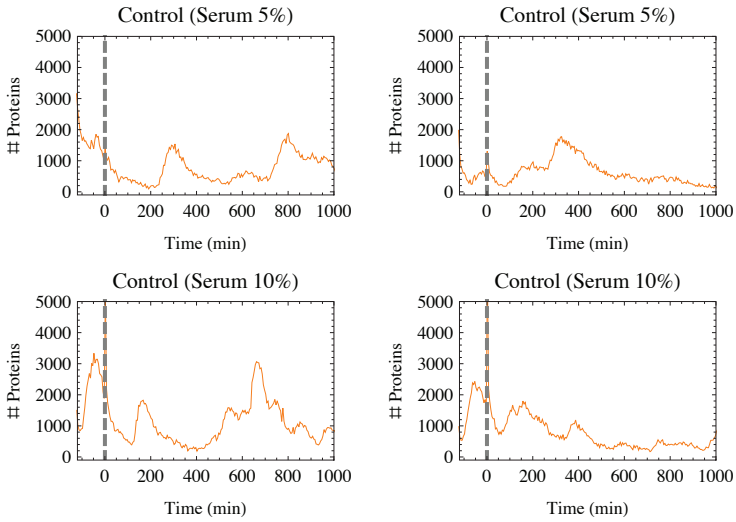

Figure S1: Control time traces at constant concentration of 5% and 10% serum.

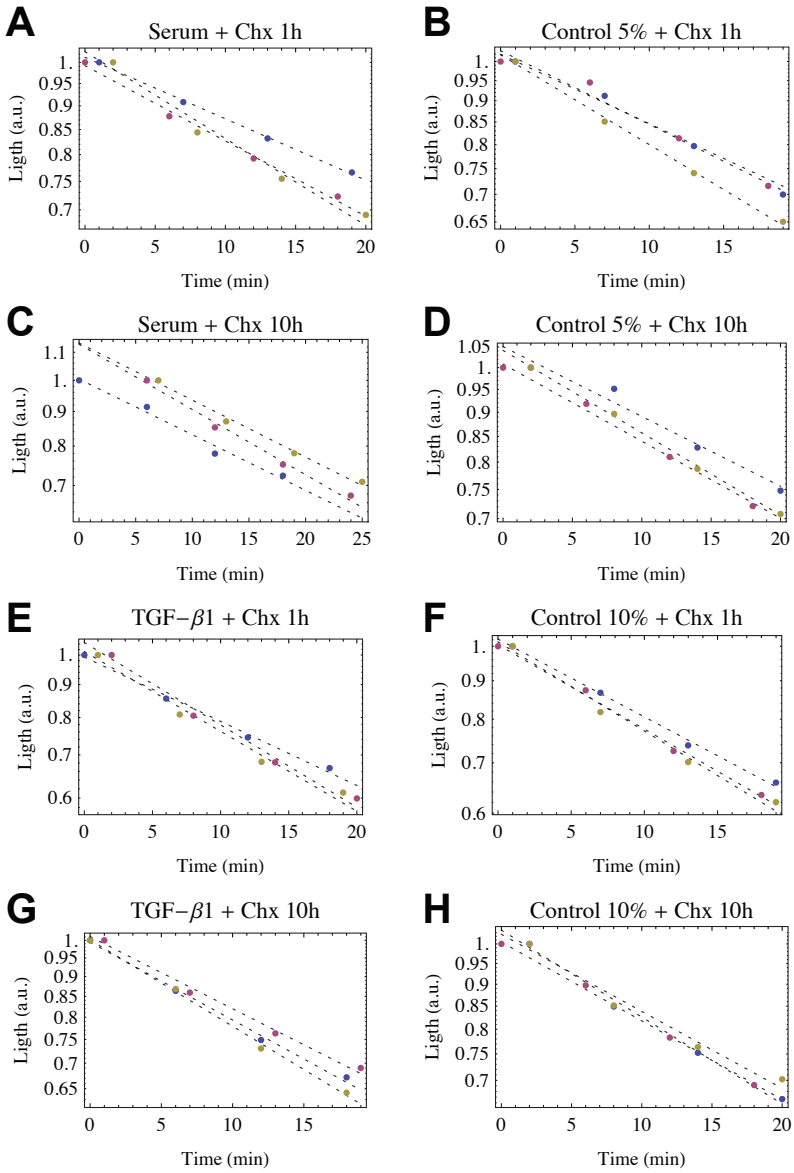

Figure S2: Luminescence decay was measured in cell populations after Cycloheximide treatment. CHX was added 1h (A) or 10h (C) after serum stimulation and 2h (E) or 10h (G) after TGF-β1 stimulation. Controls experiments without stimulation were carried out at the same time points (B,D,F and H).

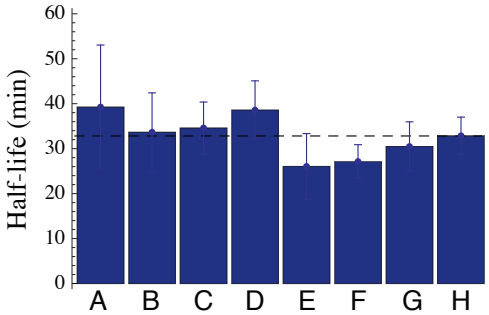

Figure S3: Estimated protein half-lives from decay experiments after blocking translation (see Fig S2).

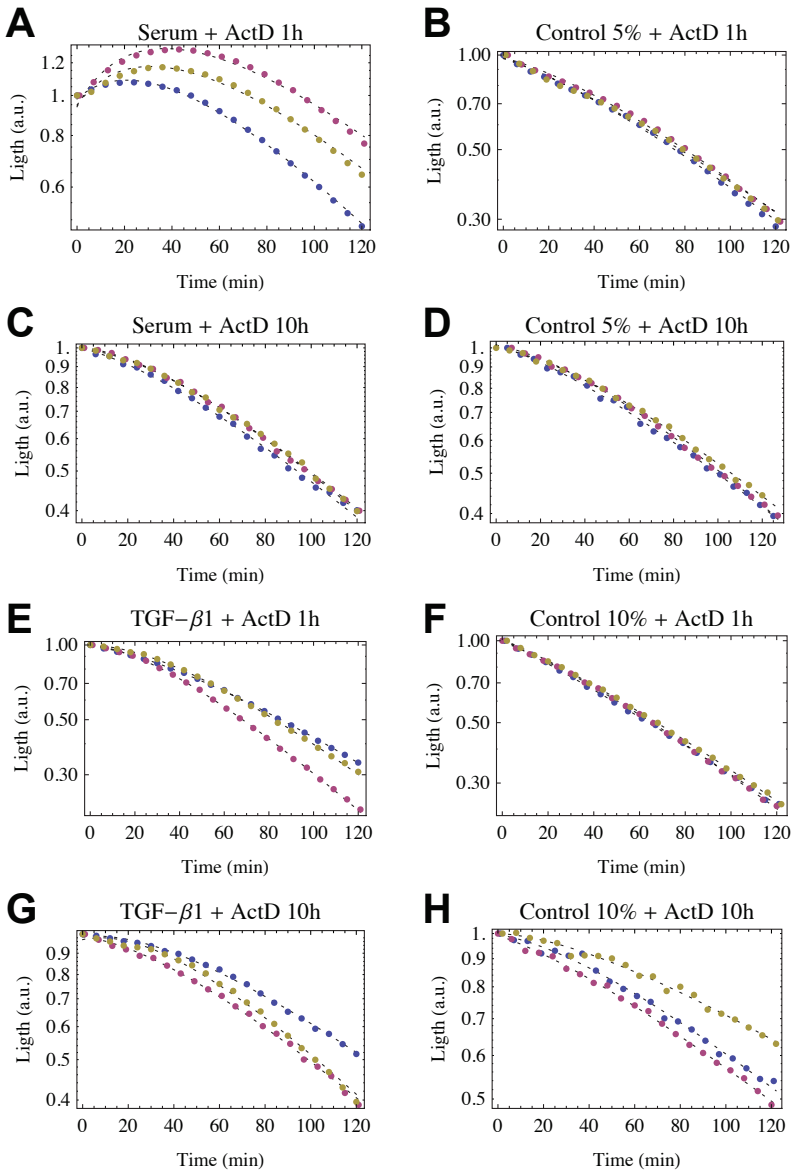

Figure S4: Luminescence decay was measured in cell populations after Actinomycin D treatment. Act-D was added 1h (A) or 10h (C) after serum stimulation and 2h (E) or 10h (G) after TGF-β1 stimulation. Controls experiments without stimulation were carried out at the same time points (B,D,F and H).

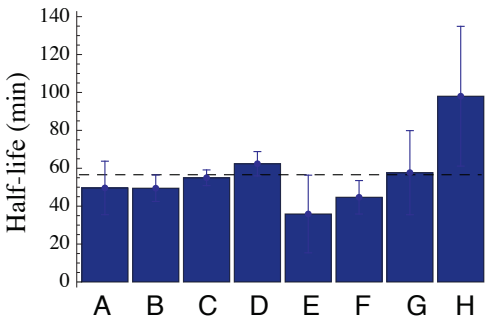

Figure S5: Estimated mRNA half-lives from decay experiments after blocking transcription (see Fig S4).

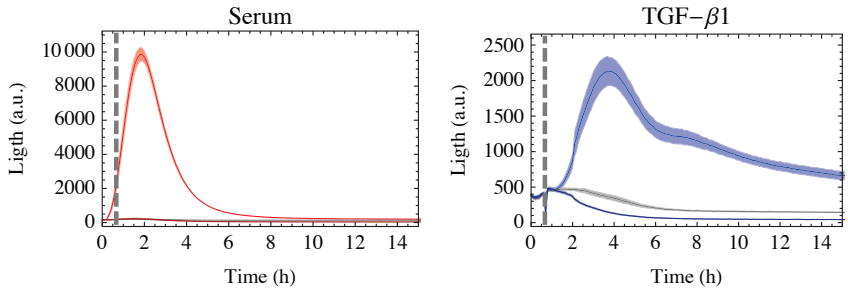

Figure S6: Simultaneous stimulation and transcription inhibition with Actinomycin D. Time of stimulation is shown as dashed gray line.

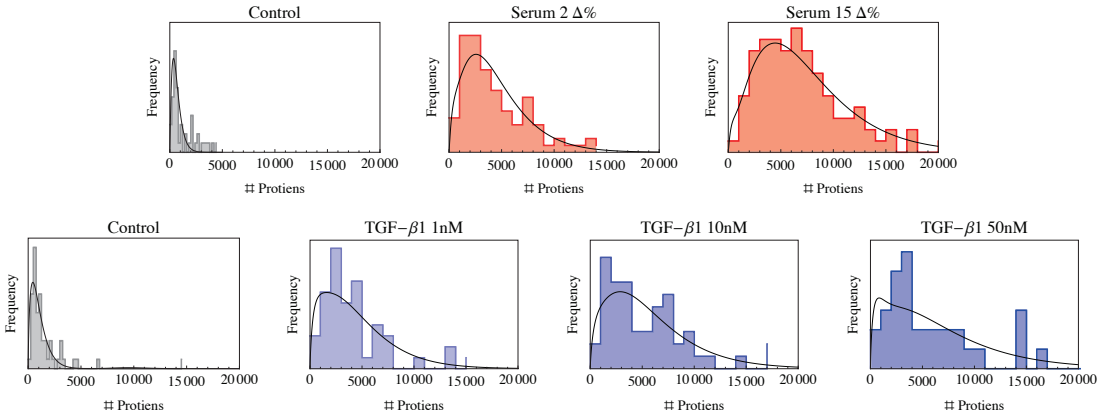

Figure S7: Distributions of mean expression levels after different stimuli and fits to a Gamma mixture model (black lines).

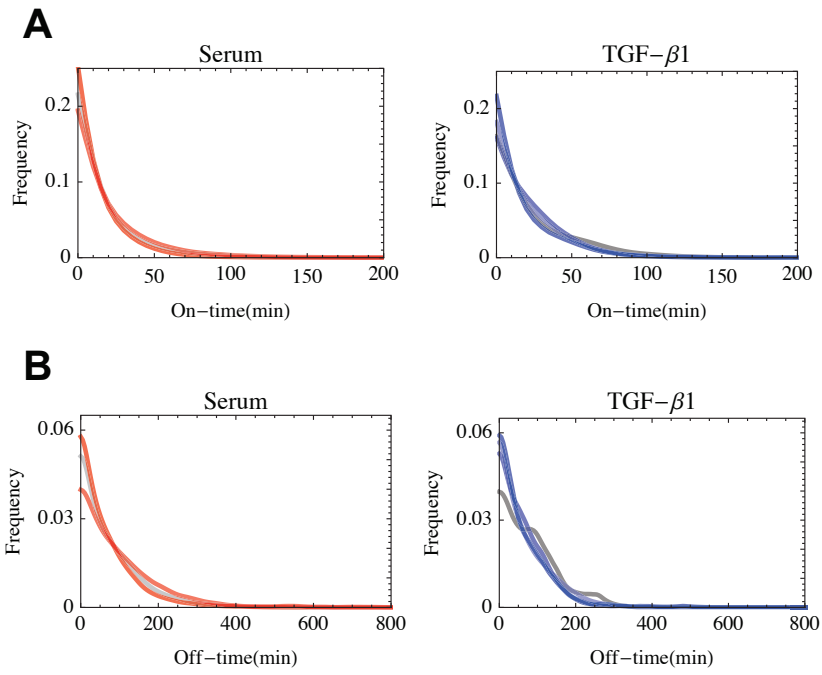

Figure S8: The distributions of 'on' times (A) and 'off' times (B) for the subsequent transcriptional events are exponential shaped independently on the stimulus. Colors are as in Figure 3.

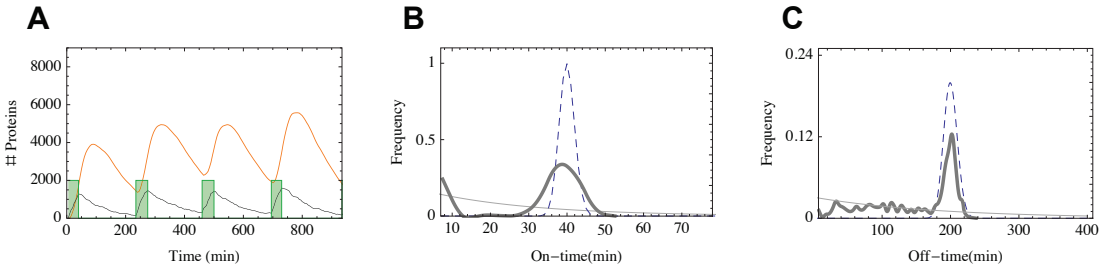

Figure S9: Deconvolution of simulated data from extremely peaked non-exponential distributions. (A) Example of a simulated trace with on-times and off-times drawn from a peaked Gamma distributions (dashed lines in B and C respectively). Inferred on-time distribution (B) and off-time distribution (C) by Gibbs sampling (thick gray lines) using an exponential distribution as prior (thin gray lines).

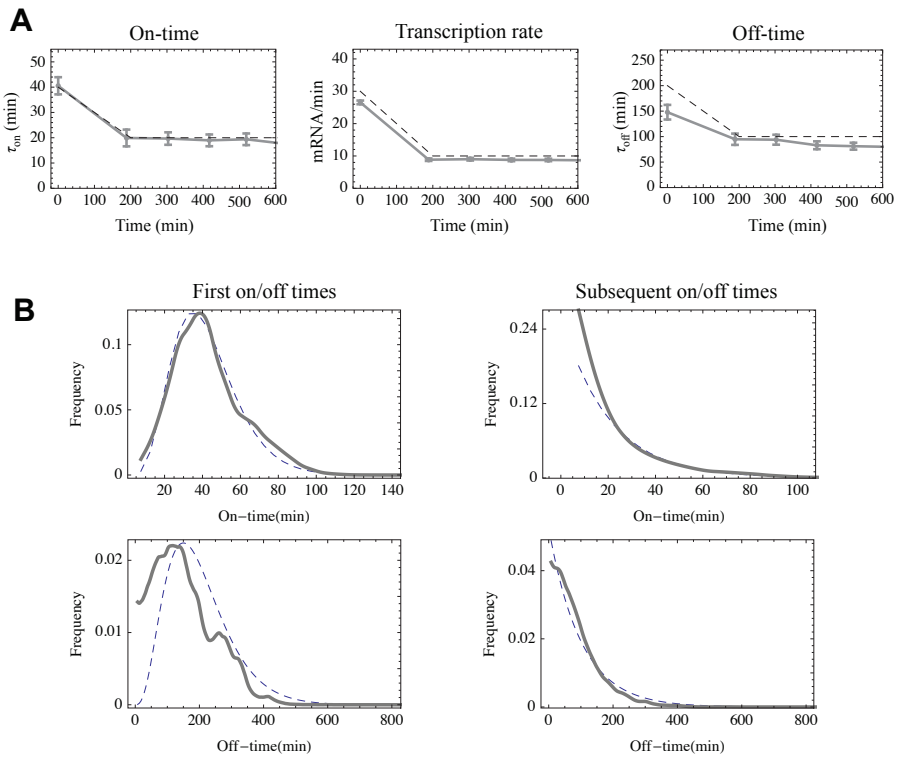

Figure S10: Validation of the algorithm using simulated data from a non-stationary and non-exponential model (dashed lines). (A) Estimated temporal behavior of the mean on-time, off-time and transcription rate. (B) On-time and off-time distributions of the first transcriptional event (left) and the subsequent events (right). Mean ± 2 SEM over the population of simulated cells are shown.

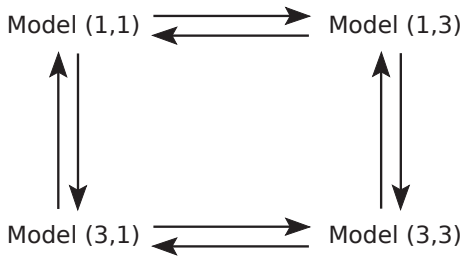

Figure S11: Jump scheme of the RJ-MCMC algorithm. Each move changes the 'on' time or the 'off' time distribution from an exponential ($n = 1$, $CV = 1$) to a Gamma ($n = 3$, $CV = 0.58$) or vice versa.

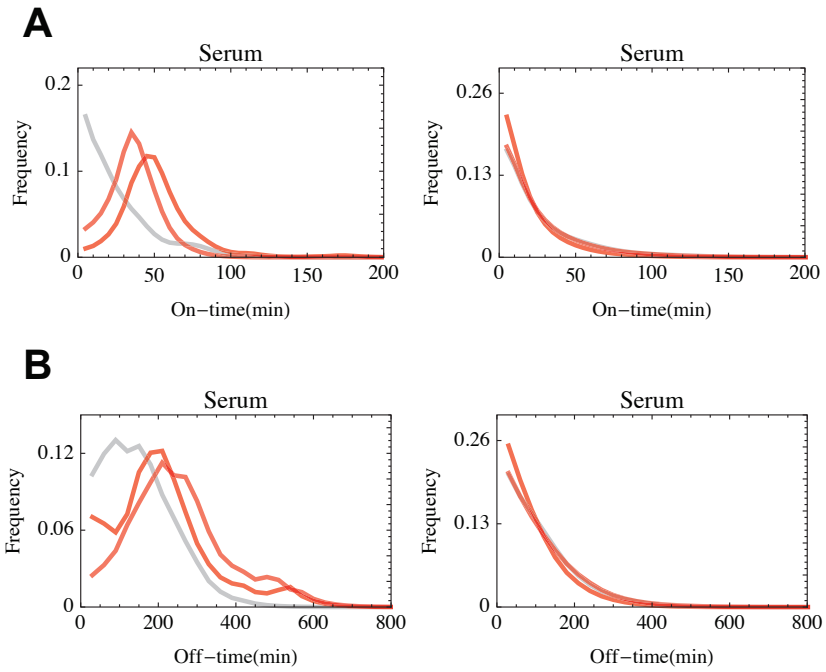

Figure S12: Distributions of 'on' times (A) and 'off' times (B) obtained by Gibbs sampling using the inferred models from Table S2 as prior. Left panels: first transcriptional events; Right: subsequent events. These distributions must be compared with Figures 4A, 5A, S8. Colors as in Figure 3.

References

[1] David M Suter, Nacho Molina, David Gatfield, Kim Schneider, Ueli Schibler, and Felix Naef. Mammalian genes are transcribed with widely different bursting kinetics. *Science*, 332(6028):472–474, Apr 2011.

[2] Peter J Green and David I Hastie. Reversible jump MCMC. *Genetics*, 155(3):1391–1403, 2009.

Bibliography

[Adan and Natale, 2002] Adan, A. and Natale, V. (2002). Gender differences in morningness-eveningness preference. *Chronobiol Int*, 19(4):709–720.

[Akashi and Takumi, 2005] Akashi, M. and Takumi, T. (2005). The orphan nuclear receptor roralpha regulates circadian transcription of the mammalian core-clock bmal1. *Nat Struct Mol Biol*, 12(5):441–448.

[Akashi et al., 2002] Akashi, M., Tsuchiya, Y., Yoshino, T., and Nishida, E. (2002). Control of intracellular dynamics of mammalian period proteins by casein kinase i epsilon (ckiepsilon) and ckidelta in cultured cells. *Molecular and Cellular Biology*, 22(6):1693–1703.

[Akhtar et al., 2002] Akhtar, R. A., Reddy, A. B., Maywood, E. S., Clayton, J. D., King, V. M., Smith, A. G., Gant, T. W., Hastings, M. H., and Kyriacou, C. P. (2002). Circadian cycling of the mouse liver transcriptome, as revealed by cdna microarray, is driven by the suprachiasmatic nucleus. *Curr Biol*, 12(7):540–550.

[Alberts et al., 2015] Alberts, B., Johnson, A., Lewis, J., Morgan, D., Raff, M., Roberts, K., and Walter, P. (2015). *The Cell Cycle - Chapter 17*, volume (6th ed.). New York: Garland Science.

[Alushin and Nogales, 2011] Alushin, G. and Nogales, E. (2011). Visualizing kinetochore architecture. *Curr Opin Struct Biol*, 21(5):661–669.

[Appleton, 1923] Appleton, E. V. (1923). The automatic synchronization of triode oscillators. *Proceedings of the Cambridge Philosophical Society*, 21((Part III)):231–248.

[Aschoff, 1983] Aschoff, J. (1983). Circadian control of body temperature. *Journal of Thermal Biology*, 8(1–2):143 – 147.

[Balsalobre et al., 2000] Balsalobre, A., Brown, S. A., Marcacci, L., Tronche, F., Kellendonk, C., Reichardt, H. M., Schutz, G., and Schibler, U. (2000). Resetting of circadian time in peripheral tissues by glucocorticoid signaling. *Science*, 289(5488):2344–2347.

[Balsalobre et al., 1998] Balsalobre, A., Damiola, F., and Schibler, U. (1998). A serum shock induces circadian gene expression in mammalian tissue culture cells. *Cell*, 93(6):929–937.

[Bassermann et al., 2014] Bassermann, F., Eichner, R., and Pagano, M. (2014). The ubiquitin proteasome system —implications for cell cycle control and the targeted treatment of cancer. *Biochimica et Biophysica Acta (BBA) - Molecular Cell Research*, 1843(1):150–162.

[Bergeland et al., 2001] Bergeland, T., Widerberg, J., Bakke, O., and Nordeng, T. W. (2001). Mitotic partitioning of endosomes and lysosomes. *Curr Biol*, 11(9):644–651.

[Bernard et al., 2007] Bernard, S., Gonze, D., Čajavec, B., Herzel, H., and Kramer, A. (2007). Synchronization-induced rhythmicity of circadian oscillators in the suprachiasmatic nucleus. *PLoS Computational Biology*, 3(4):e68.

[Bertoli et al., 2013] Bertoli, C., Skotheim, J. M., and de Bruin, R. A. M. (2013). Control of cell cycle transcription during g1 and s phases. *Nat Rev Mol Cell Biol*, 14(8):518–528.

[Bieler et al., 2014] Bieler, J., Cannavo, R., Gustafson, K., Gobet, C., Gatfield, D., and Naef, F. (2014). Robust synchronization of coupled circadian and cell cycle oscillators in single mammalian cells. *Mol Syst Biol*, 10:739.

[Bjarnason et al., 2001] Bjarnason, G. A., Jordan, R. C. K., Wood, P. A., Li, Q., Lincoln, D. W., Sothern, R. B., Hrushesky, W. J. M., and Ben-David, Y. (2001). Circadian expression of clock genes in human oral mucosa and skin. *The American Journal of Pathology*, 158(5):1793–1801.

[Boccaletti et al., 2002] Boccaletti, S., Kurths, J., Osipov, G., Valladares, D. L., and Zhou, C. S. (2002). The synchronization of chaotic systems. *Physics Reports*, 366(1–2):1–101.

[Bouchard-Cannon et al., 2013] Bouchard-Cannon, P., Mendoza-Viveros, L., Yuen, A., Kaern, M., and Cheng, H.-Y. M. (2013). The circadian molecular clock regulates adult hippocampal neurogenesis by controlling the timing of cell-cycle entry and exit. *Cell Rep*, 5(4):961–973.

[Branzei and Foiani, 2008] Branzei, D. and Foiani, M. (2008). Regulation of dna repair throughout the cell cycle. *Nat Rev Mol Cell Biol*, 9(4):297–308.

[Bresnahan et al., 1996] Bresnahan, W. A., Boldogh, I., Ma, T., Albrecht, T., and Thompson, E. A. (1996). Cyclin e/cdk2 activity is controlled by different mechanisms in the g0 and g1 phases of the cell cycle. *Cell Growth Differ*, 7(10):1283–1290.

[Brooks, 1976] Brooks, R. F. (1976). Regulation of the fibroblast cell cycle by serum. *Nature*, 260(5548):248–250.

[Brosh Jr., 2013] Brosh Jr., R. M. (2013). Dna helicases involved in dna repair and their roles in cancer. *Nat Rev Cancer*, 13(8):542–558.

[Brown et al., 2002] Brown, S. A., Zumbrunn, G., Fleury-Olela, F., Preitner, N., and Schibler, U. (2002). Rhythms of mammalian body temperature can sustain peripheral circadian clocks. *Current Biology*, 12(18):1574–1583.

[Brown, 1991] Brown, W. R. (1991). A review and mathematical analysis of circadian rhythms in cell proliferation in mouse, rat, and human epidermis. *Journal of Investigative Dermatology*, 97(2):273–280.

[Bruce and Bruce, 1981] Bruce, V. and Bruce, N. (1981). Circadian Clock-controlled Growth Cycle in Chlamydomonas reinhardi. *International Cell Biology 1980-1981*, pages 823–830.

[Bruce, 1970] Bruce, V. G. (1970). The biological clock in chlamydomonas reinhardi. *The Journal of Protozoology*, 17(2):328–334.

[Bruce, 1972] Bruce, V. G. (1972). Mutants of the biological clock in chlamydomonas reinhardi. *Genetics*, 70(4):537–548.

[Buhr and Takahashi, 2013] Buhr, E. D. and Takahashi, J. S. (2013). Molecular components of the mammalian circadian clock. *Handb Exp Pharmacol*, 217:3–27.

[Buhr et al., 2010] Buhr, E. D., Yoo, S.-H., and Takahashi, J. S. (2010). Temperature as a universal resetting cue for mammalian circadian oscillators. *Science*, 330(6002):379–385.

[Busino et al., 2007] Busino, L., Bassermann, F., Maiolica, A., Lee, C., Nolan, P. M., Godinho, S. I. H., Draetta, G. F., and Pagano, M. (2007). Scffbxl3 controls the oscillation of the circadian clock by directing the degradation of cryptochrome proteins. *Science*, 316(5826):900–904.

[Byrne et al., 1992] Byrne, T. E., Wells, M. R., and Johnson, C. H. (1992). Circadian rhythms of chemotaxis to ammonium and of methylammonium uptake in chlamydomonas. *Plant Physiol*, 98(3):879–886.

[Cardozo and Pagano, 2004] Cardozo, T. and Pagano, M. (2004). The scf ubiquitin ligase: insights into a molecular machine. *Nat Rev Mol Cell Biol*, 5(9):739–751.

[Cenciarelli et al., 1999] Cenciarelli, C., Chiaur, D. S., Guardavaccaro, D., Parks, W., Vidal, M., and Pagano, M. (1999). Identification of a family of human f-box proteins. *Curr Biol*, 9(20):1177–1179.

[Cermakian et al., 2013] Cermakian, N., Lange, T., Golombek, D., Sarkar, D., Nakao, A., Shibata, S., and Mazzoccoli, G. (2013). Crosstalk between the circadian clock circuitry and the immune system. *Chronobiol Int*, 30(7):870–888.

[Chambard et al., 2007] Chambard, J.-C., Lefloch, R., Pouyssegur, J., and Lenormand, P. (2007). Erk implication in cell cycle regulation. *Biochim Biophys Acta*, 1773(8):1299–1310.

[Chan and Debono, 2010] Chan, S. and Debono, M. (2010). Replication of cortisol circadian rhythm: new advances in hydrocortisone replacement therapy. *Therapeutic Advances in Endocrinology and Metabolism*, 1(3):129–138.

[De Mairan, 1729] De Mairan, J. J. d. (1729). Observation botanique. *Histoire de l'Academie Royale des Science 35–36 (in French)*.

[Destici et al., 2011] Destici, E., Oklejewicz, M., Saito, S., and van der Horst, G. T. (2011). Mammalian cryptochromes impinge on cell cycle progression in a circadian clock-independent manner. *Cell Cycle*, 10(21):3788–3797.

[D'Eysmond et al., 2013] D'Eysmond, T., De Simone, A., and Naef, F. (2013). Analysis of precision in chemical oscillators: implications for circadian clocks. *Phys Biol*, 10(5):56005.

[Dibner et al., 2010] Dibner, C., Schibler, U., and Albrecht, U. (2010). The mammalian circadian timing system: organization and coordination of central and peripheral clocks. *Annual review of physiology*, 72:517–49.

[Duffy et al., 1999] Duffy, J. F., Dijk, D. J., Hall, E. F., and Czeisler, C. A. (1999). Relationship of endogenous circadian melatonin and temperature rhythms to self-reported preference for morning or evening activity in young and older people. *J Investig Med*, 47(3):141–150.

[Eccles and Vincent, 1920] Eccles, W. and Vincent, J. H. (1920). British patent specifications. *163:462*.

[Eckel-Mahan et al., 2008] Eckel-Mahan, K. L., Phan, T., Han, S., Wang, H., Chan, G. C. K., Scheiner, Z. S., and Storm, D. R. (2008). Circadian oscillation of hippocampal mapk activity and camp: implications for memory persistence. *Nat Neurosci*, 11(9):1074–1082.

[Ede, 1973] Ede, M. C. M. (1973). Circadian rhythms of drug effectiveness and toxicity. *Clinical Pharmacology & Therapeutics*, 14(6):925–935.

[Edery, 2000] Edery, I. (2000). Circadian rhythms in a nutshell. *Physiol Genomics*, 3(2):59–74.

[Eide et al., 2005] Eide, E. J., Woolf, M. F., Kang, H., Woolf, P., Hurst, W., Camacho, F., Vielhaber, E. L., Giovanni, A., and Virshup, D. M. (2005). Control of mammalian circadian rhythm by ckiepsilon-regulated proteasome-mediated per2 degradation. *Mol Cell Biol*, 25(7):2795–2807.

[Ellingsen et al., 2007] Ellingsen, T., Bener, A., and Gehani, A. A. (2007). Study of shift work and risk of coronary events. *J R Soc Promot Health*, 127(6):265–267.

[Eser et al., 2011] Eser, U., Falleur-Fettig, M., Johnson, A., and Skotheim, J. M. (2011). Commitment to a cellular transition precedes genome-wide transcriptional change. *Mol Cell*, 43(4):515–527.

[Etchegaray et al., 2009] Etchegaray, J.-P., Machida, K. K., Noton, E., Constance, C. M., Dallmann, R., Di Napoli, M. N., DeBruyne, J. P., Lambert, C. M., Yu, E. A., Reppert, S. M., and Weaver, D. R. (2009). Casein kinase 1 delta regulates the pace of the mammalian circadian clock. *Mol Cell Biol*, 29(14):3853–3866.

[Ewen, 2000] Ewen, M. E. (2000). Where the cell cycle and histones meet. *Genes Dev*, 14(18):2265–2270.

[Feillet et al., 2014] Feillet, C., Krusche, P., Tamanini, F., Janssens, R., Downey, M., Martin, P., Teboul, M., Saito, S., Lévi, F., Bretschneider, T., van, d. H. G., Delaunay, F., and Rand, D. (2014). Phase locking and multiple oscillating attractors for the coupled mammalian clock and cell cycle. *Proc Natl Acad Sci U S A*, 111:9828–33.

[Feillet et al., 2015] Feillet, C., van, d. H. G., Levi, F., Rand, D., and Delaunay, F. (2015). Coupling between the Circadian Clock and Cell Cycle Oscillators: Implication for Healthy Cells and Malignant Growth. *Front Neurol*, 6:96.

[Fidorra et al., 1981] Fidorra, J., Mielke, T., Booz, J., and Feinendegen, L. E. (1981). Cellular and nuclear volume of human cells during the cell cycle. *Radiation and environmental biophysics*, 19(3):205–14.

[Filipski et al., 2009] Filipski, E., Subramanian, P., Carriere, J., Guettier, C., Barbason, H., and Levi, F. (2009). Circadian disruption accelerates liver carcinogenesis in mice. *Mutat Res*, 680(1-2):95–105.

[Foster et al., 2010] Foster, D. A., Yellen, P., Xu, L., and Saqcena, M. (2010). Regulation of g1 cell cycle progression: Distinguishing the restriction point from a nutrient-sensing cell growth checkpoint(s). *Genes & Cancer*, 1(11):1124–1131.

[Francis and Sargent, 1979] Francis, C. D. and Sargent, M. L. (1979). Effects of temperature perturbations on circadian conidiation in neurospora. *Plant Physiol*, 64(6):1000–1004.

[Fu and Kettner, 2013] Fu, L. and Kettner, N. M. (2013). The circadian clock in cancer development and therapy. *Prog Mol Biol Transl Sci*, 119:221–282.

[Fu et al., 2002] Fu, L., Pelicano, H., Liu, J., Huang, P., and Lee, C. (2002). The circadian gene Period2 plays an important role in tumor suppression and DNA damage response in vivo. *Cell*, 111(1):41–50.

[Gekakis et al., 1998] Gekakis, N., Staknis, D., Nguyen, H. B., Davis, F. C., Wilsbacher, L. D., King, D. P., Takahashi, J. S., and Weitz, C. J. (1998). Role of the clock protein in the mammalian circadian mechanism. *Science*, 280(5369):1564–1569.

[Gérard and Goldbeter, 2009] Gérard, C. and Goldbeter, A. (2009). Temporal self-organization of the cyclin/cdk network driving the mammalian cell cycle. *Proceedings of the National Academy of Sciences*, 106(51):21643–21648.

[Gérard and Goldbeter, 2012] Gérard, C. and Goldbeter, A. (2012). Entrainment of the mammalian cell cycle by the circadian clock: modeling two coupled cellular rhythms. *PLoS computational biology*, 8(5):e1002516.

[Geyfman et al., 2012] Geyfman, M., Kumar, V., Liu, Q., Ruiz, R., Gordon, W., Espitia, F., Cam, E., Millar, S. E., Smyth, P., Ihler, A., Takahashi, J. S., and Andersen, B. (2012). Brain and muscle Arnt-like protein-1 (BMAL1) controls circadian cell proliferation and susceptibility to UVB-induced DNA damage in the epidermis. *Proc Natl Acad Sci U S A*, 109(29):11758–11763.

[Gillette and Tischkau, 1999] Gillette, M. U. and Tischkau, S. A. (1999). Suprachiasmatic nucleus: the brain's circadian clock. *Recent Prog Horm Res*, 54:33–58.

[Giné, 2013] Giné, J. (2013). The stable limit cycles: A synchronization phenomenon. *Journal of the Franklin Institute*, 350(7):1649–1657.

[Glass, 2001] Glass, L. (2001). Synchronization and rhythmic processes in physiology. *Nature*, 410(6825):277–284.

[Godinho et al., 2007] Godinho, S. I. H., Maywood, E. S., Shaw, L., Tucci, V., Barnard, A. R., Busino, L., Pagano, M., Kendall, R., Quwailid, M. M., Romero, M. R., O'neill, J., Chesham, J. E., Brooker, D., Lalanne, Z., Hastings, M. H., and Nolan, P. M. (2007). The after-hours mutant reveals a role for fbxl3 in determining mammalian circadian period. *Science*, 316(5826):897–900.

[Goshima et al., 1999] Goshima, G., Saitoh, S., and Yanagida, M. (1999). Proper metaphase spindle length is determined by centromere proteins mis12 and mis6 required for faithful chromosome segregation. *Genes & Development*, 13(13):1664–1677.

[Goto and Johnson, 1995] Goto, K. and Johnson, C. H. (1995). Is the cell division cycle gated by a circadian clock? The case of Chlamydomonas reinhardtii. *The Journal of cell biology*, 129(4):1061–9.

[Gottesfeld and Forbes, 1997] Gottesfeld, J. M. and Forbes, D. J. (1997). Mitotic repression of the transcriptional machinery. *Trends in Biochemical Sciences*, 22(6):197–202.

[Granada et al., 2013] Granada, A. E., Bordyugov, G., Kramer, A., and Herzel, H. (2013). Human chronotypes from a theoretical perspective. *PLoS One*, 8(3):e59464.

[Grechez-Cassiau et al., 2008] Grechez-Cassiau, A., Rayet, B., Guillaumond, F., Teboul, M., and Delaunay, F. (2008). The circadian clock component bmal1 is a critical regulator of p21waf1/cip1 expression and hepatocyte proliferation. *J Biol Chem*, 283(8):4535–4542.

[Green et al., 2008] Green, C. B., Takahashi, J. S., and Bass, J. (2008). The meter of metabolism. *Cell*, 134(5):728 – 742.

[Green et al., 2012] Green, R. A., Paluch, E., and Oegema, K. (2012). Cytokinesis in animal cells. *Annu Rev Cell Dev Biol*, 28:29–58.

[Guillaumond et al., 2005] Guillaumond, F., Dardente, H., Giguere, V., and Cermakian, N. (2005). Differential control of bmal1 circadian transcription by rev-erb and ror nuclear receptors. *J Biol Rhythms*, 20(5):391–403.

[Gut et al., 2015] Gut, G., Tadmor, M. D., Pe'er, D., Pelkmans, L., and Liberali, P. (2015). Trajectories of cell-cycle progression from fixed cell populations. *Nat Methods*, 12(10):951–954.

[Guttinger et al., 2009] Guttinger, S., Laurell, E., and Kutay, U. (2009). Orchestrating nuclear envelope disassembly and reassembly during mitosis. *Nat Rev Mol Cell Biol*, 10(3):178–191.

[Hagting et al., 2002] Hagting, A., Den Elzen, N., Vodermaier, H. C., Waizenegger, I. C., Peters, J.-M., and Pines, J. (2002). Human securin proteolysis is controlled by the spindle checkpoint and reveals when the apc/c switches from activation by cdc20 to cdh1. *J Cell Biol*, 157(7):1125–1137.

[Hahn et al., 2009] Hahn, A. T., Jones, J. T., and Meyer, T. (2009). Quantitative analysis of cell cycle phase durations and PC12 differentiation using fluorescent biosensors. *Cell cycle (Georgetown, Tex)*, 8(7):1044–1052.

[Halberg et al., 1959] Halberg, F., Halberg, E., Barnum, C. P., and Bittner, J. J. (1959). Physiologic 24-hour periodicity in human beings and mice, the lighting regimen and daily routine. *AAAS Press, Washington DC,*.

[Halevy et al., 1995] Halevy, O., Novitch, B., Spicer, D., Skapek, S., Rhee, J., Hannon, G., Beach, D., and Lassar, A. (1995). Correlation of terminal cell cycle arrest of skeletal muscle with induction of p21 by myod. *Science*, 267(5200):1018–1021.

[Herrup and Yang, 2007] Herrup, K. and Yang, Y. (2007). Cell cycle regulation in the postmitotic neuron: oxymoron or new biology? *Nat Rev Neurosci*, 8(5):368–378.

[Hirota et al., 2010] Hirota, T., Lee, J. W., Lewis, W. G., Zhang, E. E., Breton, G., Liu, X., Garcia, M., Peters, E. C., Etchegaray, J.-P., Traver, D., Schultz, P. G., and Kay, S. A. (2010). High-throughput chemical screen identifies a novel potent modulator of cellular circadian rhythms and reveals ckialpha as a clock regulatory kinase. *PLoS Biol*, 8(12):e1000559.

[Hochegger et al., 2008] Hochegger, H., Takeda, S., and Hunt, T. (2008). Cyclin-dependent kinases and cell-cycle transitions: does one fit all? *Nat Rev Mol Cell Biol*, 9(11):910–916.

[Hong et al., 2014] Hong, C. I., Zamborszky, J., Baek, M., Labiscsak, L., Ju, K., Lee, H., Larrondo, L. F., Goity, A., Chong, H. S., Belden, W. J., and Csikasz-Nagy, A. (2014). Circadian rhythms synchronize mitosis in Neurospora crassa. *Proc Natl Acad Sci U S A*, 111(4):1397–1402.

[Hughes et al., 2012] Hughes, M. E., Hong, H.-K., Chong, J. L., Indacochea, A. A., Lee, S. S., Han, M., Takahashi, J. S., and Hogenesch, J. B. (2012). Brain-specific rescue of clock reveals system-driven transcriptional rhythms in peripheral tissue. *PLoS Genetics*, 8(7):e1002835.

[Janich et al., 2011] Janich, P., Pascual, G., Merlos-Suarez, A., Batlle, E., Ripperger, J., Albrecht, U., Cheng, H. Y., Obrietan, K., Di Croce, L., and Benitah, S. A. (2011). The circadian molecular clock creates epidermal stem cell heterogeneity. *Nature*, 480(7376):209–214.

[Janich et al., 2013] Janich, P., Toufighi, K., Solanas, G., Luis, N. M., Minkwitz, S., Serrano, L., Lehner, B., and Benitah, S. A. (2013). Human epidermal stem cell function is regulated by circadian oscillations. *Cell Stem Cell*, 13(6):745–753.

[Jaqaman et al., 2008] Jaqaman, K., Loerke, D., Mettlen, M., Kuwata, H., Grinstein, S., Schmid, S. L., and Danuser, G. (2008). Robust single-particle tracking in live-cell time-lapse sequences. *Nat Methods*, 5(8):695–702.

[Jones et al., 1999] Jones, C. R., Campbell, S. S., Zone, S. E., Cooper, F., DeSano, A., Murphy, P. J., Jones, B., Czajkowski, L., and Ptacek, L. J. (1999). Familial advanced sleep-phase syndrome: A short-period circadian rhythm variant in humans. *Nat Med*, 5(9):1062–1065.

[Jung et al., 2010] Jung, Y.-S., Qian, Y., and Chen, X. (2010). Examination of the expanding pathways for the regulation of p21 expression and activity. *Cell Signal*, 22(7):1003–1012.

[Kaldis, 1999] Kaldis, P. (1999). The cdk-activating kinase (cak): from yeast to mammals. *Cell Mol Life Sci*, 55(2):284–296.

[Kang et al., 2008] Kang, B., Li, Y.-Y., Chang, X., Liu, L., and Li, Y.-X. (2008). Modeling the effects of cell cycle M-phase transcriptional inhibition on circadian oscillation. *PLoS Comput Biol*, 4(3):e1000019.

[Kapitaniak et al., 2012] Kapitaniak, M., Brzeski, P., Czolczynski, K., Perlikowski, P., Stefanski, A., and Kapitaniak, T. (2012). Synchronization thresholds of coupled self-excited nonidentical pendula suspended on the vertically displacing beam. *Progress of Theoretical Physics*, 128(6):1141–1173.

[Karlsson et al., 2001] Karlsson, B., Knutsson, A., and Lindahl, B. (2001). Is there an association between shift work and having a metabolic syndrome? results from a population based study of 27 485 people. *Occupational and Environmental Medicine*, 58(11):747–752.

[Karlsson et al., 2003] Karlsson, B. H., Knutsson, A. K., Lindahl, B. O., and Alfredsson, L. S. (2003). Metabolic disturbances in male workers with rotating three-shift work. results of the wolf study. *Int Arch Occup Environ Health*, 76(6):424–430.

[Katok and Hasselblatt, 1997] Katok, A. and Hasselblatt, B. (1997). *Introduction to the Modern Theory of Dynamical Systems*. Encyclopedia of Mathematics and its Applications. Cambridge University Press.

[Kelly and Brown, 2000] Kelly, T. J. and Brown, G. W. (2000). Regulation of chromosome replication. *Annu Rev Biochem*, 69:829–880.

[Kerkhof and Van Dongen, 1996] Kerkhof, G. A. and Van Dongen, H. P. (1996). Morning-type and evening-type individuals differ in the phase position of their endogenous circadian oscillator. *Neurosci Lett*, 218(3):153–156.

[Kita-Matsuo et al., 2009] Kita-Matsuo, H., Barcova, M., Prigozhina, N., Salomonis, N., Wei, K., Jacot, J., Nelson, B., Spiering, S., Haverslag, R., Kim, C., Talantova, M., Bajpai, R., Calzolari, D., Terskikh, A., McCulloch, A., Price, J., Conklin, B., Chen, H., and Mercola, M. (2009). Lentiviral vectors and protocols for creation of stable hESC lines for fluorescent tracking and drug resistance selection of cardiomyocytes. *PLoS One*, 4:e5046.

[Klevecz et al., 1987] Klevecz, R. R., Shymko, R. M., Blumenfeld, D., and Braly, P. S. (1987). Circadian gating of s phase in human ovarian cancer. *Cancer Res*, 47(23):6267–6271.

[Kobayashi et al., 2002] Kobayashi, M., Wood, P. A., and Hrushesky, W. J. M. (2002). Circadian chemotherapy for gynecological and genitourinary cancers. *Chronobiol Int*, 19(1):237–251.

[Kojima et al., 2009] Kojima, K., Shimanuki, M., Shikami, M., Andreeff, M., and Nakakuma, H. (2009). The cdk1 inhibitor ro-3306 enhances p53-mediated bax activation and mitochondrial apoptosis in aml. *Cancer science*, 100(6):1128–1136.

[Kondo et al., 1997] Kondo, T., Mori, T., Lebedeva, N. V., Aoki, S., Ishiura, M., and Golden, S. S. (1997). Circadian rhythms in rapidly dividing cyanobacteria. *Science*, 275(5297):224–227.

[Kondo et al., 1993] Kondo, T., Strayer, C. A., Kulkarni, R. D., Taylor, W., Ishiura, M., Golden, S. S., and Johnson, C. H. (1993). Circadian rhythms in prokaryotes: luciferase as a reporter of circadian gene expression in cyanobacteria. *Proc Natl Acad Sci U S A*, 90(12):5672–5676.

[Kornmann et al., 2001] Kornmann, B., Preitner, N., Rifat, D., Fleury-Olela, F., and Schibler, U. (2001). Analysis of circadian liver gene expression by adder, a highly sensitive method for the display of differentially expressed mrnas. *Nucleic Acids Research*, 29(11):e51–e51.

[Kornmann et al., 2007] Kornmann, B., Schaad, O., Bujard, H., Takahashi, J. S., and Schibler, U. (2007). System-driven and oscillator-dependent circadian transcription in mice with a conditionally active liver clock. *PLoS Biol*, 5(2):e34.

[Kowalska et al., 2013] Kowalska, E., Ripperger, J. A., Hoegger, D. C., Bruegger, P., Buch, T., Birchler, T., Mueller, A., Albrecht, U., Contaldo, C., and Brown, S. A. (2013). NONO couples the circadian clock to the cell cycle. *Proceedings of the National Academy of Sciences of the United States of America*, 110(5):1592–9.

[Kramer et al., 2000] Kramer, E. R., Scheuringer, N., Podtelejnikov, A. V., Mann, M., and Peters, J. M. (2000). Mitotic regulation of the apc activator proteins cdc20 and cdh1. *Mol Biol Cell*, 11(5):1555–1569.

[Kume et al., 1999] Kume, K., Zylka, M. J., Sriram, S., Shearman, L. P., Weaver, D. R., Jin, X., Maywood, E. S., Hastings, M. H., and Reppert, S. M. (1999). mcry1 and mcry2 are essential components of the negative limb of the circadian clock feedback loop. *Cell*, 98(2):193–205.

[Kunkel, 2004] Kunkel, T. A. (2004). Dna replication fidelity. *Journal of Biological Chemistry*, 279(17):16895–16898.

[Kurabayashi et al., 2010] Kurabayashi, N., Hirota, T., Sakai, M., Sanada, K., and Fukada, Y. (2010). Dyrk1a and glycogen synthase kinase 3beta, a dual-kinase mechanism directing proteasomal degradation of cry2 for circadian timekeeping. *Mol Cell Biol*, 30(7):1757–1768.

[Lamia et al., 2009] Lamia, K. A., Sachdeva, U. M., DiTacchio, L., Williams, E. C., Alvarez, J. G., Egan, D. F., Vasquez, D. S., Juguilon, H., Panda, S., Shaw, R. J., Thompson, C. B., and Evans, R. M. (2009). Ampk regulates the circadian clock by cryptochrome phosphorylation and degradation. *Science*, 326(5951):437–440.

[Lee et al., 2010] Lee, S., Donehower, L. A., Herron, A. J., Moore, D. D., and Fu, L. (2010). Disrupting circadian homeostasis of sympathetic signaling promotes tumor development in mice. *PLoS One*, 5(6):e10995.

[Lehmann et al., 2015] Lehmann, R., Childs, L., Thomas, P., Abreu, M., Fuhr, L., Herzel, H., Leser, U., and Relógio, A. (2015). Assembly of a comprehensive regulatory network for the mammalian circadian clock: A bioinformatics approach. *PLoS ONE*, 10(5):e0126283.

[Leloup and Goldbeter, 2003] Leloup, J.-C. and Goldbeter, A. (2003). Toward a detailed computational model for the mammalian circadian clock. *Proceedings of the National Academy of Sciences of the United States of America*, 100(12):7051–6.

[Lemons, 2002] Lemons, D. S. (2002). *An Introduction to Stochastic Processes in Physics*. JHU Press.

[Levi et al., 2007] Levi, F., Filipski, E., Iurisci, I., Li, X. M., and Innominato, P. (2007). Cross-talks between circadian timing system and cell division cycle determine cancer biology and therapeutics. *Cold Spring Harb Symp Quant Biol*, 72:465–475.

[Li and Zou, 2005] Li, L. and Zou, L. (2005). Sensing, signaling, and responding to dna damage: organization of the checkpoint pathways in mammalian cells. *J Cell Biochem*, 94(2):298–306.

[Liggett and Sidransky, 1998] Liggett, W. H. J. and Sidransky, D. (1998). Role of the p16 tumor suppressor gene in cancer. *J Clin Oncol*, 16(3):1197–1206.

[Liskay, 1977] Liskay, R. M. (1977). Absence of a measurable g2 phase in two chinese hamster cell lines. *Proceedings of the National Academy of Sciences of the United States of America*, 74(4):1622–1625.

[Lolli and Johnson, 2005] Lolli, G. and Johnson, L. N. (2005). Cak-cyclin-dependent activating kinase: a key kinase in cell cycle control and a target for drugs? *Cell Cycle*, 4(4):572–577.

[Lowrey and Takahashi, 2004] Lowrey, P. L. and Takahashi, J. S. (2004). Mammalian circadian biology: elucidating genome-wide levels of temporal organization. *Annu Rev Genomics Hum Genet*, 5:407–441.

[Magidson et al., 2011] Magidson, V., O'Connell, C. B., Loncarek, J., Paul, R., Mogilner, A., and Khodjakov, A. (2011). The spatial arrangement of chromosomes during prometaphase facilitates spindle assembly. *Cell*, 146(4):555–567.

[Maier et al., 2009] Maier, B., Wendt, S., Vanselow, J. T., Wallach, T., Reischl, S., Oehmke, S., Schlosser, A., and Kramer, A. (2009). A large-scale functional RNAi screen reveals a role for CK2 in the mammalian circadian clock. *Genes Dev*, 23(6):708–718.

[Malumbres and Barbacid, 2009] Malumbres, M. and Barbacid, M. (2009). Cell cycle, cdks and cancer: a changing paradigm. *Nat Rev Cancer*, 9(3):153–166.

[Martinez-Balbas et al., 1995] Martinez-Balbas, M. A., Dey, A., Rabindran, S. K., Ozato, K., and Wu, C. (1995). Displacement of sequence-specific transcription factors from mitotic chromatin. *Cell*, 83(1):29–38.

[Matsuo et al., 2003] Matsuo, T., Yamaguchi, S., Mitsui, S., Emi, A., Shimoda, F., and Okamura, H. (2003). Control mechanism of the circadian clock for timing of cell division in vivo. *Science (New York, N.Y.)*, 302(5643):255–9.

[McGarry and Kirschner, 1998] McGarry, T. J. and Kirschner, M. W. (1998). Geminin, an inhibitor of dna replication, is degraded during mitosis. *Cell*, 93(6):1043–1053.

[Meadows and Millar, 2015] Meadows, J. C. and Millar, J. B. A. (2015). Sharpening the anaphase switch. *Biochem Soc Trans*, 43(1):19–22.

[Merrow et al., 1999] Merrow, M., Brunner, M., and Roenneberg, T. (1999). Assignment of circadian function for the neurospora clock gene frequency. *Nature*, 399(6736):584–586.

[Millar-Craig et al., 1978] Millar-Craig, M., Bishop, C., and Raftery, E. B. (1978). Originally published as volume 1, issue 8068circadian variation of blood-pressure. *The Lancet*, 311(8068):795–797.

[Miller et al., 2007] Miller, B. H., McDearmon, E. L., Panda, S., Hayes, K. R., Zhang, J., Andrews, J. L., Antoch, M. P., Walker, J. R., Esser, K. A., Hogenesch, J. B., and Takahashi, J. S. (2007). Circadian and clock-controlled regulation of the mouse transcriptome and cell proliferation. *Proceedings of the National Academy of Sciences*, 104(9):3342–3347.

[Mills et al., 1974] Mills, J. N., Minors, D. S., and Waterhouse, J. M. (1974). The circadian rhythms of human subjects without timepieces or indication of the alternation of day and night. *The Journal of Physiology*, 240(3):567–594.

[Moffat et al., 2006] Moffat, J., Grueneberg, D. A., Yang, X., Kim, S. Y., Kloepfer, A. M., Hinkle, G., Piqani, B., Eisenhaure, T. M., Luo, B., Grenier, J. K., Carpenter, A. E., Foo, S. Y., Stewart, S. A., Stockwell, B. R., Hacohen, N., Hahn, W. C., Lander, E. S., Sabatini, D. M., and Root, D. E. (2006). A lentiviral RNAi library for human and mouse genes applied to an arrayed viral high-content screen. *Cell*, 124(6):1283–1298.

[Mohawk et al., 2012] Mohawk, J. A., Green, C. B., and Takahashi, J. S. (2012). Central and peripheral circadian clocks in mammals. *Annu Rev Neurosci*, 35:445–462.

[Mohawk and Takahashi, 2011] Mohawk, J. A. and Takahashi, J. S. (2011). Cell autonomy and synchrony of suprachiasmatic nucleus circadian oscillators. *Trends Neurosci*, 34(7):349–358.

[Molina et al., 2013] Molina, N., Suter, D. M., Cannavo, R., Zoller, B., Gotic, I., and Naef, F. (2013). Stimulus-induced modulation of transcriptional bursting in a single mammalian gene. *Proceedings of the National Academy of Sciences*, 110(51):20563–20568.

[Morgan, 2007] Morgan, D. (2007). *The cell cycle: principles of control. New*. Science Press, London.

[Mori et al., 1996] Mori, T., Binder, B., and Johnson, C. H. (1996). Circadian gating of cell division in cyanobacteria growing with average doubling times of less than 24 hours. *Proceedings of the National Academy of Sciences of the United States of America*, 93(19):10183–8.

[Mukherji et al., 2013] Mukherji, A., Kobiita, A., Ye, T., and Chambon, P. (2013). Homeostasis in intestinal epithelium is orchestrated by the circadian clock and microbiota cues transduced by TLRs. *Cell*, 153(4):812–827.

[Murray and Hunt, 1993] Murray, A. W. and Hunt, T. (1993). *The cell cycle : an introduction*. New York : W.H. Freeman.

[Nagoshi et al., 2004] Nagoshi, E., Saini, C., Bauer, C., Laroche, T., Naef, F., and Schibler, U. (2004). Circadian gene expression in individual fibroblasts: cell-autonomous and self-sustained oscillators pass time to daughter cells. *Cell*, 119(5):693–705.

[Nakayama and Nakayama, 2005] Nakayama, K. I. and Nakayama, K. (2005). Regulation of the cell cycle by scf-type ubiquitin ligases. *Semin Cell Dev Biol*, 16(3):323–333.

[Newman and Zhang, 2008] Newman, R. H. and Zhang, J. (2008). Fucci: Street lights on the road to mitosis. *Chemistry & Biology*, 15(2):97–98.

[Norbury and Nurse, 1992] Norbury, C. and Nurse, P. (1992). Animal cell cycles and their control. *Annu Rev Biochem*, 61:441–470.

[Novák and Tyson, 2004] Novák, B. and Tyson, J. J. (2004). A model for restriction point control of the mammalian cell cycle. *J Theor Biol*, 230(4):563–579.

[Ohdo, 2003] Ohdo, S. (2003). Changes in toxicity and effectiveness with timing of drug administration: implications for drug safety. *Drug Saf*, 26(14):999–1010.

[O'Neill and Hastings, 2008] O'Neill, J. S. and Hastings, M. H. (2008). Increased coherence of circadian rhythms in mature fibroblast cultures. *J Biol Rhythms*, 23(6):483–488.

[Orford and Scadden, 2008] Orford, K. W. and Scadden, D. T. (2008). Deconstructing stem cell self-renewal: genetic insights into cell-cycle regulation. *Nat Rev Genet*, 9(2):115–128.

[Ortiz-Tudela et al., 2013] Ortiz-Tudela, E., Mteyrek, A., Ballesta, A., Innominato, P. F., and Levi, F. (2013). Cancer chronotherapeutics: experimental, theoretical, and clinical aspects. *Handb Exp Pharmacol*, (217):261–288.

[Paine et al., 2006] Paine, S.-J., Gander, P. H., and Travier, N. (2006). The epidemiology of morningness/eveningness: influence of age, gender, ethnicity, and socioeconomic factors in adults (30-49 years). *J Biol Rhythms*, 21(1):68–76.

[Palus and Stefanovska, 2003] Palus, M. and Stefanovska, A. (2003). Direction of coupling from phases of interacting oscillators: an information-theoretic approach. *Phys Rev E Stat Nonlin Soft Matter Phys*, 67(5 Pt 2):055201.

[Panda et al., 2002] Panda, S., Antoch, M. P., Miller, B. H., Su, A. I., Schook, A. B., Straume, M., Schultz, P. G., Kay, S. A., Takahashi, J. S., and Hogenesch, J. B. (2002). Coordinated Transcription of Key Pathways in the Mouse by the Circadian Clock. *Cell*, 109(3):307–320.

[Paschos, 2015] Paschos, G. K. (2015). Circadian clocks, feeding time, and metabolic homeostasis. *Frontiers in Pharmacology*, 6:112.

[Pavletich, 1999] Pavletich, N. P. (1999). Mechanisms of cyclin-dependent kinase regulation: structures of cdks, their cyclin activators, and cip and {INK4} inhibitors1,2. *Journal of Molecular Biology*, 287(5):821 – 828.

[Pendergast et al., 2010] Pendergast, J. S., Yeom, M., Reyes, B. A., Ohmiya, Y., and Yamazaki, S. (2010). Disconnected circadian and cell cycles in a tumor-driven cell line. *Communicative & integrative biology*, 3(6):536–539.

[Peters et al., 2008] Peters, J.-M., Tedeschi, A., and Schmitz, J. (2008). The cohesin complex and its roles in chromosome biology. *Genes & Development*, 22(22):3089–3114.

[Pikovsky and Rosenblum, 2007] Pikovsky, A. and Rosenblum, M. (2007). Synchronization. *Scholarpedia*, 2(12):1459.

[Pikovsky et al., 2003] Pikovsky, A., Rosenblum, M., and Kurths, J. (2003). *Synchronization: A Universal Concept in Nonlinear Sciences*. Cambridge Nonlinear Science Series. Cambridge University Press.

[Pittendrigh, 1960] Pittendrigh, C. (1960). Circadian rhythms and the circadian organization of living systems. *Cold Spring Harbor Symposia on quantitative biology*, 25:159–184.

[Pittendrigh, 1954] Pittendrigh, C. S. (1954). On temperature independence in the clock system controlling emerge time in drosophila. *Proceedings of the National Academy of Sciences of the United States of America*, 40(10):1018–1029.

[Plikus et al., 2013] Plikus, M. V., Vollmers, C., de la Cruz, D., Chaix, A., Ramos, R., Panda, S., and Chuong, C.-M. (2013). Local circadian clock gates cell cycle progression of transient amplifying cells during regenerative hair cycling. *Proc Natl Acad Sci U S A*, 110(23):E2106–15.

[Potapova et al., 2009] Potapova, T. A., Daum, J. R., Byrd, K. S., and Gorbsky, G. J. (2009). Fine tuning the cell cycle: Activation of the cdk1 inhibitory phosphorylation pathway during mitotic exit. *Molecular Biology of the Cell*, 20(6):1737–1748.

[Pratt et al., 2006] Pratt, D. J., Bentley, J., Jewsbury, P., Boyle, F. T., Endicott, J. A., and Noble, M. E. M. (2006). Dissecting the determinants of cyclin-dependent kinase 2 and cyclin-dependent kinase 4 inhibitor selectivity. *J Med Chem*, 49(18):5470–5477.

[Preitner et al., 2002] Preitner, N., Damiola, F., Lopez-Molina, L., Zakany, J., Duboule, D., Albrecht, U., and Schibler, U. (2002). The orphan nuclear receptor REV-ERBalpha controls circadian transcription within the positive limb of the mammalian circadian oscillator. *Cell*, 110(2):251–260.

[Pulivarthy et al., 2007] Pulivarthy, S. R., Tanaka, N., Welsh, D. K., De Haro, L., Verma, I. M., and Panda, S. (2007). Reciprocity between phase shifts and amplitude changes in the mammalian circadian clock. *Proc Natl Acad Sci U S A*, 104(51):20356–20361.

[Qiao et al., 2010] Qiao, X., Zhang, L., Gamper, A. M., Fujita, T., and Wan, Y. (2010). Apc/c-cdh1. *Cell Cycle*, 9(19):3904–3912.

[Qu et al., 2003] Qu, Z., MacLellan, W. R., and Weiss, J. N. (2003). Dynamics of the cell cycle: checkpoints, sizers, and timers. *Biophys J*, 85(6):3600–3611.

[Rahal and Amon, 2008] Rahal, R. and Amon, A. (2008). Mitotic cdks control the metaphase–anaphase transition and trigger spindle elongation. *Genes & Development*, 22(11):1534–1548.

[Ralph et al., 1990] Ralph, M. R., Foster, R. G., Davis, F. C., and Menaker, M. (1990). Transplanted suprachiasmatic nucleus determines circadian period. *Science*, 247(4945):975–978.

[Rayleigh and Lindsay, 1945] Rayleigh, J. and Lindsay, R. (1945). *The Theory of Sound*. Number v. 1 in Dover Books on Physics Series. Dover.

[Refinetti, 2010] Refinetti, R. (2010). Entrainment of circadian rhythm by ambient temperature cycles in mice. *J Biol Rhythms*, 25(4):247–256.

[Reid and Zee, 2009] Reid, K. J. and Zee, P. C. (2009). Circadian rhythm disorders. *Semin Neurol*, 29(4):393–405.

[Relogio et al., 2011] Relogio, A., Westermark, P. O., Wallach, T., Schellenberg, K., Kramer, A., and Herzel, H. (2011). Tuning the mammalian circadian clock: robust synergy of two loops. *PLoS Comput Biol*, 7(12):e1002309.

[Reyes et al., 2008] Reyes, B. A., Pendergast, J. S., and Yamazaki, S. (2008). Mammalian peripheral circadian oscillators are temperature compensated. *Journal of biological rhythms*, 23(1):95–98.

[Richter, 1968] Richter, C. P. (1968). Inherent 24-hour and lunar clocks of a primate - the squirrel monkey. *Comp. Behav. Biol. 1, 305–332*.

[Roenneberg et al., 2012] Roenneberg, T., Allebrandt, K. V., Merrow, M., and Vetter, C. (2012). Social jetlag and obesity. *Curr Biol*, 22(10):939–943.

[Roenneberg et al., 2013] Roenneberg, T., Kantermann, T., Juda, M., Vetter, C., and Allebrandt, K. V. (2013). Light and the human circadian clock. *Handb Exp Pharmacol*, (217):311–331.

[Roenneberg et al., 2007a] Roenneberg, T., Kuehnle, T., Juda, M., Kantermann, T., Allebrandt, K., Gordijn, M., and Merrow, M. (2007a). Epidemiology of the human circadian clock. *Sleep Med Rev*, 11(6):429–438.

[Roenneberg et al., 2004] Roenneberg, T., Kuehnle, T., Pramstaller, P. P., Ricken, J., Havel, M., Guth, A., and Merrow, M. (2004). A marker for the end of adolescence. *Curr Biol*, 14(24):R1038–9.

[Roenneberg et al., 2007b] Roenneberg, T., Kumar, C. J., and Merrow, M. (2007b). The human circadian clock entrains to sun time. *Curr Biol*, 17(2):R44–5.

[Roenneberg and Merrow, 2005] Roenneberg, T. and Merrow, M. (2005). Circadian clocks [mdash] the fall and rise of physiology. *Nat Rev Mol Cell Biol*, 6(12):965–971.

[Roenneberg et al., 2003] Roenneberg, T., Wirz-Justice, A., and Merrow, M. (2003). Life between clocks: daily temporal patterns of human chronotypes. *J Biol Rhythms*, 18(1):80–90.

[Rosenblum and Pikovsky, 2001] Rosenblum, M. G. and Pikovsky, A. S. (2001). Detecting direction of coupling in interacting oscillators. *Phys Rev E Stat Nonlin Soft Matter Phys*, 64(4 Pt 2):045202.

[Saini et al., 2012] Saini, C., Morf, J., Stratmann, M., Gos, P., and Schibler, U. (2012). Simulated body temperature rhythms reveal the phase-shifting behavior and plasticity of mammalian circadian oscillators. *Genes & Development*, 26(6):567–580.

[Sakaue-Sawano et al., 2008] Sakaue-Sawano, A., Kurokawa, H., Morimura, T., Hanyu, A., Hama, H., Osawa, H., Kashiwagi, S., Fukami, K., Miyata, T., Miyoshi, H., Imamura, T., Ogawa, M., Masai, H., and Miyawaki, A. (2008). Visualizing spatiotemporal dynamics of multicellular cell-cycle progression. *Cell*, 132(3):487–98.

[Salmon and Trono, 2007] Salmon, P. and Trono, D. (2007). Production and titration of lentiviral vectors. *Curr Protoc Hum Genet*, Chapter 12:Unit 12.10.

[Sato et al., 2004] Sato, T. K., Panda, S., Miraglia, L. J., Reyes, T. M., Rudic, R. D., McNamara, P., Naik, K. A., FitzGerald, G. A., Kay, S. A., and Hogenesch, J. B. (2004). A functional genomics strategy reveals rora as a component of the mammalian circadian clock. *Neuron*, 43(4):527–537.

[Schafer, 1998] Schafer, K. A. (1998). The cell cycle: A review. *Veterinary Pathology Online*, 35(6):461–478.

[Scheiermann et al., 2013] Scheiermann, C., Kunisaki, Y., and Frenette, P. S. (2013). Circadian control of the immune system. *Nat Rev Immunol*, 13(3):190–198.

[Shafer, 1995] Shafer, D. (1995). *Nonlinear Dynamics and Chaos: With Applications to Physics, Biology, Chemistry, and Engineering (Steven H. Strogatz)*, volume 37. Society for Industrial and Applied Mathematics.

[Shaik et al., 2001] Shaik, S., Liu, P., Fukushima, H., Wang, Z., and Wei, W. (2001). *Protein Degradation in Cell Cycle*. John Wiley & Sons, Ltd.

[Shi et al., 2013] Shi, S.-q., Ansari, T. S., McGuinness, O. P., Wasserman, D. H., and Johnson, C. H. (2013). Circadian disruption leads to insulin resistance and obesity. *Curr Biol*, 23(5):372–381.

[Shichiri et al., 1993] Shichiri, M., Hanson, K. D., and Sedivy, J. M. (1993). Effects of c-myc expression on proliferation, quiescence, and the g0 to g1 transition in nontransformed cells. *Cell Growth Differ*, 4(2):93–104.

[Smirnov and Bezruchko, 2003] Smirnov, D. A. and Bezruchko, B. P. (2003). Estimation of interaction strength and direction from short and noisy time series. *Physical Review E*, 68(4):046209–.

[Stark and Taylor, 2004] Stark, G. R. and Taylor, W. R. (2004). Analyzing the g2/m checkpoint. *Methods Mol Biol*, 280:51–82.

[Storch et al., 2002] Storch, K.-F., Lipan, O., Leykin, I., Viswanathan, N., Davis, F. C., Wong, W. H., and Weitz, C. J. (2002). Extensive and divergent circadian gene expression in liver and heart. *Nature*, 417(6884):78–83.

[Storch et al., 2007] Storch, K.-F., Paz, C., Signorovitch, J., Raviola, E., Pawlyk, B., Li, T., and Weitz, C. J. (2007). Intrinsic circadian clock of the mammalian retina: importance for retinal processing of visual information. *Cell*, 130(4):730–741.

[Straley and Bruce, 1979] Straley, S. C. and Bruce, V. G. (1979). Stickiness to glass: Circadian changes in the cell surface of chlamydomonas reinhardi. *Plant Physiol*, 63(6):1175–1181.

[Stratmann et al., 2010] Stratmann, M., Stadler, F., Tamanini, F., van der Horst, G. T., and Ripperger, J. A. (2010). Flexible phase adjustment of circadian albumin D site-binding protein (DBP) gene expression by CRYPTOCHROME1. *Genes Dev*, 24(12):1317–1328.

[Stratmann et al., 2012] Stratmann, M., Suter, D. M., Molina, N., Naef, F., and Schibler, U. (2012). Circadian dbp transcription relies on highly dynamic bmal1-clock interaction with e boxes and requires the proteasome. *Molecular Cell*, 48(2):277–287.

[Sumner, 1991] Sumner, A. T. (1991). Scanning electron microscopy of mammalian chromosomes from prophase to telophase. *Chromosoma*, 100(6):410–418.

[Suryadinata et al., 2010] Suryadinata, R., Sadowski, M., and Sarcevic, B. (2010). Control of cell cycle progression by phosphorylation of cyclin-dependent kinase (cdk) substrates. *Bioscience Reports*, 30(4):243–255.

[Sweeney and Hastings, 1958] Sweeney, B. M. and Hastings, J. W. (1958). Rhythmic Cell Division in Populations of Gonyaulax polyedra. *The Journal of Protozoology*, 5(3):217–224.

[Takahashi, 2004] Takahashi, J. S. (2004). Finding new clock components: past and future. *J Biol Rhythms*, 19(5):339–347.

[Tamai et al., 2012] Tamai, T. K., Young, L. C., Cox, C. A., and Whitmore, D. (2012). Light acts on the zebrafish circadian clock to suppress rhythmic mitosis and cell proliferation. *J Biol Rhythms*, 27(3):226–236.

[Tanaka and Araki, 2013] Tanaka, S. and Araki, H. (2013). Helicase activation and establishment of replication forks at chromosomal origins of replication. *Cold Spring Harbor Perspectives in Biology*, 5(12).

[Taylor, 1960] Taylor, J. H. (1960). Nucleic acid synthesis in relation to the cell division cycle. *Ann N Y Acad Sci*, 90:409–421.

[Taylor et al., 2010] Taylor, S. R., Webb, A. B., Smith, K. S., Petzold, L. R., and Doyle, F. J. r. (2010). Velocity response curves support the role of continuous entrainment in circadian clocks. *J Biol Rhythms*, 25(2):138–149.

[Thomas et al., 2011] Thomas, H. D., Wang, L.-Z., Roche, C., Bentley, J., Cheng, Y., Hardcastle, I. R., Golding, B. T., Griffin, R. J., Curtin, N. J., and Newell, D. R. (2011). Preclinical in vitro and in vivo evaluation of the potent and specific cyclin-dependent kinase 2 inhibitor nu6102 and a water soluble prodrug nu6301. *Eur J Cancer*, 47(13):2052–2059.

[Thornton and Toczyski, 2003] Thornton, B. R. and Toczyski, D. P. (2003). Securin and b-cyclin/cdk are the only essential targets of the apc. *Nat Cell Biol*, 5(12):1090–1094.

[Toh et al., 2001] Toh, K. L., Jones, C. R., He, Y., Eide, E. J., Hinz, W. A., Virshup, D. M., Ptacek, L. J., and Fu, Y. H. (2001). An hper2 phosphorylation site mutation in familial advanced sleep phase syndrome. *Science*, 291(5506):1040–1043.

[Toyoshima and Hunter, 1994] Toyoshima, H. and Hunter, T. (1994). p27, a novel inhibitor of g1 cyclin-cdk protein kinase activity, is related to p21. *Cell*, 78(1):67–74.

[Traynard et al., 2015] Traynard, P., Fages, F., and Soliman, S. (2015). *Model-Based Investigation of the Effect of the Cell Cycle on the Circadian Clock Through Transcription Inhibition During Mitosis*, volume 9308, pages 208–221. Springer International Publishing.

[van den Heiligenberg et al., 1999] van den Heiligenberg, S., Depres-Brummer, P., Barbason, H., Claustrat, B., Reynes, M., and Levi, F. (1999). The tumor promoting effect of constant light exposure on diethylnitrosamine-induced hepatocarcinogenesis in rats. *Life Sci*, 64(26):2523–2534.

[van der Pol, 1927] van der Pol, B. (1927). Vii. forced oscillations in a circuit with non-linear resistance. (reception with reactive triode). *The London, Edinburgh, and Dublin Philosophical Magazine and Journal of Science*, 3(13):65–80.

[van Leuken et al., 2008] van Leuken, R., Clijsters, L., and Wolthuis, R. (2008). To cell cycle, swing the apc/c. *Biochimica et Biophysica Acta (BBA) - Reviews on Cancer*, 1786(1):49–59.

[Vink et al., 2001] Vink, J. M., Groot, A. S., Kerkhof, G. A., and Boomsma, D. I. (2001). Genetic analysis of morningness and eveningness. *Chronobiol Int*, 18(5):809–822.

[Vitaterna et al., 2006] Vitaterna, M. H., Ko, C. H., Chang, A.-M., Buhr, E. D., Fruechte, E. M., Schook, A., Antoch, M. P., Turek, F. W., and Takahashi, J. S. (2006). The mouse clock mutation reduces circadian pacemaker amplitude and enhances efficacy of resetting stimuli and phase–response curve amplitude. *Proceedings of the National Academy of Sciences*, 103(24):9327–9332.

[Vitaterna et al., 1999] Vitaterna, M. H., Selby, C. P., Todo, T., Niwa, H., Thompson, C., Fruechte, E. M., Hitomi, K., Thresher, R. J., Ishikawa, T., Miyazaki, J., Takahashi, J. S., and Sancar, A. (1999). Differential regulation of mammalian period genes and circadian rhythmicity by cryptochromes 1 and 2. *Proceedings of the National Academy of Sciences*, 96(21):12114–12119.

[Vodermaier, 2004] Vodermaier, H. C. (2004). Apc/c and scf: Controlling each other and the cell cycle. *Current Biology*, 14(18):R787–R796.

[Waizenegger et al., 2002] Waizenegger, I. C., Giménez-Abián, J. F., Wernic, D., and Peters, J.-M. (2002). Regulation of human separase by securin binding and autocleavage. *Current Biology*, 12(16):1368–1378.

[Walczak et al., 2010] Walczak, C. E., Cai, S., and Khodjakov, A. (2010). Mechanisms of chromosome behaviour during mitosis. *Nat Rev Mol Cell Biol*, 11(2):91–102.

[Welsh et al., 2004] Welsh, D. K., Yoo, S. H., Liu, A. C., Takahashi, J. S., and Kay, S. A. (2004). Bioluminescence imaging of individual fibroblasts reveals persistent, independently phased circadian rhythms of clock gene expression. *Curr Biol*, 14(24):2289–2295.

[Wright et al., 1999] Wright, J. H., Munar, E., Jameson, D. R., Andreassen, P. R., Margolis, R. L., Seger, R., and Krebs, E. G. (1999). Mitogen-activated protein kinase kinase activity is required for the g(2)/m transition of the cell cycle in mammalian fibroblasts. *Proc Natl Acad Sci U S A*, 96(20):11335–11340.

[Wright et al., 2012] Wright, K. P., Lowry, C. A., and LeBourgeois, M. K. (2012). Circadian and wakefulness-sleep modulation of cognition in humans. *Frontiers in Molecular Neuroscience*, 5:50.

[Wright et al., 2002] Wright, Jr., K. P., Hull, J. T., and Czeisler, C. A. (2002). Relationship between alertness, performance and body temperature in humans. *American Journal of Physiology - Regulatory, Integrative and Comparative Physiology*.

[Xu et al., 2005] Xu, Y., Padiath, Q. S., Shapiro, R. E., Jones, C. R., Wu, S. C., Saigoh, N., Saigoh, K., Ptacek, L. J., and Fu, Y.-H. (2005). Functional consequences of a ckidelta mutation causing familial advanced sleep phase syndrome. *Nature*, 434(7033):640–644.

[Yamazaki et al., 2000] Yamazaki, S., Numano, R., Abe, M., Hida, A., Takahashi, R., Ueda, M., Block, G. D., Sakaki, Y., Menaker, M., and Tei, H. (2000). Resetting central and peripheral circadian oscillators in transgenic rats. *Science*, 288(5466):682–685.

[Yang et al., 2010] Yang, Q., Pando, B. F., Dong, G., Golden, S. S., and van Oudenaarden, A. (2010). Circadian gating of the cell cycle revealed in single cyanobacterial cells. *Science (New York, N.Y.)*, 327(5972):1522–6.

[Ye et al., 2011] Ye, R., Selby, C. P., Ozturk, N., Annayev, Y., and Sancar, A. (2011). Biochemical analysis of the canonical model for the mammalian circadian clock. *J Biol Chem*, 286(29):25891–25902.

[Yeom et al., 2010] Yeom, M., Pendergast, J. S., Ohmiya, Y., and Yamazaki, S. (2010). Circadian-independent cell mitosis in immortalized fibroblasts. *Proceedings of the National Academy of Sciences of the United States of America*, 107(21):9665–70.

[Yoo et al., 2004] Yoo, S.-H., Yamazaki, S., Lowrey, P. L., Shimomura, K., Ko, C. H., Buhr, E. D., Siepka, S. M., Hong, H.-K., Oh, W. J., Yoo, O. J., Menaker, M., and Takahashi, J. S. (2004). Period2::luciferase real-time reporting of circadian dynamics reveals persistent circadian oscillations in mouse peripheral tissues. *Proceedings of the National Academy of Sciences of the United States of America*, 101(15):5339–5346.

[Zaidi et al., 2003] Zaidi, S. K., Young, D. W., Pockwinse, S. M., Javed, A., Lian, J. B., Stein, J. L., van Wijnen, A. J., and Stein, G. S. (2003). Mitotic partitioning and selective reorganization of tissue-specific transcription factors in progeny cells. *Proc Natl Acad Sci U S A*, 100(25):14852–14857.

[Zámborszky et al., 2007] Zámborszky, J., Hong, C. I., and Nagy, A. C. (2007). Computational analysis of mammalian cell division gated by a circadian clock: quantized cell cycles and cell size control. *J Biol Rhythms*, 22(6):542–553.

[Zhang et al., 2009] Zhang, E. E., Liu, A. C., Hirota, T., Miraglia, L. J., Welch, G., Pongsawakul, P. Y., Liu, X., Atwood, A., Huss 3rd, J. W., Janes, J., Su, A. I., Hogenesch, J. B., and Kay, S. A. (2009). A genome-wide RNAi screen for modifiers of the circadian clock in human cells. *Cell*, 139(1):199–210.

[Zhang et al., 2014] Zhang, R., Lahens, N. F., Ballance, H. I., Hughes, M. E., and Hogenesch, J. B. (2014). A circadian gene expression atlas in mammals: Implications for biology and medicine. *Proceedings of the National Academy of Sciences of the United States of America*, 111(45):16219–16224.

[Zheng et al., 2001] Zheng, B., Albrecht, U., Kaasik, K., Sage, M., Lu, W., Vaishnav, S., Li, Q., Sun, Z. S., Eichele, G., Bradley, A., and Lee, C. C. (2001). Nonredundant roles of the mper1 and mper2 genes in the mammalian circadian clock. *Cell*, 105(5):683–694.

[Zielke and Edgar, 2015] Zielke, N. and Edgar, B. A. (2015). Fucci sensors: powerful new tools for analysis of cell proliferation. *Wiley Interdiscip Rev Dev Biol*, 4(5):469–487.

[Zimmerman et al., 1968] Zimmerman, W. F., Pittendrigh, C. S., and Pavlidis, T. (1968). Temperature compensation of the circadian oscillation in drosophila pseudoobscura and its entrainment by temperature cycles. *J Insect Physiol*, 14(5):669–684.

Acknowledgements

First of all, I would like to thank Felix Naef for giving me the great possibility to work as a member of his research group and for his supporting, constructive and very patient supervision during my PhD and the drafting of this thesis.

A very big and heartfelt "thank you" goes then to my colleague Jonathan Bieler; I strongly appreciated working with him during these years and having the opportunity to develop this work in a very enriching and collaborative manner. The "synchronization" between our different backgrounds, skills and personal qualities made very enjoyable the production of this work.

I would like to thank all the co-workers who participated in the realization of this thesis and the related manuscripts: Kyle Gustafson, Cedric Gobet, Nicolas Villa and Eric Paquet for their work on the data analysis, David Gatfield and Mara de Matos for the production of shRNA cell lines, Emi Nagoshi for providing the NIH3T3-Rev-VNP cell line and the Rev-VNP construct, the members of the EPFL imaging facility (BIOP) and the EPFL Biomolecular Screening Facility (BSF) for assistance with microscopy.

Thank you as well to all the current and previous members of the Naef lab, for valuable feedbacks and discussions and funny coffee breaks. Thanks especially to my office-mate Saeed Omidi for his nice and friendly presence in the last months, and to Eric Paquet for his prompt aid and his positive drive.

A very special thanks goes to the wet-lab part of the group, and more specifically to Jerome Mermet and Damien Nicolas. I could not imagine a better daily working environment than the one I got with their presence. Their friendly collaboration and support along these years gave me a lot of motivation and strength, that turn out to be crucial in the toughest times.

I need to thank as well the support of the people who shared with me the beginning and most of the time of my PhD life, among which I strongly thank my friend Fabrizia Dutto for her lovely and ever-present help, and Livio Lattanzio for his encouraging and patient sustain. Moreover, thanks to the very long list of friends now scattered all over the word, who shared my private life along the previous years.

Acknowledgements

A very profound “thank you” to my closest friends for their tireless, authentic and caring support in the challenging and difficult last year of my life. Thanks Bea (Beatrice Volpe) for your love, your constant presence, your sweetness, your empathy, your endless generosity and your profound care. Thanks Lisa (Lisa Pollaro) for your cheerful friendship, your rational and irrational points of view and your optimistic and understanding attitude. Thanks Ale (Alessandro De Simone) for your funny, amusing and very smart humor that makes things become lighter. Thanks Marco Borotto e Marco Lai for all the cheering chats and your careful and sweet attention. Thanks Vale (Valentina Salonna), for all the deep and at the same time lhilarious conversations, for your power of defusing tough situations. Thanks Paoletta (Paola Valabrega), my flat-mate, sister and friend, because you gave me such a strength and tons of positive energies whenever I needed them, because you always trusted me. Thanks Dani e Giorgia (Danilo Ferragina e Giorgia Ritrovato), physically far away from me, but emotionally always close.

A huge thanks to my family, to which I am dedicating this thesis. *Grazie mamma e papà, perché avete sempre creduto in me, supportandomi nelle mie scelte, lasciandomi sempre la libertà di decidere il mio percorso, dandomi consigli pieni di amore e di fiducia. Grazie sorelle e fratellini, Debora, Sara, Giuseppe e Lorenzo. Ognuno di voi nel suo piccolo mi ha dato tanto, ciascuno con la propria personalità ed i propri mezzi. Grazie a tutti, siete stati fondamentali per me, da quando ho deciso di partire fino a quando ho finalmente concluso con fatica questo percorso accademico. Grazie per avermi supportato nei momenti peggiori e per avermi incoraggiato a non mollare e a continuare a credere in me stessa.*

Finally, thanks Pau Mato, for the joy you brought in my life in these last months. Thanks for your love, your calm, your kindness, your understanding, your sharing, your intelligence and your trust. *“Que tinguem sort . . . i que la vida ens doni un camí ben llarg.”*

Lausanne, September 2016 R. C.

ROSAMARIA CANNAVO

CURRICULUM VITAE

Personal details:
Place and Date of birth: Polistena (RC), ITALY, 24/08/1985
Address: Rue de l'Ale 38 CH-1003, Lausanne (Switzerland).
E-mail: rosamariacannavo@gmail.com
Phone: +41 78 942 7626
Languages: Italian (Mother tongue), English and French

Education:

2003-2006: Bachelor's degree in Biotechnology, University "Magna Graecia" of Catanzaro, Italy
Thesis title: *"Functional analysis of Inhibitor of Bruton's tyrosine kinase (IBTK)phosphorylation sites"*. Supervisor: Prof. Giuseppe Scala, MD

2006- 2009: Master's degree in Medical Biotechnologies, Second University of Naples, Naples, Italy
Thesis title: *"Computational analysis and in vivo validation of a microRNA encoded by the IBTK gene"*. Supervisor: Prof. Ileana Quinto, MD

2010–2011: Internship in the "PhD program in Cancer and Immunology", Université de Lausanne, Lausanne, Switzerland.
Project title: *"Crosstalk between Notch and p53 in paracrine control of keratinocytes and cancer cell differentiation"*. Supervisor: Prof. Gian Paolo Dotto, MD

2011-present: PhD studentship in the "Doctoral Program in Molecular Life Sciences" (EDMS) , EPFL, Lausanne, Switzerland
Thesis title: *"Circadian rhythm and cell cycle: two synchronized processes"*. Supervisor: Prof. Felix Naef

Publications:

Biochimie. 2011, *Structural and functional insights into IκB-α/HIV-1 Tat interaction*. Vitagliano L, Fiume G, Scognamiglio PL, Doti N, **Cannavò R**, Puca A, Pedone C, Scala G, Quinto I, Marasco D.

Proc Natl Acad Sci USA. 2013, *Stimulus-induced modulation of transcriptional bursting in a single mammalian gene.* Molina N, Suter DM, **Cannavo R**, Zoller B, Gotic I, Naef F.

Mol Syst Biol. 2014, *Robust synchronization of coupled circadian and cell cycle oscillators in single mammalian cells.* Bieler J, **Cannavo R**, Gustafson K, Gobet C, Gatfield D, Naef F.